WESTERN SYDNEY
UNIVERSITY

Crack Breathing Mechanism in a Cracked Shaft Subject to Nontrivial Mass Unbalance

by
Mobarak Hossain

A thesis submitted for the degree of
Doctor of Philosophy in Mechanical Engineering

Supervisors
Principal Supervisor: Dr Helen Wu
Co-Supervisor: Professor Richard Yang

School of Computing, Engineering and Mathematics
Western Sydney University, Australia
September 2018

Acknowledgments

First, I would like to acknowledge the blessings of Allah, the Almighty, who kept me strong and patient throughout this research.

I would like to express my heartfelt gratitude to my Principal Supervisor Dr. Helen Wu for her sincere guidance, continued encouragement and invaluable support and suggestions throughout my study at Western Sydney University. She has been a great source of motivation for me, continuously providing insightful comments with detailed attention to my arguments and timely advice on my work. She offered comprehensive comments and suggestions on reviewing my writings, while at the same time respecting my voice as author. I am greatly indebted to Helen for sparing her valuable time and for her efforts throughout this thesis.

I would also like to express my gratitude to my co-supervisor Professor Richard Yang for his sincere advice, support and recommendation.

I would like to thank Dr. Keqin Xiao for his time and expertise. I also would like to thank Declan Williams for his contribution to develop area moment of inertia formulas. I would like to extend my appreciation to all the academic, administrative and technical staff at the School of Computing, Engineering and Mathematics, Western Sydney University. Moreover, I offer thanks to my fellow Ph.D. colleagues and friends for being supportive and providing courage and inspiration during the study period.

I gratefully acknowledge Western Sydney University for awarding me the WSU Postgraduate Scholarship.

Finally, I would like to show my sincere and heartfelt gratitude to my respected parents for their silent inspiration. I would especially like to thank my passionate life partner and beloved wife Zarin Zaman Shammy and sweet daughters Mahaseen Mobarak and Samreen Mobarak for their continuous unconditional support and sacrifices to make my study smooth.

Statement of Authentication

I, Mobarak Hossain, declare that all the materials presented in the Ph.D. thesis entitled ‘Crack Breathing Mechanism in a Cracked Shaft Subject to Nontrivial Mass Unbalance’ are my work, and that any work adopted from other sources is duly cited and referenced as such.

This thesis contains no material that has been submitted previously, in whole or in part, for any award or degree in other university or institution.

……

Mobarak Hossain
September 2018

Publications

The following papers, published in peer-reviewed journals and conference proceedings, are the outcome of this thesis:

Journal Papers

1. Mobarak, H. M., Wu, H., Spagnol, J.P., & Xiao, K. (2018). New crack breathing mechanism under the influence of unbalance force. *Archive of Applied Mechanics, 88*, 341–372.

2. Mobarak, H. M., & Wu, H. (2018). Crack breathing behaviour of unbalance rotor system: A quasi-static numerical analysis. *Journal of Vibroengineering, 20*, 1459–1469.

3. Mobarak, H. M., Wu, H., & Yang, C. (2017). Dependence of shaft stiffness on the crack location. *International Journal of Mechanical, Aerospace, Industrial, Mechatronic and Manufacturing Engineering, 11*, 300–305.

4. Mobarak, H. M., Wu, H., & Xiao, K. (2017). Numerical analysis of effect of crack location on the crack breathing behaviour. *International Journal of Aerospace and Mechanical Engineering, 11*, 1811–1815.

5. Mobarak, H. M., Wu, H., & Yang, C. (2018). Effect of unbalance force on the crack breathing mechanism. *International Journal of Mechanical Engineering and Robotics Research (IJMERR), 7*, 174–178.

Conference Proceedings

1. Mobarak, H. M., Wu, H, & Yang, C. (2017). *Influence of angular position of unbalance force on crack breathing mechanism*. Paper presented at the Fifth International Symposium on Robotics & Mechatronics (ISRM2017), Sydney, Australia.

2. Mobarak, H. M., & Wu, H. (2016). Crack breathing as a function of crack location under the effect of unbalance force. In *Proceedings of 24th Australasian Conference on the Mechanics of Structures and Materials: Advancements and Challenges (ACMSM24)*, Hong Hao & Chunwei Zhang (Eds), London, England: Taylor & Francis, 377–382.

Table of Contents

List of Tables

List of Figures

List of Abbreviations

CCL	Crack closure line
CWT	Continuous wavelet transform
DOF	Degree of freedom
LS	Least-squares
SERR	Strain energy release rate
SIF	Stress intensity factor
3D FE	Three-dimensional finite element
3D FEA	Three-dimensional finite element analysis
3D FEM	Three-dimensional finite element method

Abstract

Rotating machinery is widely used in many industrial fields and is often damaged owing to the breathing of the fatigue crack. The fatigue crack opens and closes once per revolution during shaft rotation. The breathing of the fatigue crack reduces the stiffness of the shaft and hence alters its dynamic response. It changes the vibration characteristics of the shaft. Fatigue cracks are a common occurrence in large rotor systems and can cause catastrophic failure. Detecting faults in rotating machinery before failure is the best way to avoid damage. However, a generalised method of positively identifying a fatigue crack as the cause of anomalous vibrations is not yet available.

Vibration diagnostics deliver insights into the mechanical 'health' of rotating machinery in real-time when the machine is running. However, studying the vibrations of naturally occurring fatigue cracks is difficult because shafts will often either fail before, or be taken out of service once, the crack is identified. Artificially introduced cracks do not exhibit behaviour identical to that of natural ones owing to the difficulty in cutting into a shaft and leaving a slot with close to zero radius at the crack tip. Therefore, considerable efforts have been devoted to numerically modelling cracked rotors and simulating their operating conditions so that the vibrations can be studied. Numerical modelling techniques are many and varied. In the present thesis, the literature on cracked rotor dynamics is reviewed. Of the crack modelling techniques reviewed, the second area moment method is identified as having potential for improvement.

The second area moment method accounts for reduction in bending stiffness of a cracked rotor. Breathing of the fatigue crack is directly related to the second area moment at the crack location. It leads to changes in one of the shaft mechanical properties, stiffness. In a shaft with a crack, the shaft stiffness will change periodically at different rotational angles. Modelling the breathing of the fatigue crack is the key step to analyse the vibration response of a cracked shaft. This breathing phenomenon must be modelled accurately to detect the crack in a rotor. However, it is not yet fully understood how partial crack closure interacts with

changes in shaft stiffness, and further, with key variables of the crack detection problem.

Unfortunately, almost all existing models are not applicable near the shaft critical speed, because equations of motion developed under the assumption of rotor weight dominance are no longer suitable for analysis near the critical speed. Moreover, localised reduction in stiffness is directly related to crack depth, whereas global reduction in stiffness is directly related to the crack depth and crack location along the shaft. However, researchers opt to either ignore crack location or mitigate its effects. From the literature review, it is evident that accurate modelling, which considers the influence of the crack location and the effect of the unbalance force on the crack breathing behaviour of the fatigue crack to calculate the second area moment of inertia of a cracked shaft to form the stiffness matrix, is still absent.

The first topic in this research work is developing a new unbalance model—effectual bending angle—to evaluate the crack breathing response and calculate the second area moment of inertia at any crack location along the shaft length. It is developed considering the effects of unbalance force, rotor weight, rotor physical and dimensional properties and a more realistic fixed-end boundary condition. It governs the opening and closing of a shaft crack that describes the proximity of the shaft bending direction (or shaft deformation direction) relative to the crack direction. The crack breathing behaviours have been studied for every possible crack location and shaft rotation angle. The presented model identifies unique crack breathing behaviours under the influence of unbalance force and rotor physical and dimensional properties, showing the strong dependence of the breathing mechanism on the crack location. Further, the newly developed model is used to obtain the second area moment of inertia of crack cross-section closed area at any crack location along the shaft length under the unbalance force effect about the centroid. The newly developed unbalance model results are validated through 3D FEM results. This thesis finds that this analytical unbalance model captures the main features of crack breathing and is in good agreement with the 3D FEM. However, the approach adopted in this study of using the existing balance model to identify the crack breathing behaviour and the second area moment of inertia needs to be improved.

In this research work, a new method is developed to determine crack breathing, which is an improvement in terms of accuracy on adopted methods. The improvement is owing to the removal of two simplifying assumptions used by previous authors, namely, that the cracked shafts will only experience symmetrical bending and the neutral axis would lie perpendicular to the bending direction, that is, always be horizontal. Both assumptions are shown to be invalid on comparison with results from a three-dimensional finite element model. The newly developed method is then used to evaluate nonlinear crack breathing behaviour under different weight–unbalance force ratios at different crack locations by examining the percentage of opening of a crack. The breathing response predicted by the developed method is validated using the three-dimensional finite element model. The results of the algorithm show a significant improvement in accuracy when compared with data from the three-dimensional finite element model of cracked rotors.

The mathematical modelling of calculating the cross-section properties, namely, the second area moment and centroid location, is also improved in this research work by considering neutral axis inclination, removing the assumption of collinearity between the bending moment and neutral axis at the crack location. The newly developed equations are used to evaluate the second area moment of inertia as a function of the crack locations and shaft's angle of rotation about centroid axes. It is found to be highly dependent on crack location, similar to crack breathing behaviours. The work presented in this thesis demonstrates that a common assumption in the literature—that the effects of axial position of a crack can be neglected—is incorrect.

The second topic of this research work is analysis of the crack breathing behaviour of an unbalance shaft with a more realistic transverse slant crack and elliptical crack at different crack locations along the shaft length. A three-dimensional finite element model consisting of a two-disk rotor with a crack is simulated with unbalance mass. The finite element model is simulated using Abaqus/standard. It is simulated considering the effects of unbalance force, rotor weight, rotor physical and dimensional properties and a more realistic fixed-end boundary condition. Crack breathing behaviours are visualised by the variation of the crack closed area and represented quantitatively by the percentage of the closing of the crack. Crack breathing behaviour is found to strongly depend on its axial position, angular

position and depth ratios as well as unbalance force ratios and angular position of unbalance force. Compared with the balance shaft crack breathing behaviour, two different crack breathing regions along the shaft length are identified, where shaft stiffness is larger or smaller, depending on the unbalance force orientation, magnitude and crack location. However, four specific crack locations along the shaft length are identified where the crack remains fully closed or open or the same as in balance shaft crack breathing during shaft rotation under different loading conditions.

The presented research results suggest that a more accurate prediction of the dynamic response of cracked rotors can be expected on considering the effects of unbalance force and individual rotor physical properties on crack breathing. The presented method and results of this research can be used to obtain the stiffness matrix of a cracked shaft element and then to study the vibration response of a cracked rotor where the rotor-weight-dominant assumption on crack breathing no longer holds.

Chapter 1 : Introduction

1.1 Introduction

Machine failure can be catastrophic and lead to economic issues as well as personal injury. Considering that shafts are a fundamental component of high-speed rotating machinery used in industries such as aerospace, nuclear power, oil and transportation and in industry processes in general, the issues of fatigue crack generation and propagation in a shaft become more significant (Andreaus, Baragatti, Casini, & Iacoviello, 2017; Fayed, 2017). Owing to the ever-increasing importance placed on safety and economic efficiency, research on prevention and early diagnosis of defective machinery is becoming more valuable. The presence of a crack in a mechanical component can alter its behaviour in various ways, including the increase of displacements and decrease in frequency owing to a rise in component flexibility (Giannopoulos, Georgantzinos, & Anifantis, 2015; Hou, Chen, Cao, & Lu, 2016; Jain, Rastogi, & Agrawal, 2016; Ren, Zhou, Gong & Wen, 2015).

The breathing of the fatigue crack in rotating machinery has attracted significant attention in the literature as one of the main causes of damage in rotor systems. Crack breathing occurs in rotating machinery because of the opening and closing of the crack. The stresses and strains acting upon the crack are a result of static loads (self-weight and bearing reaction forces) and dynamic loads (mass unbalance and inertial force) in the form of the bending moment, while the effect of torsion is negligible (Bachschmid, Pennacchi, & Tanzi, 2010; Walker, Vayanat, Perinpanayagam, & Jennions, 2014).

When cracks are present in a shaft, there is a transient change in shaft stiffness about the crack region corresponding to the breathing of the crack (Mayes & Davies, 1984). When the stresses on a crack surface are compressive, the crack remains closed and the shaft has almost the same stiffness as an intact shaft. When the stress becomes tensile, the crack will open, in which case the stiffness of the shaft is reduced significantly. The intermediate situation between the fully open and fully closed state is a partially open or partially closed crack. For partially open/closed crack statuses, the shaft stiffness is between the maximum and minimum values (Wang, Guo, & Heyns, 2012).

The changes in shaft stiffness owing to the breathing of the fatigue crack lead to sudden and destructive vibration scenarios (Bovsunovsky & Surace, 2015). The change in the vibration characteristics of a shaft has the potential to cause unpredicted equipment failure and damage that may lead to a loss of life and equipment.

1.2 Research Background: Brief Outline

The early detection of the vibration signs of a cracked rotor was based on vibration analysis, and many different methods of the vibration model have been proposed to forecast the characteristic vibration responses of a rotor with a crack (Bachschmid, Pennacchi, Tanzi, & Vania, 2000; Tiwari & Chougale, 2014). The success of these methods largely depended on the accuracy of the modelling of the crack breathing behaviour. The crack breathing model considers that a crack can switch states from fully open to fully close when rotating to a horizontal position, and the research conducted shows the simplified difference of the actual crack breathing (Barenblatt, 1962; Williams, 1961). The issue with this model is that chaotic and quasiperiodic vibrations owing to the sudden change of the crack state have not been observed in experimental tests (Al-Shudeifat, Butcher, & Stern, 2010). A later modification is the switch model, which provides a smooth and gradual change of the crack opening and closing status by using different trigonometric functions (Bachschmid & Pennacchi, 2008; Bachschmid et al., 2010). For this transient breathing model, the crack status remains fully open and fully closed at two single positions, when the crack points downwards and upwards. The crack remains fully open during a range of shaft rotation angles, and the same occurs in the fully closed state (Bachschmid & Tanzi, 2004). A new crack breathing mechanism was proposed by Al-Shudeifat and Butcher (2011) where the crack is no longer observed to be fully open or fully closed at a single rotation angle.

To find the periodic stiffness of a cracked shaft element, two important theories have been proposed. The first approach is based on the strain energy release rate (SERR) theory (Papadopoulos, 2008; Darpe, Gupta, & Chawla, 2004; Wu, Sawicki, Friswell, & Baaklini, 2005), which is used to calculate a local compliance matrix using an approximated stress intensity factor (SIF) at each point along the crack front. Darpe, Gupta and Chawla (2004) and Papadopoulos (2004) used the SERR approach and

calculated the breathing by evaluating on the rectilinear crack tip where the crack begins to close, assuming that the closed part of the crack surface is delimited by a boundary, the crack closure line (CCL). The same approach was used by Wu, Sawicki, Friswell and Baaklini (2005) in time step calculations where vibrations determined breathing. Bachschmid and Tanzi (2004) used the three-dimensional finite element method (3D FEM) to show that depending on the applied forces, there are no constant strains and stresses along the crack tip. Some studies (Papadopoulos, 2008; Darpe et al., 2004; Pennacchi, Bachschmid, & Vania, 2006) have found that the SERR approach is valid only for the fully open crack for calculating the additional flexibility owing to the crack, but cannot be extended to other intermediate situations, because of the breathing mechanism. In this case, for comparison purposes, it was assumed the 'breathing' mechanism was known (from FEM or from the simplified model), and the SERR approach was applied to the cracked cross-section, with its open and closed portions, to calculate the beam-bending stiffness.

The second approach is based on a theoretical model of a transverse crack by reducing the area moment of inertia of the element at the location of the crack where this change in area moment is used to develop time-varying stiffness matrix equations. Such a method is observed in various studies (Bachschmid et al., 2010; Guo et al., 2013; Jun & Gadala, 2008; Sinou, 2007) and further developed in Al-Shudeifat and Butcher (2011). Mayes and Davies (1984) first demonstrated that a transverse crack in a rotor shaft might be represented by the reduction of the area moment of the element at the crack location. They established that the cross-section of the rotor shaft at the crack location has asymmetric area moment of inertia about the neutral axis of bending. Sinou and Lees (2005) obtained the stiffness matrix owing to the transverse crack at the crack location by using the standard FEM, and they revealed that the opening and closing behaviour owing to the rotor rotation and shaft self-weight results in time-dependent stiffness. Guo et al. (2013) implemented the area moment of inertia models in the literature (Al-Shudeifat, 2013; Al-Shudeifat & Butcher, 2011; Al-Shudeifat et al., 2010) to perform a parametric stability analysis on a cracked Jeffcott rotor using the Floquet theory. The FEM was used in modelling the equations of motion of the cracked rotor, whereas the flexibility matrix was used in modelling the stiffness matrix of the cracked element (Darpe, 2007). The finite element stiffness matrix of a rod in space found by Pilkey (2002) was used to

represent the time-varying stiffness matrix of the cracked element (Al-Shudeifat et al., 2010; Sinou & Lees, 2007; Sinou, 2007, 2008; Sinou & Lees, 2005). The transfer matrix method was employed in studying the behaviour of the cracked rotor system where the second harmonic characteristics were used in detecting the crack in the system (Green & Casey, 2005).

Some studies have considered the effects of significant dynamic loads on the crack breathing mechanism and vibration responses. Previously, Bachschmid, Pennacchi and Tanzi (2010) considerably reduced the damping of the cracked rotor system to study the effect of the nonlinear breathing mechanism on the crack in a more severe condition. The hypothesis was developed from the fact that unstable vibration often exhibited the full opening of crack in breathing behaviour. As a result, it was found that system stability was restored at times by the presence of this unbalance. Cheng, Li, Chen and He (2011) also observed that rotor stability could be restored owing to the unbalance. A further proposal was made that the minimum amplitude of vibration is related to the eccentric mass being located at the crack direction and the maximum amplitude of vibration occurs owing to the eccentric mass being located opposite the crack.

Some studies used commercial FEM software (Rubio, Munoz-Abella, Rubio, & Montero, 2014) to simulate a cracked Jeffcott rotor to study the impact of mass unbalance on the crack breathing mechanism. Here, specific attention was given to the significance of eccentric mass with respect to (w.r.t.) the crack position, particularly highlighting the fact that in case of some crack depths, the crack can be fully closed when the eccentric mass is opposite the crack location. Conversely, the event of crack and eccentricity being in the same direction causes the crack to remain fully open. It was found that the crack breathing behaviour in the presence of the unbalance greatly differs from the weight-governed crack breathing.

1.3 Research Problem Statement

Studies based on large rotating machinery widely consider the crack breathing mechanism to be dominated by self-weight (weight-dominant breathing) (Rao, 2011). For lightweight rotors, vertical machinery and lightly damped rotors, the breathing mechanism is not always weight dominated since dynamic loads exert

significant influence (Cheng, Chen, & He, 2011). Moreover, almost all existing models are not applicable near the shaft critical speed because the lower damping expands the range that dynamic behaviour dominates. As such, equations of motion developed under the assumption of rotor weight dominance are no longer suitable for analysis near the critical speed (Cheng et al., 2011; Gasch, 1993).

The localised reduction in stiffness is directly related to crack depth, whereas crack depth influences both the global reduction in stiffness and crack location along the shaft (Lin & Chu, 2010). Unfortunately, researchers opt to either ignore crack location or mitigate its effects. Existing models in the literature are based on simplified models. Often, researchers ignored the effects of unbalance force, rotor weight, rotor physical and dimensional properties and a more realistic fixed-end boundary condition. Moreover, researchers considered the cracked shafts will only experience symmetrical bending and the neutral axis would lie perpendicular to the bending direction, that is, always be horizontal. It is evident that an accurate model, which considers the influence of crack location on the crack breathing behaviour of the fatigue crack under the effect of the unbalance force and can calculate the area moment of inertia of a cracked shaft to form the local stiffness matrix, is still absent.

1.4 Research Objectives

The objectives of this research are as follows:

1. To develop a unbalance model to study the crack breathing behaviour of the fatigue crack under the effects of unbalance force, rotor weight, rotor physical and dimensional properties and a more realistic fixed-end boundary condition.

    a) First, a parameter known as the effectual loading angle is developed to describe the nonlinear relational between shaft bending direction relative to the crack direction under the influence of the dynamic loading, shaft and disk weights and the boundary condition.
    b) This newly developed model is used to analyse the breathing behaviour of cracks under different weight–unbalance force ratios at different crack locations by examining the duration of each crack state (open, closed and partially open/closed) and percentage of opening of the crack.

c) This newly developed unbalance model is then used to calculate the change in the area moment of inertia of a cracked shaft at every possible crack location and shaft rotation angle.
d) The obtained results are verified through 3D FEM results.

2. To develop an improved crack breathing mechanism considering the inclination of neutral axis that will remove two simplifying assumptions used by previous authors, namely, that the cracked shafts will only experience symmetrical bending and the neutral axis would lie perpendicular to the bending direction, that is, always be horizontal.

   a) First, a model to describe the actual breathing mechanism of the crack is developed for numerous crack location/unbalance configurations.
   b) Then, this model is used to evaluate nonlinear crack breathing behaviour under different weight–unbalance force ratios at different crack locations by examining the percentage of opening of a crack.
   c) Results of this newly developed crack breathing mechanism are verified using 3D simulated model results.

3. To develop mathematical formulas to calculate the area moment of inertia at the cracked cross-section of the unbalance shaft, this can be used by other researchers and engineers to predict the dynamic response of a cracked shaft.

   a) First, mathematical formulas to calculate the area moment of inertia at the cracked cross-section of the unbalance shaft are developed.
   b) Then, this model is used to determine the area moment of inertia about the centroid axes under different weight–unbalance force ratios at different crack locations.

4. To analyse the crack breathing behaviour of the unbalance shaft with more realistic fatigue cracks, such as slant crack and elliptical crack, at different crack locations along the shaft length under the effects of unbalance force, rotor weight, rotor physical and dimensional properties and a more realistic fixed-end boundary condition.

a) First, a three-dimensional finite element (3D FE) model of a two-disk rotor with a transverse crack (slant and elliptical cracks) is simulated using Abaqus/standard.
b) Then, crack breathing behaviours are analysed by visualising the status of crack and the percentage of the closing of the crack under the coupling influence of rotor weight and unbalance force.

1.5 Research Method: Brief Outline

The research is conducted through two studies, namely, analytical and numerical, to fulfil the study objectives.

1.5.1 Analytical study

The analytical study of this research mainly consists of deriving the formulas for the cracked rotor system considering the influence of the crack location, unbalance force, rotor weight, rotor physical and dimensional properties and a more realistic fixed-end boundary condition, which include:

a) effectual bending angle
b) key instants of crack breathing mechanism: a crack begins to close and right after crack becomes fully closed
c) centroid coordinates of the crack cross-section closed area
d) area of crack cross-section closed area
e) second area moment of inertia of crack cross-section closed area about centroid axes.

The following configurations of cracks and unbalance forces are considered in deriving these formulas:

a) the unbalance force ratio, η, the ratio of the gravitational force (shaft self-weight and two disk weights) and the unbalance force, to evaluate the influence of the unbalance force magnitude
b) the crack location factor, λ, the ratio of the crack position, $l_{0,}$ and the total shaft length, L, to evaluate the influence of the crack position

c) angular positions of the crack or shaft rotational angles, θ, varying from 0° to 360° to evaluate the influence of the crack angular position
d) the angular position of unbalance force, β, varying from 0° to 360° to evaluate the influence of the unbalance force angular position w.r.t. the crack cross-section plane
e) the crack depth ratio, μ, the ratio of the crack depth and shaft radius, to evaluate the influence of the crack depth.

A series of analyses are performed using the MATLAB software to solve the aforementioned formulas to evaluate the following characteristics of the cracked rotor system considering these configurations of cracks and unbalance forces:

a) effectual bending angle
b) crack status
c) percentage of opening or closing of the crack
d) centroid coordinates of the crack cross-section closed area
e) areas of crack cross-section closed area
f) area moment of inertia of crack cross-section closed area about centroid axes.

1.5.2 Numerical study

The numerical study of this research mainly consists of modelling and analysis of the cracked rotor system. A full 3D FE model of a two-disk rotor with a transverse slant crack and elliptical crack is employed using Abaqus/standard to investigate the crack breathing mechanism under the coupling influence of crack location, unbalance force, rotor weight, rotor physical and dimensional properties and a more realistic fixed-end boundary condition. The crack section is generated by joining two shafts together using the Abaqus 'Tie constraint' function, which constitutes the intact part of the cracked section. Both normal and tangential properties of crack surfaces are defined in the finite element numerical model to avoid the penetration between the crack surfaces as well as the relative sliding between two crack surfaces when the crack is closed.

The shaft is meshed by using an element called linear hexahedral element of type C3D8R. The mesh density used is much higher around the crack in transversal and

longitudinal directions. The mesh size is obtained after a convergence test of the results through mesh sensitivity analyses. The simulation is conducted as a series of static problems with different crack locations along the shaft length and shaft rotation angles. The following configurations of crack location and angular position are considered:

a) 40 different crack location factor, λ, varying from 0 to 1 with an increment of 0.025 to evaluate the influence of the crack position along the shaft length
b) 24 different angular positions of the crack varying from 0° to 360° with an increment of 15° to evaluate the influence of the crack angular position.

The unbalance force is taken as a rotational force and at an angular position w.r.t. the crack on the shaft cross-section plane. The following unbalance configurations are considered:

a) 5 different ratios of unbalance force to the rotor weight (two disks and shaft), that is, 5, 10, 20, 100 and ∞ (balance), to evaluate the influence of the unbalance force magnitude
c) 5 different angular positions of unbalance force, namely, 0°, 45°, 90°, 135° and 180°, to evaluate the influence of the unbalance force angular position w.r.t. the crack cross-section plane. Only half of the angular range of unbalance force (0° to 180°) is considered because of the symmetry.

The shaft self-weight is applied as a gravitational force, and two disk weights are applied as the concentrated forces in the vertical direction (downward). Unbalance force is applied as a concentrated force in the horizontal and vertical directions of the shaft cross-section at the right disk. A large number of simulations are performed to examine the influence of crack location, crack angular position, unbalance force ratio and its angular position on the crack opening and closing. The results are compared with those of the balance shaft. Steady-state vibrations for unbalance shaft under some configurations are also simulated.

1.6 Research Contributions

In this thesis, new mathematical models and 3D FEM are developed to analyse the crack breathing behaviour and calculate the area moment of inertia of a cracked shaft considering the effect of crack location, unbalance force, rotor weight, rotor physical and dimensional properties and a more realistic fixed-end boundary condition. Crack breathing behaviour and the area moment of inertia are found to strongly depend on its axial position, angular position and depth ratios as well as unbalance force ratios and angular position. The presented research results suggest that a more accurate prediction of the dynamic response of cracked rotors can be expected on considering the effects of unbalance force and individual rotor physical properties on crack breathing. The developed model can be further used by other researchers and engineers to obtain the local stiffness matrix of a cracked shaft element to predict the vibration response of a cracked rotor and to develop online crack detection techniques, in particular, near the shaft critical speeds or where the rotor-weight-dominant assumption on the crack breathing no longer holds.

The major contributions of this thesis include:

1. A new parameter, effectual loading angle, is developed to describe the nonlinear relational between shaft bending direction relative to the crack direction considering the effect of crack location, rotor weight, rotor physical and dimensional properties, the unbalance force and the boundary condition. It governs the opening and closing of a shaft crack. It is used to evaluate the crack breathing response and calculate the second area moment of inertia at any crack location along the shaft length considering the effect of rotor weight, rotor physical and dimensional properties, the unbalance force and the boundary condition.
2. An improved crack breathing mechanism is developed to evaluate nonlinear crack breathing behaviour under different weight–unbalance force ratios at different crack locations by examining the percentage of opening of a crack considering the inclination of neutral axis. The newly developed improved crack breathing model is improved because of the removal of two simplifying assumptions used by previous authors, namely, that the cracked shafts will

only experience symmetrical bending and the neutral axis would lie perpendicular to the bending direction, that is, always be horizontal.

3. Mathematical formulas are developed to calculate the area moment of inertia at the cracked cross-section of the unbalance shaft, which can be used to form the local stiffness matrix to identify a unique vibration signal that will be able to reflect the dynamic behaviour of a cracked shaft.
4. The presented research in this thesis reveals that crack breathing—unlike weight-dominated crack breathing—is largely influenced by the unbalance force and the individual rotor physical parameters, generating a dependence of crack breathing on its location at the shaft. This research provides important insights into the modelling of local stiffness matrix through crack breathing. This matrix is usually used to calculate the dynamic response of cracked rotors. Based on the steady-state vibration analysis, it is demonstrated that for more accurate prediction of the dynamic response and damage severity of cracked rotors, researchers must consider the effects of unbalance force and individual rotor physical properties on the crack breathing.

1.7 Thesis Outline

This thesis consists of eight chapters, with a brief background on the research, statement of the research problem, research objectives and contribution presented in Chapter 1.

Chapter 2: This chapter contains the literature review, which explores previous research in the Rotordynamic field, about cracked rotor models and different approaches to vibration analysis. A case is made in Section 2.5 for the summary of current gaps in research and the mathematical and numerical models, which are covered in Chapters 3 to 7, are proposed.

Chapter 3: In this chapter, a new unbalance model, which considers the coupling effects of unbalance force, rotor weight and rotor physical and dimensional properties and a more realistic fixed-end boundary condition, is developed to study the breathing mechanisms of the transverse fatigue crack in a cracked rotor system, which is explained in detail in Section 3.4, and to calculate the

area moment of inertia of a cracked shaft, which is explained in detail in Section 3.5. In Sections 3.2 and 3.3, the effectual bending angles for a different combination of unbalance force ratio, crack location along the shaft length and angular position of unbalance force and crack are developed and analysed. In Section 3.4, the breathing of the crack for different force ratios at different crack locations during shaft rotation is identified using the values of the newly developed parameter, effectual bending angle. In Section 3.5, centroidal orbits and area moment of inertia of the unbalance cracked shaft are analysed. In Section 3.6, the breathing response predicted by the developed method is validated using the three-dimensional finite element model.

Chapter 4: In this chapter, a new model is developed to determine crack breathing, which is an improvement in terms of accuracy on adopted methods in Chapter 3. It is developed considering the inclination of neutral axis and by removing two simplifying assumptions used by previous authors, namely, that the cracked shafts will only experience symmetrical bending and the neutral axis would lie perpendicular to the bending direction, that is, always be horizontal. In Section 4.2, the new model is developed to determine the actual crack breathing mechanism of an unbalance cracked shaft. In Section 4.3, this newly improved crack breathing model is used to evaluate nonlinear crack breathing behaviour under different weight–unbalance force ratios at different crack locations by examining the percentage of opening of a crack. The results of the newly developed crack breathing behaviour model are compared with 3D FEM and unbalance model crack breathing mechanism results presented in Chapter 3.

Chapter 5: This chapter focuses on the ultimate purpose of this study, which is to establish an improved model to calculate the area moment of inertia at the cracked cross-section of the unbalance shaft that can be used by other researchers and engineers to obtain local stiffness matrix of a cracked shaft element to predict the vibration response of a cracked rotor and to develop online crack detection techniques, in particular, near the shaft critical speeds or where the rotor-weight-dominant assumption on the crack breathing no

longer holds. In Section 5.2, formulas related to the crack closed area and centroid coordinates of crack cross-section closed area are developed. Formulas related to the area moment of inertia and principal area moments of inertia are developed in Sections 5.3 and 5.4 respectively. In Section 5.5, formulas to calculate the inclination of the neutral axis are developed. In Section 5.6, the area moment of inertia about the centroid axes are calculated using the newly improved formulas presented in Sections 5.2 to 5.5. The results of the newly developed formulas of the area moment of inertia are compared with unbalance model area moment of inertia results presented in Chapter 3.

Chapter 6: In this chapter, numerically analyses of the crack breathing behaviour of unbalance shaft with a more realistic transverse slant crack at different crack locations along the shaft length are presented. Simulations of crack breathing behaviour are conducted considering the effects of unbalance force, rotor weight, rotor physical and dimensional properties and a more realistic fixed-end boundary condition. In Section 6.2, a full 3D rotor model is simulated with a slant crack. In Section 6.3, crack breathing behaviours are visualised by the variation of the crack closed area and represented quantitatively by the percentage of the closing of the crack. In Section 6.4, centroidal orbits of a crack cross-section are analysed to predict the dynamic response of a cracked rotor with a slant crack at different crack locations along the shaft length.

Chapter 7: In this chapter, numerical analyses of the crack breathing behaviour of unbalance shaft with a more realistic elliptical crack at different crack locations along the shaft length are presented. Simulations of crack breathing behaviour are conducted considering the effects of unbalance force, rotor weight, rotor physical and dimensional properties and a more realistic fixed-end boundary condition. In Section 7.2, a full 3D rotor model is simulated with an elliptical crack. In Section 7.3, crack breathing behaviours are visualised by the variation of the crack closed area and represented quantitatively by the percentage of the closing of the crack.

Chapter 8: This chapter provides a summary of the results and concluding remarks with recommendations for future research.

Chapter 2 : Literature Review

2.1 Introduction

The literature review is structured as follows: First, key concepts necessary for understanding cracks and crack detection are explored in rough order of most relevant to least relevant. Next, previous research in the Rotordynamic field about cracked rotor models and different approaches to vibration analysis is explored. Finally, a case is made for the summary of current gaps in research.

2.2 Characteristics of a Cracked Shaft

Crack breathing is one of the popular approaches adopted by many researchers for studying the dynamics of a cracked shaft (Sekhar, Mohanty, & Prabhakar, 2005). In large industrial turbine-generator rotors, static deflection often dictates shaft vibration patterns. If any cracks are present in this type of rotor, the crack will open and close according to the shaft rotation (Pennacchi et al., 2006).

Crack breathing behaviour lead to changes in one of the shaft mechanical properties, stiffness (Mayes & Davies, 1984). An intact shaft's stiffness normally has the same value at different angles of rotation. However, when a shaft has a crack, the shaft stiffness will change periodically at different rotational angles.

This breathing phenomenon is one of the crucial characteristics of the cracked shaft (Lee et al., 2014). It attracts many researchers to focus on it for the study of cracked shaft diagnostics. However, it is not yet fully understood how partial crack closure interacts with changes in shaft stiffness, and further, with key variables of the crack detection problem. Crack breathing mechanism plays an important role in the analysis of dynamic behaviour of a cracked rotor. This breathing phenomenon must be modelled accurately to detect the crack in a rotor (Kumar & Rastogi, 2009).

2.2.1 Development of fatigue cracks

The development of fatigue cracks in rotor systems exhibits three phases, crack initiation, the subsequent propagation of the crack and the rotor remaining untreated (Yan, Stefano, Matta, & Feng, 2013). Fatigue cracks in a shaft may arise from some

influences, such as material defects, sudden geometry changes or thermal stresses. These inconsistencies possess a commonality where affected regions of the shaft are exposed to an immense level of stress concentration relative to the surrounding areas (Silani, Ziaei-Rad, & Talebi, 2013). To avoid repetition, when a material inconsistency decreases the area of applied force there will be a subsequent increase in stress about that region. Further, if there is a decrease in fatigue strength by impurities or other external factors, then cracks are more likely to appear in the affected locations.

Surface scratches, material porosity and material inclusion are material defects that may arise during manufacturing or handling processes. In short, surface scratches are scrapes, marks or chips present on the exterior surface. Porosity relates to the void space percentage of the total volume and inclusion that occurs when foreign material taints the homogeneity of another material. Surface scratches and material porosity increase the likelihood of crack initiation by decreasing the area at which the loading is applied. Material inclusion, particularly when the impurity contains material with lower fatigue strength, will definitely result in cracks appearing in the area of impurity before the surrounding locations, assuming no sudden geometry changes are observed in nether regions (Ricci & Pennacchi, 2012).

Sharp changes in the geometry of the rotor are an integral part of engineering design, and therefore, the resulting areas of high-stress concentration are unavoidable. Changes in diameter or geometry of the shaft are created when holes, key slots, threading and various other mechanical elements are present (Bachschmid et al., 2010). Further, the development of thermal stresses in a concentrated region of the shaft can occur in some rotating machinery. Steam and gas turbines may generate thermal stresses or thermal shocks that are responsible for high local SIFs as a result of thermodynamic interactions of the working fluid and the ambient surroundings (Bachschmid et al., 2010).

A rotating shaft is subjected to different types of mechanical stresses, such as bending, torsional, shear and static radial loads (Han & Chu, 2012). A crack will be initiated in the local region where stresses exceed the yield strength of the shaft material, which may have already been reduced owing to fatigue. As the crack grows to a certain depth, the shaft cannot support the static and dynamic loading anymore.

Consequently, the shaft would often experience a sudden fracture, causing enormous costs in downtime and possible injuries to people (Tian, Jin, Wu, & Ding, 2011; Wang & Heyns, 2011).

2.2.2 Types of fatigue crack

A variety of literature examines many types of cracks, namely transverse, conical and helical cracks; however, transverse cracks are the most frequent in rotors. Some papers in the literature that focus on a specific type of crack, such as transverse cracks and slant cracks, are reviewed in this subsection.

2.2.2.1 Transverse cracks

Transverse cracks are defined as having a crack surface that is orthogonal to the rotation axis of the shaft (Bachschmid et al., 2010). Intrinsically, a horizontally supported rotor is likely to develop transverse cracks about its top and underside since these regions experience the highest alternating stresses. Transverse cracks formed in this manner experience a nonlinear concept known as breathing, where the crack area alternates between an open state and a closed state because of the self-weight bending experienced during rotation (Ishida & Yamamoto, 2013).

The study of transverse cracks has been extensive because being perpendicular to the shaft they reduce the cross-sectional area and result in significant damages to rotors (Liong & Proppe, 2011; Zhou, Sun, Xu, & Han, 2005). Many factors can influence the occurrence of shaft cracks (Sabnavis, Kirk, Kasarda, & Quinn, 2004). A transverse crack caused by material fatigue is a very common defect in rotating equipment that operates for extended periods under heavy load (Kulesza & Sawicki, 2012; Ricci & Pennacchi, 2012).

A transverse crack is typically found midlength in the longitudinal direction and is a result of maximum bending stresses occurring in this region. Giannopoulos, Georgantzinos and Anifantis (2015) used a Laval rotor with a transverse surface crack and unbalance disk to show resonance occurring once per revolution, twice per revolution and thrice per revolution crack force excitation. Darpe (2007) used wavelet transforms for studying resonant bending vibrations to detect transverse

cracks. This technique had a high sensitivity to changes in crack depth and displayed the ability to detect cracks as small as 5% of the rotor diameter.

2.2.2.2 Slant cracks

Slant cracks can be a result of repeated torsional loads with simultaneous bending in rotors. Han, Zhao, Lu, Peng and Chu (2014) used the direction spectral method to study the force response of the geared rotor system with slant cracked shaft. The forced response spectra were closely examined to consider the effect of crack type and crack depth on systems with and without torsional excitations. Conversely, systems containing torsional excitations heavily influenced the force response spectra. The spectra relating to rotating speed were insensitive to shallow cracks (Han, Zhao, Lu, Peng, & Chu, 2014). The latter discovery renders such a method ineffective for early diagnosis of cracks. Despite this shortcoming, the authors highlighted subcritical resonances in the frequency response owing to crack breathing. For geared rotor systems, identification of subcritical resonance appears to be partly indicative of the presence of cracks; however, such analysis has no bearing on the early development of cracks.

2.2.3 Breathing of fatigue crack

The breathing of the fatigue crack refers to the crack opening and closing once per revolution during the shaft rotation. As the shaft starts to rotate, at a certain angle the crack starts to close when the upper end of the crack edge reaches the compression stress field. The crack remains closed when the stresses on the crack surface are compressive. The crack becomes fully closed at a certain angle when the crack fully reaches the compression stress field. The shaft has almost the same stiffness as an intact shaft. Similarly, the crack starts to open at a certain angle when the crack edge starts to enter the tensile stress field and becomes fully open at a certain angle when the crack enters the tensile stress field fully, remaining open until the end of the crack edge reaches the compression stress field. In this case, the stiffness of the shaft is reduced significantly. The intermediate situation between the fully open and fully closed state is a partially opened or partially closed crack. For partially open/closed crack statuses, the shaft stiffness is between the maximum and minimum values (Anvari, Scheider, & Thaulow, 2006; Patel & Darpe, 2008; Sekhar & Prabhu, 1994a;

Siegmund & Brocks, 2000). Usually, shaft cracks breathe when crack sizes are small, running speeds are low and radial forces are large (Papadopoulos, 2008). The different possible states of the breathing crack for a different angle of rotation are shown in Figure 2-1.

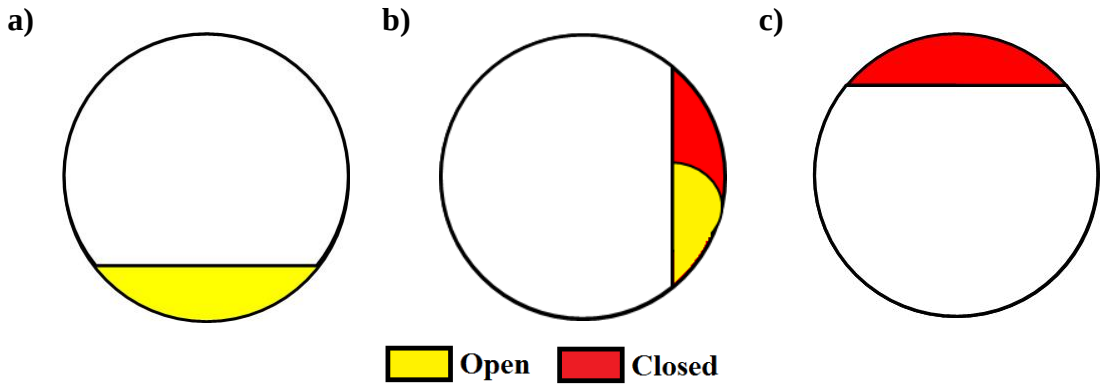

Figure 2-1: Different possible states of the crack: (a) fully open, (b) partially open/closed and (c) fully closed

2.2.4 Modelling of Rotor System

2.4.1 Weight-dominant rotor system

The transverse crack is tied to the key concept of weight dominance. It means that the shaft sags below the bearing centreline owing to its weight. Further, the entire shaft orbit remains below the bearing centreline during rotation to fulfil this criterion (Bouboulas & Anifantis, 2011). Figure 2-2 shows an exaggerated image of shaft sag. When this is the case, the transverse shaft crack is forced to open and close with every shaft revolution owing to the shaft's bending (Batra, 2010). However, in the case where rotor vibration amplitudes exceed the magnitude of shaft sag owing to gravity, the crack may not open and close predictably, which may not produce parametric excitation (Adams, 2010).

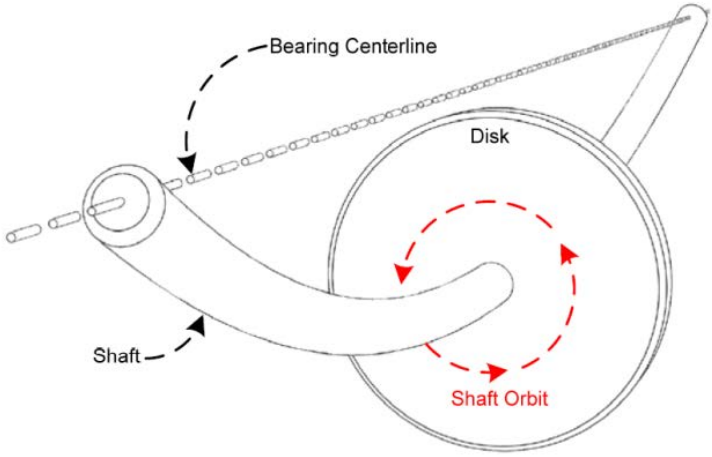

Figure 2-2: Illustration of the weight dominance concept

Detecting and diagnosing transverse shaft cracks hinge on how well the crack model emulates the actual cracked system. The key aspect of any crack model is the reduction in stiffness introduced by the crack (Guo, Huang, & Cui, 2009). Localised reduction in stiffness is directly related to crack depth, whereas global reduction in stiffness is influenced by both crack depth and crack location along the shaft (Xiang, Zhong, Chen, & He, 2008). Unfortunately, many researchers opt to either ignore crack location or mitigate its effects.

2.2.2 Unbalance rotors system

Among the vast number of unbalance classifications, mechanical unbalance is the only form of unbalance corrected through the balancing of the rotor (Mobley, 2002). This form of unbalance occurring once per revolution is also known as residual mass imbalance, which is a result of, but not limited to, manufacturing errors, thermal deformation, material inhomogeneity, wear and corrosion (Ishida & Yamamoto, 2013). Mechanical unbalance can be further classified into static, couple, quasistatic unbalance; static unbalance and dynamic unbalance are more relevant herein. The system is statically unbalance when the axis of rotation of a rotor does not coincide with the principal axis of inertia. In the other case, the system is dynamically unbalance when the principal axis of inertia intersects the axis of rotation, creating an angle known as the skew angle (Ishida & Yamamoto, 2013).

Rotor vibrations exist as, or as a combination of, lateral rotor vibrations or torsional rotor vibrations in all rotating machinery. When concerned with mass unbalance of a rotor-bearing system, lateral rotor vibration is a pervasive phenomenon that occurs in the radial plane at the micrometre scale. More specifically, the flexibility of the rotor and bearings, mass distribution of the rotor and maximum angular velocity determine whether or not a residual rotor will result in forced lateral rotor vibration resonance (Adams, 2010). As a result, systems with the potential for rotor beam-bending type deflections will have significant lateral rotor vibration characteristics.

A few studies have recommended that the weight-only breathing models may not be suitable for lightweight rotors, vertical rotors or rotors operating around their critical speed of rotation (Bachschmid et al., 2010; Cheng, Qian, Zhao, & Zhang, 2010), since there is significant influence from dynamic loads. Bachschmid et al., (2010) studied the effect of nonlinear breathing behaviour of the crack and found that system stability was restored at times by the presence of the unbalance. Cheng et al., (2011) also found that the rotor's stability can be restored owing to the unbalance. Rubio and Fernandez-Saez (2012), Rubio, Munoz-Abella, Rubio and Montero (2014) and Rubio, Rubio, Munoz-Abella and Montero (2015) highlighted the influence of the eccentricity on the breathing behaviour in a rotating cracked shaft in terms of crack opening percentage and SIF. A 3D FE classical Jeffcott rotor concept model was simply supported at both ends, with a massless shaft and a disc at the midspan of the shaft. The crack was normal to the shaft axis, which is situated at the midspan. The addition of an unbalance force has a large influence on the crack breathing mechanism. These articles analyse the orientation of a constant eccentric force but not the effect of unbalance force magnitude on the breathing.

2.3 Detection Techniques of Fatigue Crack

Diagnosis of shaft cracks in rotating machinery has been a research challenge for both industry and academia for several decades (Georgantzinos & Anifantis, 2008; Saavedra & Cuitino, 2002). Such cracks can cause total shaft failure and enormous costs in downtime (Kumar & Rastogi, 2009). Accordingly, owners of critical plant machinery are particularly interested in early detection of symptoms that can lead to in-service failure of machinery and equipment. Safe and reliable operation of

equipment relies on proactive maintenance aided by newly emerging diagnostic technologies.

In the field of vibration condition monitoring, the diagnostics of rotating machinery has been gaining importance in recent years (Ishida & Yamamoto, 2013). Shafts are basic components in most high-performance rotating equipment and utility plants, such as high-speed compressors, steam and gas turbines, generators and pumps (Xiang et al., 2008). Although usually quite robust and well designed, serious defects can develop in shafts without much apparent warning (Xu & Marangoni, 1994). Total shaft failure can be catastrophic (Yang & Suh, 2006). The study focuses on the characteristic of cracked shafts and their vibration dynamic behaviour. A few types of shaft cracks can develop during the operation of rotating machines. The transverse crack remains the most important type of crack since the machine safety is significantly influenced by its occurrence (Guo et al., 2013).

Shaft crack detection methods adopted in the literature can be broadly grouped into two types: vibration-based and model-based methods. The former relies on detecting changes in vibration signals since a crack in a structure tends to modify its dynamic characteristics, such as the natural frequencies and mode shapes. Conversely, through monitoring the trend changes in measurements of the natural frequencies and mode shapes of a rotating shaft over time, a crack present in the shaft could be predicted. The stiffness of a shaft is reduced by a crack and consequently the shaft's Eigen-frequencies decline. Measuring these changes can help in identifying an early-stage crack (Sekhar & Prabhu, 1994a). Unfortunately, the available indicators cannot reliably differentiate a cracked shaft from other problems that create similar vibration spectra and waveforms, such as a misaligned or unbalance shaft. Thus, to develop more reliable diagnostic methods, a thorough understanding of periodical stiffness of a cracked shaft is necessary.

The model-based methods are based on analytical or numerical models to simulate the behaviour of cracked shafts during rotation. In model-based identification, the fault-induced change in the rotor system is taken into account by equivalent loads in the mathematical model. These equivalent loads are virtual forces and moment acting on the undamaged linear system to generate a dynamic behaviour identical to that measured in the damaged system. However, the approximations and assumptions

used in the model-based approaches could lead to large errors for the analysis of cracked shaft dynamic behaviour. Specifically, in consideration of cracked shaft stiffness, the stiffness parameters used in some of the models do not reflect its periodic change at different rotation angles.

2.3.1 Vibration-based approaches

In vibration-based identification, a common nondestructive evaluation procedure for detecting a crack location and size is to measure the natural frequency response of the structure with cracks. As mentioned previously, a cracked structure will have reduced stiffness and increased damping. As mentioned in vibration theory, stiffness reduction is related to decrease in natural frequencies observed and modifies the vibration modes of the structure.

A significant portion of the published literature on crack detection and diagnostics has focused on this direct signal measurement technique. Sekhar and Prabhu (1994b) applied vibration analysis in their paper '*Crack detection and vibration characteristics of cracked shafts*'. Moreover, they claimed that the significant changes of natural frequencies and the differential of these could be applied to crack detection. They also found that the results are more appreciable for cracked shafts with a low slenderness ratio.

Bachschmid, Pennacchi, Tanzi and Vania (2000) promoted a method for assessing the location and depth of a transverse crack in a shaft, by using vibration measurements. The literature and field experience support the conclusion that a transverse crack modifies the dynamic behaviour of the rotor, by generating periodic vibration, with 1x, 2x and 3x revolution components in a horizontal axis shaft. The crack's location is identified using a modal technique in the frequency domain. The crack depth is calculated by comparing the static bending moment, owing to the rotor weight and to the bearing alignment conditions, to the identified 'equivalent' periodic bending moment, which simulates the crack. The authors validated this method through experimental results obtained on a test rig.

Some authors combined the natural frequency data with a FEM for a better result. Sinha, Lees and Friswell (2004) presented the basic method by comparing the contour graph of the first two structural natural frequencies to analyse the crack

depth and location, using the FEM method. The intersecting point of the highest amplitude was defined that corresponded to the measured Eigen-frequency variations caused by the crack presence.

Mode shape and response-based identification are other vibration signal approaches adopted by many published papers for shaft crack identification. Dong, Chen and Zou (2004) studied the open crack of a static state rotor through vibration analysis using a continuous model and parameter identification. Under the conditions that the cracked rotor has a circular cross-section, fracture mechanics methods were applied to model the cracked region as local flexibility. They reported that the crack location and depth could be predicted by measuring the deflection at two symmetric points and using the contour method of identification.

Ishida (2008) reported a harmonic excitation method for detection of a rotor crack based on nonlinear vibration diagnoses. They applied a harmonic excitation force to the cracked rotor, investigated its excitation frequency responses and analysed the nonlinear resonances owing to the crack.

Wavelet transforms is another signal-based method that has been widely adopted by many authors. Prabhakar, Sekhar and Mohanty (2002) applied a continuous wavelet transform (CWT) to diagnose cracks in a rotor from time-domain signals. Dong et al., (2004), through the continuous wavelet time-frequency transform, compared the wavelet time-frequency properties of the uncracked rotor and the cracked rotor and discussed the difference in wavelet time-frequency properties of the cracked to the uncracked rotor.

Others signal-based applications, such as that of Guo and Peng (2007), used the Hilbert–Huang transform to detect and monitor a small transverse crack in a rotor during the start-up phase by capturing transient responses. Sinha et al., (2004) presented another signal processing tool, higher-order spectra, for identifying the presence of a transverse breathing crack. The principle of this method is based on the higher harmonics in a signal. It is typical of nonlinear dynamic behaviour in mechanical systems. A transverse crack that breathes during shaft rotation also exhibits nonlinear behaviour. However, as the authors commented, the experiments

were conducted on a small rig, and the test results obtained need an enhancement to increase the confidence level in the diagnosis.

Prabhakar et al., (2002) suggested measuring mechanical impedance for detecting and monitoring cracks in rotor-bearing systems. They found that the mechanical impedance changes substantially owing to the crack and follows definite trends with the crack parameters (depth and location) and force location. The normalised mechanical impedance of a rotor system is more sensitive to a breathing crack than an open crack. Sudden changes in mechanical impedance are observed at multiples of the running frequency of the breathing crack.

2.3.2 Model-based methods

Model-based methods have applied analytical or numerical models to simulate the dynamic behaviour of cracked shafts during rotation. In these methods, equivalent loads are incorporated in the mathematical model to simulate the fault-induced change in the rotor system. These equivalent loads are virtual forces and moment acting on the undamaged linear system to generate a dynamic behaviour identical to that measured in the damaged system (Papadopoulos, 2008). The foundations for these methods are based on some theories, although the literature has typically examined the periodic stiffness changes of the system. In particular, model-based methods have proven to be quite effective in identifying rotor faults, such as cracks, thermal bows, misalignment and unbalance, especially because experimental diagnosis alone cannot be potent. Penny and Friswell (2003) presented the three well-known simple crack models: (1) the hinge model, (2) Mayes model and (3) Jun and Gadala (2008) model. Based on a Jeffcott rotor, they analysed the stiffness matrix of a rotating shaft when the crack was in the open and closed states. In the hinge model, it is assumed that the crack changes abruptly between closed to open states when the shaft rotates, and vice versa.

Analytical analysis of rotor-bearing systems is essential for machine design. Analytical modelling techniques, such as the finite element analysis method, serve to discretise rotating machinery into some elements, where each particular element has its properties. While most modelling is linear and real models are nonlinear, analytical studies (e.g., Han et al., 2014; Lin & Chu, 2010) have approximated with

great accuracy the role of each element and their interactions. Understanding the dynamical behaviour of each machine element helps machine designers to develop a holistic theoretical vibration profile for a machine (Rao, 2011). Analytical study of rotating machinery significantly increases the longevity of machine life through the ability to identify faults. Failure-mode analyses involve studying the machine's vibration signatures, using methods including Fast Fourier Transforms and time traces, and employing mathematical models to recognise characteristics of fault signatures. Failure-mode analysis works on the principle that failure modes are common to all machines and that these vibration patterns are absolute and identifiable; however, with some machines, this is not the case (Mobley, 2002). Further, analytical studies can assist in understanding a machine's vibration profile at frequencies that are typically not used in machine maintenance. Mobley (2002) stated that the natural frequencies of rolling-element bearings substantially exceed the typical frequency range used in machine maintenance and, as a result, the dynamical behaviour of these bearings is rarely observed. The natural frequency range of these roller-element bearings is between 20 kHz and 1 MHz.

The Jun and Gadala (2008) model applied the equations of motion for a simple rotor with a breathing crack. Based on fracture mechanics, the cross-coupling stiffness and the direct stiffness were estimated when the crack opens and closes. In these three crack models, stiffness variation was considered a function of the opening and closing of the crack. However, for both the hinge model and Mayes model, no direct relationship between the shaft stiffness and the depth of crack was reported. However, the Jun and Gadala (2008) model improved on this defect at a particular rotation angle by taking into account the shaft length and diameter, the modulus of elasticity of the shaft material, the depth of the crack and the lateral force. The three models simplified the breathing crack model to a switching crack model (crack switched from open state to closed state abruptly).

Sekhar (2004) also promoted a model-based approach for identifying cracks in a rotor system. In this study, the FEM was used to model the rotor, while changes in local flexibility were used to indicate the crack. Pennacchi, Bachschmid and Vania (2006) applied a model-based approach to identify the dynamical behaviour of a cracked shaft; experiments were conducted on a large test rig to validate this method.

The results obtained, according to the authors, are more accurate. However, the artificial cracks they generated cannot reasonably represent the dynamic behaviour of a fatigue crack.

Experimental work synergises well with the analytical study, although experimental work alone is insufficient for machine maintenance. Model-based fault analysis involving both experimental and theoretical studies is observed in a significant amount of studies. One notable study (Bachschmid et al., 2000) involved the experimental validation of fault-identification models on large turbogenerators. In that study, the turbogenerators exhibited variability between their theoretical and experimental dynamical behaviour, which was later attributed to the thermal condition of the machines. In this case, experimental analysis alone had reduced reliability in detecting faults since the condition of the machine manipulated the vibration signature. Another shortcoming of experimental work was observed by Han et al., (2014), who showed that experimental methods have added inaccuracies relative to a theoretical model as a result of noise. A large amount of noise was obtained during the data collection process, which consequently skewed the true values of stiffness and damping of the system. To overcome this problem, they added 10% Gaussian noise in the theoretical model they developed.

In the most recent literature, some analytic studies have provided a more extensive understanding of bearings. Bearings play a significant role in reducing or modifying the critical speed of a rotor, and thus, they can be used to lower vibration amplitudes and ‘choose’ desirable critical speeds. Nayfeh and Mook (2008) investigated the dynamics of a rotor supported by hydrostatic journal bearings containing negative electrorheological fluid. Arem and Maitournam (2008) applied an extended transfer matrix method to study coupled lateral and torsional vibrations of an asymmetric rotor-bearing system. Batra (2010) studied the behaviour of high-speed spindle air bearings through a combination of differential transformation method and finite difference method. It was found that the vibratory response was multifaceted, containing periodic, subharmonic and quasiperiodic elements (Batra, 2010). Understanding a vast range of bearing dynamics is an inherent advantage when designing various rotor systems and models to detect and reduce crack propagation.

Some studies, such as Bouboulas and Anifantis (2011) and Han and Chu (2012), developed a nonlinear model for magnet associated bearings. More specifically, Bouboulas and Anifantis (2011) conducted a nonlinear theoretical analysis of rotating shaft supported by a repulsive magnetic bearing. In such a system, the repulsive magnetic bearing has the potential to make contact with the backup bearing at critical speed, and therefore, contact vibration between the two bearings must be investigated. Han and Chu (2012) demonstrated a nonlinear model for a magnetically supported rigid rotor in auxiliary bearings and found that an unbalance parameter largely influences the dynamic behaviour of the rotor-bearing system. They found that when large rotor imbalance magnitudes were applied to the system, nonsynchronous vibration dominated the rotor's response over a substantial speed parameter range. While magnetic bearings are beyond the scope of this present study, it is ideal to develop the most basic, but diverse, knowledge base of all rotor-bearing elements because these elements contribute to the shaft vibration response.

Investigation through the FEM is another popular model-based approach, which has been widely adopted in the published literature. Chan and Lai (1995) presented the FE-based simulation of a shaft with a transverse crack. They analysed different cases of cracked and uncracked shafts and claimed the results could be used as a reliable indicator for shaft crack detection in symmetric rotors. Darpe (2007) presented an investigation of the dynamics of a simple Jeffcott rotor model for a slant crack. A flexibility matrix of such a cracked rotor was developed. In the equations of motion, the stiffness coefficients based on the flexibility values were used. Slant and transverse cracks can be compared via flexibility and stiffness coefficients and the unbalance response characteristics.

Bachschmid and Tanzi (2004) studied the breathing of a straight front crack and a helicoidal crack in terms of the shaft deflection during rotation. In their numerical simulations, a simply cracked cylindrical beam was used. One end of the beam was clamped, and the other end was loaded mechanically. Fayed (2017) performed a two-dimensional finite element analysis using Abaqus and investigated crack breathing in terms of mixed mode I/II SIF of a crack. Rubio et al., (2015) determined mode I SIF for an elliptical breathing crack. Liong and Proppe (2013) analysed crack breathing using a cohesive zone model with the 3D FE model and also the shaft stiffness loss

during rotation. In this model, both ends of the shaft were supported rigidly. The breathing of a straight front crack represented by the local flexibilities was also studied in a 3D FE shaft model with a fixed-end boundary condition (Georgantzinos & Anifantis, 2008; Giannopoulos et al., 2015). Recently, Rubio et al., (2014) and Rubio et al., (2015) presented a 3D FE study of the influence of the eccentricity on the breathing behaviour in a rotating cracked shaft in terms of crack opening percentage and SIF.

Sudhakar and Sekhar (2011) formulated an efficient and effective solution to flaws observed by Jain and Kundra (2004) using a vibration minimisation method with the equivalent load minimisation method. The application of the combined method saw acceptable error margins even for cases as low as 2 degree of freedom (DOF), and therefore, measurements of the transverse vibrations only need to occur at one location to successfully detect the unbalance (Sudhakar & Sekhar, 2011). Although the method was applied to unbalance identification, the techniques used to improve on the Jain and Kundra (2004) method still apply. Owing to this fact, adapting the model to include shaft cracks can potentially be a very efficient solution to identifying the presence of cracks since it is effective at a low measured DOF.

He et al. (2001) used genetic algorithms for detection of shaft cracks. One conspicuous advantage of using genetic algorithms is that it bypasses the need to develop robust mathematical models from the root of the inverse problem, that is, shaft cracks. The stiffness, damping and gyroscopic matrices of the cracked single disk rotor model were deduced through finite element modelling, and hence, the resulting dynamic equation could form a reference point for their results. Computational efficiency dictates the success of the method, and therefore, one could argue that in an era of rapidly developing processor technologies such an issue will be minimised, making genetic algorithms a viable nonexpert method for crack detection. An excellent linear matrix inequality approach was presented by Kulesza, Sawicki and Gyekenyesi (2012) as a proposed robust fault detection filter. Finite element theory was used to independently formulate the cracked rotor model that is also observed in certain studies (Gasch, 1993; Penny & Friswell, 2003; Sawicki, Wu, Baaklini, & Gyekenyesi, 2003). The well-known model is in the form of:

$$M\ddot{q} + (Dd + \Omega Dg)\dot{q} + \left(k_u - \Delta k_c f(t)\right)q = p \qquad (2\text{-}1)$$

It is a linear time-invariant equation that can be developed using Lagrangian Mechanics. To complement this equation, Kulesza et al., (2012) ensured their rigid finite element model design procedures did not include any direct iterative calculations. The absence of iterative calculations removes the need for lengthy processing time, an often-taxing requirement of model-based systems. Moreover, the developed filter accomplished shallow crack identification, that is, 2% and 5% deep cracks, while being insensitive to noise. To gain appreciation for shallow crack identification, one can acknowledge how very subtle the changes in the vibration signatures are owing to shallow cracks.

Since it is typical for two or more faults to exist simultaneously in a rotor, it is critical to have methods capable of discerning all types of faults. To achieve this, the multiple-fault-identification literature has used a vast mixture of qualitative or quantitative techniques. Qualitative methods include, but are not limited to, fault-symptom matrices, artificial neural networks and if-then rules, and quantitative methods are commonly model-based methods whose goal is to model the dynamics of rotating machinery closely and accurately.

There is a lack of investigation into the breathing crack in a partially open and partially closed state. It is clear that the switching crack model cannot reflect the real nature of crack stiffness variation with rotational angles since the crack remains in a partially open (or closed) state most of the time during rotation.

Several methods have been used to model cracked rotors numerically. The method used depends on the requirements of the study. Three-dimensional finite element analysis (3D FEA) with nonlinear contact surfaces are frequently used in static and quasistatic studies (Bachschmid & Tanzi, 2004; Liong & Proppe, 2013; Rubio et al., 2014). Because of the generally accepted reliability of 3D FEA for static linear elastic problems, it is often used a means of validating simpler one-dimensional models.

One-dimensional models are generally one of two types: analytical Euler beam or finite element. Analytical methods often model the crack using a SERR approach. The SERR approach assumes that the shape of the elastic curve of the rotor is unchanged on either side of the crack from that of an uncracked rotor. The additional displacement of a cracked rotor is the result of a discontinuity in the rotation of the shaft at the crack location, are shown in Figure 2-3.

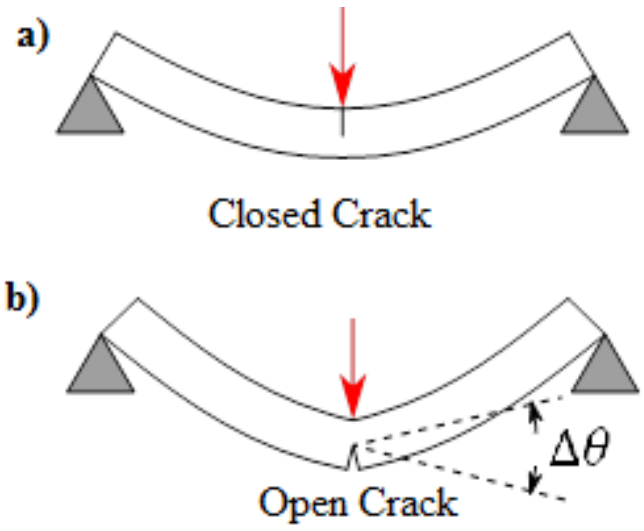

Figure 2-3 : Strain energy release rate method uses a discontinuity in the rotation of the shaft to account for additional flexibility owing to breathing of a crack

The magnitude of this discontinuity is proportional to the bending moment at the crack location. In the simplest case considering traverse displacement of the beam with no axial loads applied, the discontinuity is expressed as:

$$\Delta\theta = \lambda M \tag{2-2}$$

The constant of proportionality λ is called the flexibility coefficient (Rubio, Munoz-Abella, & Loaiza, 2011). The flexibility coefficient can be calculated by integrating the SIF over the area of the crack section.

$$\lambda = \frac{2(1-\nu^2)}{E}\int_A \left(\frac{K_{1,M}}{M}\right)^2 dA \tag{2-3}$$

where E and ν are the Young's modulus and Poisson's ratio of the material respectively. $K_{1,M}$ is the SIF in mode 1 at the crack front. Evaluating the SIF is usually done numerically using 3D FEA on a number of nondimensional models and curve fitting the results for use in general cases. Likewise, the integral $\int_A \left(\frac{K_{1,M}}{M}\right)^2 dA$ is usually evaluated numerically by trapezoidal integration or a similar process. Rubio, Munoz-Abella and Loaiza (2011) evaluated the above integral for many crack sizes and shapes and produced a set of polynomial curves of best fit for flexibility coefficient. They also considered the impact of axial loads on the crack rotor. When evaluating displacements of a crack shaft under both bending and axial loads, there is coupling between the loads. The bending moment will affect the axial displacement and the axial force will affect the rotation discontinuity at the crack.

The flexibility coefficients as calculated using the Rubio, Munoz-Abella and Loaiza (2011) curve fit showed good agreement when compared with the known true values. Similarly, results for the deflection of a statically loaded cracked rotor showed close agreement for their proposed analytical method when compared with both 3D FEA and experimental measurements. The SERR approach presented by Rubio, Munoz-Abella and Loaiza (2011) is only valid for cases where the bending direction of the shaft is parallel to the direction of the crack. It would be difficult to apply to problems involving out-of-plane bending for two reasons. Such bending will have coupling between the bending responses in each of the orthogonal planes. It will often cause a crack to partially close, thereby changing the shape of the crack front and invalidating any analytical expressions for the SIF derived for fully open cracks.

These drawbacks have resulted in SERR-based crack models being less widely used in dynamic studies of cracked rotors. An exception to this is the simplistic complete cracked rotor model called the Laval rotor (Gasch, 1993). It consists of a slender shaft conforming to simple beam theory with a disc mounted at the midspan. The shaft is supported by pinned joints at each end, making it a statically determinate model. The use of the switching-type crack based on the SERR model further reduces its complexity but also makes it incapable of accurately predicting the behaviour of a breathing crack.

Beam element FEA dynamic studies have mostly used a reduced area moment in a region close to the crack to account for the reduced stiffness of the shaft (Al-Shudeifat et al., 2010).

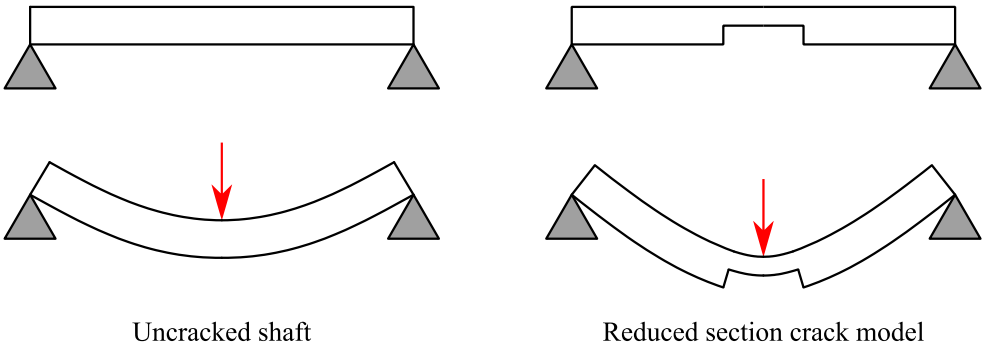

Figure 2-4: Abstract view of the application of the reduced section method

Because the faces of the crack section are still able to bear compressive stress, if a bending moment at the crack location tends to close the crack, the shaft will behave like an uncracked shaft would. Bending moment that tend to open the crack will have free surfaces at the crack area, and hence, the stress field will be confined to the uncracked sectional area. A rotating shaft subject to static weight force will experience a rotating bending moment relative to the crack front. Figure 2-5 illustrates some of the parameters used to describe straight-edged traverse cracks.

However, despite the suitability of the reduced section crack model for solving dynamic problems, the trigonometric breathing function leaves much room for improvement, while an analytical expression for the second moment of the area of an irregular shape, such as the section of a partially closed crack, is not always possible. In the case of a breathing crack, interdependency exists between the open percentage of the crack area and the location and orientation of the neutral axis of bending that makes an explicit solution difficult.

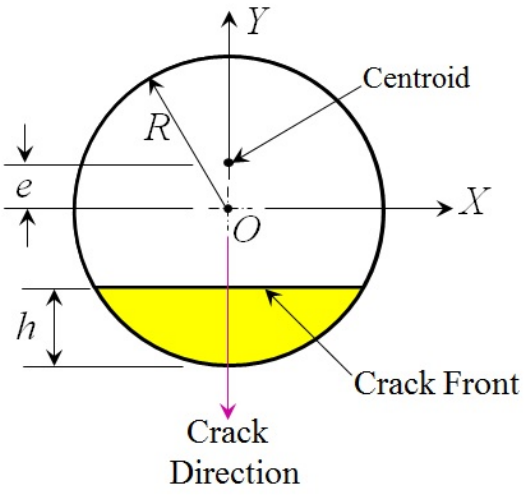

Figure 2-5: Definitions of various crack parameters

Most recently, the breathing mechanism of the breathing crack model for a balanced shaft was proposed by Al-Shudeifat and Butcher (2011). A new breathing function of the breathing crack was reported. This new model applied the FEM, established the correct periodically time-varying stiffness matrix and formulated and incorporated it into the global stiffness matrix. This approach drew on Mayes and Davis (1984) concept of a local reduction of the crack area moment of inertia.

Al-Shudeifat and Butcher (2011) used the assumption that a linear stress distribution across the cross-section at the crack location prevails, as in the simple beam theory. The authors asserted that this assumption holds well when comparing their study results with those from 3D nonlinear FEA. They developed equations that accurately characterise the breathing mechanism of a crack. Among their simplifying assumptions were the following: weight forces determine the shaft bending direction and crack breathing state, and torsional and longitudinal vibrations do not affect crack breathing. Al-Shudeifat and Butcher (2011) defined a set of four shaft rotation angles that characterise shaft breathing behaviour. They are the angles at which the crack starts to close, is fully closed, starts to reopen and is fully open again. They are a function of the ratio of crack depth to shaft radius only. This ratio, also known as nondimensional crack depth, is defined as:

$$\mu = \frac{h}{R} \qquad (2\text{-}4)$$

where *h* is the depth of the crack and R is the shaft radius (see Figure 2-5). For shaft rotation angles where the crack is either fully open or fully closed, analytical expressions for the area moment of inertia are possible. For shaft rotations where the crack is in a partially open state, precise second area moment of the section were developed by an iterative process. Fourier series expansions for the second moment of the area were then developed.

2.3.3 Other approaches

Other than the techniques mentioned above, there are some nontraditional techniques and methods reported in the literature for analysing the dynamics of a cracked rotor. Sekhar (2004) proposed a combined approach (vibration signal-based and model-based) for crack detection. This approach modelled the rotor using FEM, while the fault nature and symptoms of the model were characterised using a Fast Fourier Transform or an advanced signal processing tool–CWT. It was found that the accuracy of shaft crack identification improved with this method.

Bachschmid, Pennacchi and Vania (2002) experimentally validated fault-identification models on large turbogenerators. The method involved distinguishing faults from those events with similar vibration signatures and also locating the fault and determining its severity. Strong variability in the turbogenerators was observed when monitoring the dynamical behaviour of the gas turbogenerator owing to the thermal condition and history of the machines. Additionally, the theoretical models used in the study did not properly account for the resonance of the machine foundation, thus leading to poor quality experimental data and vibration signatures not caused by the unbalance.

Pennacchi et al., (2006) improved on the least-squares (LS) method commonly used in vibration diagnostics through use of M-estimators. In short, LS estimates determine position. However, the method is not very accurate when noise and gross errors are present in the system. By introducing the M-estimate, the need for experts to define the weights for the machine's corresponding LS algorithm is removed because the method in question automatically defines these weights. Such use of M-estimators is a significant step forward in allowing nonexpert users to achieve

accurate results, and additionally minimises intervention required by the machine operator.

Another study (Green & Casey, 2005) applied parameter estimation and parity equations to real, mundane machinery, such as DC motor actuators, diesel engines and robots to list a few. The findings are a strong reminder to new researchers of the effectiveness and limitations of linear models applied to nonlinear dynamic systems. Ultimately, methods should be adapted to the mechanical behaviour of the processes and data from sensor signals while being true to the actual nonlinear nature of the system.

A variety of nondestructive identification methods have been used to determine the presence of cracks in rotating machinery. These methods are preventative by nature; thus, they are of utmost importance for preventing catastrophic failure in machinery. An application example is observed in the maintenance of aircraft gas turbines; the turbines are examined over some flight hours for any surface cracks since these are typically invisible to the unaided human eye (Ishida, 2008). Coloured dye penetrative testing involves a dye liquid being applied to the surface of a rotor to soak. After a period, the excess dye is removed, and the rotor is turned—if cracks are present, the dye would have seeped through the cracks. Florescent dye testing involves a similar process as coloured dye penetrative testing, except that ultraviolet light is used to illuminate the dye to visualise the cracks. Ultrasonic testing uses the reflective properties of sound waves to advantageously detect internal cracks (Ishida, 2008). Acoustic waves are projected into the material, and if a crack is present, some of the signals will be reflected back. Magnetic particle testing involves the use of ferromagnetic materials, such as cast iron and steel, and magnetic fields to project patterns indicative of cracks. Finally, eddy current testing employs electromagnetic induction to identify cracks by monitoring changes in the magnitude of eddy currents—if a change occurs, cracks are present in the material.

2.4 Modelling of Fatigue Crack

Transverse shaft cracks are typically categorised as either gaping or breathing. Gaping cracks remain open regardless of the shaft's angular orientation; the faces of the crack never contact. A breathing crack is defined by the opening and closing behaviour of the crack faces. As such, the shaft's stiffness is a function of its angular orientation. Breathing cracks are often modelled as having either smoothly varying stiffness or stepped stiffness (i.e., the crack is either entirely closed or entirely open) (Ramesh Babu, Srikanth, & Sekhar, 2008; Stoisser, & Audebert, 2008).

2.4.1 Gaping cracks

Gaping cracks remain open regardless of the angular orientation of the shaft; even when the crack is in compression, the faces of the crack do not contact. Therefore, the gaping crack creates a stiffness asymmetry, which is constant in a rotating reference frame but contingent on the shaft's angular orientation in an inertial frame. The connection between globally asymmetric shafts and gaping cracks is recognised intuitively since the cross-section of the shaft at the gaping crack is equivalent to the cross-section at any location along a globally asymmetric shaft.

A gaping fatigue crack differs from a notch in that the crack's width is assumed to be negligible. As the name suggests, the mechanism driving the formation of gaping fatigue cracks is fatigue. Fatigue cracks terminate in a sharp edge and are capable of propagation. Gaping fatigue crack models are often analytically employed but rarely experimentally tested for two primary reasons. First, gaping fatigue cracks are difficult to manufacture. A stress concentration must be introduced on the shaft at the desired location of the crack. Then, the shaft must be subjected to prolonged cyclic bending fatigue to initiate and propagate the crack. Second, even if a crack forms at the desired location, the crack characteristics (e.g., depth, width and profile) are difficult to control and quantify.

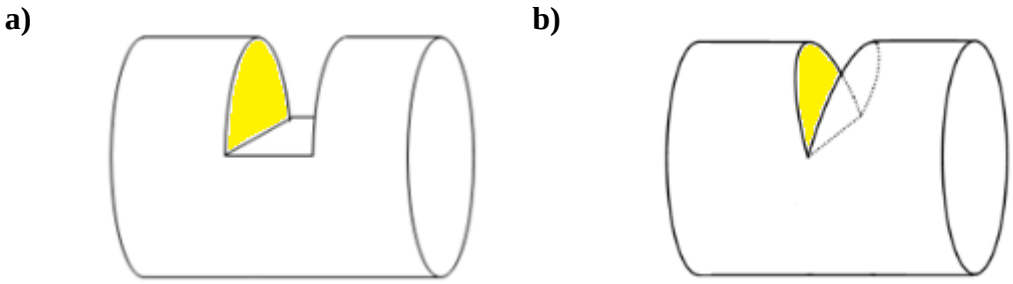

Figure 2-6: Comparison of gaping cracks: (a) Notch and (b) gaping fatigue crack

The difficulty in manufacturing true fatigue cracks has led many researchers to utilise definite-width notches in both their analytical and experimental work. This conclusion is corroborated by the literature reviews performed by Dimarogonas (1996), which stated that most experimental work focuses on notches because they are simple to fabricate. Fatigue is the primary mechanism driving the initiation and propagation of cracks in real rotordynamic systems. Many authors have developed various techniques for estimating the stiffness of rotordynamic systems displaying gaping fatigue cracks, although a majority of methods employ concepts from fracture mechanics. Dimarogonas and Paipetis (1983) pioneered a method for estimating crack compliance using strain energy methods. The technique employed fracture mechanics principals, and specifically the SERR, to estimate local crack compliance. Dimarogonas and Papadopoulos (1983) first employed the concept on nonrotating shafts, emphasising the appearance of coupling effects induced by the crack. They expanded the SERR-based crack compliances by developing a 6 DOF crack compliance matrix. These concepts were subsequently extended to rotating shafts. Penny and Friswell (2003) clarified that although many techniques exist for estimating fatigue crack compliance, the best method is yet to be determined. However, several authors have experimentally obtained crack compliances.

Green and Casey (2005) employed the complex extended transfer matrix method developed by Lees and Friswell (1997) to analyse an overhung rotordynamic system. The system contained a gaping fatigue crack 6.35 mm from the support. Green and Casey (2005) provided transfer matrices for a 4 DOF overhung rotor system, including gyroscopic effects, damping effects and forcing owing to gravity. In addition, the transfer matrices were provided in a rotating reference frame such that the stiffness of the shaft was invariant relative to the frame. The analysis results indicated that the 2X harmonic is small when the shaft speed is far from the 2X

resonance frequency. In addition, they demonstrated that as crack depth increases, the magnitude of the 2X tilt resonance increases while the 2X resonance frequency decreases. The analytic results were verified experimentally, as discussed by Green and Casey (2005). Dimarogonas and Papadopoulos (1983) confirmed this observation by comparing analytic results for the stiffness of a gaping fatigue crack to experimental results for a notched shaft obtained by Grabowski (1984).

A majority of authors discussing transverse fatigue cracks and asymmetric shafts have solved the full equations of motion. Dimarogonas and Papadopoulos (1983) obtained a system of linear differential equations for a system with a gaping crack at the shaft's midspan. The DOF employed were the lateral displacements of the rotor located at the midpoint of the shaft. The equations of motion were solved analytically to expose the 2X harmonic component of the system response. Dimarogonas (1996) and Dimarogonas and Paipetis (1983) obtained the equations of motion of various cracked beams (i.e., nonrotating shafts) via finite element formulations. The results were extended to rotating shafts in further studies by Papadopoulos (2004) and Papadopoulos and Dimarogonas (1987a). In both works, the equations of motion were solved via steady-state harmonic response techniques, and the crack's influence on the coupling between various rotors DOF discussed. Wauer (1990) developed a system of 6 DOF equations of motion for a cracked Timoshenko shaft and solved the equations analytically using variational principals. Wauer then provided the first fundamental frequency decrease as a function of crack depth for several crack locations.

Note that in all of these works addressing equations of motion, only those employing discrete formulations, such as FEMs or the transfer matrix, incorporated the effects of crack location. Further, out of the studies employing finite element techniques, only Papadopoulos (2008) provided quantitative results for the influence of crack location on the dynamic response. According to Papadopoulos (2008), the assumption of a gaping crack is valid only when static displacements are small. In his review, Dimarogonas and Paradopoulos (1983) provided a word of caution considering the treatment of notches versus cracks: Many authors model cracks but manufacture notches, when thin notches and real cracks behave very differently. Dimarogonas stated that in his experience, notches result in a substantially less

stiffness reduction than a crack of commensurate depth. Gomez, Sinou, Nosov, Thouverez and Zambrano (2004) verified this observation experimentally.

2.4.2 Breathing cracks

The nature of the breathing crack can introduce nonlinearities, which complicate efforts to solve and interpret the system's dynamic response. However, breathing behaviour often provides a more realistic transverse fatigue crack model, since static displacements typically dominate vibration amplitudes. As the shaft rotates, force in a constant inertial direction (such as gravity) keeps a portion of the shaft cross-section in compression and a portion in tension. The section of the crack face under tensile stress opens, while the section of the crack face under compression closes. Therefore, for cracks smaller than the radius of the shaft, there is an angular position at which the crack is completely closed (the shaft behaves as if there is no crack) and an angular position at which the crack completely opens. Most breathing crack models have relied on the assumption that vibration amplitudes are negligible compared with static displacements. The small vibration amplitude assumption allows the shaft stiffness to be calculated as a function of only the shaft's angular position.

2.4.2.1 Switching crack

The complicated nature of breathing behaviour in cracks results in a slew of approximations. These approximations are categorised in order of increasing complexity as switching models, sinusoidal-varying models and vibration-dependent models. The simplest breathing crack models are switching models (also known as hinge or step models). Gasch (1993 & 2008) discussed such a hinge model, in which the shaft's stiffness is bilinear. Papadopoulos and Dimarogonas (1987b) used a similar step function to approximate the switching behaviour of a breathing crack.

The switching crack breathing model considers that a crack can switch states from fully open to fully close when rotating to a horizontal position, and the research conducted shows the simplified difference of the actual crack breathing (Barenblatt, 1962; Williams, 1961). The issue with this model is that chaotic and quasiperiodic vibrations owing to the sudden change of the crack state have not been observed in experimental tests (Al-Shudeifat et al., 2010).

2.4.2.2 Trigonometric crack

Mayes and Davies (1984) pioneered the use of smoothly varying breathing models to describe shaft stiffness as a function of shaft angular position through the use of the following trigonometric function:

$$(\theta) = \frac{1+\cos\theta}{2} \tag{2-5}$$

where θ is the angle of shaft rotation. Modulating the stiffness of the shaft, Equation (2-1) provides a method for incorporating breathing behaviour. Such a method better approximates the breathing of the crack by allowing a smooth transition between the open and closed states of the crack. Several other authors (Al-Shudeifat, 2013; Al-Shudeifat & Butcher, 2011; Al-Shudeifat et al., 2010) also used such a trigonometric function. Grabowski (1984) also employed a method for determining the stiffness of the cracked shaft as a function of angular position and graphically provided the shaft stiffness as a function of shaft rotation.

The most complicated breathing models are those in which the open-closed state of the crack is vibration-dependent. Darpe (2007) provided a robust method for capturing the breathing behaviour of a cracked rotating shaft using the CCL. The CCL is the position along the crack edge where the crack faces switch from being open to being closed. In the fully open state, the compliance of the crack is calculated by the method of Papadopolous and Dimarogonas (1987a). A total SIF is found at each location along the crack edge to determine the position of the CCL. The SIF depends on the nodal forces at the crack and thus is vibration-dependent. Further, the sign of this SIF dictates whether the stress at that location is tensile or compressive. The position where the SIF changes from positive to negative signifies where the crack faces have switched from being open to being closed. Although only several examples of breathing crack models are provided here, Papadopoulos and Dimarogonas (1987b), Dimarogonas (1996) and Sabnavis, Kirk, Kasarda and Quinn (2004) provide many references to various breathing crack models in their excellent literature reviews.

In the past decade, many works have addressed nonlinear aspects of the response of breathing crack models. Kulesza and Sawicki (2012) developed a 3 DOF modified Jeffcott model of a cracked rotordynamic system, including a torsional DOF. Breathing was accounted for using a smooth trigonometric function, and three forms of excitation were applied: gravity, imbalance and harmonic torsional excitation.

The equations of motion were solved numerically, and the lateral and torsional response was provided in the form of bifurcation diagrams, power spectra and rotor orbits. Coupling induced the appearance of torsional excitation frequencies in the lateral vibration spectrum. Further, chaotic behaviour was observed; the authors suggested that these response characteristics could be employed to diagnose the crack parameters, although the crack location is not discussed in their results.

Wu et al., (2005) expanded the work by Sawicki, Friswell, Kulesza, Wroblewski and Lekki (2011) by modelling a two-mass turbine-generator system; the presence of the additional mass necessitates the inclusion of an additional torsional DOF. The equations were integrated numerically, and various shaft speed harmonic peaks were observed when the torsional and lateral natural frequencies are an integer fractional ratio (such as the 1X, 2X and 3X harmonics). For different ratios of the torsional to lateral natural frequencies, the critical speeds are no longer integer fractional multiples of the natural torsional frequency. Only a single crack location was discussed, and no conclusions were drawn concerning crack detection and diagnosis. Darpe et al., (2006) employed a finite element formulation of a breathing crack system. The stiffness was approximated using the Crack above Closure Line, and the subsequent nonlinear equations of motion were integrated numerically. The shaft's stiffness is re-evaluated at every degree of rotation.

The incorporation of breathing behaviour into a dynamic model of a cracked rotordynamic system represents a significant increase in complexity over similar gaping crack models. Breathing cracks differ from gaping cracks in that the stiffness of the cracked shaft is time-dependent even in a rotating reference frame. Comparison of the area moment of inertia of a balanced shaft obtained using different breathing functions are shown in Figure 2-7.

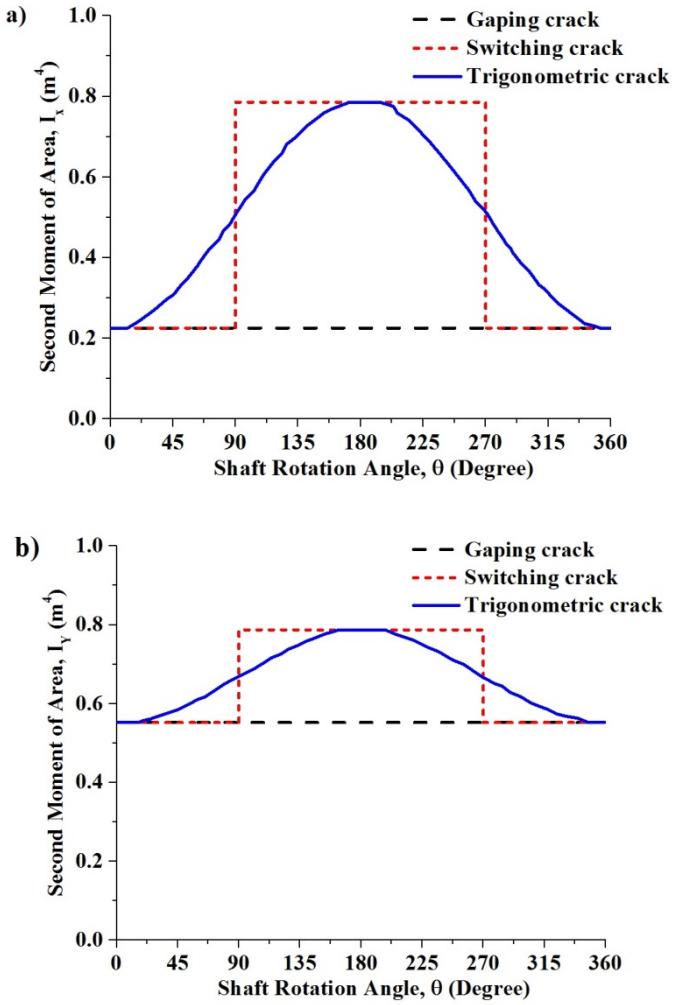

Figure 2-7: Comparison of the area moment of inertia of a balanced shaft obtained using different breathing functions (where $\mu = 0.75$)

2.5 Research Gaps

The literatures on types of cracks, causes of cracks, the unique characteristics of the cracked shaft and various crack detection techniques were briefly reviewed. The review indicates that the crack detection techniques in rotating system are active and continuously developing. Different types of crack detection techniques were reported in literature, namely model-based method, signal and vibration based analysis, and combined approach. Model-based method plays an important role in the development of on-line crack detection techniques. This method relies on simplifying the crack breathing mechanism in order to obtain local stiffness matrix of a cracked shaft element and then calculate the dynamic response by solving the equations of motion of the system. Two important theories were proposed to obtain local stiffness matrix. The first approach is based on the strain energy release rate (SERR) theory. Researchers found that the SERR approach is valid only for the fully open crack, but cannot be extended to other crack scenarios due to the breathing mechanism. The second approach is based on a theoretical model of a transverse crack by reducing the area moment of inertia of the element at the location of the crack where this change in area moment of inertia of the cracked shaft is used to develop time varying stiffness matrix equations. Unfortunately, many mechanisms remain unresolved, especially how crack breathing mechanism (how the closing and opening of a crack) affects the reduction of the area moment of inertia of the element at the location of the crack during rotation.

Although many analytical and numerical investigations of the crack breathing mechanism were reported in literature, a comprehensive crack breathing mechanism has not yet to emerge. There is no a generic algorithm or technique that can be applied to detect all the different types of cracks in rotating systems. Updated methods are therefore needed to develop for a future understanding and new knowledge is gained in engineering fields of practical rotating systems.

Moreover, all previous studies based on large rotating system considered the crack breathing mechanism to be dominated by self-weight (weight-dominant breathing), the effects of dynamic loading on crack breathing mechanisms were not yet examined in literature. However, the breathing behaviour of a shaft with large dynamic loading, specifically mass unbalance, is driven by the proximity of the

bending load angle to the crack direction. Unfortunately, large rotational unbalance is likely to arise in lightweight horizontal and vertical rotors thus the assumption of weight dominance disallows the true modelling of these rotors. Furthermore, almost all existing models are not applicable near the shaft critical speed because the lower damping expands the range which dynamic behaviour dominates. As such, equations of motion developed under the assumption of weight dominance are no longer suitable for the analysis near the critical speed or when the unbalance is high.

Despite for this wealth of knowledge, standard procedures for online crack diagnosis in rotating systems are lacking. The reason for this gap is the effects of crack location and unbalance on the crack breathing mechanism difficult to understand. Many previous studies on the crack breathing mechanism ignored or vastly simplified the influence of crack location. Further, most of the studies on the crack breathing mechanism suggested complicated, expensive and impractical procedures for analysing the crack parameters of interest.

Further, existing crack breathing models were developed under the simple support boundary condition and without considering the rotor physical and dimensional properties. By applying such easy models crack breathing is independent of crack location, which may not be right.

Therefore, it is evident that an accurate crack breathing model is urgently required to evaluate the nonlinear crack breathing behaviour of a fatigue crack under effect of unbalance force, rotor properties and more realistic fixed end boundary conditions. This model should be used to obtain the stiffness matrix of a cracked shaft element and then to study vibration responses of a cracked rotor, in which the rotor-weight-dominant assumption on crack breathing no longer holds.

The development of such an accurate model is the core of the present thesis.

Chapter 3 : Developing a New Unbalance Model

3.1 Introduction

In this chapter, a new unbalance model, which considers the coupling effects of unbalance force, rotor weight, rotor physical and dimensional properties and a more realistic fixed-end boundary condition, is developed. The unbalance model is developed to study the crack breathing mechanisms and area moment of inertia of the crack cross-section of the transverse fatigue crack in a cracked rotor system. The newly developed model can be used to obtain local stiffness matrix of a cracked shaft element to predict the vibration response of a cracked rotor and ultimately develop the online crack detection technique under the effects of unbalance force, rotor weight, rotor physical and dimensional properties and a more realistic fixed-end boundary condition.

First, the effectual bending angle that describes the proximity of the shaft bending direction (or shaft deformation direction) relative to the crack direction is developed and visualised for numerous crack location/unbalance configurations. The effectual bending angle governs the opening and closing of a shaft crack.

Second, this model is used to evaluate the nonlinear crack breathing behaviour under different weight–unbalance force ratios at different crack locations by examining the percentage of opening of a crack. Third, this model is then used to analyse the orbits of the centroid and area moment of inertia of the crack cross-section closed area to predict the vibration responses of the unbalance crack shaft. Finally, the results using the newly developed unbalance model are validated by 3D FEM results.

3.2 Determination of Effectual Bending Angle

The model observed in Figure 3-1 represents a two-disk rotor supported rigidly by two bearings. The parameters of the rotor model are presented in Table 3-1. It consists of a straight front oriented crack on a plane normal to the axis of the shaft with nondimensional crack depth ratio $\mu = h/R$, where h is the crack depth in the radial direction and R is the shaft radius. A_1 is the uncracked cross-sectional area, A_c is the area of the crack segment and e is the locations of the centroid, as shown in Figure 3-2(a). The unbalance force has been taken as a rotational force $F_{un} = m_u\omega^2 d$

owing to an additional mass m_u at a radial distance d from the centre of the shaft when the shaft rotates at ω rad/sec. The direction of the rotational unbalance force is $(\theta + \beta)$, where θ is the shaft rotation angle and β is a fixed angular position relative to the crack direction, as shown in Figure 3-2(b); it is considered that the unbalance force is located on the right-side disk (see Figure 3-1).

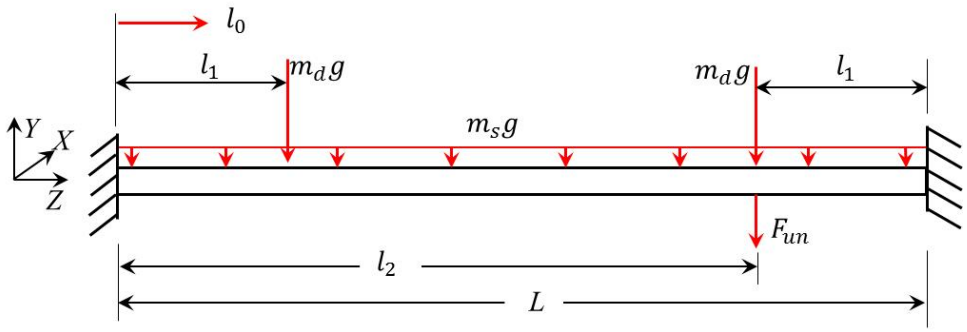

Figure 3-1: A two-disk rotor supported rigidly

Table 3-1: Parameters of the chosen rotor system

Description	**Value**
Shaft Length, L	724 mm
Shaft Radius, R	6.35 mm
Shaft Density, ρ	7800 kg/m^3
Disk Outer Radius, R_0	54.50 mm
Disk Inner Radius, R_i	6.35 mm
Disk Mass, m_d	0.50 kg
Disk-1 Location, l_1	181 mm
Disk-2 Location, l_2	543 mm
Crack Location, l_0	Variable
Crack Depth Ratio, μ	0.5

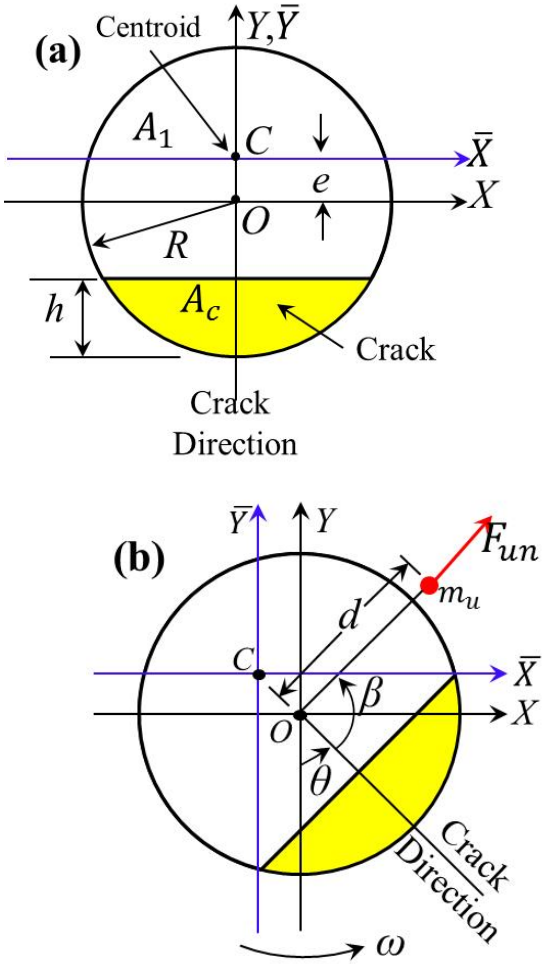

Figure 3-2: Schematic diagrams of (a) crack cross-section and (b) relative position of unbalance force with respect to the crack direction

Evenly distributed shaft self-weight $m_s g$ will generate a moment along the shaft, where m_s is the mass of the shaft and its vector aligns along the *X*-axis. The value of this moment at a location l_0 along the shaft length or *Z*- axis is described in Equation (3-1).

$$M_{msg} = \frac{m_S g}{12L}\,(6Ll_0 - L^2 - 6l_0^2) \qquad (3\text{-}1)$$

The moment in the X-axis at a location l_0 along the shaft length owing to the weight of two disks $2m_d g$ is described in Equation (3-2).

$$M_{m_d g} = m_d g \left[l_0 - \frac{l_1 (L - l_1)}{L} \right] \text{ When } l_0 \leq l_1 \qquad (3\text{-}2)$$

$$M_{m_d g} = m_d g \left[l_1 - \frac{l_1 (L - l_1)}{L} \right] \text{ When } l_1 < l_0 < l_2$$

$$M_{m_d g} = m_d g \left[(L - l_0) - \frac{l_1 (L - l_1)}{L} \right] \text{ When } l_0 \geq l_2$$

Correspondingly, the varying moment at a location l_0 along the shaft length owing to the unbalance force F_{un} is described in Equation (3-3).

$$M_{un} = F_{un} \left[\frac{l_1^2 l_0}{L^3} (l_1 + 3l_2) - \frac{l_1^2 l_2}{L^2} \right] \text{ When } l_0 \leq l_2 \qquad (3\text{-}3)$$

$$M_{un} = F_{un} \left[\frac{l_2^2 (L - l_0)}{L^3} (3l_1 + l_2) - \frac{l_1 l_2^2}{L^2} \right] \text{ When } l_0 > l_2$$

where $F_{un} = \frac{m_s g + 2m_d g}{\eta}$ and η is the ratio of the gravitational force (shaft self-weight, $m_s g$, and two disk weights, $2m_d g$) to the unbalance force F_{un}.

The gravitational moment $M_{m_s g}$ and $M_{m_d g}$ are constant in magnitude and may change their directions along the *X*-axis, but always perpendicular to the gravitational forces. The rotational force F_{un} acts in the radial direction $(\theta + \beta)$. Accordingly, M_{un} also rotates in the *XY* plane and perpendicular to F_{un} (see Figure 3-3). According to the principal of superposition theory, the total moment of the system at a location l_0 along the shaft length is described in Equations (3-4) and (3-5).

$$In \text{ X} - \text{axis}, \sum M_X = M_{m_s g} + M_{m_d g} + M_{un} \cos(\theta + \beta) \qquad (3\text{-}4)$$

$$In \text{ Y} - \text{axis}, \sum M_Y = M_{un} \sin(\theta + \beta) \qquad (3\text{-}5)$$

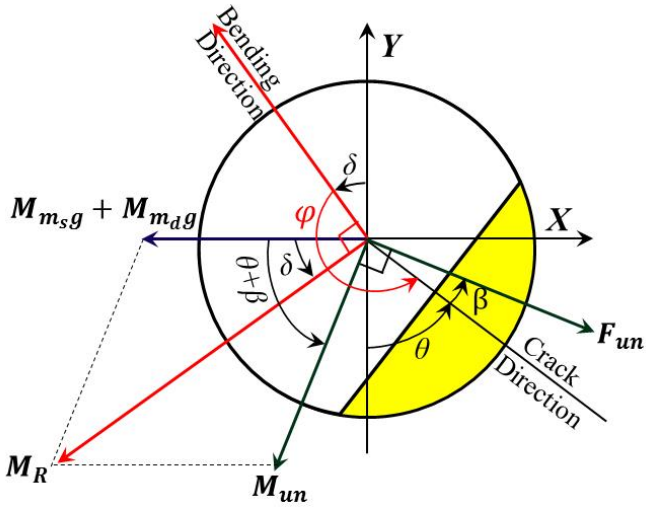

Figure 3-3: Definition of the effectual bending angle

As shown in Figure 3-3, shaft bending direction or deformation direction in the crack cross-section is always perpendicular to the resultant moment direction. The angle δ of the resultant moment w.r.t. X-axis is the same as δ of the bending direction w.r.t. Y-axis. It should be pointed out that unbalance force is not located at the crack plane, and F_{un} is only a projection of unbalance force on the crack plane. The effectual bending angle, φ, is defined as the angle from bending direction to crack direction and it solely determines the breathing behaviour of the crack. The parameters δ and φ at a crack location are described in Equations (3-6) and (3-7), respectively; however, modifications were made to ensure that these angles are within the co-domain of a full rotation of shaft between 0° to 360°.

$$\delta = \tan^{-1}\left(\frac{\sum M_Y}{\sum M_X}\right) \tag{3-6}$$

$$\varphi = 180° + \theta - \delta \tag{3-7}$$

For calculation simplicity, moment are calculated using the simple beam theory (Staff, 1996) with an intact shaft. In the calculations of bending angle as described in Equations (3-6) and (3-7), the effect of a crack on the moment at the crack cross-section in X and Y directions are considered approximately the same. This assumption is further examined in Section 3.6 through the comparison between analytical and Abaqus results.

3.3 Effectual Bending Angle on Crack Location and Shaft Rotation Angle

In this chapter, the following configurations of cracks and unbalance forces are considered:

a) the unbalance force ratio, η, the ratio of the gravitational force (shaft self-weight and two disk weights) and the unbalance force, to evaluate the influence of the unbalance force magnitude
b) the crack location factor, λ, the ratio of the crack position, $l_{0,}$ and the total shaft length, L, to evaluate the influence of the crack position
c) angular positions of the crack or shaft rotational angles, θ, varying from 0° to 360° to evaluate the influence of the crack angular position
d) angular position of unbalance force, β, varying from 0° to 360° to evaluate the influence of this angular position w.r.t. the crack cross-section plane.

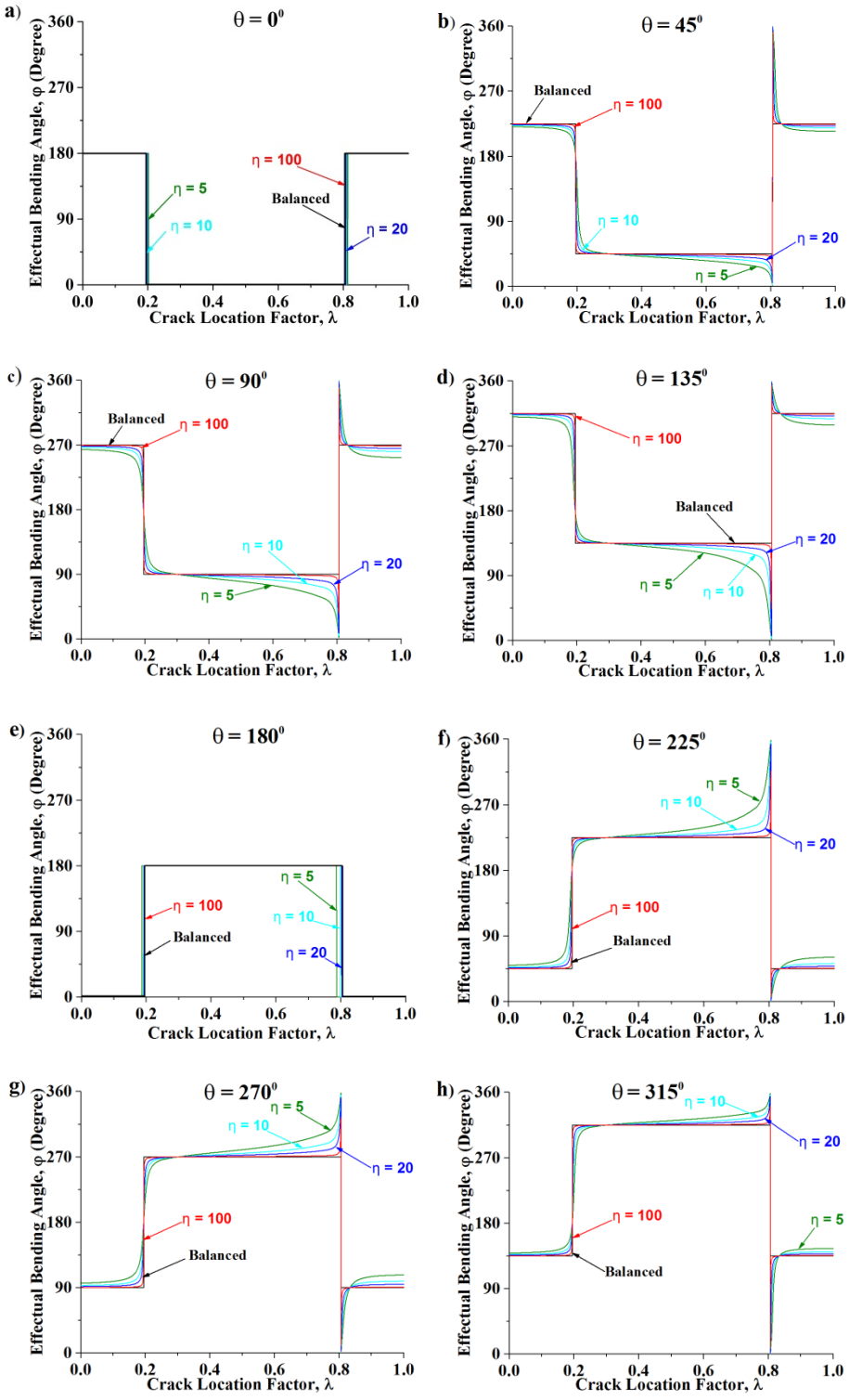

Figure 3-4: Effectual bending angles along the shaft length for different shaft rotation angles with different weight–unbalance force ratios where $\beta = 0°$

A series of analyses are performed using the MATLAB software. In this analysis, the shaft rotation is anticlockwise, and the initial crack direction aligns with the negative *Y*-axis. A crack with a ratio of crack depth $\mu = 0.5$ is chosen to perform the analysis.

The evolution of the effectual bending angles along the shaft length for different shaft rotation angles and different weight–unbalance force ratios is illustrated in Figure 3-4. The effectual bending angles of the balance shaft are constant but have a change of 180° at crack locations λ = 0.1946 and 0.8053 where bending moment owing to total gravitational force (shaft and disks) is zero and the moment changes direction across these two inflection points (see Figure 3-5). Between two inflection points, the moment is in the positive *X*-axis and bending direction aligns along the negative *Y*-axis. Hence, the relation between effectual bending angle and shaft rotation angle is $\varphi = \theta$, which is in agreement with the result in Al-Shudeifat and Butcher (2011). This relation is clearly explained in the given example in Figure 3-5. For the two remaining crack regions, the relationship between effectual bending angle and shaft rotation angle is $\varphi = 180° + \theta$.

For an unbalance shaft, the effectual bending angles along the shaft length are remarkably different from those of the balance one. A few findings can be summarised as follows:

a) There are two shaft rotational angles where the variation pattern of φ along shaft length is similar to the balance shaft; see Figure 3-4(a) and (e). At θ =0°, the unbalance force is in the same direction as the gravitational force of the rotor and at θ =180° the unbalance force is in the opposite direction to the gravitational force. Further, the locations of zero points of combined moment owing to the gravitational force and unbalance force change only slightly at the former shaft rotational angle but dramatically at the latter angle.
b) There are two pairs of crack locations along the shaft where the bending angle is independent of the force ratio η. As mentioned earlier, at inflection points λ = 0.1946 and 0.8053, the gravitational moment is zero (see Figure 3-5), and therefore, the deformation direction or bending direction is solely determined by the unbalance force moment. It should be pointed out that two crack locations are in different unbalance force moment regions, namely, it is negative at the first location and positive at the second location, as shown in Figure 3-6. As a result, the effectual bending angle is 180° at the former crack location and 0° at the latter.

Further, as shown in Figure 3-4, bending angles at these two locations are not only independent of the force ratio but also of the shaft rotational angle. A small amount of unbalance force would have the same effect on the bending angle as a large unbalance force. Therefore, if the crack is located in these two positions, the effect of unbalance force on the crack breathing behaviour must be considered. It should be also mentioned that the jump of bending angle from 0° to 360° or 360° to 0° at $\lambda = 0.8053$ is a result of the crack direction changing from leading to following the bending direction.

c) The other interesting pair of crack locations is at $\lambda = 0.3$ and 0.8335 where the bending angles for all force ratios have at the same value as those for the balance shaft. At these two crack locations, unbalance force moment is zero (see Figure 3-6) and the gravitational force moment is solely responsible for the bending of the shaft. As a result, the cracks will breathe as they would in a balance shaft.

d) For $0° < \theta < 180°$, effectual bending angles decrease nonlinearly when crack location increases from the shaft's left end up to the right end; see Figure 3-4(b), (c) and (d). This variation of φ with the rack location is reversed for the second half of the shaft rotation angle from $180° < \theta < 360°$; see Figure 3-4(f), (g) and (h).

e) As unbalance force decreases (force ratio increases), the bending angles will progressively approach those for the balance shaft, which shows that the unbalance model will be finally in agreement with a balance model when the force ratio is sufficiently large.

The effectual bending angle as a function of shaft rotational angle at some interesting crack locations is shown in Figure 3-7 for some chosen force ratios. It is observed that the bending angle for the balance shaft is one-to-one proportional to the shaft rotation angle. It is a characteristic relationship of the balance shaft previously observed by many researchers. Further, at those locations between two gravitational moment inflection locations λ_2 and λ_5, bending angles are zero at $\theta = 0°$ and they become 180° at locations outside this region, which is consistent with the observation from Figure 3-4(a).

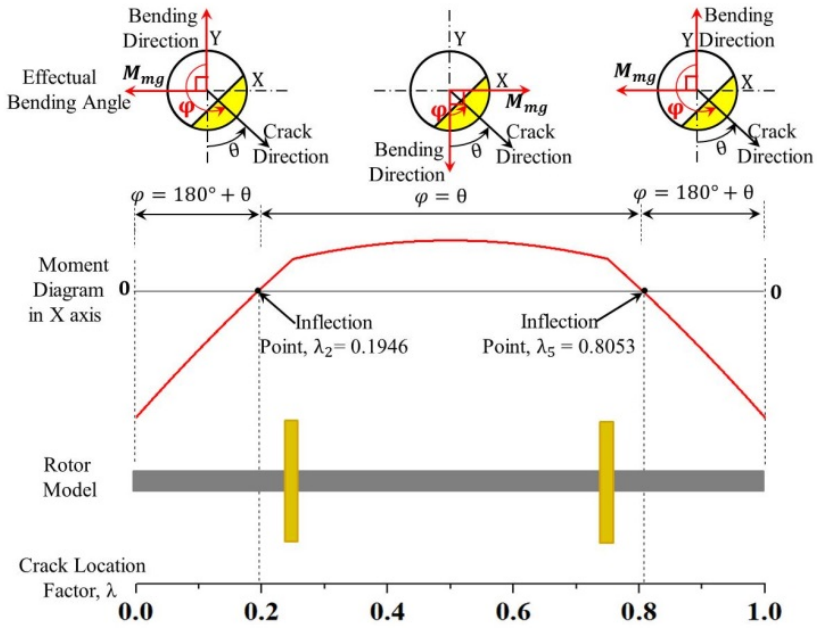

Figure 3-5: Effectual bending angle owing to gravitational moment only where

$$M_{mg} = M_{m_sg} + M_{m_dg}$$

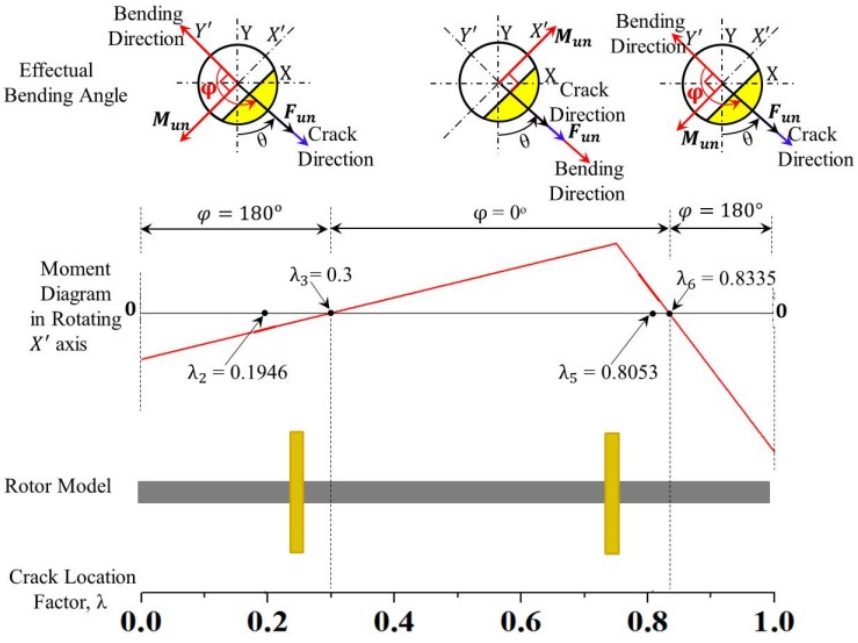

Figure 3-6: Bending angle owing to unbalance force moment only where $\beta = 0°$

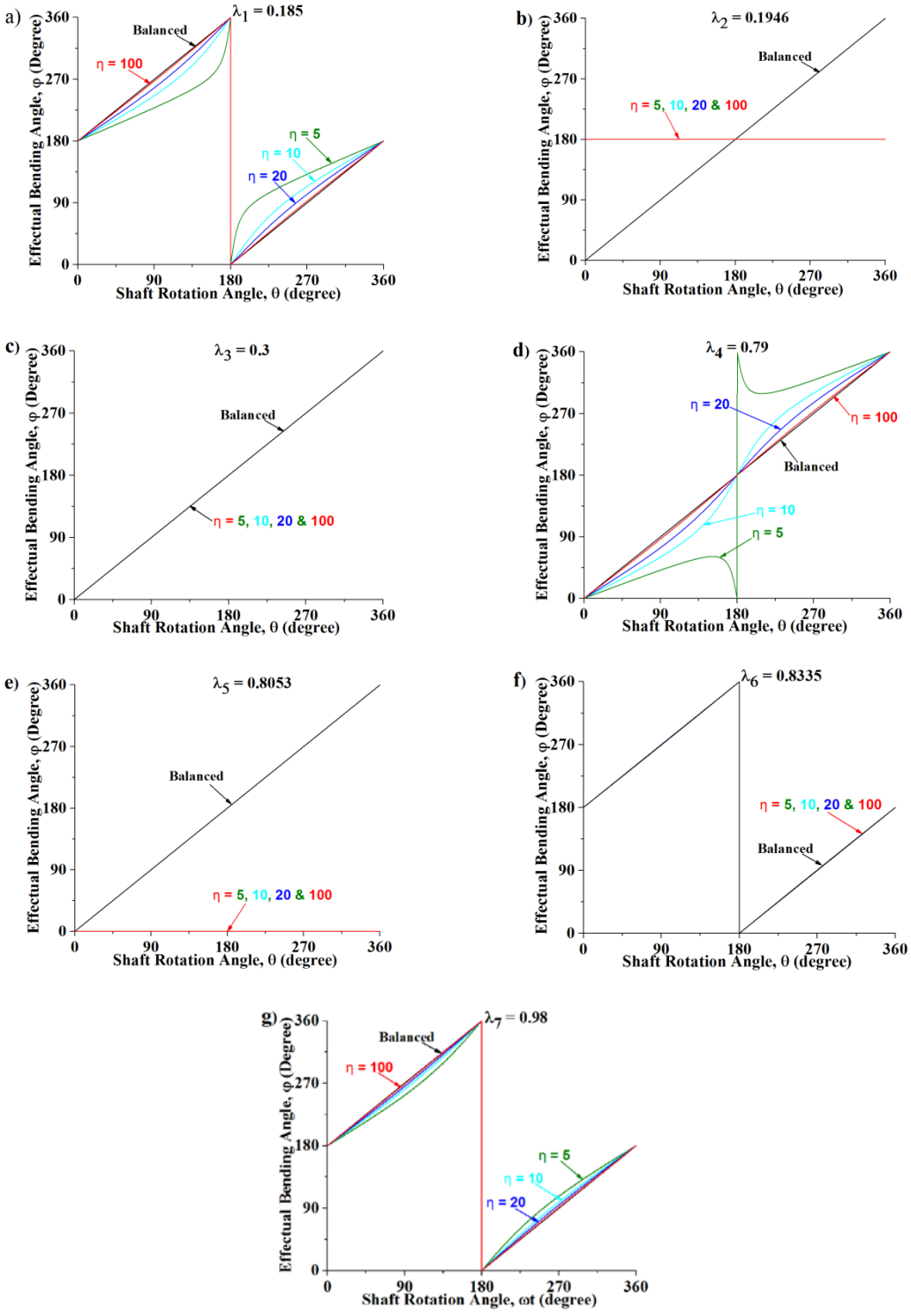

Figure 3-7: Effectual bending angle during a full shaft rotation at selected crack locations for different force ratios where $\beta = 0°$

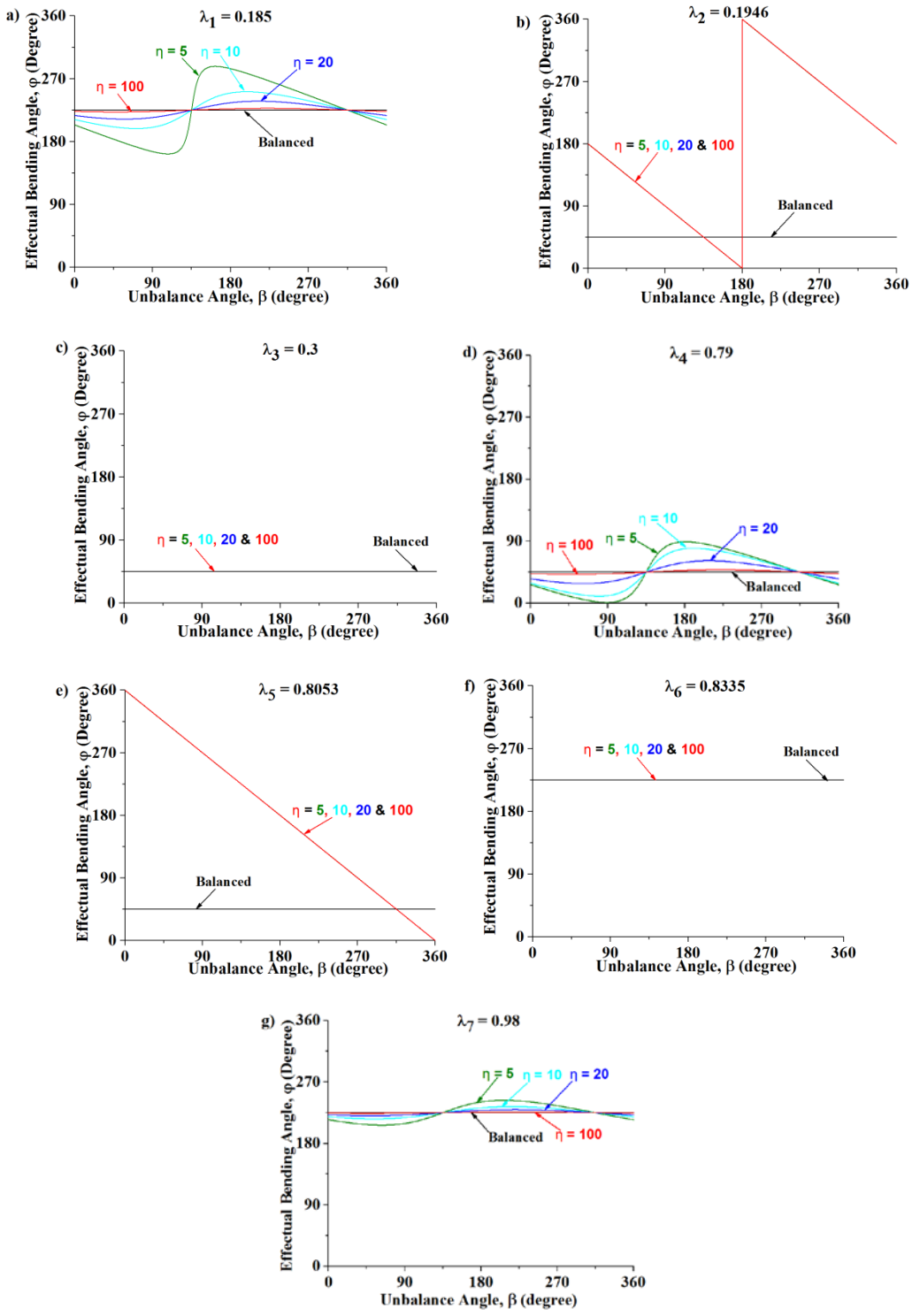

Figure 3-8: Effectual bending angle versus unbalance force orientation angle β where $\theta = 45°$

As regards the unbalance shaft, it is observed again that at zero gravitational moment λ_2 and λ_5, the deformation of the shaft is solely determined by the unbalance force moment and the bending angle is independent of shaft rotational angle, as shown in

Figure 3-7(b) and Figure 3-7(e). The 180° difference in φ between Figure 3-7(b) and Figure 3-7(e) is ascribed to the directional change of the unbalance force moment (see Figure 3-6). Conversely, at zero unbalance force moment locations λ_3 and λ_6, the shaft bending direction is determined by the gravitational moment, and hence, the effectual angle is equal to θ—see Figure 3-7(c)—or $180^o + \theta$—see Figure 3-7(f)—as is the case with a balance shaft. At other crack locations, the bending angle shows a wave-like curve on top of the straight line of the balance shaft.

The effect of angular position of unbalance force on the bending angle can be observed in Figure 3-8. It is clear that β does not affect the bending angle for the balance shaft because no unbalance force is considered. However, for the unbalance shaft at zero gravitational moment locations, $\lambda_2 = 0.1946$ and $\lambda_5 = 0.8053$, the effectual bending angle is equal to 180°-β or 360°-β; see Figure 3-8(b) and Figure 3-8 (e). At zero unbalance force moment $\lambda_3 = 0.3$ and $\lambda_6 = 0.8335$, the bending angle is constant across all β values, which is the same as the balance shaft; see Figure 3-8 (c) and (f). As observed earlier, at these four locations φ is free of the effect of the force ratio. For all other crack locations, there exist two special β values of 135^o and 315^o. When $\beta = 315°$, unbalance force rotates to gravitational force direction because $\beta + \theta = 315^o + 45° = 360^o$. Consequently, the shaft deforms in the same direction and has the same φ value as the balance shaft (see Figure 3-8(a), Figure 3-8(d) and Figure 3-8(g)). When the unbalance force rotates to the opposite direction to the gravitational force ($\beta + \theta = 135° + 45^o = 180^o$), the shaft bends in the direction determined by the larger moment between gravitational and the unbalance force moment. In all cases presented here, the gravitational moment is larger than the unbalance force moment. As a result, the bending angle in the unbalance shaft has the same value as that in the balance shaft.

3.4 Breathing Mechanism of a Crack

Two special shaft rotation angles are θ_1 where the crack starts to close and θ_2 where crack become fully closed. The both angles are a function of cracked shaft geometry as given in Equations (3-8) and (3-9) respectively, where *e* is the location of the centroid and A_1 is the uncracked cross-sectional area as shown in Figure 3-2(a) and described in Equations (3-10) and (3-11) respectively. Equations (3-8) and (3-9) were developed for the balance shaft considering the crack at the midlength of the shaft and the shaft rotational angle as a bending angle (θ=φ) by Al-Shudeifat and Butcher (2011).

$$\theta_1 = \tan^{-1}\left(\frac{e+R(1-\mu)}{R\sqrt{\mu(2-\mu)}}\right) \quad (3\text{-}8)$$

$$\theta_2 = \frac{\pi}{2} + \cos^{-1}(1-\mu) \quad (3\text{-}9)$$

$$e = \frac{2R^3}{3A_1}\sqrt[3]{\mu(2-\mu)} \quad (3\text{-}10)$$

$$A_1 = R^2\left[\pi - cos^{-1}(1-\mu) - (1-\mu)\sqrt{\mu(2-\mu)}\right] \quad (3\text{-}11)$$

The newly developed parameter, the effectual bending angle along the shaft length, is different for both loading conditions. It governs the opening and closing of a crack. The statuses of the crack for different force ratios at different crack locations during shaft rotation can be identified using the values of effectual bending angle, φ. A crack in the unbalance shaft has the same opening/closing status as a crack in the balance shaft as long as they have the same effectual bending angle, which in clearly indicated in Figure 3-9. Therefore, a crack in a balance or an unbalance shaft will start to close at a certain shaft rotation angle (θ) when the effectual bending angle is $\varphi = \varphi_1 = \theta_1$ and the crack will become fully closed at a certain shaft rotation angle (θ) when the effectual bending angle is $\varphi = \varphi_2 = \theta_2$ as shown in Figure 3-9. The main difference between a balance shaft and an unbalance shaft is that the bending direction of the latter keeps changing with the change of shaft rotational angle, unbalance force magnitude and orientation, and crack location. Equations (3-8) and (3-9) are modified to identify the statuses of the crack for different force ratios at different crack locations during shaft rotation using the values of effectual bending angle, φ, as given in Equations (3-12) and (3-13) respectively. The detailed statuses

of the breathing of the crack for a complete effectual bending angle rotation (360^0) are presented in Table 3-2.

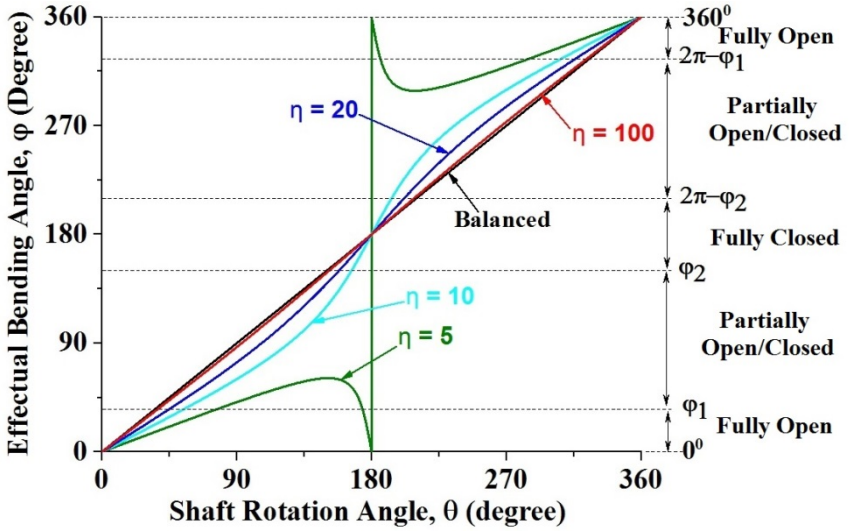

Figure 3-9: Statuses of the crack identified using the values of effectual bending angle

$$\varphi_1 = \tan^{-1}\left(\frac{e+R(1-\mu)}{R\sqrt{\mu(2-\mu)}}\right) \quad (3\text{-}12)$$

$$\varphi_2 = \frac{\pi}{2} + \cos^{-1}(1-\mu) \quad (3\text{-}13)$$

Table 3-2: Status of the crack for a complete effectual bending angle rotation (360^0)

Effectual bending angle $0° \leq \varphi < 360^0$	Status of the crack
$0° \leq \varphi < \varphi_1$	Fully open
$\varphi_1 \leq \varphi \leq \varphi_2$	Partially open/closed
$\varphi_2 < \varphi < 2\pi - \varphi_2$	Fully closed
$2\pi - \varphi_2 \leq \varphi \leq 2\pi - \varphi_1$	Partially open/closed
$2\pi - \varphi_1 < \varphi \leq 360°$	Fully open

The statuses of the crack at different crack locations during shaft rotation are evaluated quantitatively using percentages of the opening of a crack. The percentage of opening of a crack Λ as described in Equation (3-14) is determined using the effectual bending angle by studying the transient change in the area of the cracked cross-section. A_c is the area of the crack segment, as shown in Figure 3-2(a), and $A_2(t)$ is the closed portion of the crack segment when the effectual bending angle $\varphi_1 \leq \varphi \leq \varphi_2$ or $(2\pi-\varphi_2) \leq \varphi \leq (2\pi-\varphi_1)$ (see Figure 3-10). A_c can be calculated by Equation (3-15), and $A_2(t)$ is determined using a procedure proposed in balance shaft analysis (Al-Shudeifat & Butcher, 2011) to calculate the variation of $A_2(t)$ with shaft rotational angle. It is obvious, as shown in Figure 3-10, that $A_2(t)$ in the unbalance shaft is equal to that in a balance shaft when the bending angle in the former is equal to the rotational angle in the latter. For the calculation of $A_2(t)$ in the unbalance shaft, first, $A_2(t)$ for the balance shaft are calculated using formulas from Al-Shudeifat and Butcher (2011). This $A_2(t)$ becomes that for the unbalance shaft at a bending angle equal to the shaft rotational angle in the balance shaft. Then, using Equations (3-1) to (3-7), the $A_2(t)$ with different force ratios at a shaft rotational angle for the unbalance shaft is obtained. It is suggested that readers consult the adopted study (Al-Shudeifat & Butcher, 2011) for the expressions of $A_2(t)$ for the balance shaft. For a fully open crack and fully closed crack, the percentage of opening of a crack Λ is equal to 100 and 0, respectively.

$$\Lambda\,(\%) = \frac{A_c - A_2(t)}{A_c} \times 100 \tag{3-14}$$

$$A_c = R^2 \cos^{-1}(1-\mu) - R^2(1-\mu)\sqrt{\mu(2-\mu)} \tag{3-15}$$

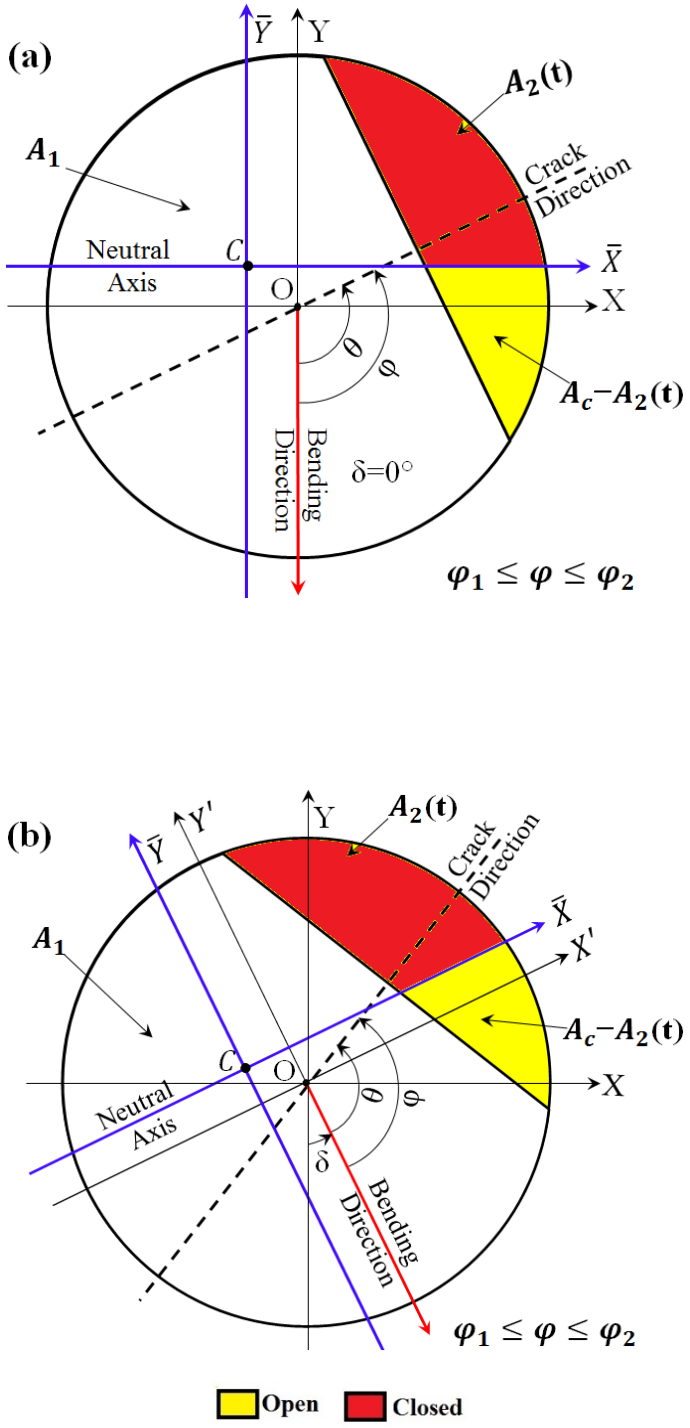

Figure 3-10: Schematic diagrams of the closed portion of a breathing crack for (a) a balance shaft and (b) an unbalance shaft

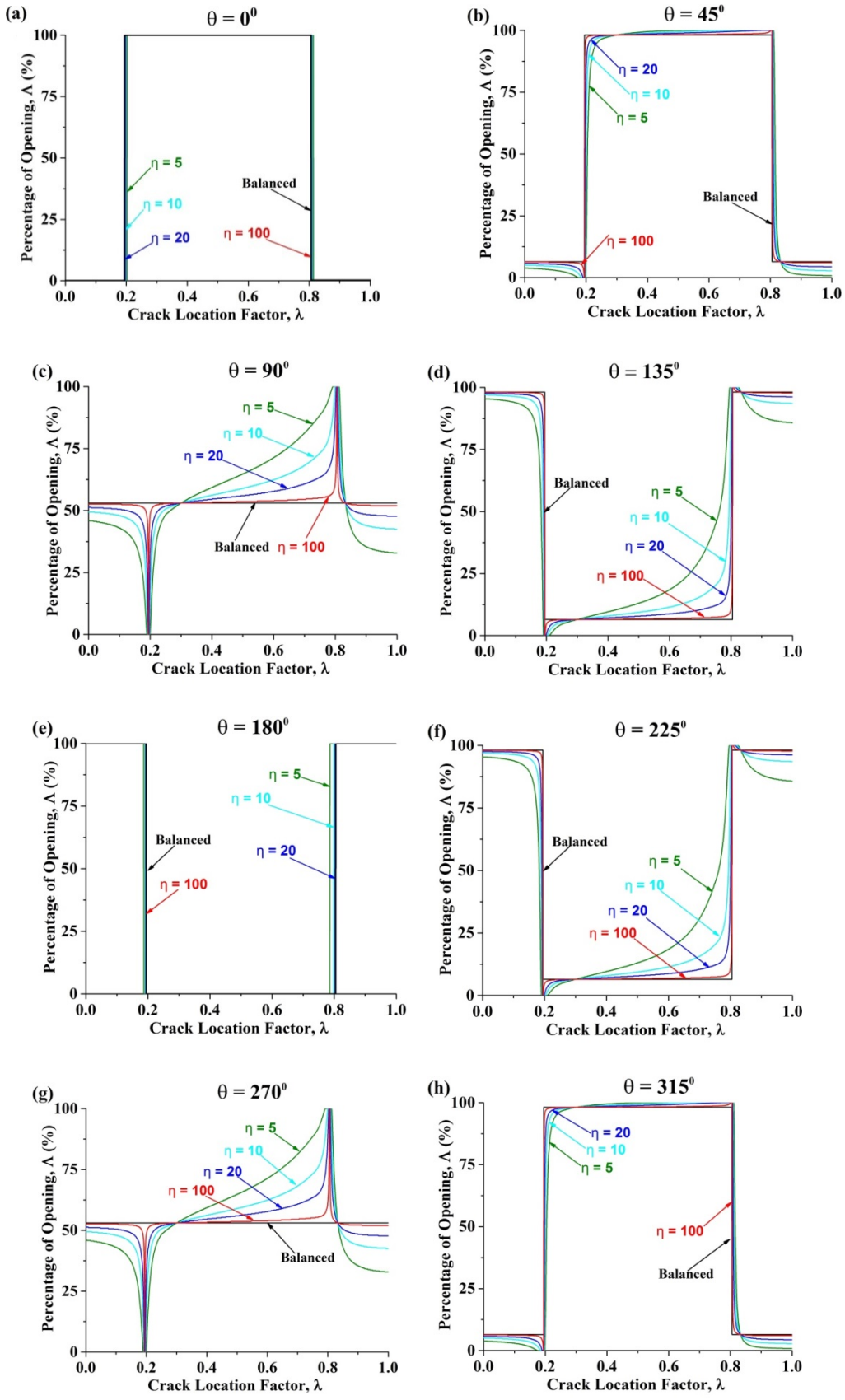

Figure 3-11: Percentage of the opening of a crack as a function of crack location for different shaft rotation angles, θ, and force ratios, η, where $\beta = 0°$

Crack breathing behaviour can be evaluated quantitatively using the percentage of opening of the crack, Λ, as displayed in Figure 3-11. Similar to the variation of bending angle with the crack location, λ, the percentages of opening for all force ratios are the same at $\lambda_2 = 0.1946$ and $\lambda_5 = 0.8053$ and approach the value of a balance shaft at the crack locations $\lambda_3 = 0.3$ and $\lambda_6 = 0.8335$. Shaft stiffness variation with crack location can be divided into three regions at the zero points of gravitational moment λ_2 and λ_5. Increasing λ from 0 to λ_2 leads to a stiffening processing of the shaft because of decreasing in Λ, then a softening process from λ_2 to λ_5 and finally a stiffening process again from λ_5 to the right end of the shaft. Zero points of the unbalance force moment λ_3 and λ_6 also divide shaft length into three regions where the overall stiffness of the shaft during rotation is different from that of the balance shaft. When the crack is located between λ_3 and λ_6, it is obvious that the percentage of opening of the crack for the unbalance shaft is larger than that for the balance counterpart, which indicates that the unbalance shaft is more flexible than the balance shaft (also see Figure 3-12(d)). For the remaining two regions, the unbalance shaft becomes stiffer (also see Figure 3-12(a) and Figure 3-12(g)).

It is also clear in Figure 3-12 that variation of Λ with crack location depends strongly on the shaft rotational angle. The percentage of opening Λ for the balance shaft remains unchanged throughout the entire shaft length when the shaft rotates at 90° and 270°. Λ for the balance shaft is symmetrical about the shaft middle point. However, for the unbalance shaft Λ is no longer symmetrical. Moreover, along with the shaft length, a small difference in Λ is observed between the balance shaft and unbalance one, when the shaft is at the early stage, or near the completion, of rotation as shown in Figure 3-12(a), Figure 3-12(b) and Figure 3-12(h).

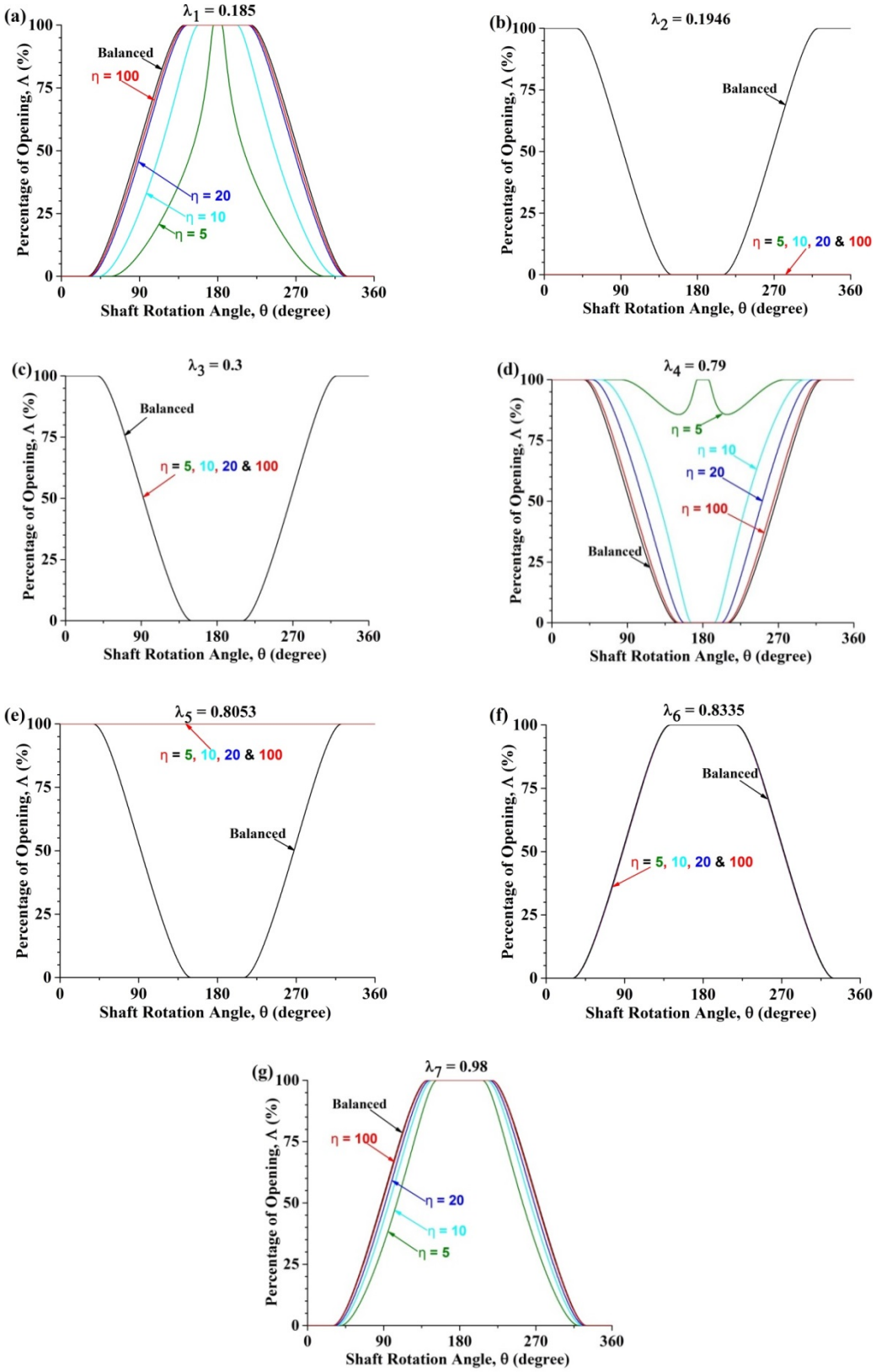

Figure 3-12: Percentage of the opening of the crack as a function of shaft rotation angle for different crack locations, λ, and different force ratios, η, where $\beta = 0°$

The percentage of opening of the crack as a function of shaft rotation angle is depicted in Figure 3-12. During a full shaft rotation of 360°, the shaft will experience two processes, namely, a stiffening process corresponding to the decreasing in Λ and a softening process corresponding to the increase in Λ. These two processes are observed to be symmetrical about θ = 180°. The flat part of the curve corresponds to either a fully open range (Λ = 100%) or a fully closed range (Λ = 0%). When a crack is at λ_2 = 0.1946, the crack in the unbalance shaft will never open during rotation, causing the unbalance shaft to behave like an uncracked one (see Figure 3-12(b)). A crack in the unbalance shaft will never close during rotation, and the unbalance shaft will behave like a shaft with a notch crack at λ_5 = 0.8053 (see Figure 3-12 (e)). At λ_3 and λ_6, a crack will breathe completely like one in the balance shaft (see Figure 3-12 (c) and Figure 3-12 (f)).

A special case where the unbalance force aligns with the crack direction (β = 0°) is represented in Figure 3-11 and Figure 3-12. For the general unbalance force orientations as shown in Figure 3-13, it is identified that the unbalance shaft is overall stiffer than the balance one when the unbalance force is located in the half area of the cross-section opposite the crack (90° < β < 270°). In particular, when β = 180° the shaft is stiffest (comparing Figure 3-13 (d), Figure 3-13 (e) and Figure 3-13 (f)). Conversely, the unbalance shaft is overall more flexible than the balance counterpart when the unbalance force is located at the same half area of the cross-section of the crack (0° ≤ β < 90° and 270° < β ≤360°) and with β = 0° the shaft has the least stiffness (see Figure 3-13(a), Figure 3-13 (b) and Figure 3-13 (h)). The conclusion drawn here from Figure 3-13 at λ = 0.79 also holds true at other crack locations (results not presented). Therefore, the conclusions previously drawn from Figure 3-11 regarding the variation of opening percentage with a crack location at β = 0° will become opposite when β = 180° (or more generally 90° < β < 270°). The original direction of the unbalance force will generate a significant effect on the vibration of the cracked shaft as observed previously. Cheng et al., (2011) found that the unbalance orientation played an important role in the peak amplitude of the vibration, where the minimum and maximum vibration amplitude corresponded to the eccentric mass being located at, and opposite, the crack.

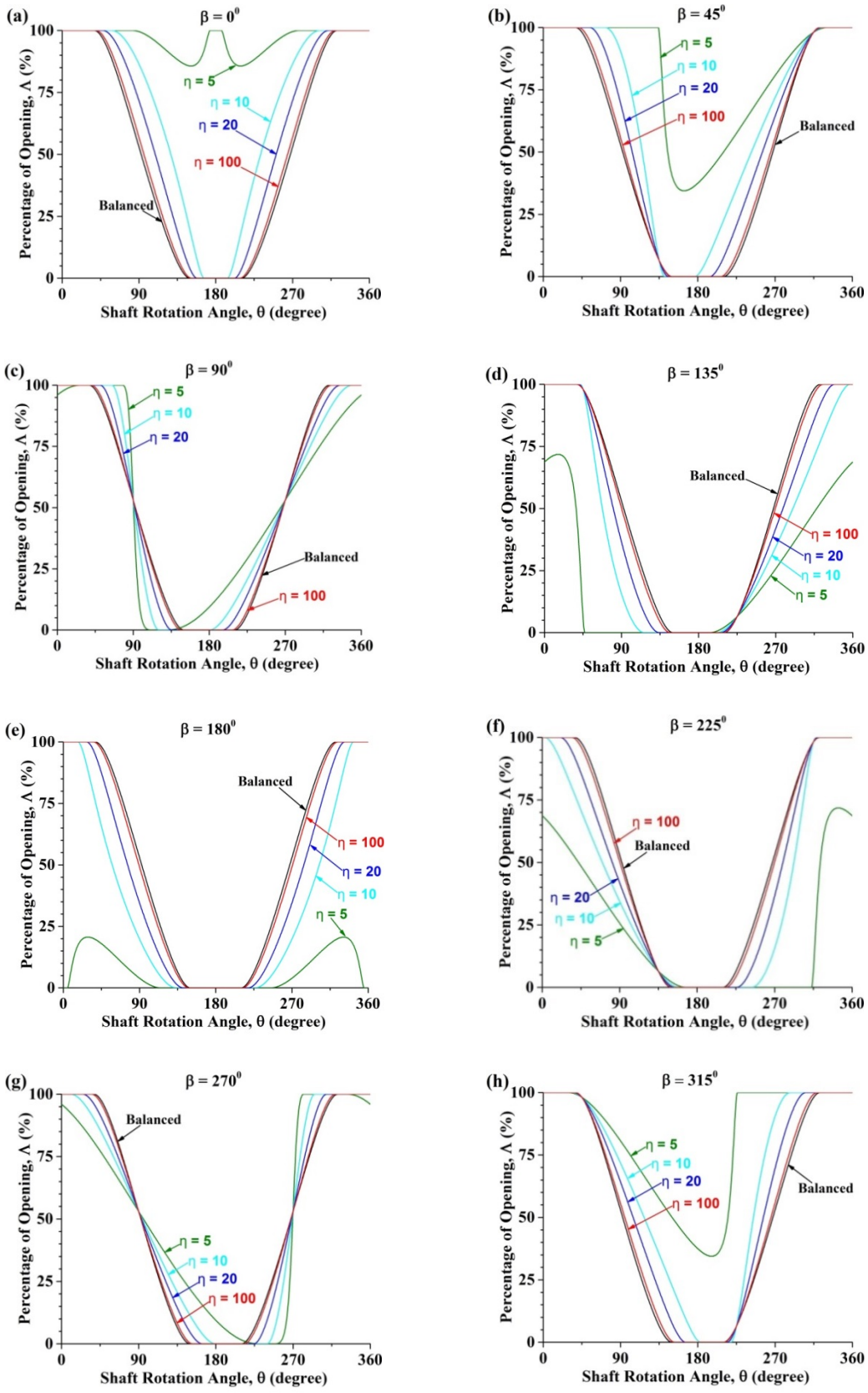

Figure 3-13: Effect of unbalance force orientation on the crack breathing behaviour at $\lambda = 0.79$

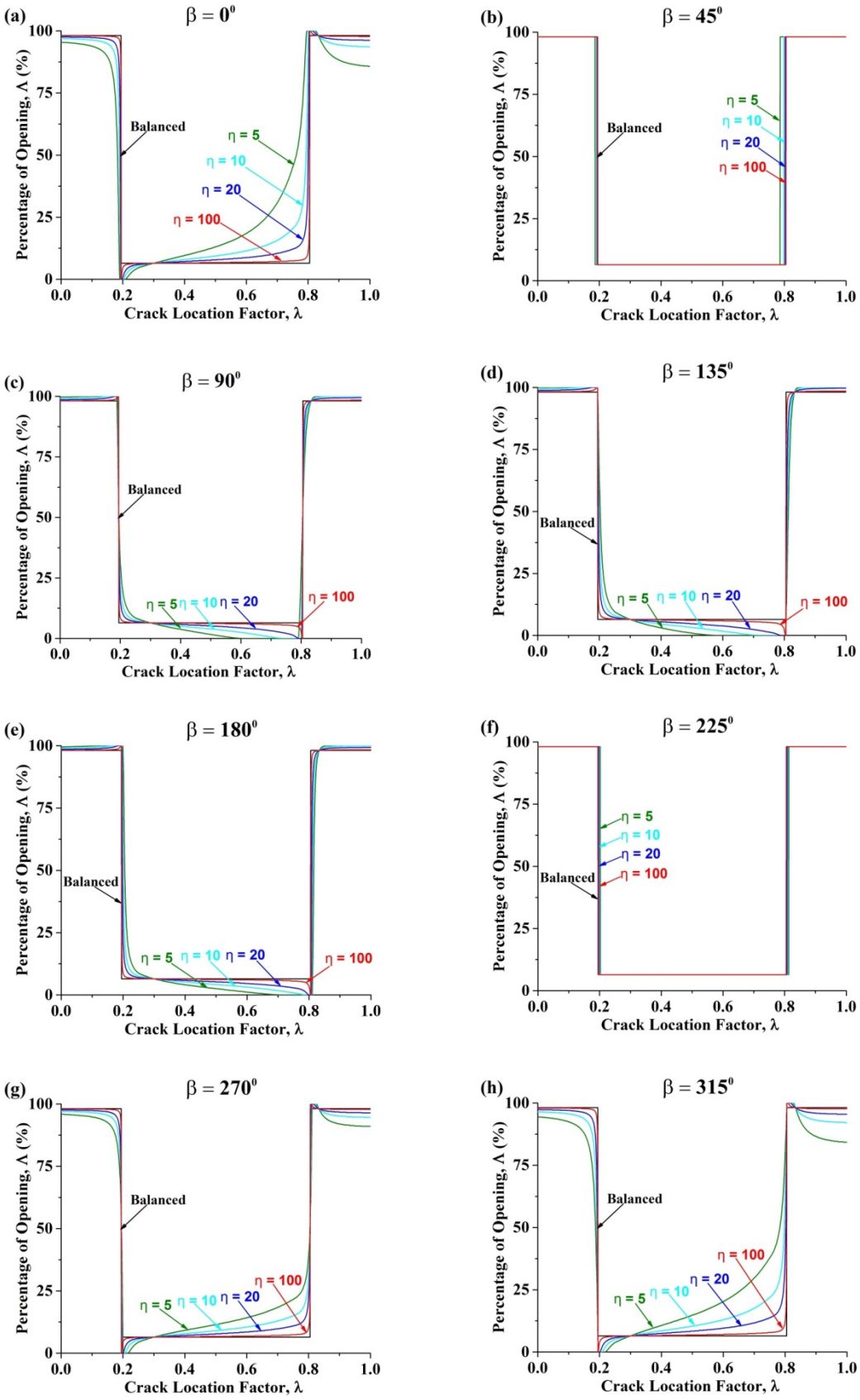

Figure 3-14: Effect of unbalance force orientation on the crack breathing behaviour where θ = 135°

Two special unbalance force orientations, that is, β = 90° and β = 270°, are identified as shown in Figure 3-13. At these two orientations, the percentage of opening of the crack for the unbalance shaft is sometimes larger than that of a balance shaft and is sometimes smaller during full shaft rotation. The result demonstrates that the overall stiffness of the unbalance shaft is more or less the same as that of the balance shaft (see Figure 3-13(c) and Figure 3-13(g)). It is also observed that the symmetry between the stiffening process and softening process to 180° shaft rotation angle disappears except for β = 0° and β = 180°. The opening percentage as a function of the crack location under selected unbalance force orientation is depicted in Figure 3-14. It is clearly observed that the difference in the percentage of the opening along the shaft length between two models is larger when 180°< β ≤ 360° (β = 0° in Figure 3-14(a)).

3.5 Centroidal Orbits and Area Moment of Inertia of a Crack

Studying the change in the area moment of inertia of a cracked shaft can link the breathing mechanism to the stiffness matrix in the rotor and ultimately facilitate calculation of the vibration responses. Al-Shudeifat and Butcher (2011) developed an iterative method to calculate the area moment of inertia of the time-varying crack cross-section closed area $A_{ce}(t)$ for a balance shaft (shown in Figure 3-10(a)). In their study, the effect of the unbalance force and shaft support condition on the crack breathing is neglected. The time-varying crack cross-section closed area, $A_{ce}(t)$, is equal to $A_1 + A_2(t)$, where A_1 is the area of the uncracked element (see Figure 3-2(a)) and $A_2\,(t)$ is the area of the closed portion of the crack at time *t* (see Figure 3-10). First, the method calculates the areas $A_2(t)$ and A_1 and their respective centroid locations to obtain the overall magnitude and centroid location of $A_{ce}(t)$. Then, the area moment of inertia of $A_{ce}(t)$ about the centroidal axes $\bar{X}$ and $\bar{Y}$ are obtained.

For the unbalance system, as shown in Figure 3-10(b), the modified centroid coordinates X_{ce} and Y_{ce} of crack cross-section closed area $A_{ce}(t)$ about the original nonrotated coordinate *X* and *Y* axes are described in Equations (3-16) and (3-17),

where X'_{ce} and Y'_{ce} are the centroid coordinates w.r.t. the X' and Y' axes, which are the same as those w.r.t. the X and Y axes in the balance model.

$$X_{ce} = X'_{ce}\cos\delta - Y'_{ce}\sin\delta \quad (3\text{-}16)$$

$$Y_{ce} = X'_{ce}\sin\delta + Y'_{ce}\cos\delta \quad (3\text{-}17)$$

For unbalance shaft, the area moment of inertia of the crack cross-section closed area about $\bar{X}$ and $\bar{Y}$ are obtained by comparing the geometric similarity between two models. When the bending angle in the unbalance shaft is equal to the shaft rotational angle in the balance shaft, the area moment of inertia of the crack cross-section closed area about the respective $\bar{X}$ and $\bar{Y}$ in two models are also equal. After obtaining the area moment of inertia for the balance shaft using expressions in Al-Shudeifat and Butcher (2011), the area moment of inertia with different force ratios at a shaft rotational angle for an unbalance shaft are obtained using the relationship between the bending angle and shaft rational angle in Equation (3-7).

The centroid orbits of the crack cross-section closed area, $A_{ce}(t)$, about the X and Y axes at different crack locations under different force ratios are illustrated in Figure 3-15. Although effectual bending angle, the status of the cracks and percentage of opening for the balance shaft all depend on the crack location, the orbits remain unchanged along the crack length. Similar to the previous results, the centroid orbit for the unbalance shaft also has special behaviours at four crack locations. Notably, at λ_2 the orbit is just a single point lying on the origin indicating a fully-closed-never-opened crack and is independent of the force ratio (see Figure 3-15(b)). At λ_5, a circle is observed indicating a fully opened crack also independent of the force ratio (see Figure 3-15 (e)). Further, the orbit for the unbalance shaft at λ_3 and λ_6 overlaps that of the balance shaft (see Figure 3-15(c) and Figure 3-15(f)). The orbit at other locations generally changes the shape and largeness of the circle depending on the crack location and force ratio. In general, an enlarged orbit means a small overall stiffness of the shaft. When the orbit for the balance shaft encircles that for the unbalance shaft as shown in Figure 3-15(a) and Figure 3-15(g), the overall stiffness of the balance shaft is smaller than that of the unbalance shaft and vice versa as shown in Figure 3-15(d). The observations on the orbit agree with previous results.

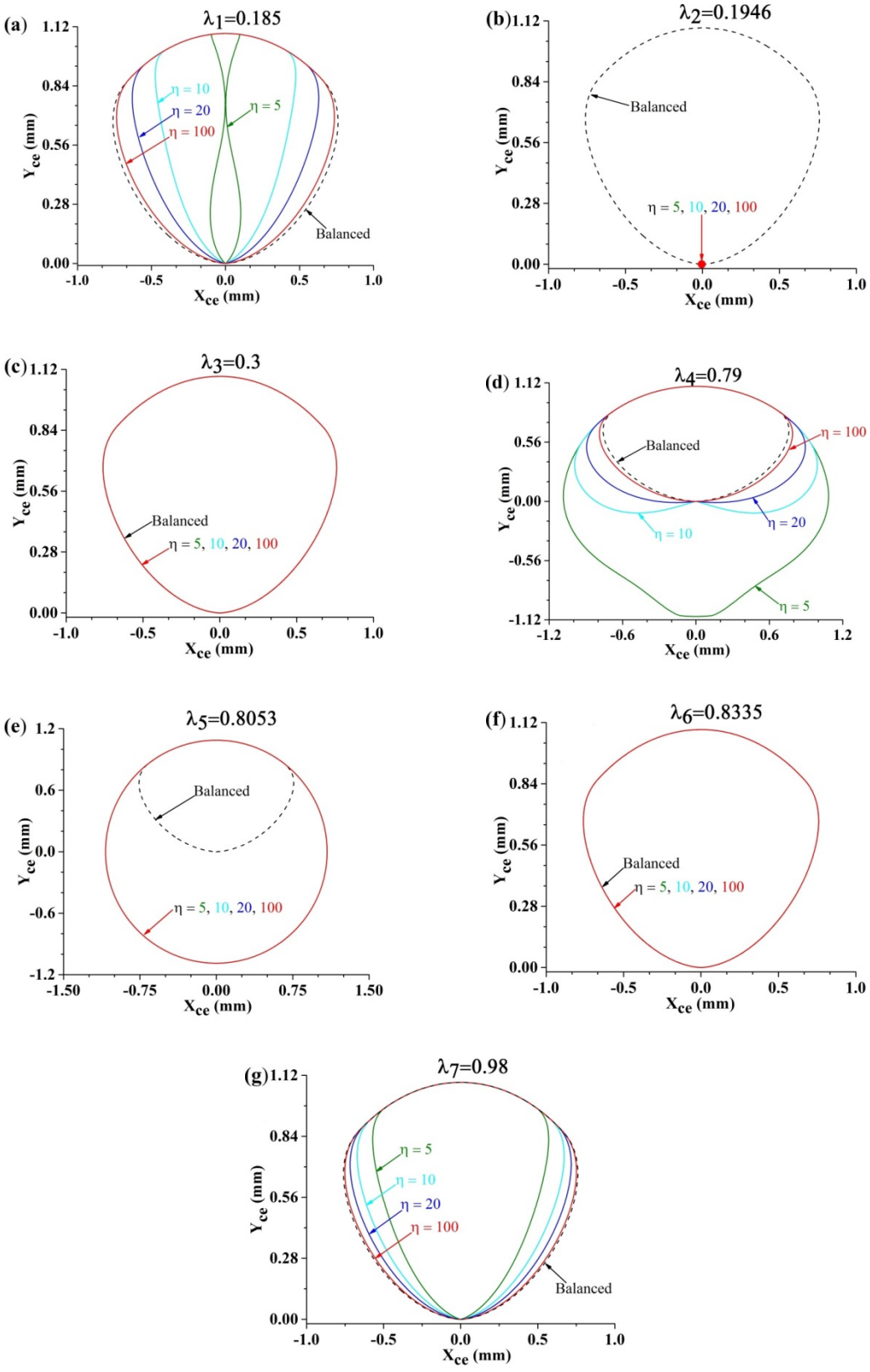

Figure 3-15: Orbits of the centroid of the crack cross-section closed area , $\boldsymbol{A_{ce}(t)}$, for different crack locations, λ, and weight–unbalance force ratios, η, where β = 0°

The area moment of inertia along the shaft length about centroid axes $\bar{X}$ and $\bar{Y}$ are illustrated in Figure 3-16 to Figure 3-20. The value for $I_{\bar{X}}$ that corresponds to a fully closed crack status is 1.27×10^{-9} m^4 (same as for the uncracked shaft $\frac{\pi R^4}{4}$) and 0.65×10^{-9} m^4 for a fully opened crack (comparing Figure 3-14(a) and Figure 3-18(a)). $I_{\bar{X}}$ changes between these two values during shaft rotation and along the shaft length. The value for $I_{\bar{Y}}$ at these two crack statuses is 1.27×10^{-9} m^4 and 1.11×10^{-9} m^4, respectively (see Figure 3-19(a)). Interestingly, $I_{\bar{Y}}$ could be larger for a fully open crack than for a partially open/closed crack. Further, a variation of $I_{\bar{Y}}$ with shaft rotational angle, θ, differs from that of $I_{\bar{X}}$ showing dual minimum behaviour, as shown in Figure 3-20. As regards the effect of the crack location, previous conclusions on the crack breathing behaviour at two pairs of special locations can also be deduced from the area moment of inertia (see Figure 3-18(c), (d), (e), (f), (i), (j), (k) and (l)). It is expected that a large difference between two models in the area moment of inertia during shaft rotation and along shaft length will generate a large difference in vibrations accordingly. Further study on the vibration behaviour of a cracked rotor under the influence of unbalance force is currently underway.

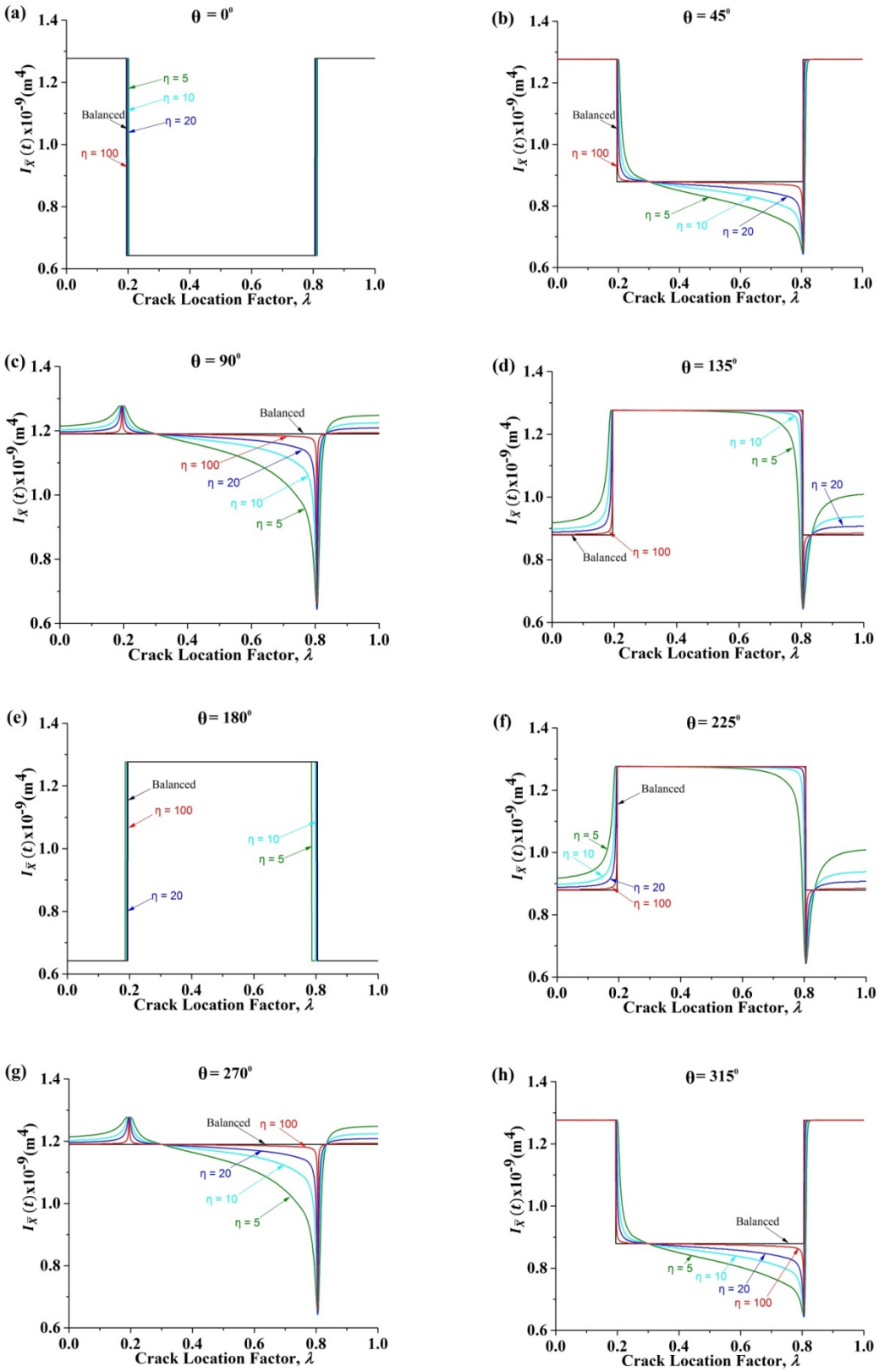

Figure 3-16: Area moment of inertia $I_{\bar{X}}$ of the crack cross-section closed area, $\mathbf{A_{ce}(t)}$, along the shaft length where $\beta = 0°$

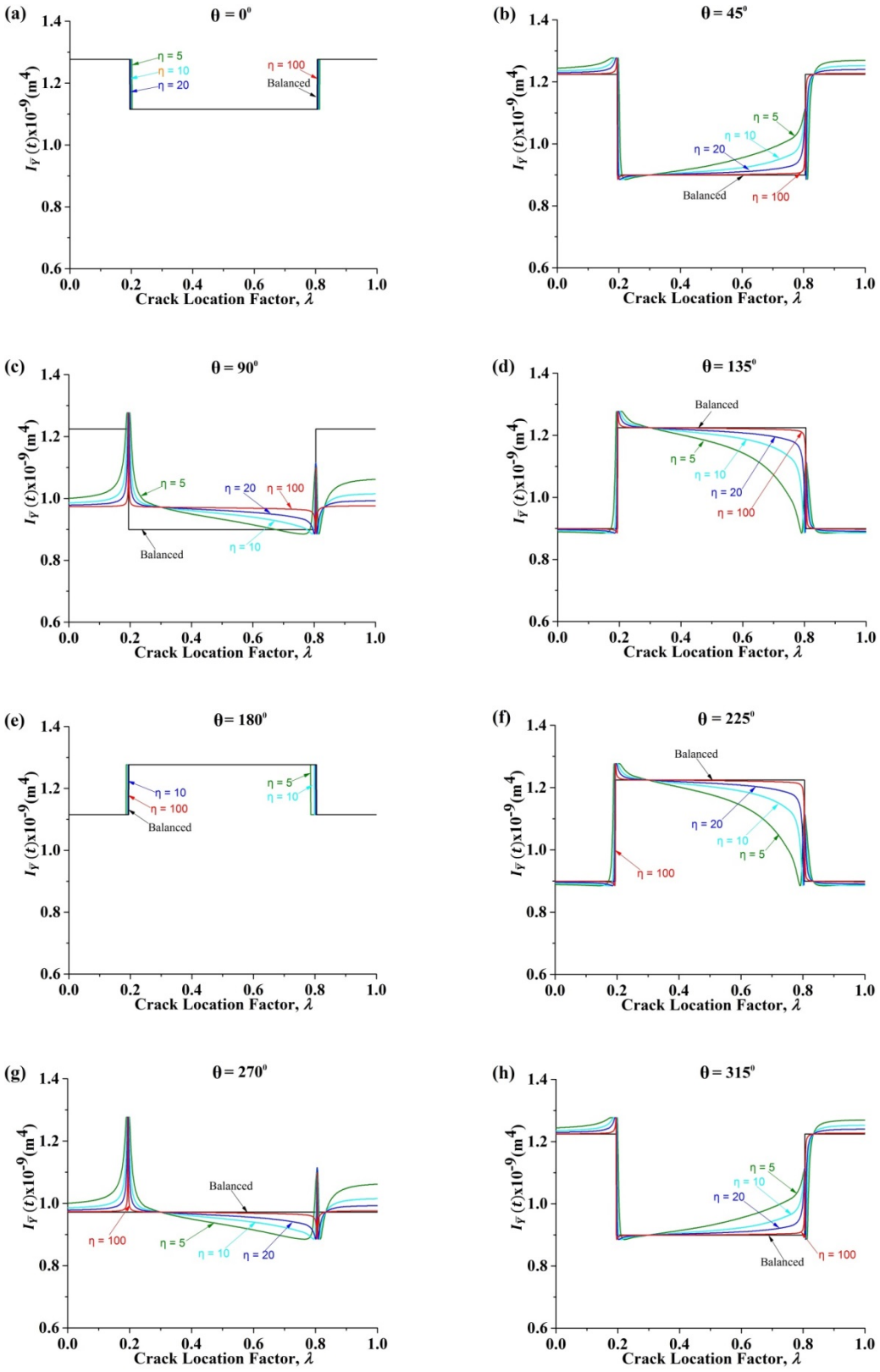

Figure 3-17: Area moment of inertia $I_{\bar{Y}}$ of crack cross-section closed area, $\mathbf{A_{ce}(t)}$, along the shaft length where $\beta = 0°$

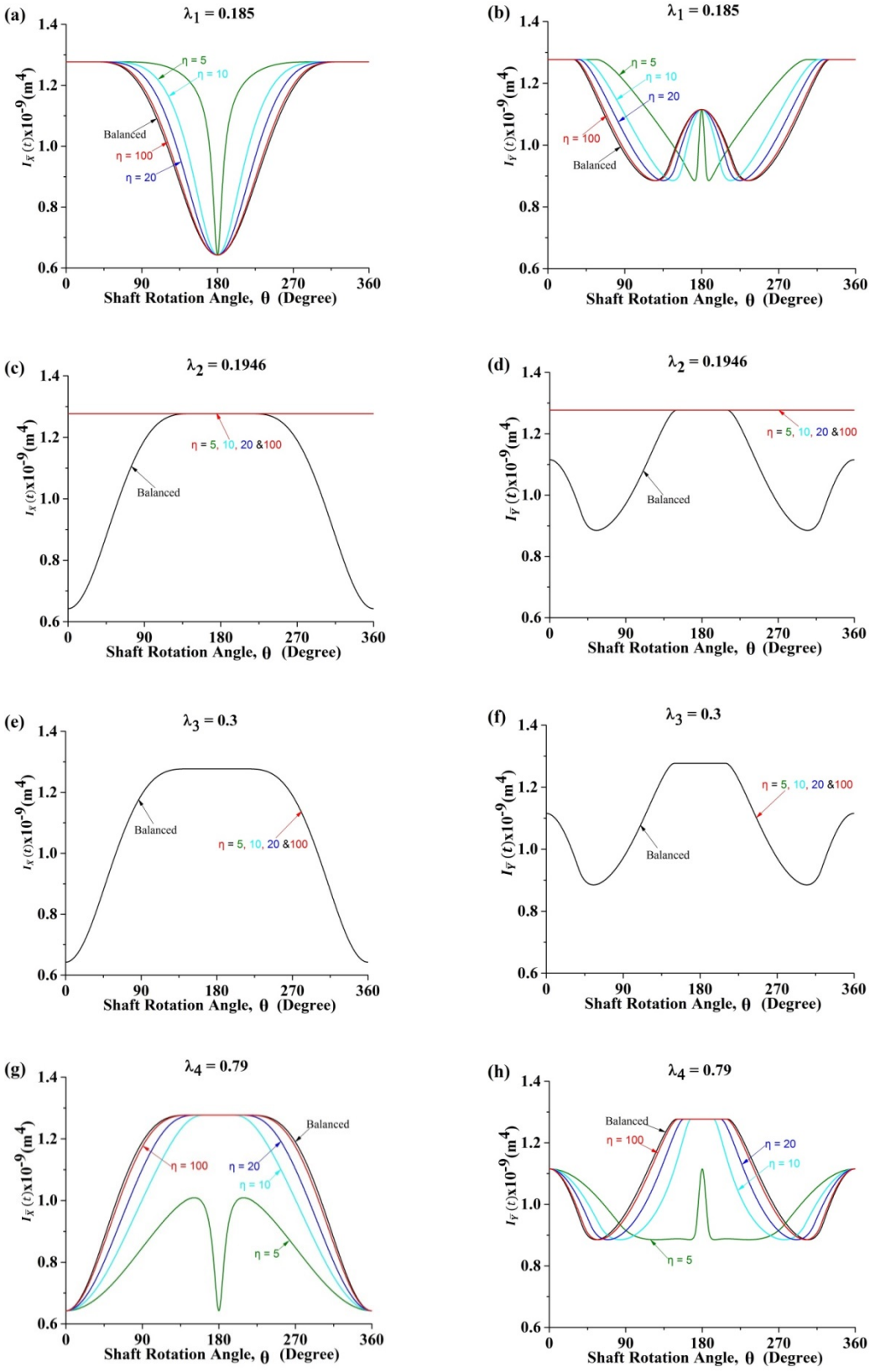
(a)
λ1 = 0.185
η = 5
η = 10
Balanced
η = 100
η = 20
(b)
λ1 = 0.185
η = 5
η = 10
η = 20
η = 100
Balanced
(c)
λ2 = 0.1946
η = 5, 10, 20 &100
Balanced
(d)
λ2 = 0.1946
η = 5, 10, 20 &100
Balanced
(e)
λ3 = 0.3
Balanced
η = 5, 10, 20 &100
(f)
λ3 = 0.3
η = 5, 10, 20 &100
Balanced
(g)
λ4 = 0.79
Balanced
η = 100
η = 20
η = 10
η = 5
(h)
λ4 = 0.79
Balanced
η = 100
η = 20
η = 10
η = 5
Shaft Rotation Angle, θ (Degree)

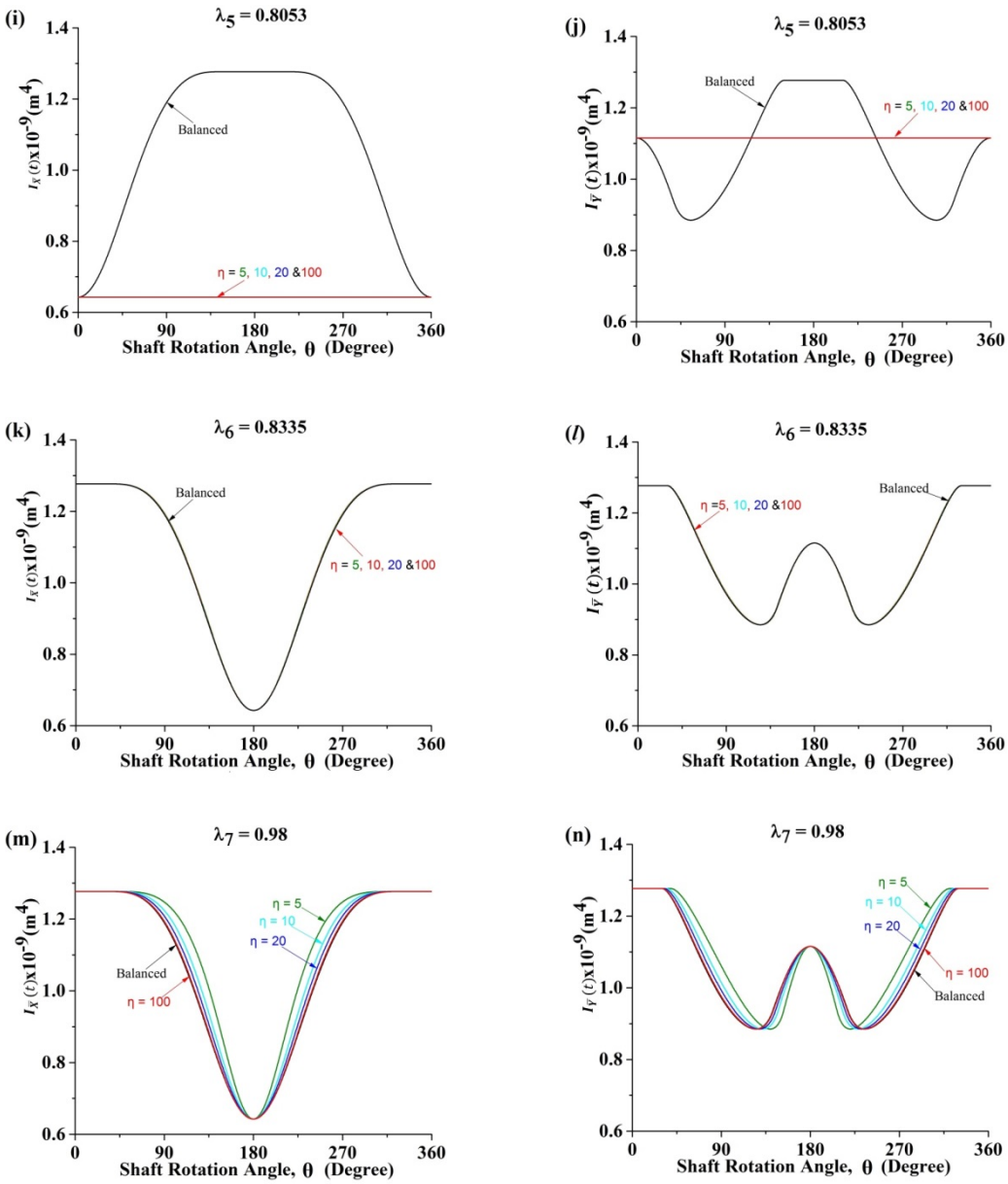

Figure 3-18: Area moment of inertia of $\boldsymbol{I_{\bar{X}}}$ and $\boldsymbol{I_{\bar{Y}}}$ of crack cross-section closed area, $\boldsymbol{A_{ce}(t)}$, over a full shaft rotation, θ, where β = 0°

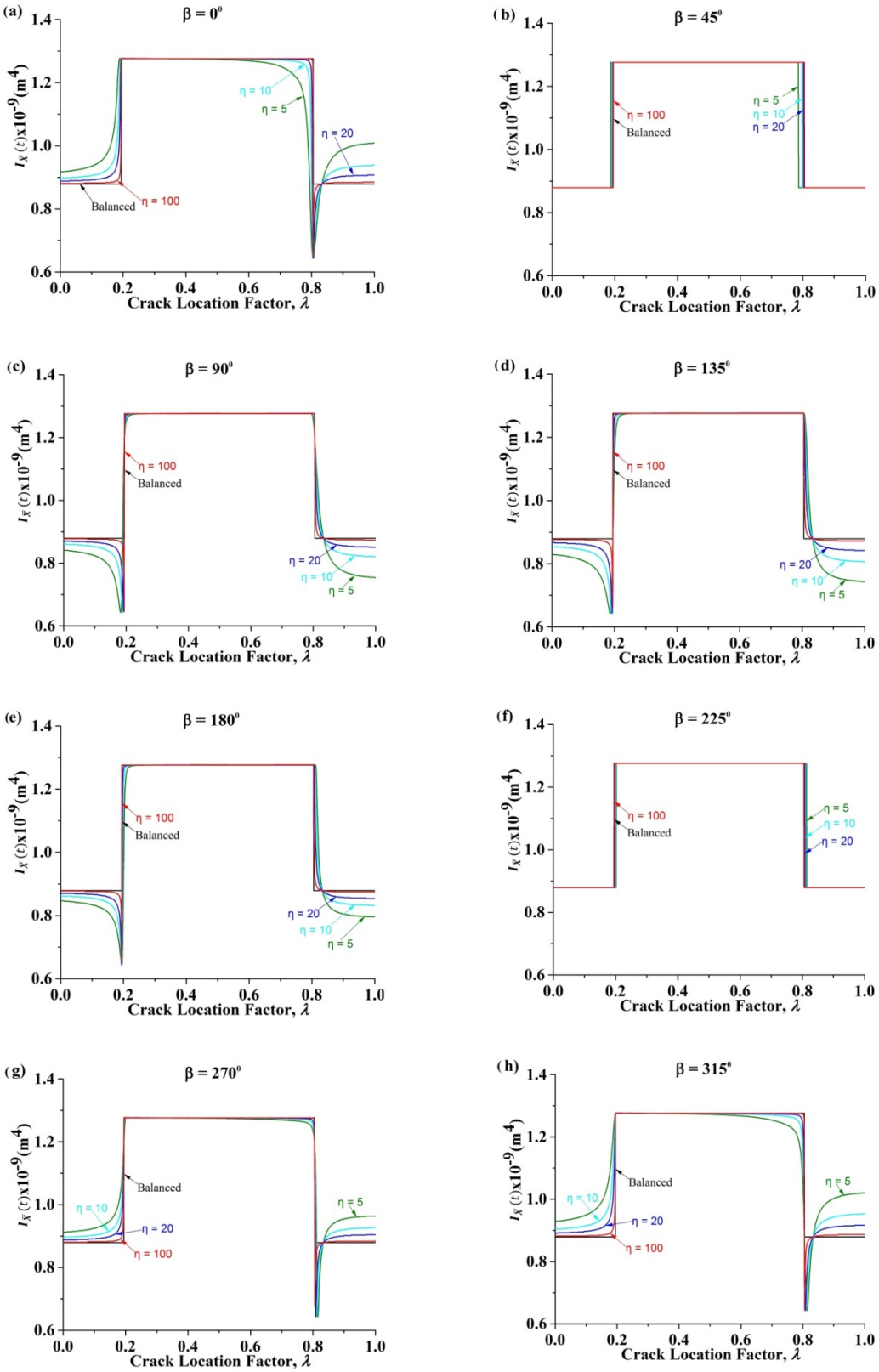

Figure 3-19: Area moment of inertia of $\boldsymbol{I_{\bar{X}}}$ of crack cross-section closed area, $\boldsymbol{A_{ce}(t)}$, for different β along the shaft length where θ = 135°

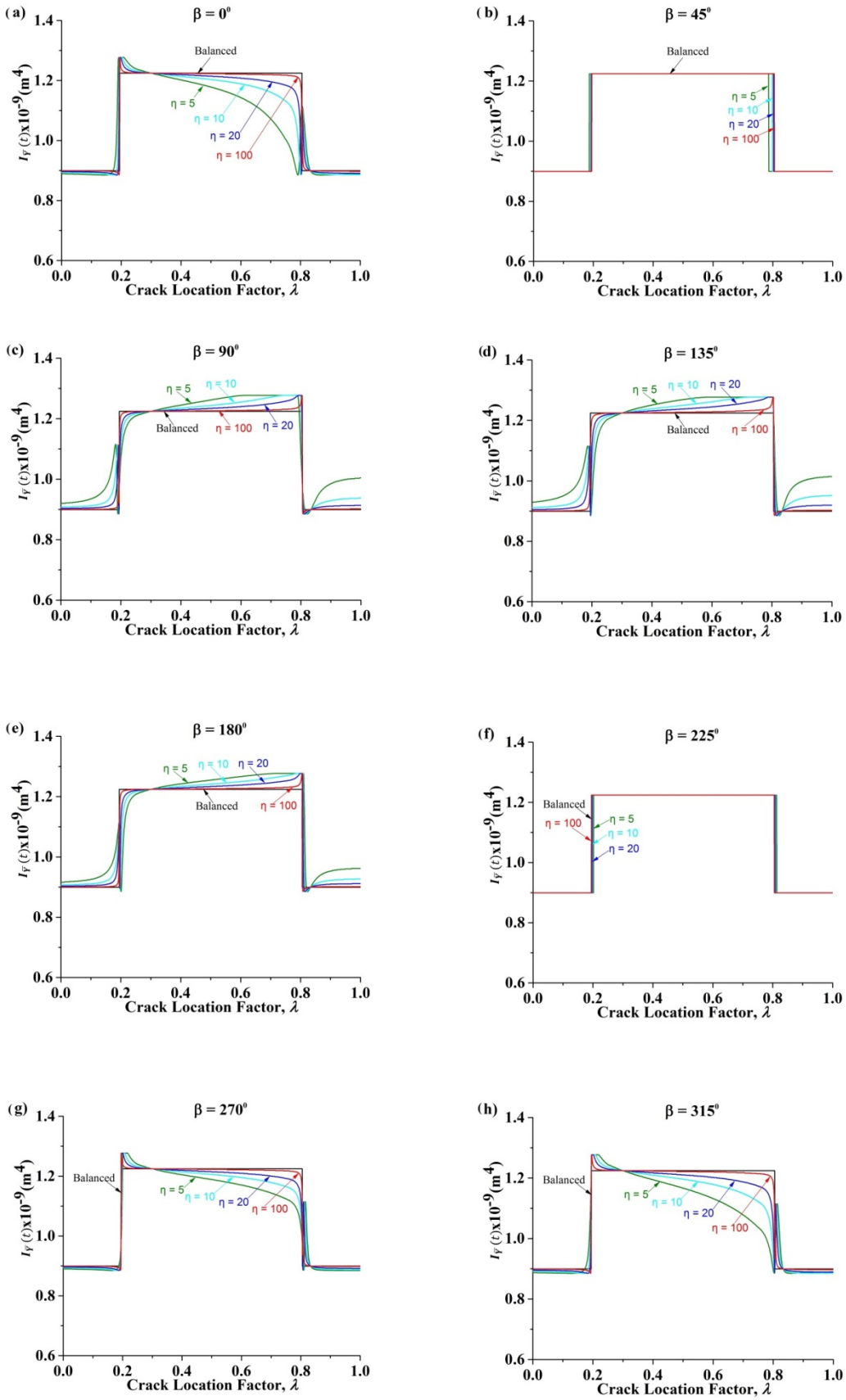

Figure 3-20: Area moment of inertia of $\boldsymbol{I_{\bar{Y}}}$ of crack cross-section closed area, $\boldsymbol{A_{ce}(t)}$, for different β along the shaft length where θ = 135°

3.6 Validation of Newly Developed Unbalance Model

3.6.1 Three-dimensional finite element modelling

Objectively validating the work presented in this chapter is not easily achieved through experimental methods. Experimental measurements typically revolve around mechanical strain or kinetic parameters, such as deflection, velocity, force and acceleration. By contrast, the newly developed breathing function deals with more abstract parameters, such as crack contact area, area moment of inertia and neutral axis position. A full 3D FE model of a cracked rotor was created as it provides a method of directly validating some parameters. The numerical validation is performed using the commercial code of Abaqus/standard. The 3D finite element model of the shaft is presented in Figure 3-21.

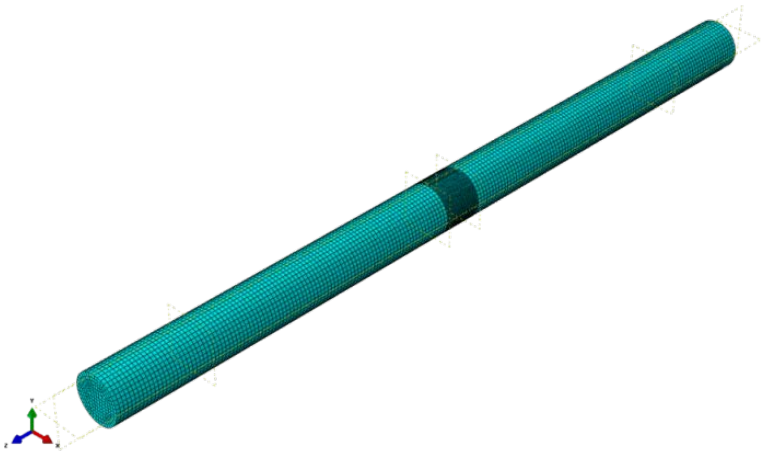

Figure 3-21: Complete 3D finite element model of the shaft

The simulation is conducted as a series of static problems with different crack locations along the shaft length in axial and angular positions. A transverse straight crack with nondimensional crack depth ratio, $\mu = h/R$, is simulated where h is the crack depth in the radial direction and R is the shaft radius. A_{crack} is the area of the crack segment as shown in Figure 3-22(a). The unbalance force is considered a rotational force and its angular position β w.r.t. the crack direction on the shaft cross-section plane is shown in Figure 3-22(b).

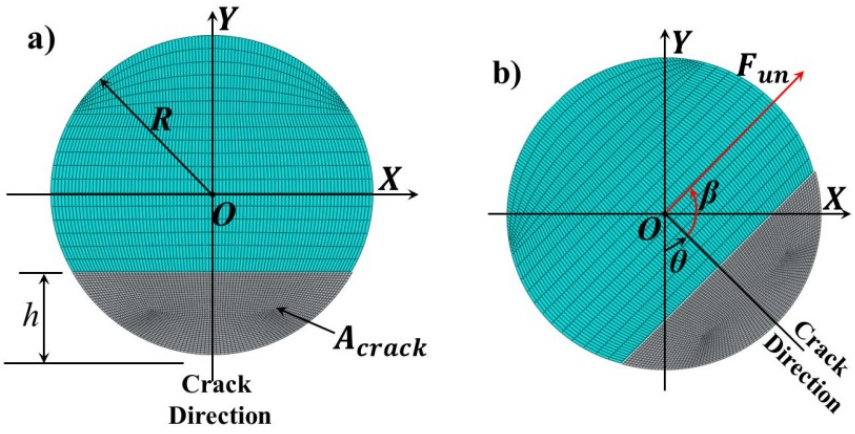

Figure 3-22: Schematic diagrams of (a) crack cross-section and (b) relative orientation between unbalance force and the crack on the shaft cross-section plane

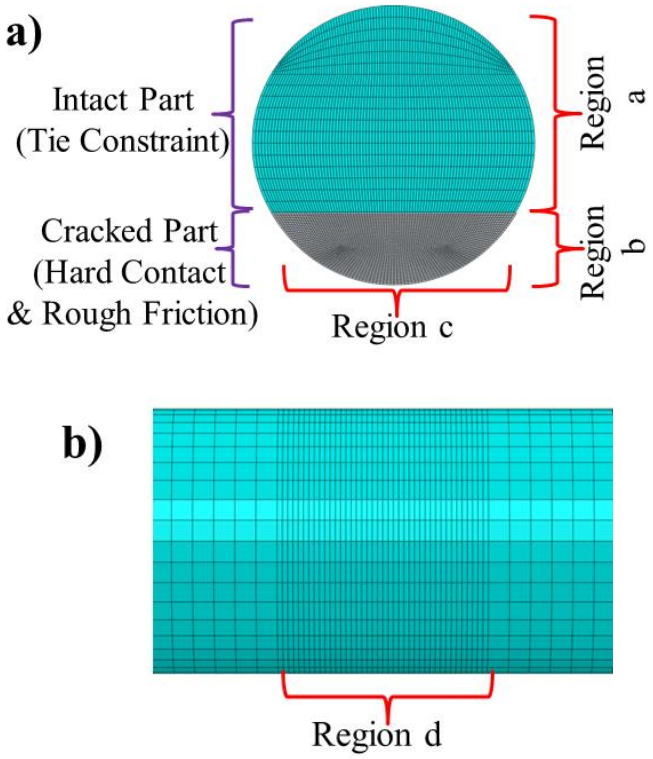

Figure 3-23: Simulation details for the crack cross-section and mesh around the crack in (a) transversal and (b) longitudinal directions

The two shafts are joined together to generate a crack section using the 'Tie Constraints' function that establishes the intact part of the cracked section. The contact interaction is defined in the finite element numerical model as normal, and the tangential properties of the created cracked surfaces are established. To prevent penetration between the crack surfaces when the crack closes, the normal property

'hard contact' is selected. To avoid sliding between the crack surfaces, the tangential property 'rough friction' is applied to generate an infinite friction coefficient. The simulation details for the crack cross-section are displayed in Figure 3-23(a) where the upper part is the intact section while the lower area corresponds to the cracked section of the shaft.

The shaft is meshed by using an element named C3D8R. The mesh size is obtained after a convergence test of the results through mesh sensitivity analyses. As shown in Figure 3-23, the mesh density is much higher around the crack in the transversal and longitudinal directions. The results of the convergence test for the balance case, with a crack at the midpoint of the shaft and a shaft rotation angle 90°, are presented in Table 3-4. It is observed that the opening percentage converges after the numbers of mesh in four regions, denoted as a, b, c and d in Figure 3-23, reach 18, 36, 80 and 40. The percentage of opening is described later in detail.

Table 3-3: Mesh sensitivity analyses of 3D FEM

Test Cases	Number of Elements	Percentage of opening
1	a:8; b:26; c:30; d:20	83.36%
2	a:10; b:28; c:40; d:24	79.36%
3	a:12; b:30; c:50; d:28	73.36%
4	a:14; b:32; c:60; d:32	69.75%
5	a:16; b:34; c:70; d:36	67.27%
6 (Selected)	a:18; b:36; c:80; d:40	66.26%
7	a:20; b:38; c:90; d:44	66.26%

A full 3D FE model for a two-disk rotor is simulated with fixed end supports since the rotor symmetry no longer exists in the unbalance shaft, as shown in Figure 3-24. The modelling parameters of the rotor model are stated in Table 3-5. The shaft self-weight, $m_s g$, is applied as a gravitational force and two disk weights, $2m_d g$, are applied as the concentrated force at 181 mm from the two shaft ends. m_s is the mass of the shaft, and m_d is the mass of a disk (m_d = 0.5 kg). The unbalance force, F_{un}, is also applied as a concentrated force in *X*-axis $[\frac{m_s g+2m_d g}{\eta}] \times sin(\theta+\beta)$ and in *Y*-axis $[\frac{m_s g+2m_d g}{\eta}] \times cos(\theta+\beta)$ at the right disk.

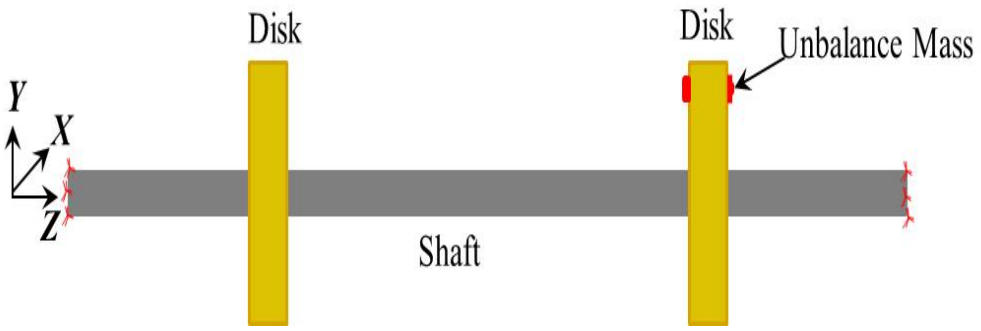

Figure 3-24: Schematic diagram of the unbalance two-disk rotor system model

Table 3-4: Parameters of the three-dimensional finite element model

Description	Value
Shaft Length, L	724 mm
Shaft Radius, R	6.35 mm
Density, ρ	7800 kg/m^3
Young's Modulus, E	210GPa
Poisson Ratio, v	0.3
Disk Mass, m_d	0.50 kg
Disk-1 Location, l_1	181 mm
Disk-2 Location, l_2	543 mm
Crack Location, l_0	Variable
Crack Depth Ratio, μ	0.5

3.6.2 Comparison between unbalance model and 3D FEM

In the numerical simulation, the same geometrical and material properties and the load conditions of the cracked shaft are used. The analysis is performed as a succession of static problems with different angular positions of the shaft, θ, w.r.t. the fixed reference axis. The status of the crack is obtained directly from Abaqus field outputs by selecting Field Output Request/Contact/CSTATUS (Contact status).

The percentage of the opening of a crack, Λ, is calculated using Equation (3-16). Here, A_{crack} is the area of the crack segment, as shown in Figure 3-22(a), and A_{closed} is the closed portion of the crack area during the rotation, as shown in Figure 3-25. A_{crack} is calculated by Equation (3-19) where μ is the nondimensional crack depth

and R is the shaft radius. A_{closed} is obtained directly from Abaqus history outputs by selecting History Output Request/Contact/CAREA (Total area in contact). In Abaqus, a crack area is treated as being closed when the area is under compression and A_{closed} is calculated accordingly. For a fully open and fully closed crack, the percentage of a crack open area, Λ, is equal to 100% and 0% respectively.

$$\Lambda\,(\%) = \frac{A_{crack} - A_{closed}}{A_{crack}} \times 100 \tag{3-18}$$

$$A_{crack} = R^2 \cos^{-1}(1-\mu) - R^2(1-\mu)\sqrt{\mu(2-\mu)} \tag{3-19}$$

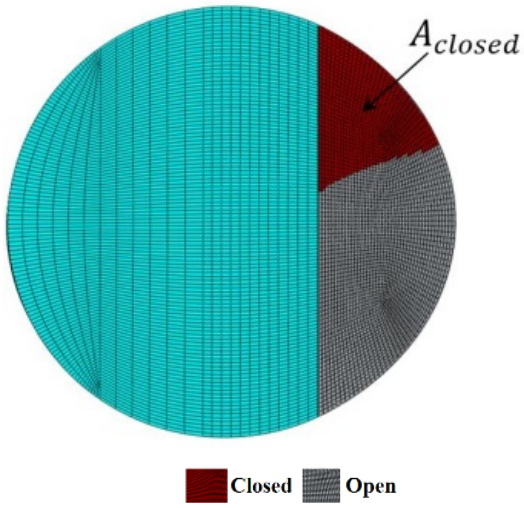

Figure 3-25: Representation of closed portion of the crack segment

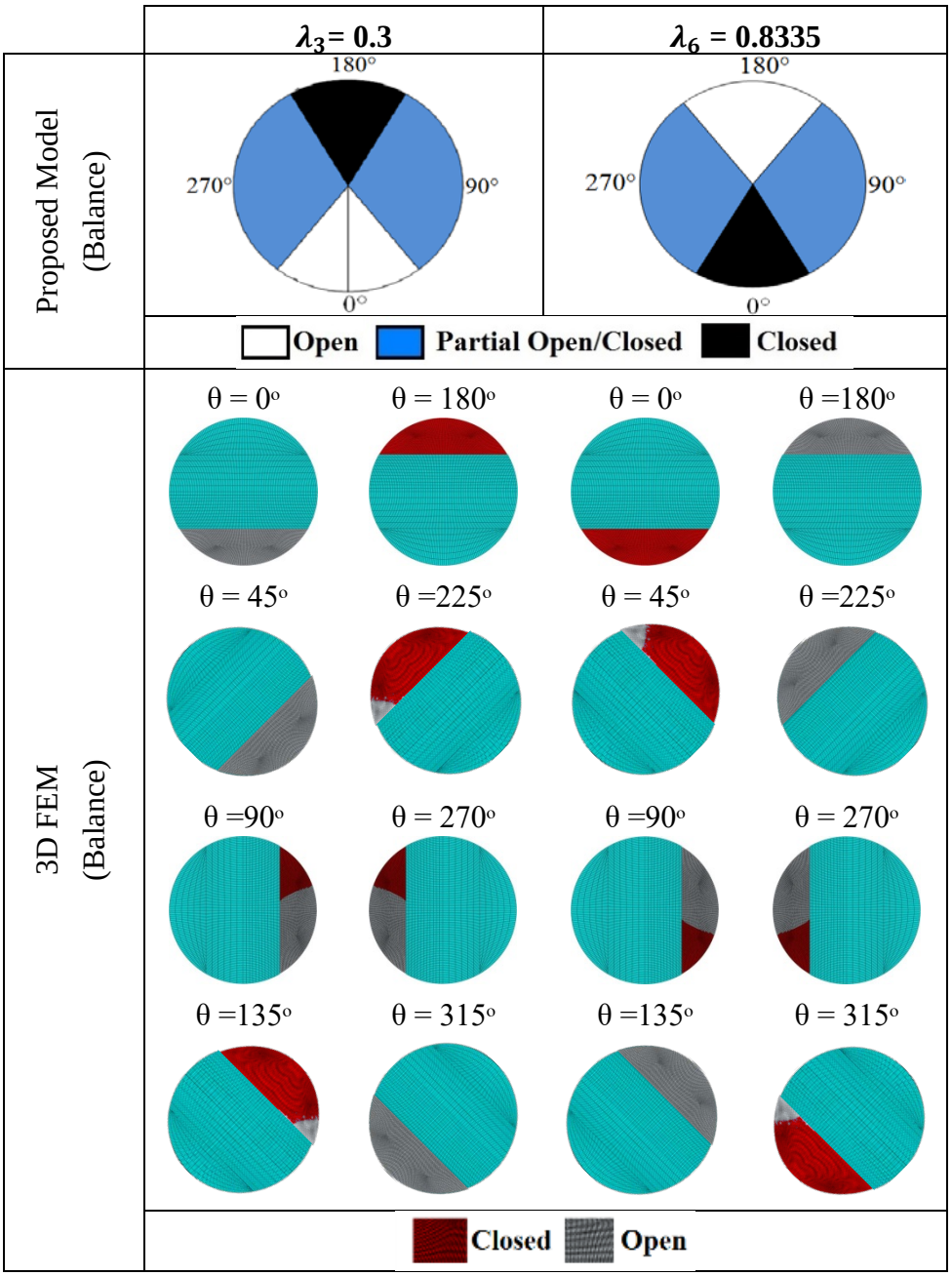

Figure 3-26: Comparison of the status of the crack between the proposed balance model and 3D FEM at crack locations $\boldsymbol{\lambda_3}$ = 0.3 and $\boldsymbol{\lambda_6}$= 0.8335

First, crack breathing behaviours at two pairs of specific crack locations are evaluated and compared. The statuses of the crack of a balance and unbalance shaft for a full shaft rotation angle at λ_3 = 0.3 and λ_6= 0.8335 are depicted in Figure 3-26 and Figure 3-27. As already stated, the unbalance model shows that at these two locations the crack will behave like in the balance shaft with symmetrical and sequential changes during a full shaft rotation, beginning with fully open at λ_4= 0.3

and fully closed at λ_6= 0.8335. These features are demonstrated completely in Figure 3-26 and Figure 3-27. Further, that the crack at λ_2 = 0.1946 will never open and will never close at λ_5 = 0.8053 are also well reproduced in the 3D FEM, as shown in Figure 3-28.

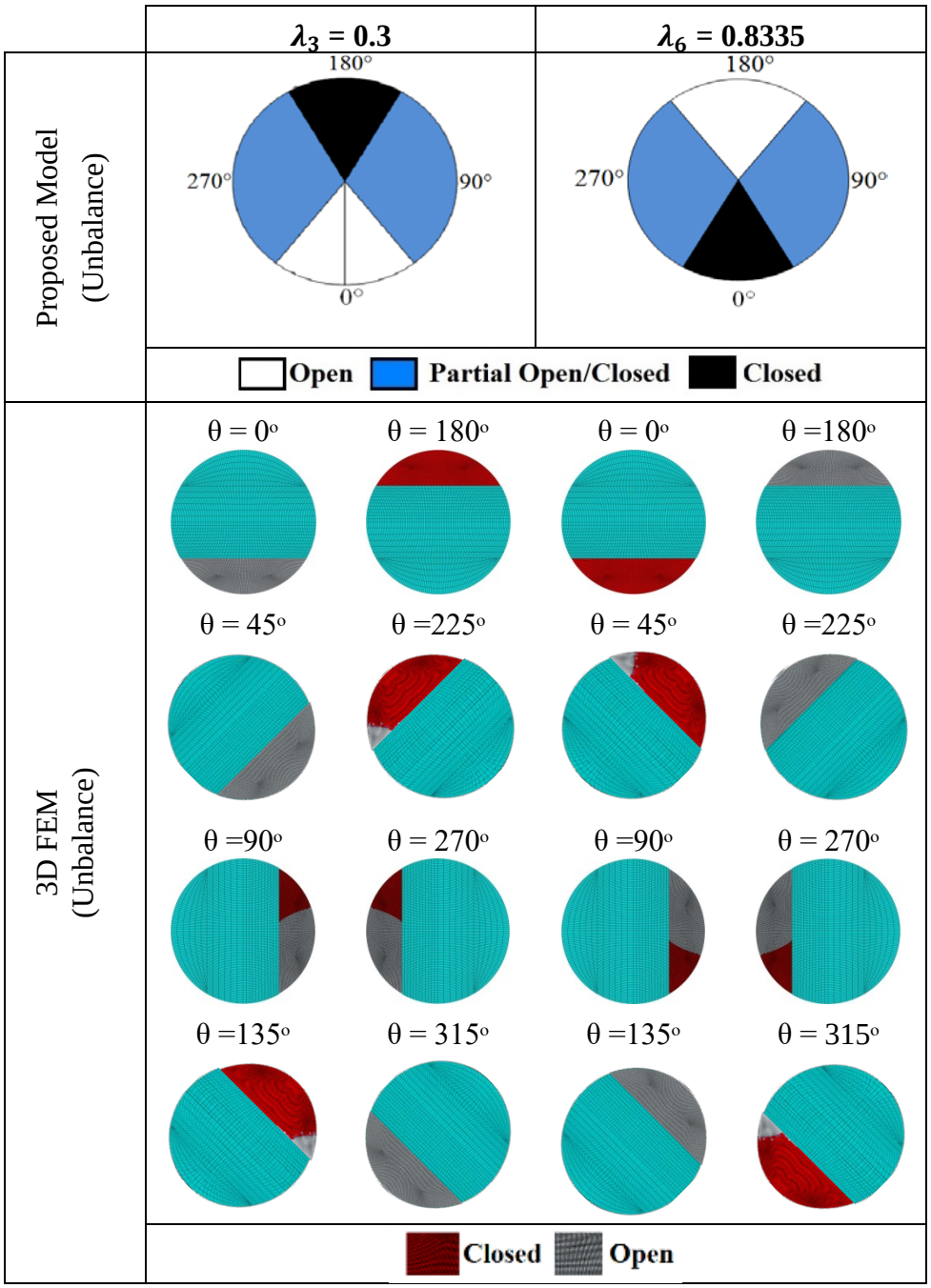

Figure 3-27: Comparison of the status of the crack between the proposed unbalance model (η = 10 & β = 0°) and 3D FEM at crack locations λ_3 = 0.3 and λ_6= 0.8335

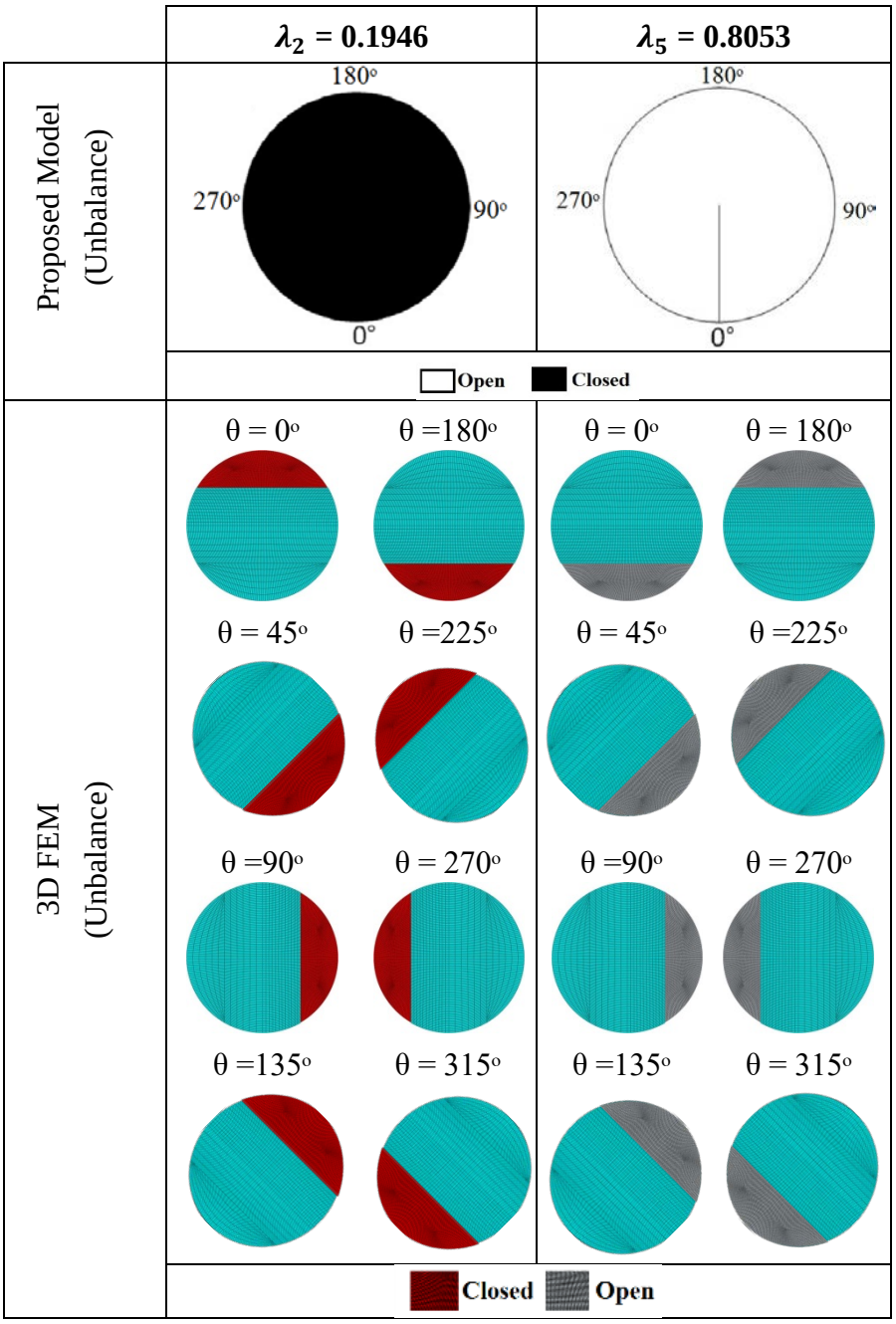

Figure 3-28: Comparison of the status of the crack between the proposed unbalance model (η = 10 & β = 0°) and 3D FEM at crack locations $\boldsymbol{\lambda_2}$ = 0.1946 and $\boldsymbol{\lambda_5}$ = 0.8053

Second, a quantitative comparison through a percentage of the opening at crack location λ_4= 0.5 is displayed in Figure 3-29 for the balance and unbalance shafts (η = *10 &* β = 0°). In general, it is found that the proposed unbalance model captures the main features of crack breathing and is in good agreement with the 3D FEM. The possible difference may be attributed to the curved boundary between the opening area and the closed area of the crack in the 3D FEM (see Figure 3-25) and the

straight boundary line in the balance model (see Figure 3-10), which is adopted from Al-Shudeifat and Butcher (2011). A curved boundary line was also observed in previous 3D FEM for the balance shaft (Bachschmid et al., 2010) and unbalance shaft with simple support ends (Rubio & Fernandez-Saez, 2012; Rubio et al., 2014).

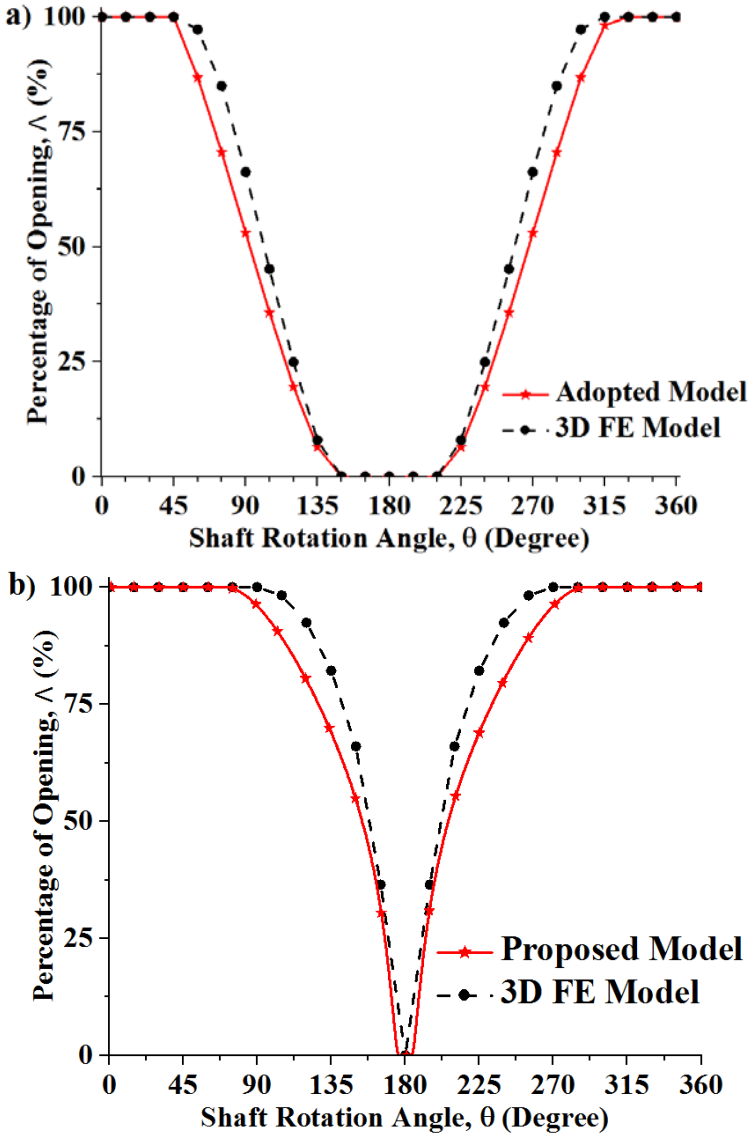

Figure 3-29: Comparison of the percentage of the opening of the crack at the crack location $\boldsymbol{\lambda_4}$= 0.5 for (a) adopted balance and (b) proposed unbalance ($\eta = 10$ & β = 0°) model with 3D FE model

The adopted model (Al-Shudeifat and Butcher, 2011) was developed based on simplified assumptions, namely, that the cracked shafts will only experience symmetrical bending, and so, the neutral axis will be always horizontal. The

assumptions are shown to be invalid on comparison with the results from the 3D FE model (see Figure 3-30).

The neutral axis inclination of the 3D FE model is inferred from 3D FE model results by probing the nodal stresses at various points of the cross-section at the crack location. If any pair of nodes that lie on the same edge of an element experience oppositely signed normal stresses, there would be a point on the line connecting the two nodes where the normal stress is zero as shown in Figure 3-31. For a given pair of probed nodes, the X and Y coordinates of the point of zero stress can be calculated by assuming a linear stress field. The X and Y coordinates of this point are given in Equations (3-20) and (3-21) in terms of the coordinates and stresses at the probed points. By locating several points of zero stress in the cross-section at the crack location, the neutral axis inclination and offset could be determined.

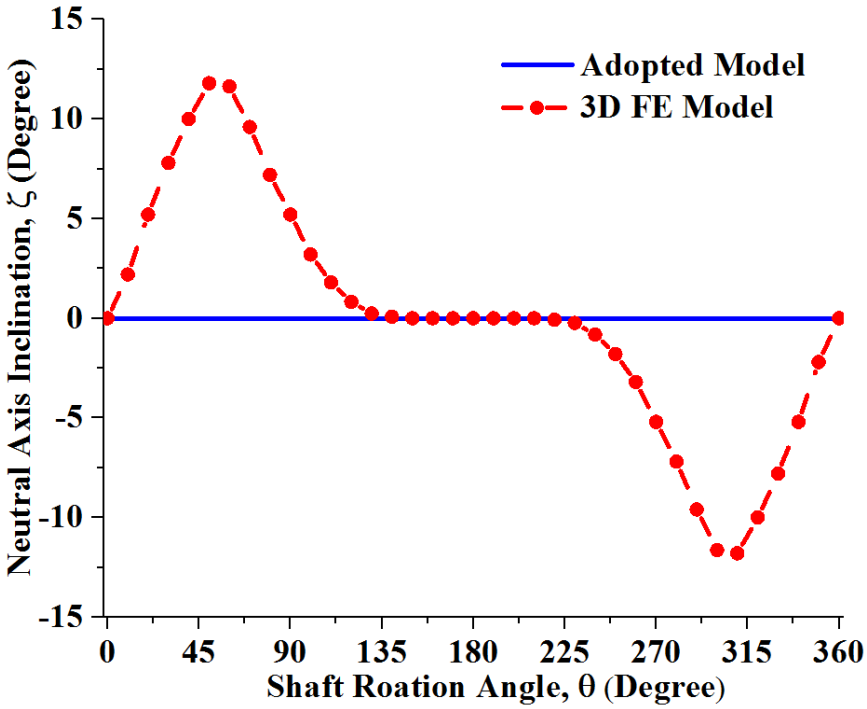

Figure 3-30: Comparison of neutral axis inclination for μ = 0.5

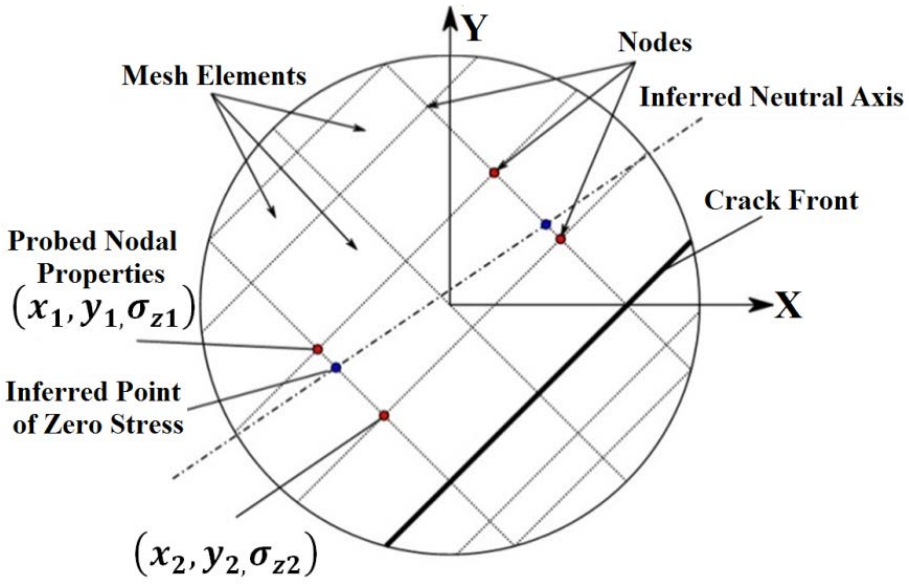

Figure 3-31: Schematic diagrams of the neutral axis inclination of the FEA model

$$x_0 = \frac{\sigma_{z1} x_2 + \sigma_{z2} x_1}{\sigma_{z1} + \sigma_{z2}} \quad (3\text{-}20)$$

$$y_0 = \frac{\sigma_{z1} y_2 + \sigma_{z2} y_1}{\sigma_{z1} + \sigma_{z2}} \quad (3\text{-}21)$$

It can be inferred that the calculations for the unbalance models using the effectual bending angle, φ, Equation (3-7) do not introduce any error since the error between the present unbalance model and 3D FEM in Figure 3-29. However, the adopted method (Al-Shudeifat and Butcher, 2011) needs to be improved.

3.7 Summary

In this chapter, a new unbalance model is developed to study crack breathing behaviour and to calculate the area moment of inertia of the crack cross-section closed area in terms of crack location along shaft length, shaft rotational angle, unbalance force orientation and the ratio of gravitational force and unbalance force.

Throughout the chapter, the focus is on the influence of the unbalance force and crack location on the breathing behaviour and area moment of inertia. The presented model identified unique crack breathing behaviours under the influence of unbalance force and rotor physical and dimensional properties, showing the strong dependence of the breathing mechanism on the crack location.

The newly developed unbalance model was validated through 3D FEM results. It is found that the proposed unbalance model captures the main features of crack breathing and is in good agreement with the 3D FEM. However, the adopted method to evaluate the crack breathing behaviour and the second area moment of inertia identified needs to be improved.

The developed model can be further used by other researchers and engineers to obtain local stiffness matrix of a cracked shaft element to predict the vibration response of a cracked rotor and to develop the online crack detection technique, in particular, near the shaft critical speeds or where the rotor-weight-dominant assumption on the crack breathing no longer holds.

Chapter 4 : Developing a New, Improved Crack Breathing Model

4.1 Introduction

In this chapter, a more accurate approach is developed to study the crack breathing mechanism under different weight–unbalance force ratios at different crack locations. The approach is developed considering the inclination of the neutral axis. Because the cross-section of the crack element is irregular when the crack is fully open, the shaft is subject to asymmetric bending near the crack. Two assumptions used in the adopted balance model (Al-Shudeifat and Butcher, 2011) are discarded in the process.

The newly developed model is used to evaluate nonlinear crack breathing behaviour under different weight–unbalance force ratios at different crack locations by examining the percentage of opening of a crack. Finite element simulations of a cracked shaft subjected to identical loading conditions are used to validate the newly developed model results. The proposed method results are also compared with the results in Section 3.4 of Chapter 3. Excellent agreement is found between the proposed method and FEM analysis method. It has improved accuracy compared with the results in Section 3.4 of Chapter 3.

4.2 Determination of Key Instants of Crack Breathing

4.2.1 A crack begins to close

The crack will start to gradually close as the shaft rotates and the crack area moves into the compressive stress region. It will occur when the crack front moves past the neutral axis of bending. Because the section is irregular when the crack is fully open, the shaft is subject to asymmetric bending near the crack. The neutral axis and the bending moment vector will intersect at the centroid of the section. If the bending moment is not parallel with either of the principal axes, the neutral axis will not be collinear with it (because $I_u \neq I_v$) as shown in Figure 4-1, where I_u and I_v are the first and second principal area moment of inertia of the shaft section respectively.

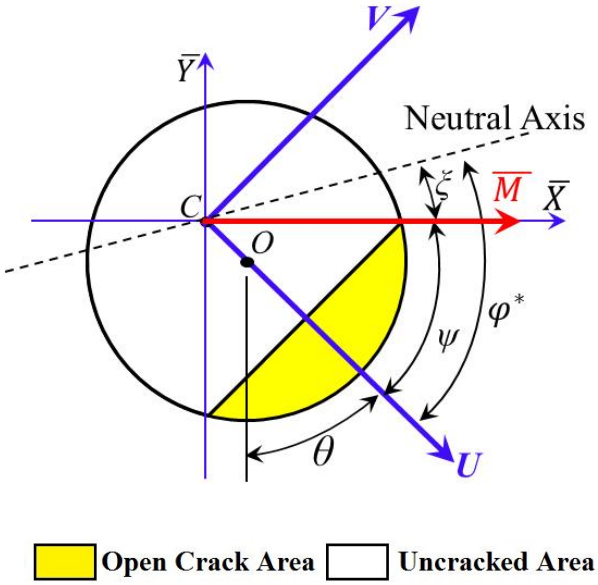

Figure 4-1: Orientation of the neutral axis about $\bar{\boldsymbol{X}}$-axis

The neutral axis will be inclined by an angle of ξ measured from the positive $\bar{X}$ axis. The engineer's theory of bending provides the following relationship between the angles of the bending moment (ψ) and the neutral axis (φ^*) about the first principal axis (U axis) as described in Equation (4-1).

$$\varphi^* = \tan^{-1}\left(\frac{I_U}{I_V}\tan(-\psi)\right) \tag{4-1}$$

From Figure 4-1, we observe that $\psi = \frac{\pi}{2} - \theta$ and $\xi = \varphi^* - \psi$, and hence, we can express ξ as a function of θ as described in Equation (4-2):

$$\xi = \tan^{-1}\left(\frac{I_U}{I_V}\tan\left(\theta - \frac{\pi}{2}\right)\right) + \theta - \frac{\pi}{2} \tag{4-2}$$

At this point, it is helpful to identify the leading apex of the cracked region as point *D* (see Figure 4-2). If we define a vector between points *C* and *D*, we will obtain a line that intersects the neutral axis at *C* and forms an angle of ζ with the positive $\bar{\boldsymbol{X}}$ axis. If we know the coordinates of the leading apex (point D) of the crack region, we can determine the point at which the cracked region crosses the neutral plane as shown in Figure 4-2.

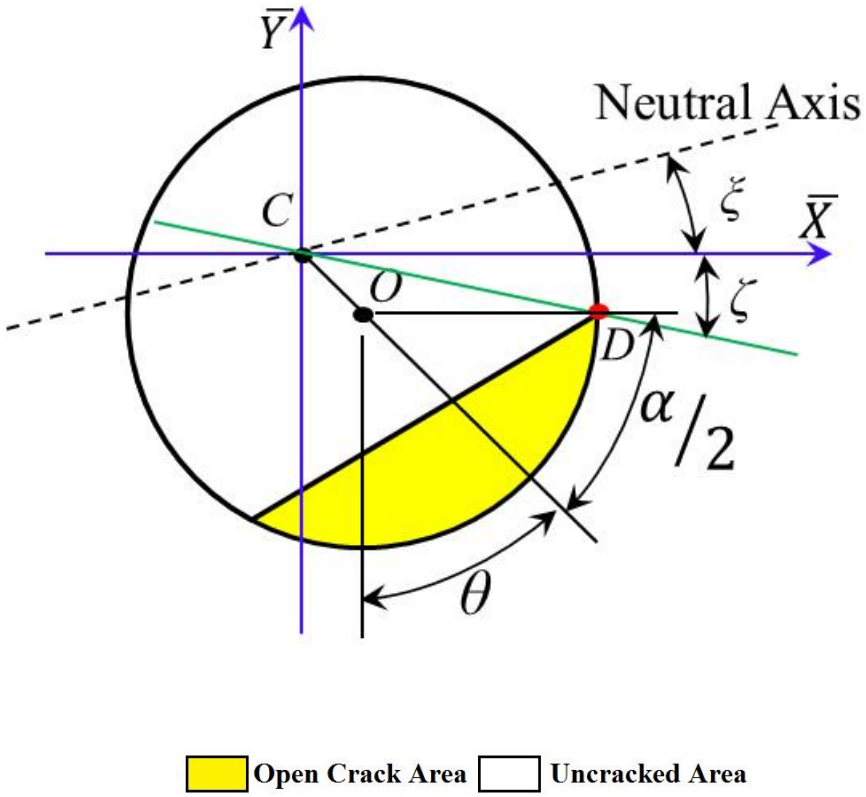

Figure 4-2: Coordinates of the leading apex (point D) of the crack region

Ultimately, the crack will start to close when point *D* crosses the neutral axis. It will occur when the following condition is met:

$$\zeta(\theta) = \xi(\theta)$$

We can also express ζ as a function of θ since the coordinates of points *C* and *D* can be determined as described in Equation (4-3).

$$\zeta(\theta) = \tan^{-1}\left(\frac{Y_D - Y_C}{X_D - X_C}\right) = \tan^{-1}\left(\frac{-R\cos\left(\theta + \frac{\alpha}{2}\right) - e\cos\theta}{R\sin\left(\theta + \frac{\alpha}{2}\right) + e\sin\theta}\right) \qquad (4\text{-}3)$$

The crack starts to close at a certain shaft rotation angle when $\theta = (\theta_1)_{new}$ where the upper end of the crack edge reaches the compression stress field. Evaluating this angle is a matter of equating (4-1), (4-2) and (4-3) and solving for $(\theta_1)_{new}$:

$$\tan^{-1}\left(\frac{I_U}{I_V}\tan\left((\theta_1)_{new}-\frac{\pi}{2}\right)\right)+(\theta_1)_{new}-\frac{\pi}{2}$$
$$=\tan^{-1}\left(\frac{-R\cos\left((\theta_1)_{new}+\frac{\alpha}{2}\right)-e\cos(\theta_1)_{new}}{R\sin\left((\theta_1)_{new}+\frac{\alpha}{2}\right)+e\sin(\theta_1)_{new}}\right)$$

It can be used to obtain an implicit expression for $(\theta_1)_{new}$ as shown in Equation (4-4).

$$(\theta_1)_{new}=\tan^{-1}\left(\frac{-\cos\left((\theta_1)_{new}+\frac{\alpha}{2}\right)-\frac{e}{R}\cos(\theta_1)_{new}}{\sin\left((\theta_1)_{new}+\frac{\alpha}{2}\right)+\frac{e}{R}\sin(\theta_1)_{new}}\right) \quad (4\text{-}4)$$
$$-\tan^{-1}\left(\frac{I_U}{I_V}\tan\left((\theta_1)_{new}-\frac{\pi}{2}\right)\right)+\frac{\pi}{2}$$

Note that the terms, $\frac{e}{R}$, $\frac{\alpha}{2}$ and $\frac{I_U}{I_V}$ are functions of the relative crack depth, μ, alone as described in Equations (4-5) to (4-8). Equation (4-4) can be solved numerically using a software package, such as MATLAB. Hence, $(\theta_1)_{new}=f(\mu)$

$$\frac{\alpha}{2}=\cos^{-1}(1-\mu) \quad (4\text{-}5)$$

$$e=\frac{2R\times\sqrt[3]{\mu(2-\mu)}}{3\left(\pi-\cos^{-1}(1-\mu)+(1-\mu)\sqrt{\mu(2-\mu)}\right)} \quad (4\text{-}6)$$

$$I_U=\frac{\pi R^4}{4}-\frac{R^4}{12}\left((1-\mu)(2\mu^2-4\mu-3)\sqrt{\mu(2-\mu)}\right. \quad (4\text{-}7)$$
$$\left.+3\sin^{-1}\left(\sqrt{\mu(2-\mu)}\right)\right)$$

$$I_V=\frac{\pi R^4}{8}+\frac{R^4}{4}\left((1-\mu)(2\mu^2-4\mu+1)\sqrt{\mu(2-\mu)}+\sin^{-1}(1-\mu)\right) \quad (4\text{-}8)$$
$$-R^2\left[\pi-cos^{-1}(1-\mu)-(1-\mu)\sqrt{\mu(2-\mu)}\right]\times e^2$$

It is currently unknown if a closed-form expression of $f(\mu)$ exists. However, it has been calculated numerically by selecting an arbitrary initial estimate for $(\theta_1)_{new}$ and iteratively evaluating Equation (4-4). This has been performed for crack depths from $\mu=0$ through to $\mu=1$. A polynomial approximation of the shaft rotation angle at

which the crack starts to close changes with the crack depth as is shown with the exact function in Figure 4-3.

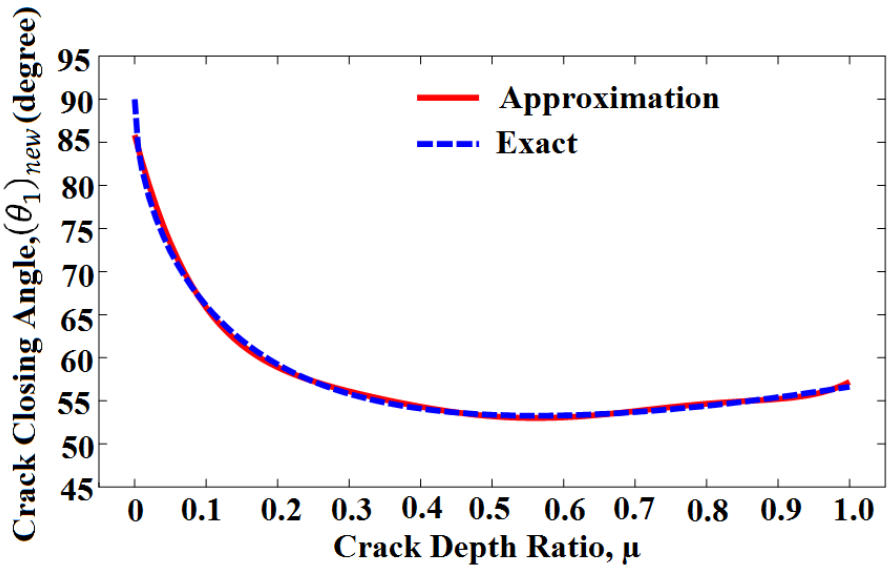

Figure 4-3: Shaft rotation angle at which the crack starts to close changes with the crack depth

A polynomial approximation of $(\theta_1)_{new}(\mu)$ is obtained as described in Equation (4-9) using Microsoft Excel's trend line function and is shown in red in Figure 4-3.

$$(\theta_1)_{new} \approx 24\mu^6 - 81.03\mu^5 + 108.06\mu^4 - 72.85\mu^3 + 26.87\mu^2 - 5.56\mu + 1.50 \quad (4\text{-}9)$$

The polynomial approximation of $(\theta_1)_{new}(\mu)$ can be used to determine if the crack is in a fully open state in applications where the breathing state of the crack needs to be evaluated continuously as the shaft rotates. The precise value of $(\theta_1)_{new}$ carries little physical meaning beyond determining the method required for calculating the breathing state and the shaft stiffness at the crack location.

Because the parameters that are of interest are continuous functions, if they are evaluated at a shaft rotation angle close to $(\theta_1)_{new}$ using the wrong method, that is, the crack is assumed to be fully open when it is fully closed or vice versa, the error should be small. If the estimate for $(\theta_1)_{new}$ is within a few degrees of the true value, there will be a negligible loss of accuracy, and it will only be at rotation angles close to $(\theta_1)_{new}$.

4.2.2 A crack becomes fully closed

The crack becomes fully closed at a certain shaft rotation angle when $\theta = \theta_2$ where the crack fully reaches the compression stress field as described in Figure 4-4. When the crack is fully closed, the shaft has the stiffness of an uncracked shaft. The precise value of θ_2 is a function of the crack depth as described in Equation (4-10).

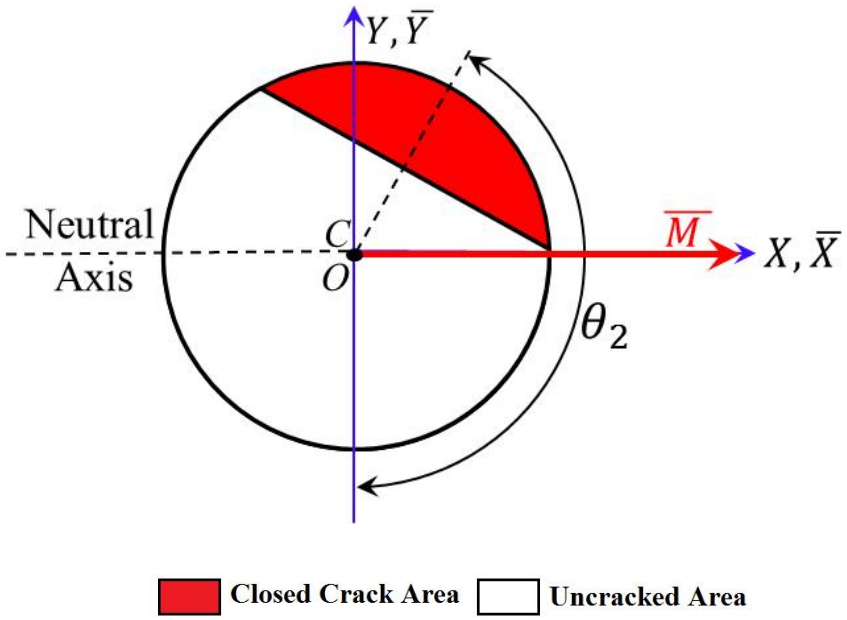

Figure 4-4: Crack becomes fully closed at $\theta = \theta_2$

$$\theta_2 = \frac{\pi}{2} + \cos^{-1}(1 - \mu) \tag{4-10}$$

4.2.3 Complete breathing mechanism of a crack

To identify the statuses of the crack for different force ratios at different crack locations during shaft rotation using the values of effectual bending angle, φ, Equations (4-9) and (4-10) are modified as given in Equations (4-11) and (4-12) respectively. The detailed statuses of the breathing of the crack for a complete effectual bending angle rotation (360^0) are presented in Table 4-1.

$$(\varphi_1)_{new} \approx 24\mu^6 - 81.03\mu^5 + 108.06\mu^4 - 72.85\mu^3 + 26.87\mu^2 - 5.56\mu + 1.50 \tag{4-11}$$

$$\varphi_2 = \frac{\pi}{2} + \cos^{-1}(1 - \mu) \tag{4-12}$$

Table 4-1: Improved status of the crack for a complete effectual bending angle rotation (360^0)

Effectual bending angle $0° \leq \varphi < 360^0$	**Status of the crack**
$0° \leq \varphi < (\varphi_1)_{new}$	Fully open
$(\varphi_1)_{new} \leq \varphi \leq \varphi_2$	Partially open/closed
$\varphi_2 < \varphi < 2\pi - \varphi_2$	Fully closed
$2\pi - \varphi_2 \leq \varphi \leq 2\pi - (\varphi_1)_{new}$	Partially open/closed
$2\pi - (\varphi_1)_{new} < \varphi \leq 360°$	Fully open

4.3 Comparison between the Improved Unbalance Model, Unbalance Model and 3D FE Model

The following configurations of cracks and unbalance forces are considered to compare the crack breathing behaviour between the improved unbalance model, unbalance model (Section 3.4 of Chapter 3) and 3D FEM results.

a) the unbalance force ratio, η, the ratio of the gravitational force (shaft self-weight and two disk weights) and the unbalance force, to evaluate the influence of the unbalance force magnitude
b) the crack location factor, λ, the ratio of the crack position, $l_{0,}$ and the total shaft length, L, to evaluate the influence of the crack position
c) angular positions of the crack or shaft rotational angles, θ, varying from 0° to 360° to evaluate the influence of the crack angular position
d) angular position of unbalance force, β, varying from 0° to 360° to evaluate the influence of this angular position w.r.t. the crack cross-section plane
e) the crack depth ratio, μ, the ratio of the crack depth and shaft radius, to evaluate the influence of the crack depth.

The crack breathing behaviour analysis in Section 3.4 of Chapter 3 is revised using the newly developed effectual bending angle $(\varphi_1)_{new}$. The crack breathing behaviours are evaluated quantitatively using percentages of the opening of a crack,

which is explained in detail in Section 3.4 of Chapter 3. Improved new unbalance model percentage of opening of a crack Λ is determined using Equation (3-14). A_c is calculated by Equation (3-15). To calculate the variation of $A_2(t)$ with shaft rotational angle, a procedure proposed by Al-Shudeifat and Butcher (2011) for balance shaft analysis is used. It is obvious, as shown in Figure 3-10, that $A_2(t)$ in the unbalance shaft is equal to that in a balance shaft when the bending angle in the former is equal to the rotational angle in the latter. For the calculation of $A_2(t)$ in the unbalance shaft, first, $A_2(t)$ for the balance shaft are calculated using formulas from Al-Shudeifat and Butcher (2011). This $A_2(t)$ becomes that for the unbalance shaft at a bending angle equal to the shaft rotational angle in the balance shaft. Then, using the values of effectual bending angle, φ, relative to the regions formed by $(\varphi_1)_{new}$ and φ_2, the percentage of opening of a crack for different force ratios at different crack locations during shaft rotation are obtained.

The new improved proposed method results are compared with the unbalance model results (results in Section 3.4 of Chapter 3) and 3D FE model results. A complete 3D FE model of a cracked shaft subjected to identical loading conditions is used to compare the newly developed model results. The detailed modelling of the 3D FE model of a cracked rotor is presented in Section 3.6 of Chapter 3.

Percentages of the opening of a crack are directly related to the second area moment at the crack location. Hence, it is studied by evaluating it for every possible crack location and shaft rotation angle. Excellent agreement is found between the proposed newly improved unbalance model and 3D FEM results. The plots in Figure 4-5 to Figure 4-11 illustrate the improved accuracy that the newly improved unbalance model offers over the unbalance model results (results in Section 3.4 of Chapter 3).

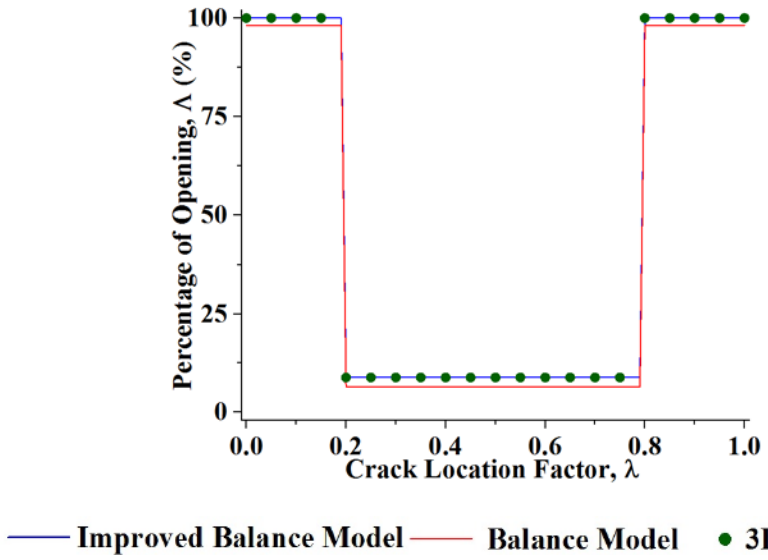

Figure 4-5: Comparison of the percentage of the opening of the crack along the shaft length for balance shaft where θ = 135° and μ = 0.5

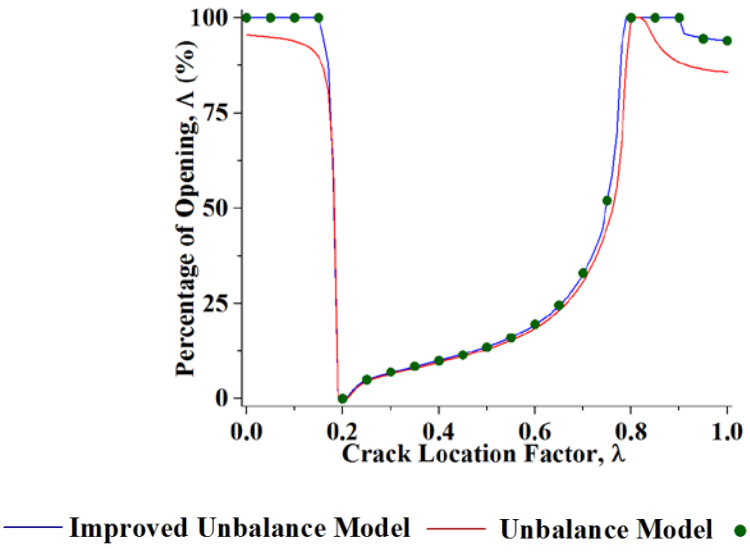

Figure 4-6: Comparison of the percentage of the opening of the crack along the shaft length for unbalance shaft (η = 5 and β = 0°) where θ = 135°

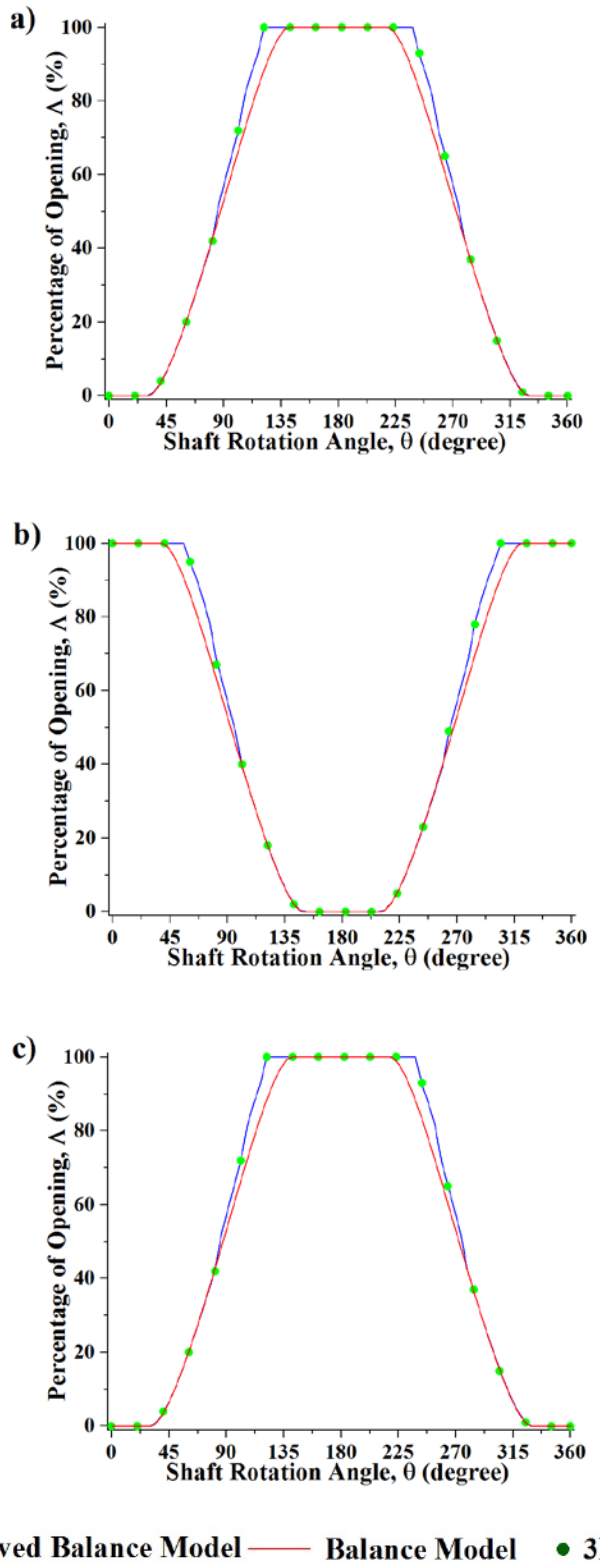

Figure 4-7: Comparison of the percentage of the opening of the crack for balance shaft at crack locations (a) $\lambda = 0.15$, (b) $\lambda = 0.5$ and (c) $\lambda = 0.85$ where $\mu = 0.5$

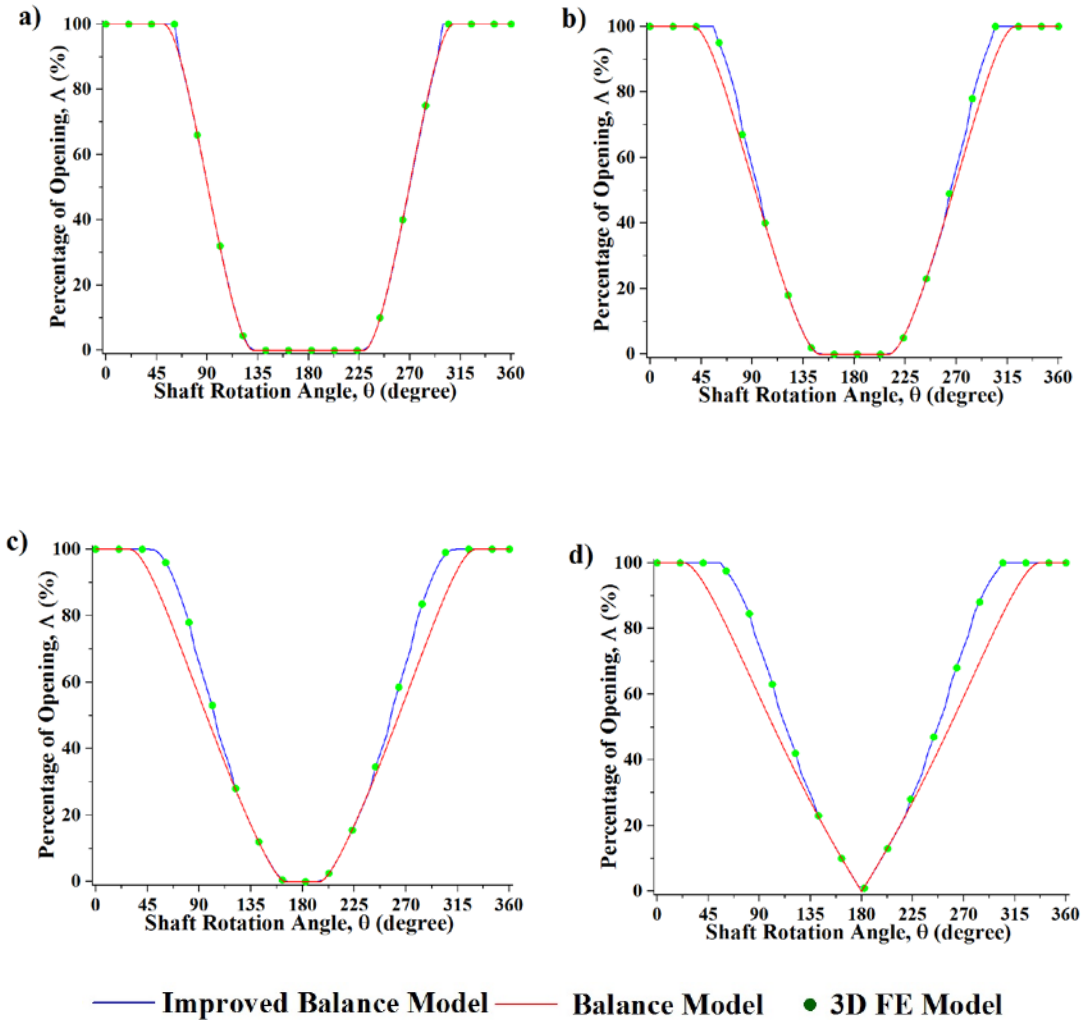

Figure 4-8: Comparison of the percentage of opening of the crack for the balance shaft at crack location λ = 0.5 for different crack depth ratios (a) μ = 0.25, (b) μ = 0.5, (c) μ = 0.75 and (d) μ = 1

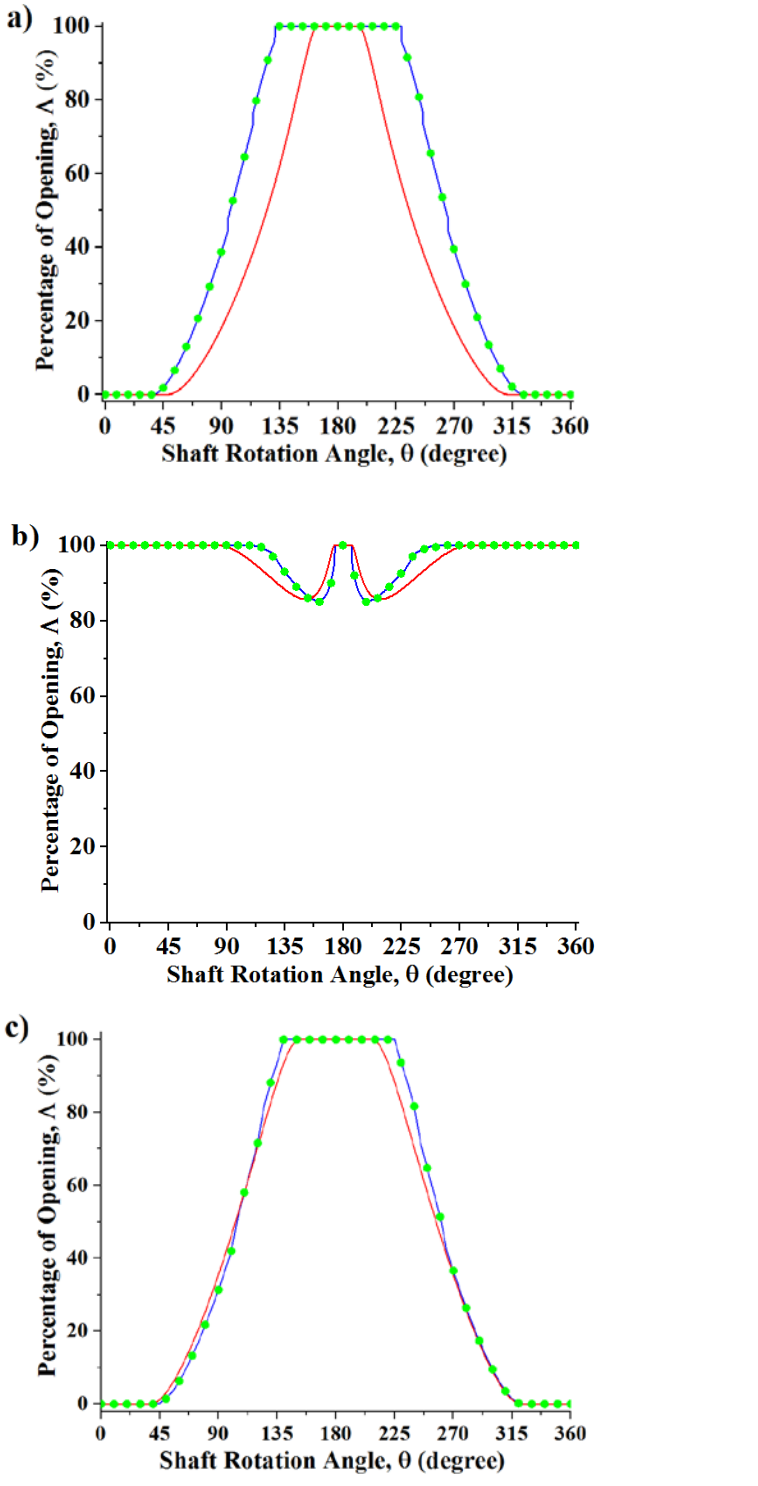

Figure 4-9: Comparison of the percentage of the opening of the crack for the unbalance shaft ($\eta = 5$ and $\beta = 0°$) at crack locations (a) $\lambda = 0.15$, (b) $\lambda = 0.5$ and (c) $\lambda = 0.85$

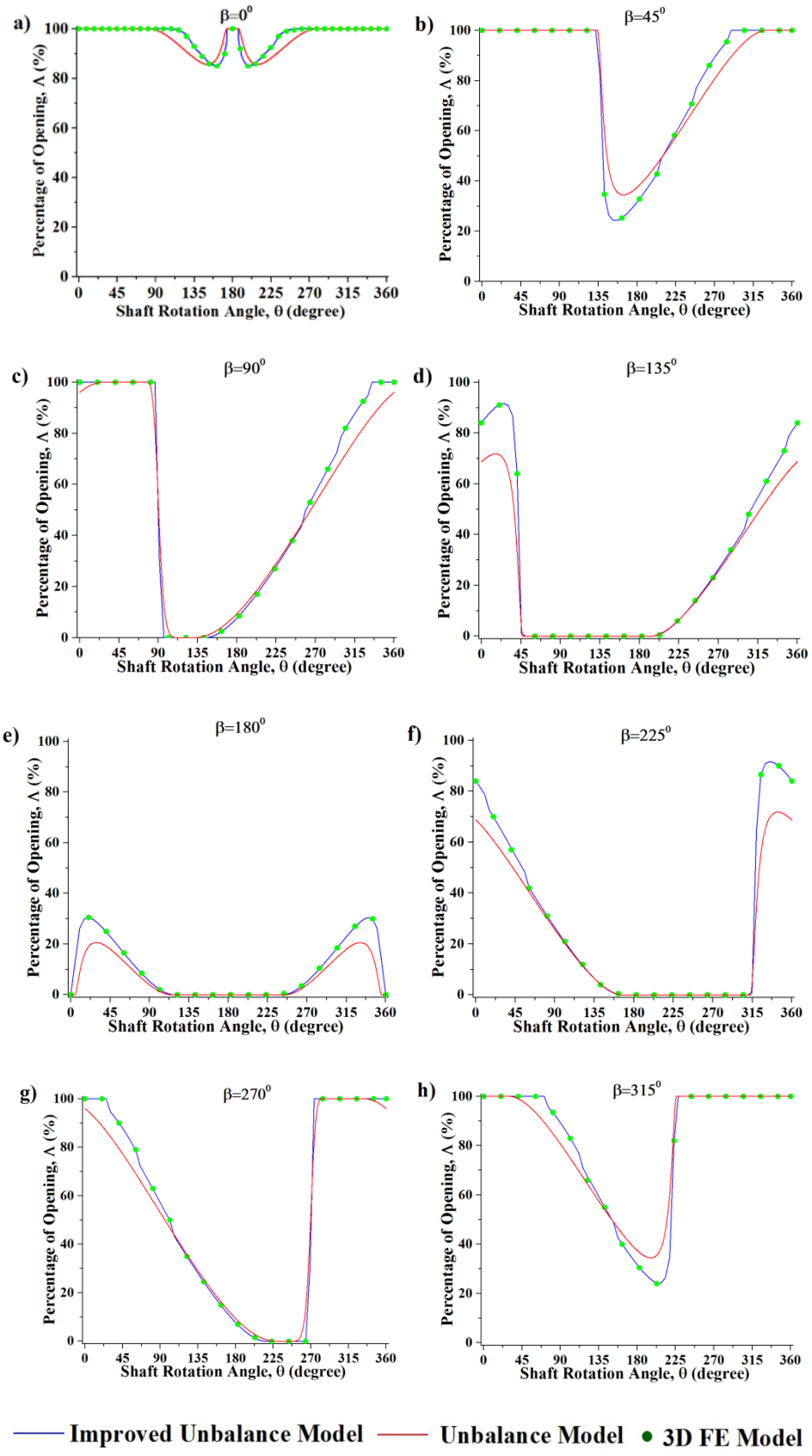

Figure 4-10: Comparison of the percentage of opening of the crack for the unbalance shaft ($\eta = 5$) at crack location $\lambda = 0.5$ for different angular positions of unbalance force β

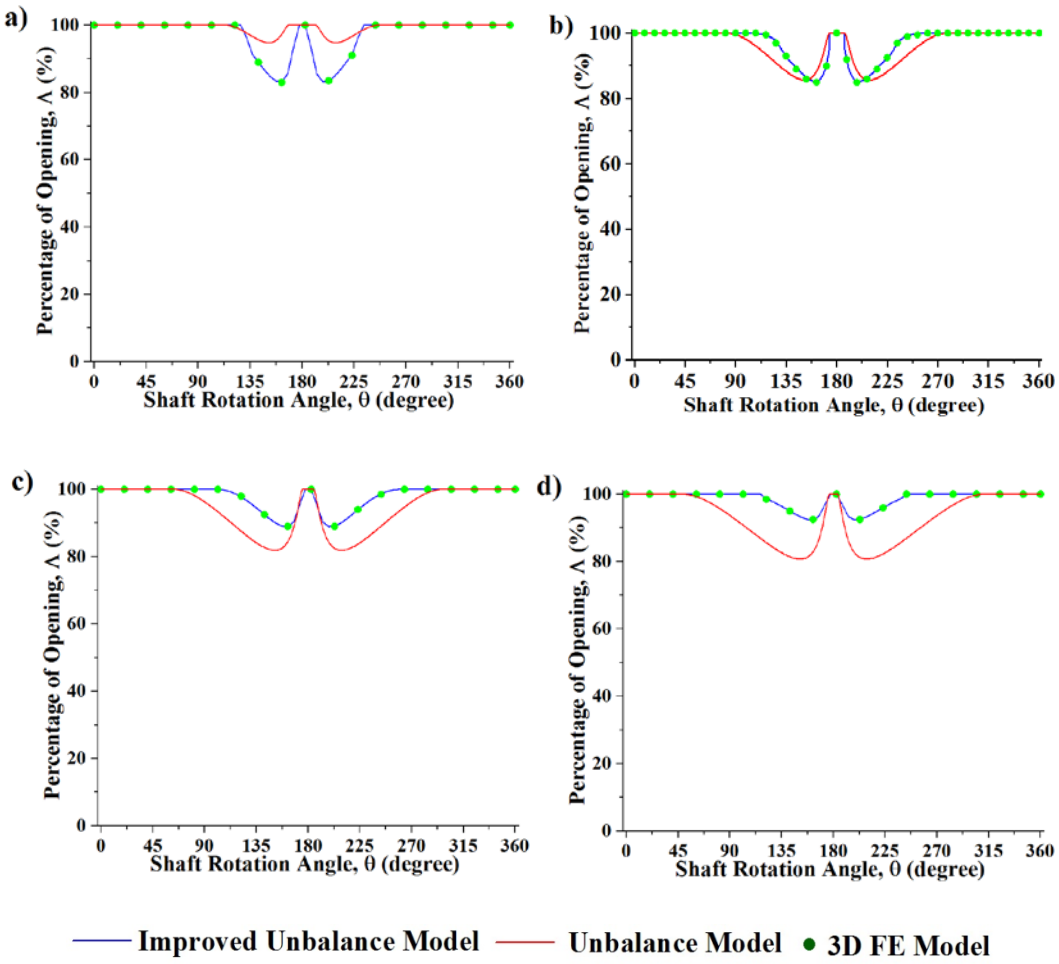

Figure 4-11: Comparison of the percentage of opening of the crack for the unbalance shaft ($\eta = 5$ and $\beta = 0°$) at crack location $\lambda = 0.5$ for different crack depth ratios (a) $\mu = 0.25$, (b) $\mu = 0.5$, (c) $\mu = 0.75$ and (d) $\mu = 1$

4.4 Summary

In this chapter, a new improved crack breathing method was developed to analyse the actual crack breathing mechanism. The newly developed method eliminated two simplifying assumptions used by other authors, namely, that the cracked shafts will only experience symmetrical bending and that the bending moment vector at the crack location is collinear with the neutral axis of bending.

The newly developed model was used to study crack breathing behaviour regarding crack location along shaft length, shaft rotational angle, unbalance force orientation and the ratio of gravitational force and unbalance force. The proposed method results were compared with the results in Section 3.4 of Chapter 3 and results from the 3D FEA model. Throughout the chapter, the focus was on improving the accuracy of determining the crack breathing behaviour. The proposed method demonstrated better agreement with the 3D FEM compared with the results in Section 3.4 of Chapter 3.

The developed model can be further used to improve the calculation of the area moment of inertia of crack cross-section closed area to form the local stiffness matrix of a cracked shaft element and then to study the vibration response of a cracked rotor.

Chapter 5 : Developing New, Improved Area Moment of Inertia Formulas

5.1 Introduction

The ultimate purpose of this study is to develop mathematical formulas to calculate the area moment of inertia at the cracked cross-section of the unbalance shaft. Because the area moment of inertia constitutes the elements of the local stiffness matrix of a cracked shaft element, the related results can be used to calculate the cracked shaft vibration response numerically by solving the equations of system motion. The second area moment of inertia for a fully open cracked cross-section can be evaluated using equations available in the literature. However, when the crack is in a partially closed state, the problem becomes more complex.

In this chapter, the mathematics of calculating the second area moment and centroid location is improved. The approach is developed by considering that since the cross-section of the crack element is irregular when the crack is fully open, the shaft is subject to asymmetric bending near the crack. The inclination of the neutral axis is also considered to derive the improved mathematical formulas. First, the expression of the closed portion of the crack area and coordinates of the centroid of the shaft and crack cross-session are developed. Then, a set of Fourier expansions are derived by converting the second area moment about arbitrary axes into the principal area moment of inertia. The inclination of the neutral axis by considering its relationship with the bending moment in the shaft in the principal coordinate system is also developed.

The second area moment of inertia at the cracked cross-section of the unbalance shaft about centroid axes between the new proposed improved unbalance model and the unbalance model (in Section 3.5 of Chapter 3) are compared. It is observed that in the unbalance model, $I_{\bar{X}}$ up to 6.65% need to be overestimated and $I_{\bar{Y}}$ up to 19.15% need to be underestimated. Finally, the newly developed equations are used to evaluate the second area moment of inertia at the cracked cross-section of the balance and unbalance shafts under different weight–unbalance force ratios at different crack locations as a shaft angle of rotation about centroid axes.

5.2 Calculating Areas and Centroid Coordinates

5.2.1 A fully open crack

Consider a shaft of radius *R* with a transverse crack of depth *h*. The crack front will have a length of *S* and an angular width of α measured from *O*, the shaft centre, as shown in Figure 5-1.

The relative crack depth μ is the ratio of the crack depth to the shaft radius as in Equation (5-1).

$$\mu = \frac{h}{R} \tag{5-1}$$

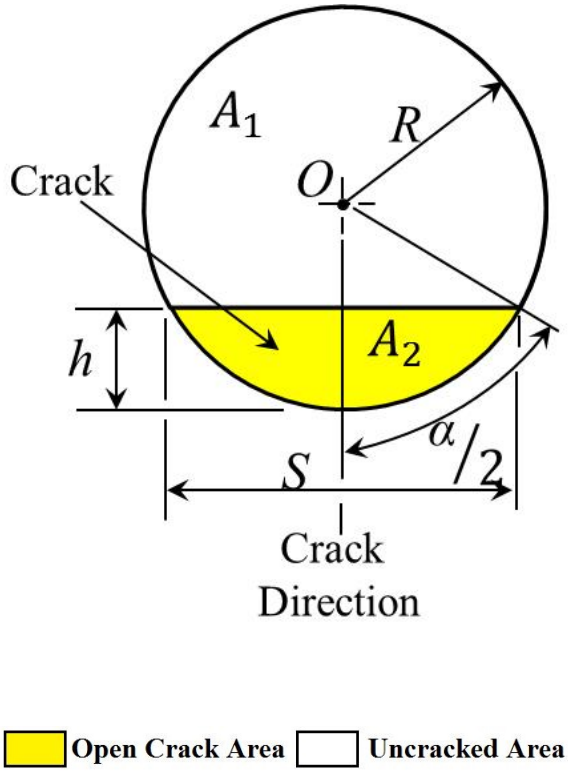

Figure 5-1: Schematic diagram of a crack cross-section

The relative crack length γ is the ratio of the crack front length to the shaft diameter and can be expressed regarding the relative crack depth as in Equation (5-2).

$$\gamma = \frac{s}{2R} = \sqrt{\mu(2-\mu)} \tag{5-2}$$

The angular width of the crack front α can also be expressed regarding the relative crack depth as in Equation (5-3).

$$\alpha = 2\cos^{-1}(1-\mu) \qquad (5\text{-}3)$$

The crack front divides the cross-section of the shaft into two regions. The uncracked region of the shaft is white in Figure 5-1 and has an area of A_1. The uncracked region is interchangeably referred to as A_1 throughout this chapter. The formula for A_1 is described in Equation (5-4); it is a function of the shaft radius and the relative crack depth. The yellow region of the shaft cross-section in Figure 5-1 is called the cracked region. It has an area of A_2. When the crack is in a fully open state, A_2 is a free surface and hence does not transmit any tensile or compressive stress. It reduces the effective cross-section of the shaft for carrying bending loads to just the uncracked region. The formula for A_2 is described in Equation (5-5); it is also a function of the shaft radius and the relative crack depth.

$$A_1 = R^2\left(\pi - \cos^{-1}(1-\mu) + (1-\mu)\sqrt{\mu(2-\mu)}\right) \qquad (5\text{-}4)$$

$$A_2 = R^2\left(\cos^{-1}(1-\mu) - (1-\mu)\sqrt{\mu(2-\mu)}\right) \qquad (5\text{-}5)$$

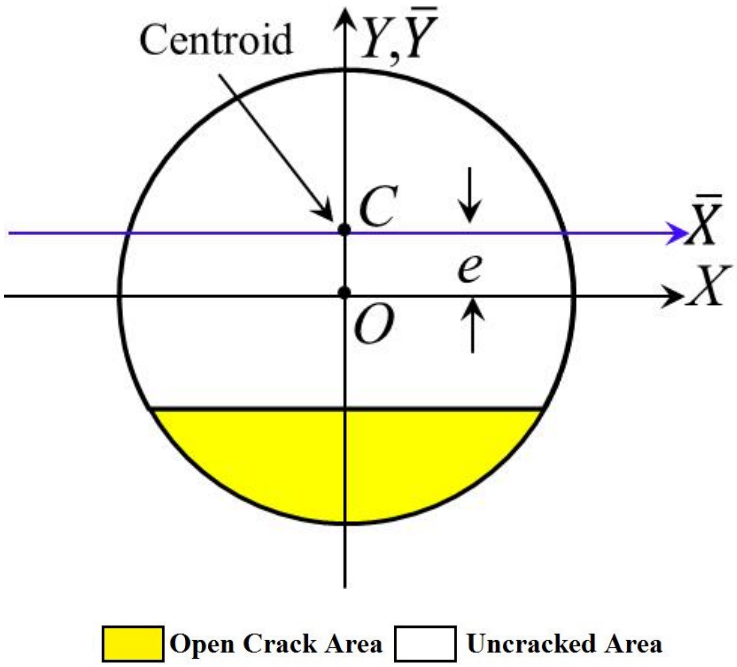

Figure 5-2: Centroid of the effective cross-section with a fully open crack

Because the area of the crack is effectively removed from the cracked element cross-section, the centroid of the shaft, *C*, no longer coincides with the geometric centre of the shaft, *O*. Instead, the centroid of the cracked element cross-section is located a distance *e* from the shaft centre (see Figure 5-2). The distance *e* is a function of the shaft radius, and the relative crack depth is described in Equation (5-6).

$$e = \frac{2R \times \sqrt[3]{\mu(2-\mu)}}{3\left(\pi - \cos^{-1}(1-\mu) + (1-\mu)\sqrt{\mu(2-\mu)}\right)} \tag{5-6}$$

At this point, it is useful to define two sets of coordinate axes that are used throughout this study. The X-Y axes are fixed with the origin located at the shaft's centre. The $\bar{X}$-$\bar{Y}$ axes are moving axes with the origin located at the centroid of the effective section of the shaft crack cross-section. They remain parallel to the fixed axes and are referred to as the coordinate axes throughout this chapter.

While the crack is fully open, the straight-line distance between the centroid of the cracked element cross-section, *C*, and the geometric centre of the shaft, *O*, do not change when the shaft is rotated by angle θ (see Figure 5-3). However, the coordinates of the centroid will change per the relationships, as shown in Equations (5-7) and (5-8).

$$X_1 = -e\sin\theta \tag{5-7}$$

$$Y_1 = e\cos\theta \tag{5-8}$$

Throughout this chapter, X_1 and Y_1 are used to denote the centroid coordinates of the uncracked region, A_1.

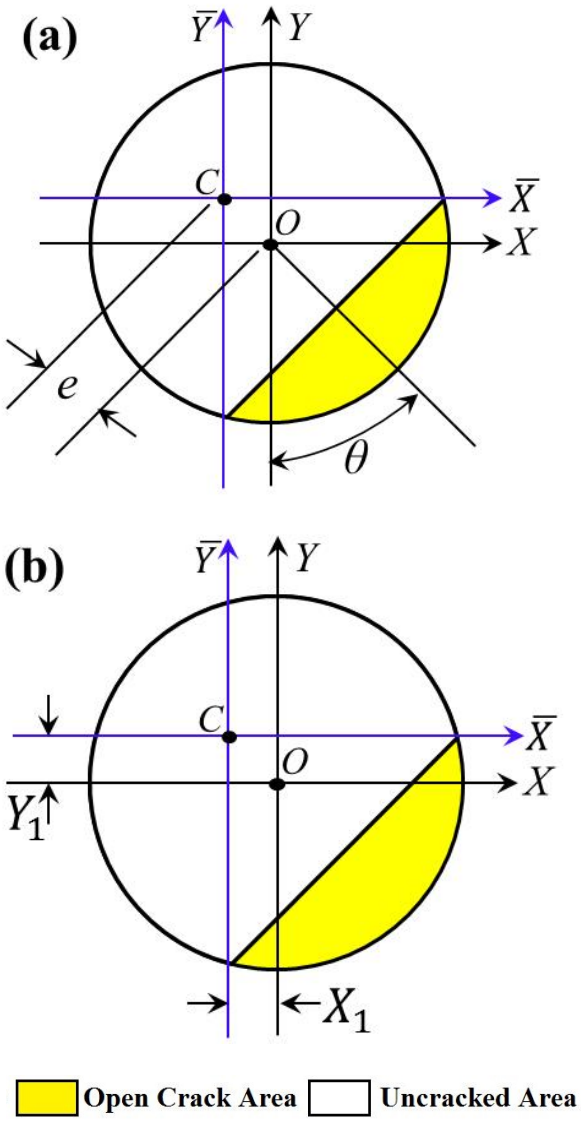

Figure 5-3: Centroidal coordinate axes are related to the fixed coordinate axes by the parameters (a) e & θ and (b) X_1 & Y_1

5.2.2 A partially closed crack

In a shaft with a straight traverse crack in a partial breathing state, the closed area of the crack can be described by three points, as shown in Figure 5-4, with the numbers 1, 2 and 3. The X–Y coordinates of these points are the points of intersection between two straight lines and the outer circumference of the shaft section.

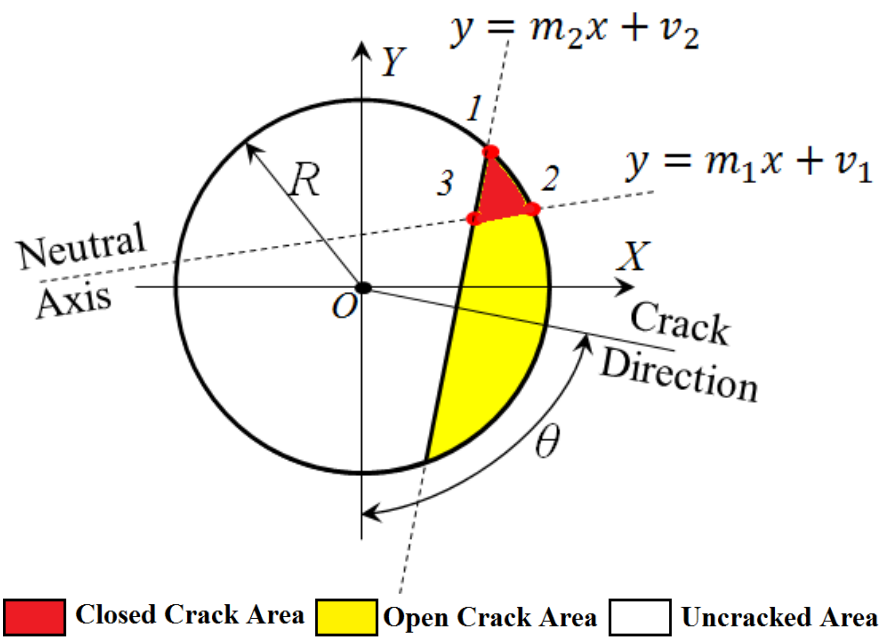

Figure 5-4: Closed portion of the crack region described by three points

The first straight line is collinear with the neutral axis and is described by the coordinates of the centroid of the shaft and the inclination of the neutral axis. Neither of these parameters is analytically determinate. The second straight line is collinear with the crack front and is fully described by the crack depth and the shaft rotation angle. The equation of a circle describes the circumference of the shaft. Only the positive range of Y values needs to be considered in a shaft.

The areas bounded by the three intersecting curves are divided into three regions for evaluating its area, centroid coordinates and area moment of inertia as shown in Figure 5-5. To this end, an additional point, point 4, is defined as the point of intersection between the line $\overrightarrow{3,1}$ and a horizontal line extending from point 2 as shown in Figure 5-5. The coordinates of points 1 through 4 have been assigned variable names as shown in Table 5-1. The coordinates of the points that describe the closed portion of the crack are shown in the context of the shaft's centroid and rotation centre in Figure 5-6.

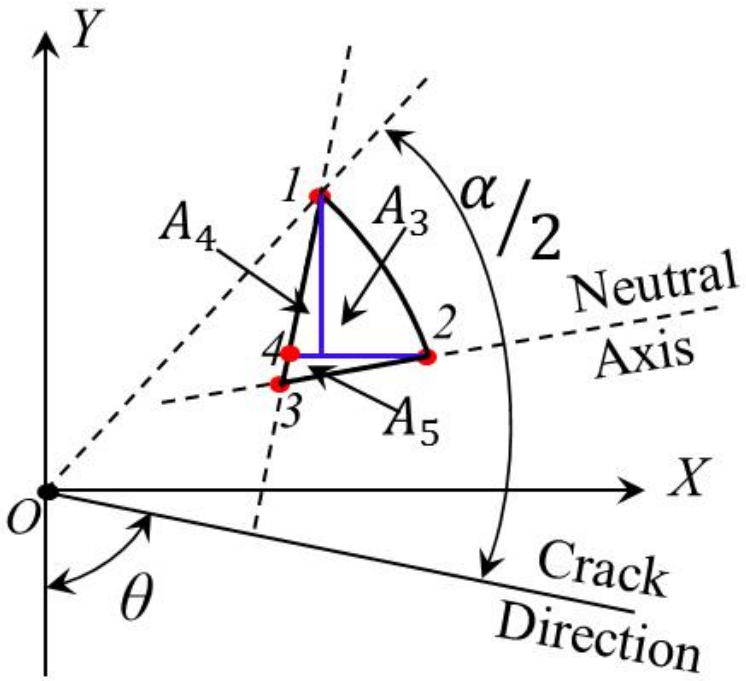

Figure 5-5: Closed portion of the crack divided into three areas

Table 5-1: Coordinates of the closed crack area

Coordinate	**Points**			
	1	2	3	4
X	a_1	a_2	a_3	a_4
Y	b_1	b_2	b_3	b_2

The coordinates of point 1 can be evaluated directly as described in Equations (5-9) and (5-10).

$$b_1 = -R\cos(\theta + \beta/2) \tag{5-9}$$

$$a_1 = R\sin(\theta + \beta/2) \tag{5-10}$$

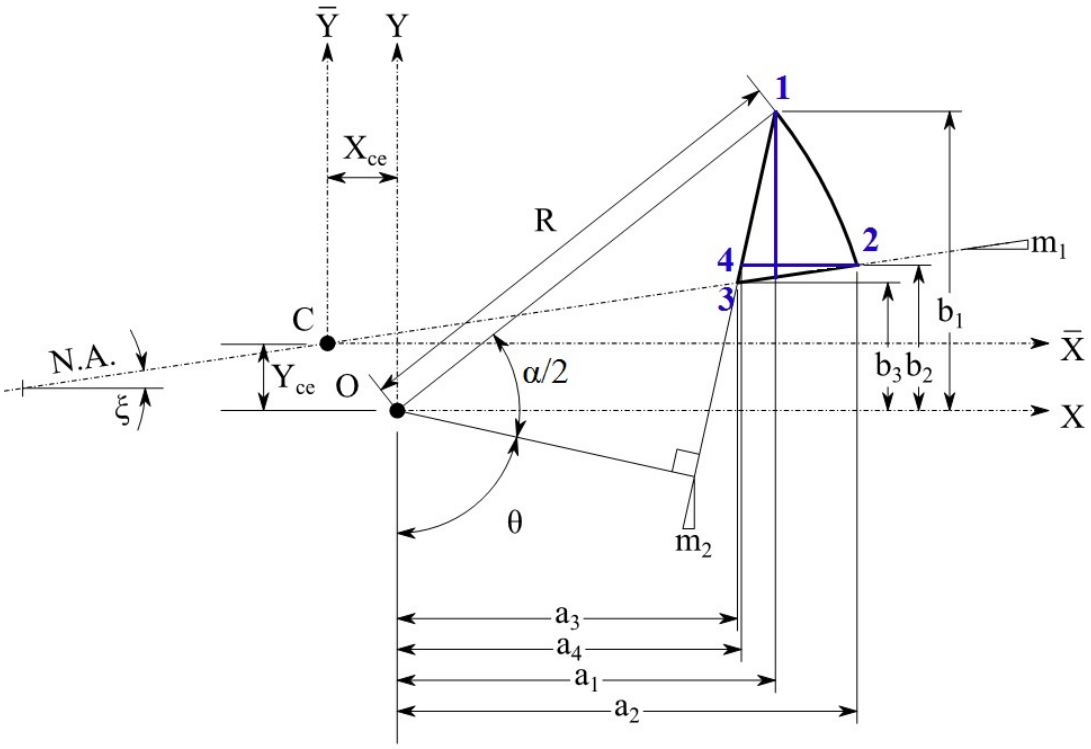

Figure 5-6: Coordinates of the three areas of the closed portion of the crack

The slope and y-intercept of the neutral axis are not known from the outset, and hence, an initial estimated value of $\xi = 0$ and a section centroid coincident with the centroid of the uncracked region ($Y_{ce} = Y_1$ and $X_{ce} = X_1$) are used. For later iterations of the calculations, updated values for these parameters are used.

$$m_1 = \tan(\xi) \tag{5-11}$$

$$Y_{ce} = m_1 X_{ce} + v_1 \tag{5-12}$$

$$v_1 = Y_{ce} - m_1 X_{ce} = Y_{ce} - X_{ce} \tan(\xi) \tag{5-13}$$

With the slope and y-intercept of the neutral axis evaluated, the coordinates of point 2 can be found using a quadratic system of equations. The first equation states that point 2 lies on the neutral axis as described in Equation (5-14) and the second equation states that point 2 is on the arc of the circle describing the outer edge of the shaft as described in Equation (5-15).

$$b_2 = m_1 a_2 + v_1 \tag{5-14}$$

$$b_2 = \sqrt{R^2 - {a_2}^2} \tag{5-15}$$

The Y coordinate of point 2 is eliminated for the present so that we can solve for the X coordinate as shown in Equation (5-16).

$$a_2 = \frac{-(2m_1v_1) + \sqrt{(2m_1v_1)^2 - 4(1 + {m_1}^2)({v_1}^2 - R^2)}}{2(1 + {m_1}^2)} \tag{5-16}$$

The Y coordinate of point 2 can now be evaluated by substituting the value of the X coordinate into either of Equations (5-14) and (5-15). The slope of the crack front can be calculated from the shaft rotation angle as shown in Equation (5-17).

$$m_2 = \tan(\theta) \tag{5-17}$$

The X coordinate of point 3 can be found by finding the point of intersection between the neutral axis and crack front.

$$a_3 = \frac{v_2 - v_1}{m_1 - m_2} \tag{5-18}$$

The Y coordinate of point 3 can now be found by substituting its X coordinate into the equation of the neutral axis.

$$b_3 = m_1 a_3 + v_1 \tag{5-19}$$

Point 4 shares its Y coordinate with point 2 as described in Equation (5-15). The corresponding X coordinate is found by substituting the Y coordinate into the equation of the crack front and solving for a_4.

$$a_4 = \frac{b_2 - v_2}{m_2} \tag{5-20}$$

The areas of A_3, A_4 and A_5 can now be evaluated using these evaluated coordinates. The centroid coordinates of A_3 are represented by X_3 and Y_3 as described in Figure 5-7.

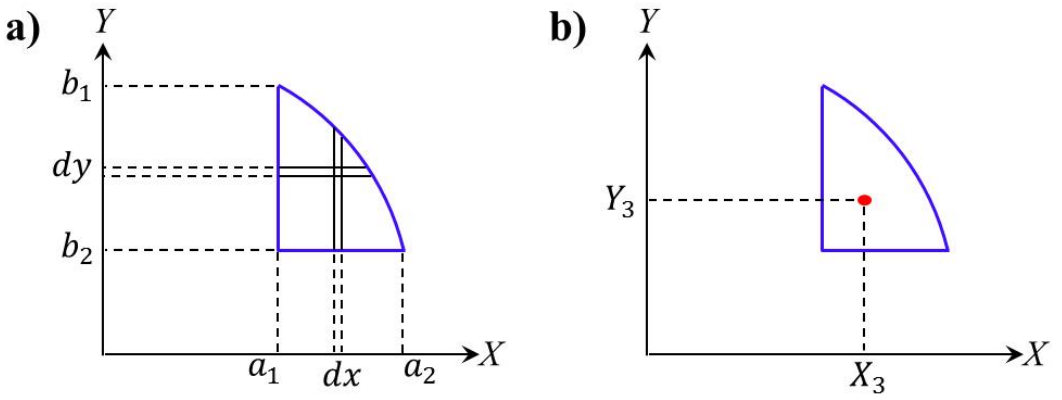

Figure 5-7: Limits of integration of area A_3 and its centroid coordinates with respect to the fixed coordinate axes

The area can be found by evaluating the following double integral as described in (5-21).

$$A_3 = \int_{a_1}^{a_2} \int_{b_2}^{\sqrt{R^2-x^2}} dy\, dx \tag{5-21}$$

Note that integration w.r.t. Y is performed first since the alternative will yield erroneous results at large shaft rotations for deep cracks as described in Equation (5-22).

$$A_3 = \int_{a_1}^{a_2} \sqrt{R^2 - x^2} - b_2\, dx \tag{5-22}$$

The above integral is evaluated by inspection using the indefinite integral provided by Gradshteyn and Ryzhik (2014) as described in Equation (5-23).

$$\int \sqrt{a + cx^2}\, dx = \frac{1}{2} x\sqrt{a + cx^2} + \frac{1}{2} a \frac{1}{\sqrt{-c}} \sin^{-1}\left(x\sqrt{\frac{-c}{a}}\right) \tag{5-23}$$

By substituting $a = R^2$, $c = -1$ and the limits of x, the following definite integral is obtained as described in Equation (5-24).

$$A_3 = \frac{1}{2}\Big[a_2\sqrt{R^2 - {a_2}^2} - a_1\sqrt{R^2 - {a_1}^2} + R^2\left(\sin^{-1}\left(\frac{a_2}{R}\right) - \sin^{-1}\left(\frac{a_1}{R}\right)\right)\Big] + b_2(a_1 - a_2) \tag{5-24}$$

The Y coordinate of the A_3 centroid is found by dividing its first area moment about the X-axis by A_3 as described in Equation (5-25).

$$Y_3 = \frac{1}{A_3}\int_{a_1}^{a_2}\int_{b_2}^{\sqrt{R^2-x^2}} y dy\, dx \tag{5-25}$$

The first integration of this double integral yields a simple polynomial expression as described in Equation (5-26).

$$Y_3 = \frac{1}{A_3}\int_{a_1}^{a_2}\frac{1}{2}\left(R^2 - x^2 - {b_2}^2\right)dx$$

$$Y_3 = \frac{1}{A_3}\frac{1}{2}\left[-\frac{x^3}{3} + x\left(R^2 - {b_2}^2\right)\right]_{a_1}^{a_2}$$

$$Y_3 = \frac{1}{6A_3}\left[{a_1}^3 - {a_2}^3 + 3(a_2 - a_1)\left(R^2 - {b_2}^2\right)\right] \tag{5-26}$$

Similarly, the X coordinate of the A_3 centroid is found by dividing its first area moment about the Y-axis by A_3 as described in Equation (5-27).

$$X_3 = \frac{1}{A_3}\int_{a_1}^{a_2}\int_{b_2}^{\sqrt{R^2-x^2}} x dy\, dx \tag{5-27}$$

The first integration of the above double integral yields an expression that is solvable by *u-substitution* as shown below.

$$X_3 = \frac{1}{A_3}\int_{a_1}^{a_2} x\left(\sqrt{R^2 - x^2} - b_2\right)dx$$

Let $u = R^2 - x^2$ and $du = -2x\, dx$

$$\int x\sqrt{R^2 - x^2}\, dx = -\frac{1}{2}\int \sqrt{u}\ du$$

$$\int x\sqrt{R^2 - x^2}\, dx = -\frac{1}{2}\frac{2}{3}\left(\sqrt{u}\right)^3 = -\frac{\left(\sqrt{R^2-x^2}\right)^3}{3}$$

Substituting in this indefinite integral yields the following expression for the X coordinate of the A_3 centroid as described in Equation (5-28).

$$X_3 = \frac{1}{A_3}\left[-\frac{\left(\sqrt{R^2-x^2}\right)^3}{3} - b_2 x\right]_{a_1}^{a_2}$$

$$X_3 = \frac{1}{3A_3}\left[\left(\sqrt{R^2-{a_1}^2}\right)^3 - \left(\sqrt{R^2-{a_2}^2}\right)^3 - 3b_2(a_2-a_1)\right] \qquad (5\text{-}28)$$

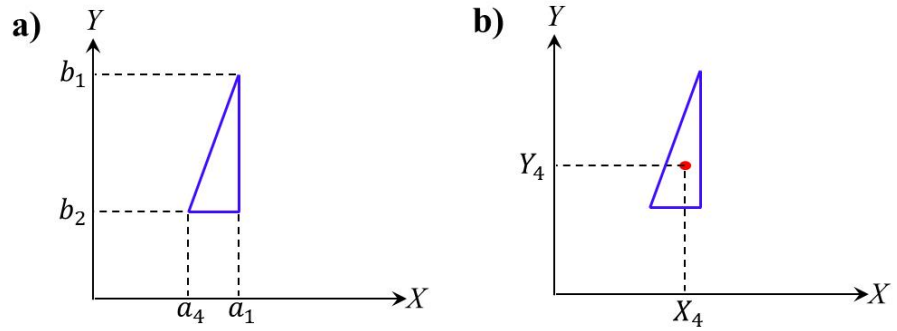

Figure 5-8: Dimensions of area A_4 and its centroid coordinates with respect to the fixed coordinate axes

$$A_4 = 0.5(a_1 - a_4)(b_1 - b_2) \qquad (5\text{-}29)$$

The area of region A_4 can be found since it is a right triangle as shown in Figure 5-8. Note that at shaft rotation angles larger than 90°, $a_1 < a_4$, which will result in a negative value for A_4, using Equation (5-29). This is intentional, because when $\theta >$ 90°, A_3 and its associated parameters will be overestimated by an amount equal to that of A_4. The negative sign of A_4 corrects for this overestimation. The Y coordinate of the A_4 centroid is found by adding 1/3 of the triangle's height to the Y coordinate of the bottom edge as described in Equation (5-30).

$$Y_4 = b_2 + \frac{1}{3}(b_1 - b_2) \qquad (5\text{-}30)$$

Similarly, the X coordinate is found by adding 2/3 of the triangle's base length to the X coordinate of the left-hand apex as described in Equation (5-31).

$$X_4 = a_4 + \frac{2}{3}(a_1 - a_4) \qquad (5\text{-}31)$$

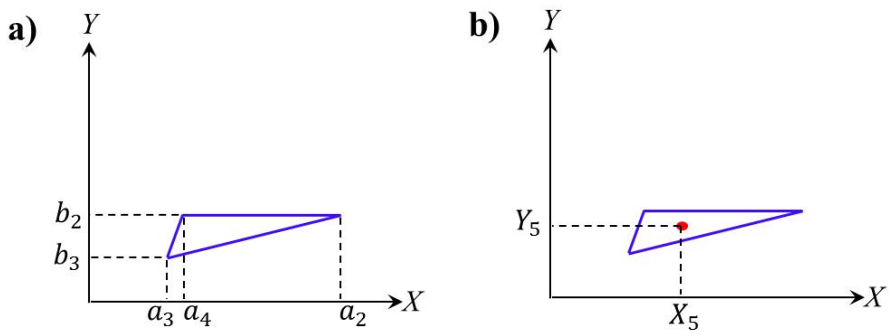

Figure 5-9: Dimensions of area A_5 and its centroid coordinates with respect to the fixed coordinate axes

The area and centroid coordinates of region A_5 are now evaluated as described in Equations (5-32) to (5-34).

$$A_5 = 0.5(a_2 - a_4)(b_2 - b_3) \tag{5-32}$$

$$Y_5 = b_3 + \frac{2}{3}(b_2 - b_3) \tag{5-33}$$

$$X_5 = a_3 + \frac{1}{3}(a_2 - 2a_3 + a_4) \tag{5-34}$$

The total closed portion of the crack area can now be evaluated using Equation (5-35).

$$A_{2c} = A_3 + A_4 + A_5 \tag{5-35}$$

The entire area of the cracked element cross-section can now be evaluated using Equation (5-36).

$$A_{ce} = A_1 + A_3 + A_4 + A_5 \tag{5-36}$$

The coordinates of the centroid of the area of the cracked element cross-section can now be computed by using Equations (5-38) and (5-39).

$$Y_{ce} = \left(\frac{A_1Y_1 + A_3Y_3 + A_4Y_4 + A_5Y_5}{A_1 + A_3 + A_4 + A_5}\right) \tag{5-37}$$

$$X_{ce} = \left(\frac{A_1X_1 + A_3X_3 + A_4X_4 + A_5X_5}{A_1 + A_3 + A_4 + A_5}\right) \tag{5-38}$$

5.2.3 A fully closed crack

When crack becomes fully closed, the area of the cracked element cross-section is same as the area of the solid shaft, which is a function of the shaft radius only as described in Equation (5-40). While the crack is fully closed, the centroid of the cracked element cross-section, *C*, coincides with the geometric centre of the shaft, *O* when the shaft is rotated by angle θ (see Figure 5-10). Therefore, the coordinates of the centroid of the cracked element cross-section will be e ($X_{ce} = 0, Y_{ce} = 0$) about fixed axis X and Y.

$$A_{ce} = \pi R^2 \tag{5-39}$$

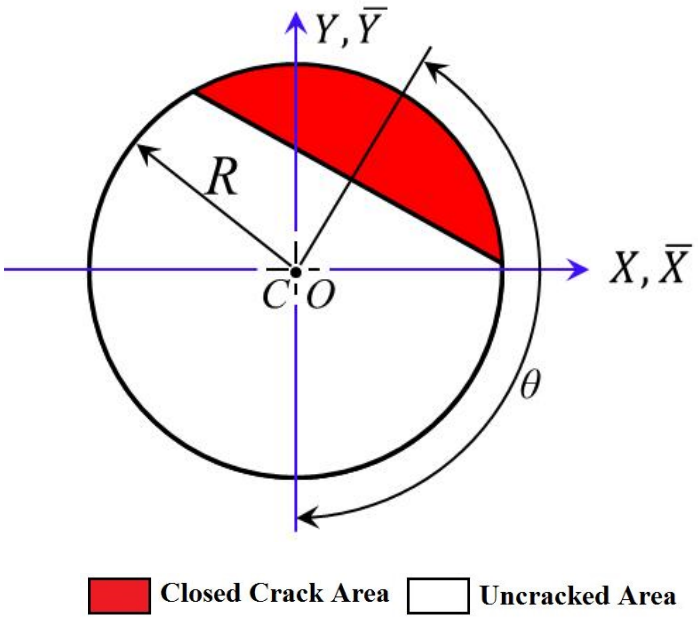

Figure 5-10: Schematic diagrams of a fully closed cracked element cross-section

5.3 Calculating Area Moment of Inertia

5.3.1 A fully open crack

Closed-form expressions for the area moment of inertia of A_1 about the fixed axes were derived as Equations (5-41) and (5-42) for shaft rotation angle of θ = 0°.

$$I_{X1} = \frac{\pi R^4}{8} + \frac{R^4}{4}\left((1-\mu)(2\mu^2 - 4\mu + 1)\gamma + \sin^{-1}(1-\mu)\right) \quad (5\text{-}40)$$

$$I_{Y1} = \frac{\pi R^4}{4} - \frac{R^4}{12}\left((1-\mu)(2\mu^2 - 4\mu - 3)\gamma + 3\sin^{-1}(\gamma)\right) \quad (5\text{-}41)$$

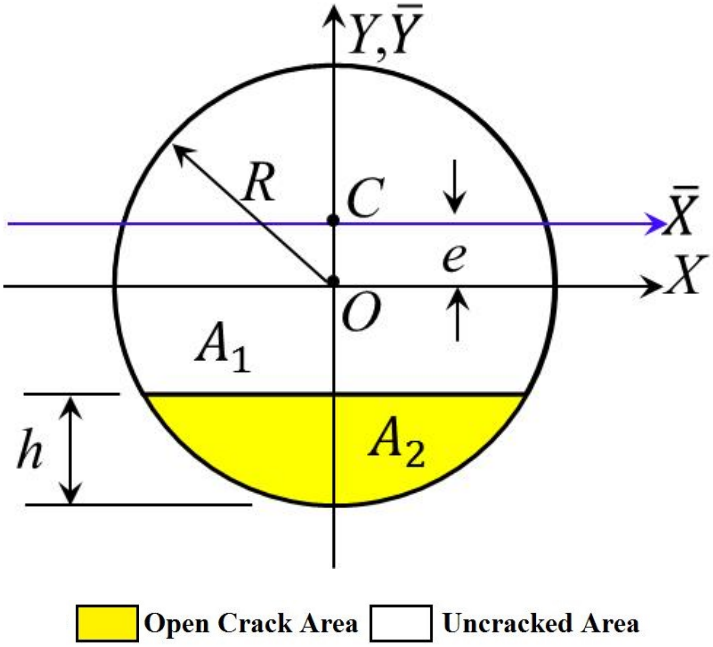

Figure 5-11: Area moment of inertia for a fully open crack evaluated about its centroid

Converting these to the area moment of inertia about the centroidal axes is performed using the parallel axis theorem for shaft rotation angle of θ = 0° as described in Equation (5-43).

$$I_{\bar{X}1} = I_{X1} - A_1 e^2 \quad (5\text{-}42)$$

Since the centroid $\bar{Y}$-axis is colinear with the fixed Y-axis, no conversion is needed for shaft rotation angle of θ = 0° as described in Equation (5-44).

$$I_{\bar{Y}1} = I_{Y1} \quad (5\text{-}43)$$

Because A_1 is symmetrical about the Y-axis, $I_{\bar{Y}1}$ is one of the principal area moment of inertia. This means that $I_{\bar{X}1}$ is the remaining principal area moment of inertia. The

first and second principal axes of the section, that is, U and V respectively, are shown in Figure 5-12.

Because of the greater area moment about X that A_1 loses to A_2, $(I_{\bar{X}1})_{\theta=0^\circ}$ will always be smaller than $(I_{\bar{Y}1})_{\theta=0}$. This means that $(I_{\bar{Y}1})_{\theta=0^\circ}$ is the first principal area moment of inertia and $(I_{\bar{X}1})_{\theta=0^\circ}$ is the second principal area moment of inertia.

$$I_{U1} = (I_{\bar{Y}1})_{\theta=0} \tag{5-44}$$

$$I_{V1} = (I_{\bar{X}1})_{\theta=0} \tag{5-45}$$

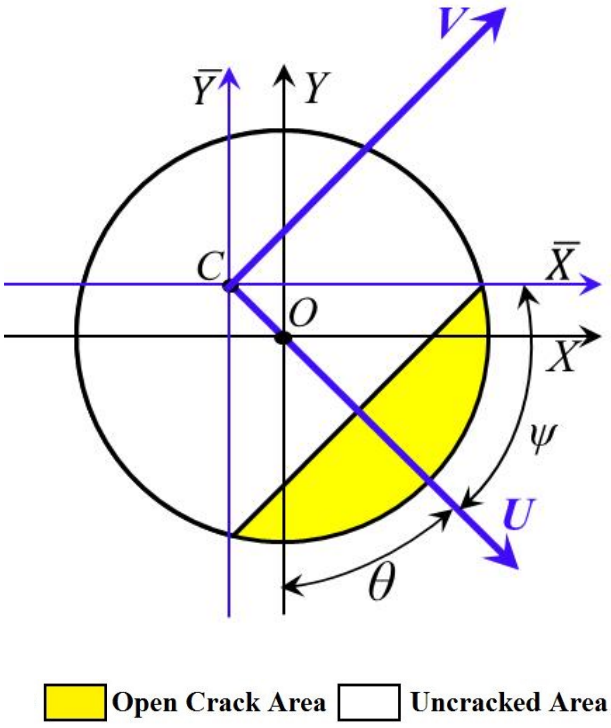

Figure 5-12: Origin of the principal coordinate axes at the centroid of the section

Throughout this paper, U and V will be used to denote the first and second principal axes of the shaft section respectively. The origin of the principal coordinate axes is at the centroid of the section. The orientation of the principal axes is described by an angle ψ, between the first principal axis and the positive $\bar{X}$ axis with counter-clockwise rotation from $\bar{X}$ taken to be positive.

If the crack is fully open, ψ is simply a function of the shaft rotation angle.

$$\psi = \frac{\pi}{2} - \theta \tag{5-46}$$

5.3.2 A partially closed crack

The area moment of inertia about the centroid can now be evaluated. First, they are evaluated about the centroids of each area component. For A_3, the area moment of inertia about the X-axis is evaluated and using the parallel axis theorem, this value is translated to values about an axis coincident with the centroid of A_3.

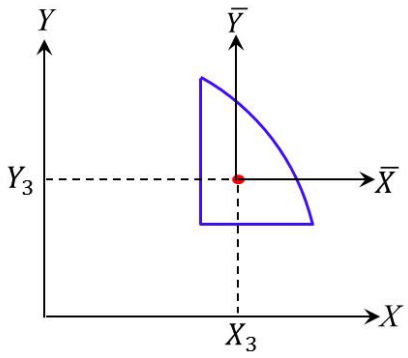

Figure 5-13: Area moment of inertia for A_3 evaluated about its centroid

The area moment about the $\bar{X}$ axis is evaluated as a double integral, with integration w.r.t to Y performed first as described in Equation (5-47).

$$I_{\bar{X}3} = \int_{a_1}^{a_2} \int_{b_2}^{\sqrt{R^2-x^2}} y^2 dy\, dx - A_3 {Y_3}^2 \tag{5-47}$$

After the first integration is performed, a relatively complicated integral result is obtained as described in Equation (5-48).

$$I_{\bar{X}3} = \frac{1}{3}\int_{a_1}^{a_2} \left(\sqrt{R^2 - x^2}\right)^3 - {b_2}^3 dx - A_3 {Y_3}^2 \tag{5-48}$$

Equation (5-48) is evaluated by inspection using the following indefinite integral provided by Gradshteyn and Ryzhik (2014):

$$\int \left(\sqrt{a + cx^2}\right)^3 dx = \frac{1}{6}x\left(\sqrt{a + cx^2}\right)^3 + \frac{3}{8}ax\left(\sqrt{a + cx^2}\right)^3 + \frac{3}{8}a^2\frac{1}{\sqrt{-c}}\sin^{-1}\left(x\sqrt{\frac{-c}{a}}\right)$$

By substituting $a = R^2$, $c = -1$ and the limits of x, the following definite integral is obtained as described in Equation (5-49).

$$I_{\bar{X}3} = \frac{1}{24}\Big[2\left(a_2\left(\sqrt{R^2 - a_2{}^2}\right)^3 - a_1\left(\sqrt{R^2 - a_1{}^2}\right)^3\right) + 3R^2\left(a_2\sqrt{R^2 - a_2{}^2} + R^2\sin^{-1}\left(\frac{a_2}{R}\right) - a_1\sqrt{R^2 - a_1{}^2} - R^2\sin^{-1}\left(\frac{a_1}{R}\right)\right) - b_2{}^3(a_2 - a_1)\Big] - A_3 Y_3{}^2 \quad (5\text{-}49)$$

Similarly, the area moment about the $\bar{Y}$ axis is evaluated using a double integral as described in Equation (5-50).

$$I_{\bar{Y}3} = \int_{a_1}^{a_2}\int_{b_2}^{\sqrt{R^2 - x^2}} x^2 dy\, dx - A_3 X_3{}^2 \quad (5\text{-}50)$$

Integration w.r.t. Y is performed first resulting in a complicated integral as described in Equation (5-51).

$$I_{\bar{Y}3} = \int_{a_1}^{a_2} x^2\left(\sqrt{R^2 - x^2} - b_2\right)dx - A_3 X_3{}^2 \quad (5\text{-}51)$$

It is evaluated by inspection using the following indefinite integral provided by Gradshteyn and Ryzhik (2014):

$$\int x^2\sqrt{a + cx^2}\, dx = \frac{1}{4}\frac{x\left(\sqrt{a+cx^2}\right)^3}{c} - \frac{1}{8}\frac{ax\sqrt{a+cx^2}}{c} - \frac{1}{8}\frac{a^2}{c}\frac{1}{\sqrt{-c}}\sin^{-1}\left(x\sqrt{\frac{-c}{a}}\right)$$

By substituting $a = R^2$, $c = -1$ and the limits of x, the following definite integral is obtained as described in Equation (5-52).

$$I_{\bar{Y}3} = \frac{1}{24}\Big[6a_1\left(\sqrt{R^2 - a_1{}^2}\right)^3 - 6a_2\left(\sqrt{R^2 - a_2{}^2}\right)^3 + 3R^2\left(a_2\sqrt{R^2 - a_2{}^2} - a_1\sqrt{R^2 - a_1{}^2} + R^2\left(\sin^{-1}\left(\frac{a_2}{R}\right) - \sin^{-1}\left(\frac{a_1}{R}\right)\right)\right) + 8b_2(a_2{}^3 - a_1{}^3)\Big] - A_3 X_3{}^2 \quad (5\text{-}52)$$

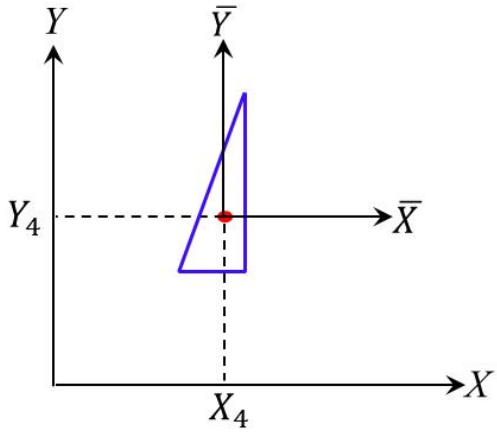

Figure 5-14: Area moment of inertia for A_4 evaluated about its centroid

Because region A_4 is a simple right triangle as shown in Figure 5-8, its area moment of inertia about its centroid axes are evaluated directly as described in Equations (5-53) to (5-54).

$$I_{\bar{X}4} = \frac{1}{36}(b_1 - b_2)^3(a_1 - a_4) \tag{5-53}$$

$$I_{\bar{Y}4} = \frac{1}{36}(b_1 - b_2)(a_1 - a_4)^3 \tag{5-54}$$

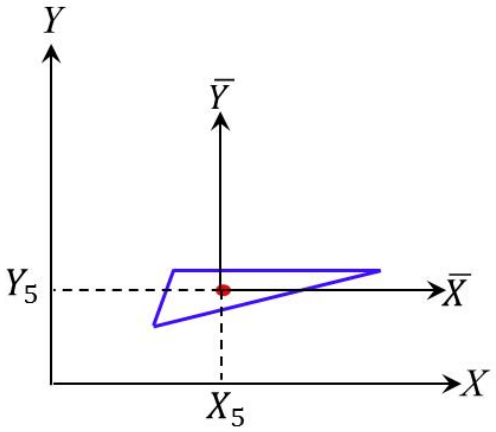

Figure 5-15: Area moment of inertia for A_5 evaluated about its centroid

Likewise, region A_5 can have its area moment of inertia evaluated directly, albeit using slightly different formulas as described in Equations (5-55) to (5-56), owing to it being a more general triangle and not necessarily a right triangle as shown in Figure 5-15.

$$I_{\bar{X}5} = \frac{1}{36}(b_2 - b_3)^3(a_2 - a_4) \tag{5-55}$$

$$I_{\bar{Y}5} = \frac{1}{36}(a_2 - a_4)(b_2 - b_3)({a_2}^2 + {a_3}^2 + {a_4}^2 - a_2a_3 - a_2a_4 - a_3a_4) \tag{5-56}$$

The area moment of inertia of the cracked element cross-section A_{ce} about the centroid can now be calculated using the parallel axis theorem as described in Equations (5-57) and (5-58).

$$I_{\bar{X}} = [I_{\bar{X}1} + A_1(Y_1 - Y_{ce})^2] + [I_{\bar{X}3} + A_3(Y_3 - Y_{ce})^2] + [I_{\bar{X}4} + A_4(Y_4 - Y_{ce})^2] + [I_{\bar{X}5} + A_5(Y_5 - Y_{ce})^2] \tag{5-57}$$

$$I_{\bar{Y}} = [I_{\bar{Y}1} + A_1(X_1 - X_{ce})^2] + [I_{\bar{Y}3} + A_3(X_3 - X_{ce})^2] + [I_{\bar{Y}4} + A_4(X_4 - X_{ce})^2] + [I_{\bar{Y}5} + A_5(X_5 - X_{ce})^2] \tag{5-58}$$

5.3.3 A fully closed crack

When the crack becomes fully closed, the area moment of inertia of the cracked element cross-section A_{ce} about the centroid and fixed reference axis are the same as that of the solid shaft as described in Equations (5-59) and (5-60).

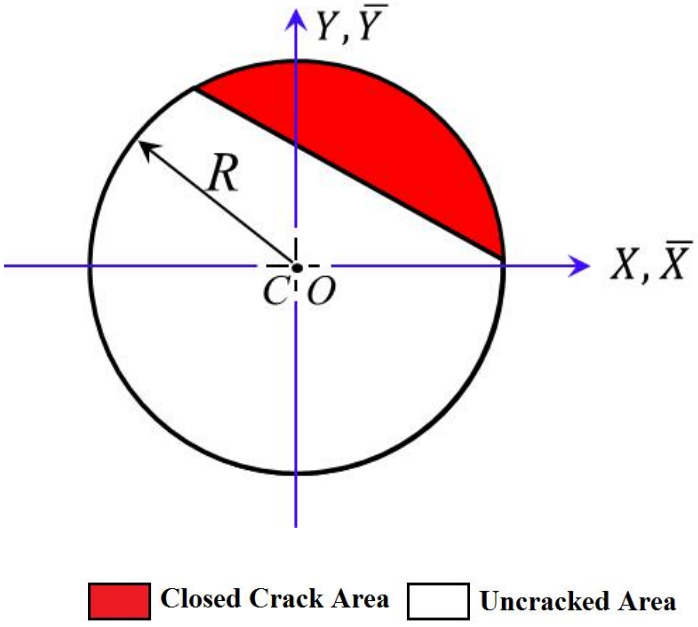

Figure 5-16: Area moment of inertia for a fully closed crack evaluated about its centroid

$$I_X = I_{\bar{X}} = \frac{\pi R^4}{4} \tag{5-59}$$

$$I_Y = I_{\bar{Y}} = \frac{\pi R^4}{4} \tag{5-60}$$

5.4 Principal Area Moment of Inertia and the Principal Axes

The principal axes of the crack section will intersect at its centroid and typically have a nonzero angular offset from the nonrotating $\bar{X}$-$\bar{Y}$ centroid coordinates. The offset is described by angle, ψ, which is measured from the positive $\bar{X}$ axis to first principal axis (U axis) with counter-clockwise rotation taken to be positive as shown in Figure 5-17.

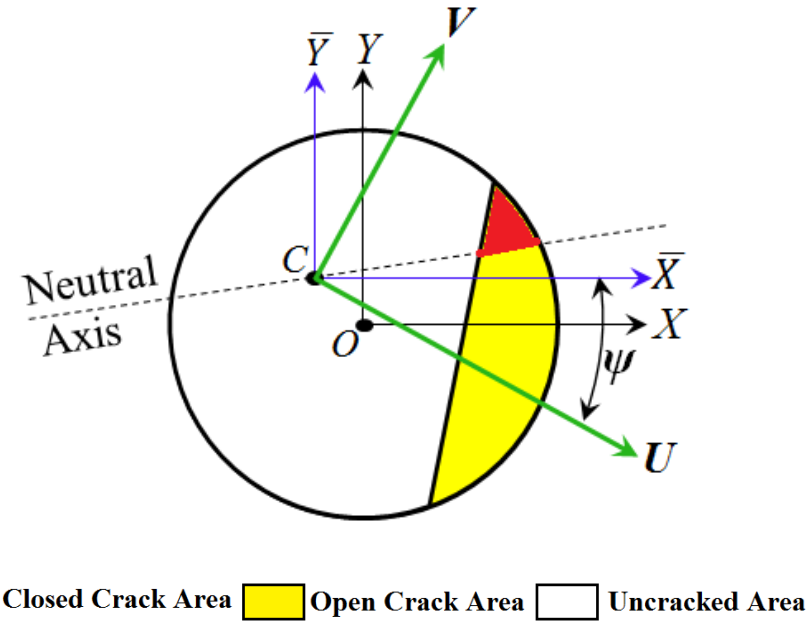

Figure 5-17: Orientation of principal axes

The principal area moment of inertia can be related to the area moment of inertia and the product of area moment of inertia about the centroid of a Mohr's circle as shown in Figure 5-18.

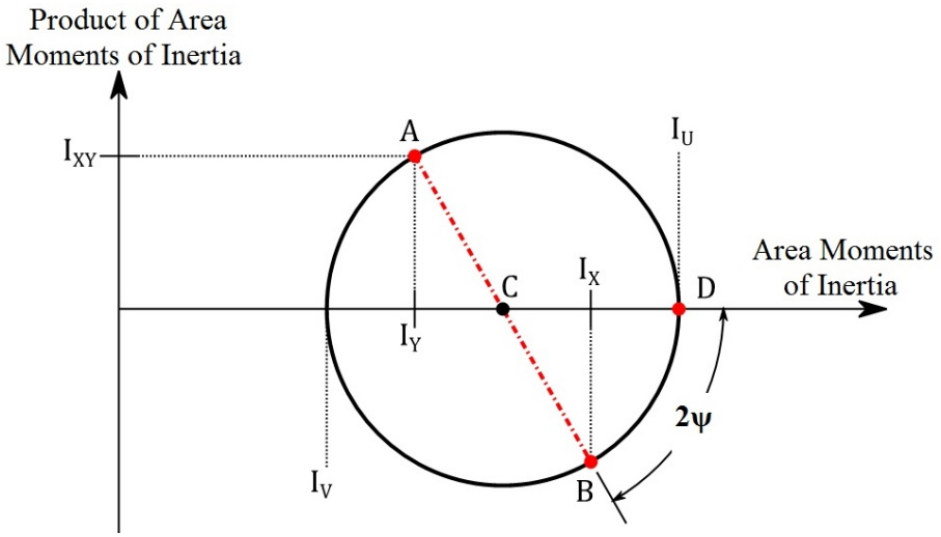

Figure 5-18: Mohr's circle of area moment of inertia

As shown in Figure 5-18, the area moment of inertia, I_Y and I_X, are the horizontal coordinates of points A and B respectively. The product of the area is the vertical coordinate of point A. For any given crack state, the straight-line distance between points A and B is constant. Point C is the midpoint of the line connecting A and B. Point C will always lie on the horizontal axis of the Mohr's circle and its position will also be constant for a given crack breathing state. Performing a rotated coordinate system transformation has the effect of rotating the line $\overrightarrow{AB}$ about point C. If the coordinate system is rotated through 180°, a complete circle centred at C is traced by points A and B. The angle of rotation required to align the coordinate system with the principal axes is denoted by the pronumeral ψ. ψ is half of the angle between the lines $\overrightarrow{CD}$ and $\overrightarrow{CB}$, with counter-clockwise rotation measured from point D taken to be positive.

The principal area moment of inertia for the entire section can now be calculated by using Equations (5-61) and (5-62).

$$I_U = \frac{1}{2}(I_{\bar{X}} + I_{\bar{Y}}) + \sqrt{\frac{(I_{\bar{X}}+I_{\bar{Y}})^2}{4} + I_{\bar{X}\bar{Y}}{}^2} \tag{5-61}$$

$$I_V = \frac{1}{2}(I_{\bar{X}} + I_{\bar{Y}}) - \sqrt{\frac{(I_{\bar{X}}+I_{\bar{Y}})^2}{4} + I_{\bar{X}\bar{Y}}{}^2} \tag{5-62}$$

In addition, the orientation of the principal axes w.r.t the centroid coordinate axes are given by Equation (5-63).

$$\psi = \begin{cases} \psi^* & I_{\bar{X}} > I_{\bar{Y}} \quad I_{\bar{X}\bar{Y}} < 0 \\ 0 & I_{\bar{X}} > I_{\bar{Y}} \quad I_{\bar{X}\bar{Y}} = 0 \\ \psi^* & I_{\bar{X}} > I_{\bar{Y}} \quad I_{\bar{X}\bar{Y}} > 0 \\ \frac{\pi}{4} & I_{\bar{X}} = I_{\bar{Y}} \quad I_{\bar{X}\bar{Y}} < 0 \\ 0 & I_{\bar{X}} = I_{\bar{Y}} \quad I_{\bar{X}\bar{Y}} = 0 \\ -\frac{\pi}{4} & I_{\bar{X}} = I_{\bar{Y}} \quad I_{\bar{X}\bar{Y}} > 0 \\ \psi^* + \frac{\pi}{2} & I_{\bar{X}} < I_{\bar{Y}} \quad I_{\bar{X}\bar{Y}} < 0 \\ \frac{\pi}{2} & I_{\bar{X}} < I_{\bar{Y}} \quad I_{\bar{X}\bar{Y}} = 0 \\ \psi^* - \frac{\pi}{2} & I_{\bar{X}} < I_{\bar{Y}} \quad I_{\bar{X}\bar{Y}} > 0 \end{cases} \tag{5-63}$$

where ψ^* is as described in Equation (5-64):

$$\psi^* = \frac{1}{2}\tan^{-1}\left(\frac{2I_{\bar{X}\bar{Y}}}{I_{\bar{Y}} - I_{\bar{X}}}\right) \tag{5-64}$$

Since ψ is used throughout this process, it possesses the following property as shown in Equation (5-65).

$$f(\psi) = f(\psi + k\pi) \tag{5-65}$$

In Equation (5-63), k is an integer. Hence, ψ can assume infinitely many values for a given crack state. To remove any ambiguity when performing tan and arctan operations, later, ψ is restricted to the range $-\frac{\pi}{2} \leq \psi \leq \frac{\pi}{2}$.

5.5 Evaluating the Neutral Axis Inclination

The inclination of the neutral axis can be evaluated by considering its relationship with the bending moment in the shaft, in the principal coordinate system.

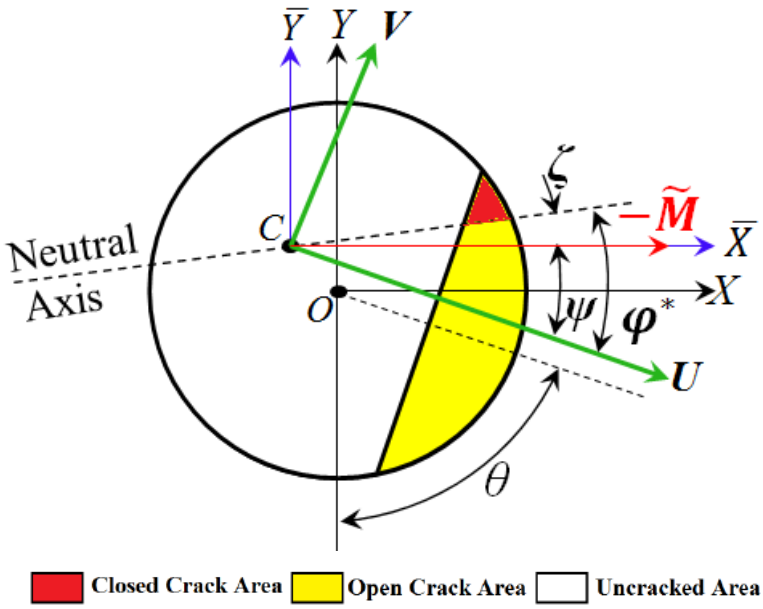

Figure 5-19: Neutral axis inclination is related to the orientation of the principal axis relative to the applied bending moment

In Figure 5-19, the bending moment $\tilde{M}$ is horizontal and acts through the centroid of the shaft section. Angle ψ is the inclination of the bending moment measured from the first principal axis U. Angle φ^* is the inclination of the neutral axis measured from the first principal axis. The engineer's theory of bending gives the relationship between ψ and φ^* described in Equation (5-56).

$$\varphi^* = \tan^{-1}\left(\frac{I_U}{I_V}\tan(-\psi)\right) \tag{5-66}$$

Note that in the above state, and any other partial breathing state for rotation angles where $\varphi^* < \pi$, angle ψ will have a negative value. To ensure that φ^* is a positive value, the negative sign is placed before ψ. The inclination of the neutral axis ξ measured from the positive $\bar{X}$ axis is described in Equation (5-67).

$$\xi = \varphi^* - (-\psi) \tag{5-67}$$

A negative sign is placed in front of ψ to ensure that ξ has a positive value. Substituting the expression for φ^* yields the following equation for ξ in terms of the principal area moment of inertia and the orientation of the principal coordinate axes as described in Equation (5-68).

$$\xi = \tan^{-1}\left(\frac{I_U}{I_V}\tan(-\psi)\right) + \psi \qquad (5\text{-}68)$$

The inclination of the neutral axis ξ can now be calculated by using Equation (5-68). Where I_U and I_V are the principal area moments of inertia for the entire section and can now be calculated by using Equations (5-61) and (5-62) respectively. ψ is the orientation of the principal axes w.r.t the centroid coordinate axes given by Equation (5-63).

Comparison of neutral axis inclination between the proposed model, the adopted model (Al-Shudeifat and Butcher, 2011) and the 3D FEA model is shown in Figure 5-20. The inclination of the neutral axis evaluation method for the 3D FEA model is described in Section 3.6.2 of Chapter 3. The adopted model (Al-Shudeifat and Butcher, 2011) considered the cracked shafts will only experience symmetrical bending, and so, the neutral axis will be always horizontal.

The graph shown in Figure 5-20 clearly demonstrates one of the central theses of this work, that the neutral axis of bending is not necessarily collinear with the bending moment vector at the crack location. It can be observed that for very deep cracks (μ = 1.0), the neutral axis can be inclined by up to 30° w.r.t the bending moment. It is this inclination of the neutral axis that causes the closed area of the crack to be overestimated by the Al-Shudeifat and Butcher (2011) method, which is clearly shown in Figure 5-21, and, in turn, the shaft's time averaged bending stiffness to be overstated.

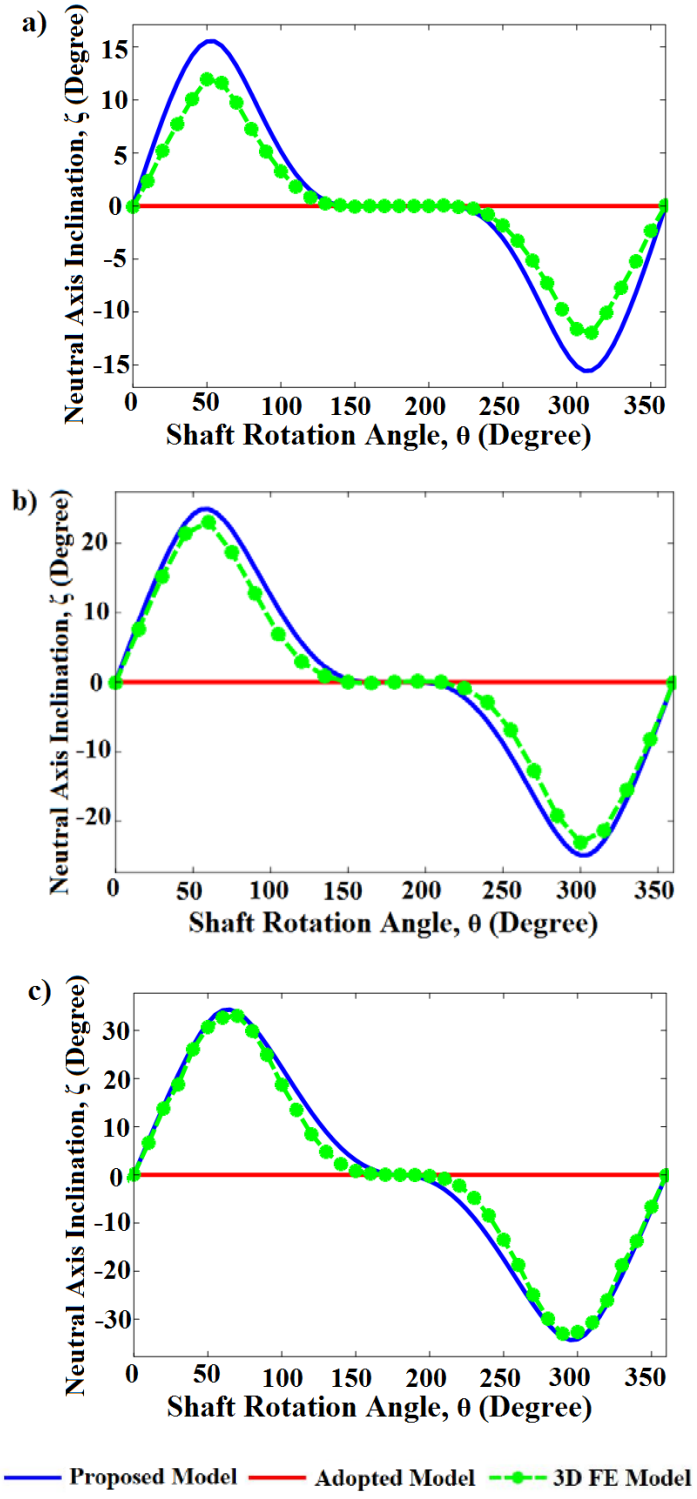

Figure 5-20: Comparison of neutral axis inclination for crack depth ratios: (a) μ = 0.5, (b) μ = 0.75 and (c) μ = 1.0

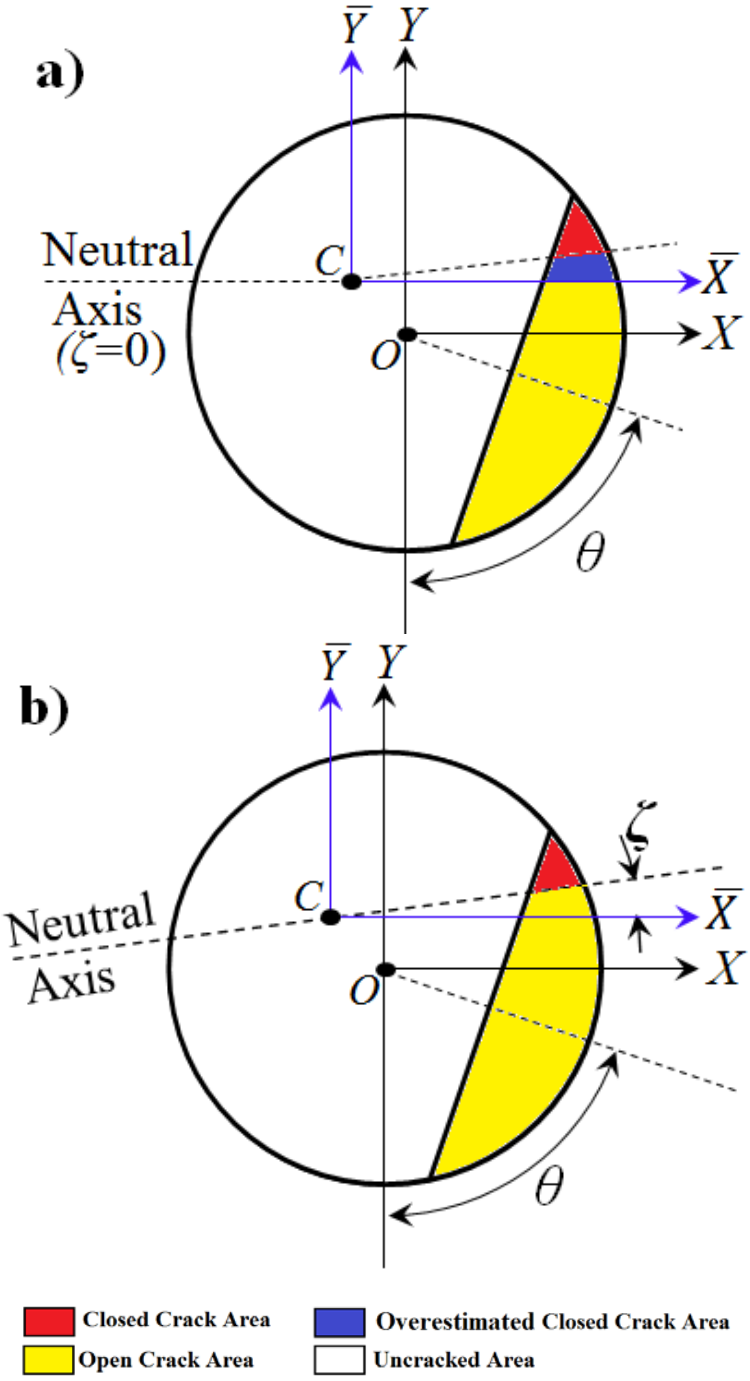

Figure 5-21: Comparison of neutral axis inclination between (a) adopted model and (b) proposed model

5.6 Analysis of Second Area Moment of Inertia

Studying the change in the area moment of inertia of a cracked shaft can link the breathing mechanism to the stiffness matrix in the rotor and ultimately aid in calculating the vibration responses. In this section, the area moment of inertia of a cracked shaft is analysed using the values of effectual bending angle, φ, calculated by the newly developed Equation (3-7), and equations developed in this chapter. An initial estimate for both the centroid location and the neutral axis rotation is used to evaluate the closed area of the crack. The centroid coordinates are then re-evaluated, with greater accuracy than the initial estimate. The process is repeated until stability in the centroid coordinates is achieved. At this point, the second area moment are evaluated and the rotation of the neutral axis is determined, again with greater accuracy than the initial estimate. The centroid coordinates are then recalculated iteratively. Eventually, a stable value for the centroid coordinates and the neutral axis rotation is achieved and the second area moment are accurately determined. A script written in MATLAB is used to implement the described procedure. The program flow chart is shown in Figure 5-22, and the full MATLAB script is presented in the Appendix.

The breathing response of fatigue cracks predicted by the proposed method was validated using 3D FEA simulations in Chapter 4. The simulations provided data to plot the relationship between percentages of the opening of a crack and the shaft rotation angle. The data were superimposed on graphs comparing the percentages of the opening of a crack as predicted by the proposed breathing equations and that predicted by the adopted equations from Al-Shudeifat and Butcher (2011). Improved accuracy in the predicted crack breathing was observed when using the proposed method.

The comparison of the second area moment of inertia at the cracked cross-section of the unbalance shaft about centroid axes between the new proposed improved unbalance model and the unbalance model (in Section 3.5 of Chapter 3) is shown in Figure 5-23, Table 5-2 and Table 5-3. It is observed that in the unbalance model, $I_{\bar{X}}$ up to 6.65% need to be overestimated and $I_{\bar{Y}}$ up to 19.15% need to be underestimated.

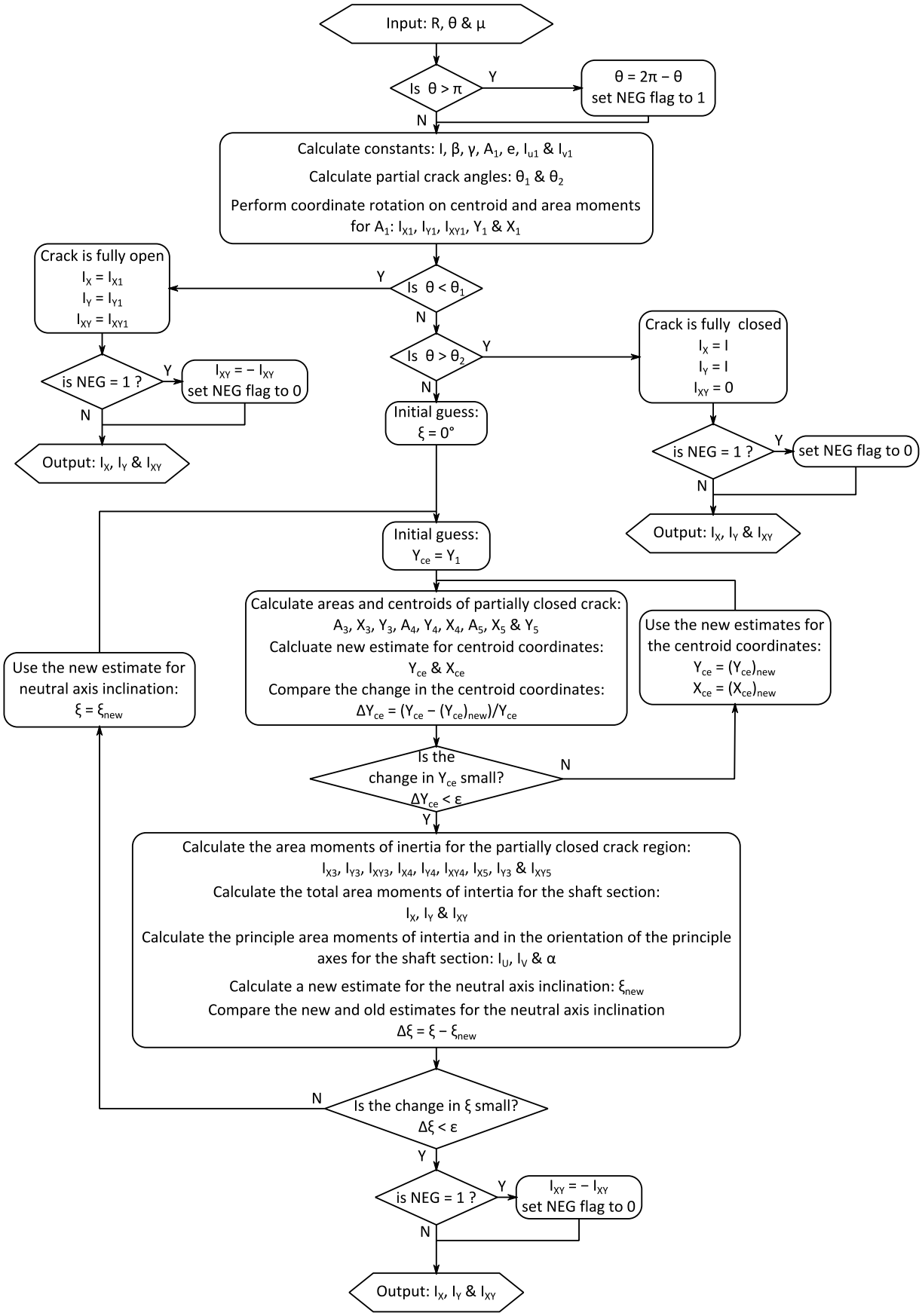

Figure 5-22: Program for the MATLAB script to evaluate area moment of inertia

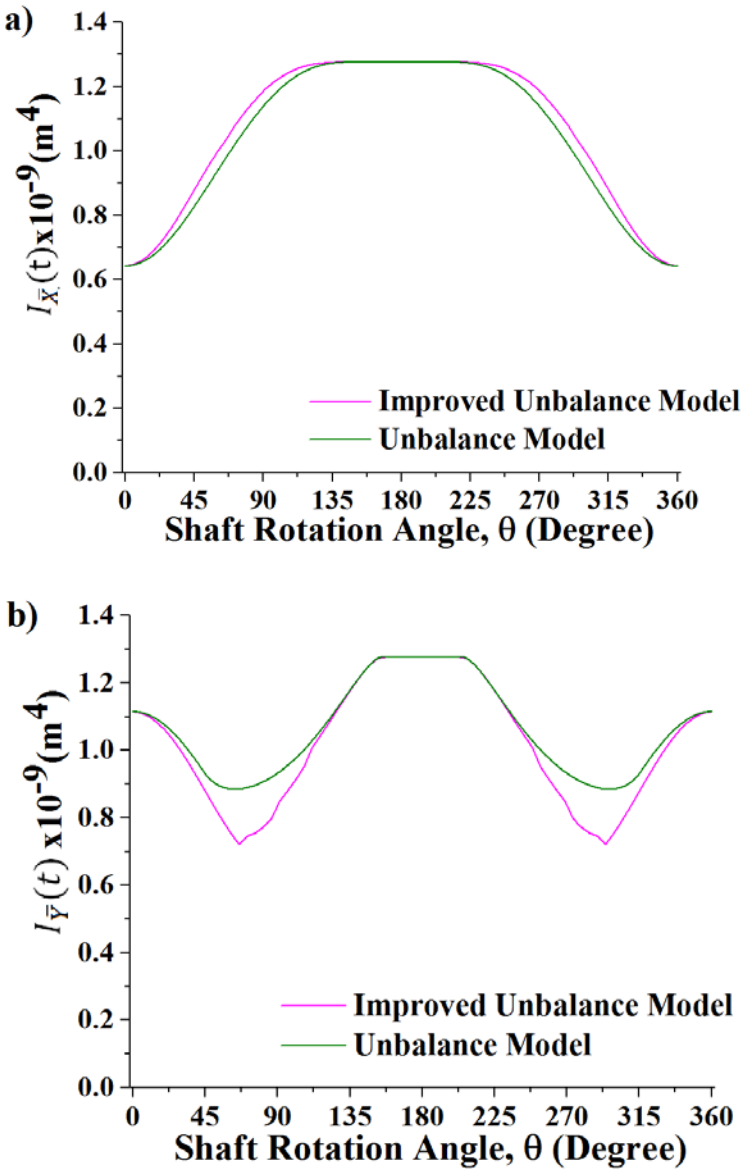

Figure 5-23: Comparison of the second area moment of inertia at the cracked cross-section of the unbalance shaft about centroid axes

Table 5-2: Comparison of $I_{\bar{X}}$ between the proposed improved unbalance model and the unbalance model (in Section 3.5, Chapter 3)

Shaft Rotation Angle, θ (°)	Proposed Improved Unbalance Model $I_{\bar{X}} \times 10^{-9}(m^4)$	Unbalance Model $I_{\bar{X}} \times 10^{-9}(m^4)$	Percentages of Difference
0	0.643	0.643	0
10	0.657	0.653	0.61
20	0.699	0.684	2.28
30	0.764	0.732	4.2
40	0.843	0.793	5.83
50	0.926	0.864	6.65
60	1.003	0.939	6.43
70	1.076	1.016	5.58
80	1.139	1.079	5.3
90	1.193	1.145	3.96
100	1.23	1.192	3.08
110	1.256	1.232	1.88
120	1.269	1.257	0.98
130	1.275	1.271	0.31
140	1.277	1.276	0.04
150	1.277	1.277	0
160	1.277	1.277	0
170	1.277	1.277	0
180	1.277	1.277	0

Table 5-3: Comparison of $I_{\bar{Y}}$ between the proposed improved unbalance model and the unbalance model (in Section 3.5, Chapter 3)

Shaft Rotation Angle, θ (°)	Proposed Improved Unbalance Model $I_{\bar{Y}} \times 10^{-9}(m^4)$	Unbalance Model $I_{\bar{Y}} \times 10^{-9}(m^4)$	Percentages of Difference
0	1.115	1.115	0
10	1.101	1.105	−0.36
20	1.059	1.074	−1.5
30	0.994	1.026	−3.22
40	0.915	0.965	−5.37
50	0.832	0.906	−8.87
60	0.755	0.886	−17.39
70	0.746	0.888	−19.15
80	0.773	0.905	−17.12
90	0.849	0.933	−9.81
100	0.915	0.979	−7.04
110	1.009	1.025	−1.54
120	1.08	1.081	−0.09
130	1.154	1.149	0.49
140	1.224	1.216	0.67
150	1.273	1.272	0.1
160	1.277	1.277	0
170	1.277	1.277	0
180	1.277	1.277	0

The second area moment of inertia at the cracked cross-section of the balance and unbalance shafts under different weight–unbalance force ratios at different crack locations as a shaft angle of rotation about centroid axes are plotted in Figure 5-24 to Figure 5-31 using the newly developed equations. The second area moment for the cracked section are shown as functions of the shaft rotation angle for various crack depths at different crack locations (Figure 5-24 to Figure 5-31). It is found dependent on the shaft's rotation angle and the closed area of the crack. The closed area of the crack is a function of the shaft bending direction at the crack location. The results are largely intuitive in that for deep cracks, there is a greater reduction in the second area moment when the crack is open.

Similar to the effectual bending angle, the status of the cracks and percentage of opening results, the area moment of inertia also has special behaviours at four crack

locations. It should be noted that at $\lambda = 0.2$, the area moment of inertia about the nonrotating centroid axes is just a horizontal line indicating a fully-closed-never-opened crack and is independent of the force ratio (see Figure 5-30).

At $\lambda = 0.8$, a sinewave is observed indicating a fully opened crack also independent of the force ratio (see Figure 5-30). Further, the area moment of inertia for the unbalance shaft at $\lambda = 0.3$ and $\lambda = 0.833$ are the same as for the balance shaft (compared between Figure 5-24, Figure 5-25 and Figure 5-31). The area moment of inertia about the nonrotating centroid axes at other locations are relatively more complex shapes depending on the crack location and force ratio.

Interestingly, $I_{\bar{Y}}$ could be larger for a fully open crack than for a partially open/closed crack. Further, a variation of $I_{\bar{Y}}$ with shaft rotational angle, θ, differs from that of $I_{\bar{X}}$ showing dual minimum behaviour, as shown in Figure 5-27 and Figure 5-28.

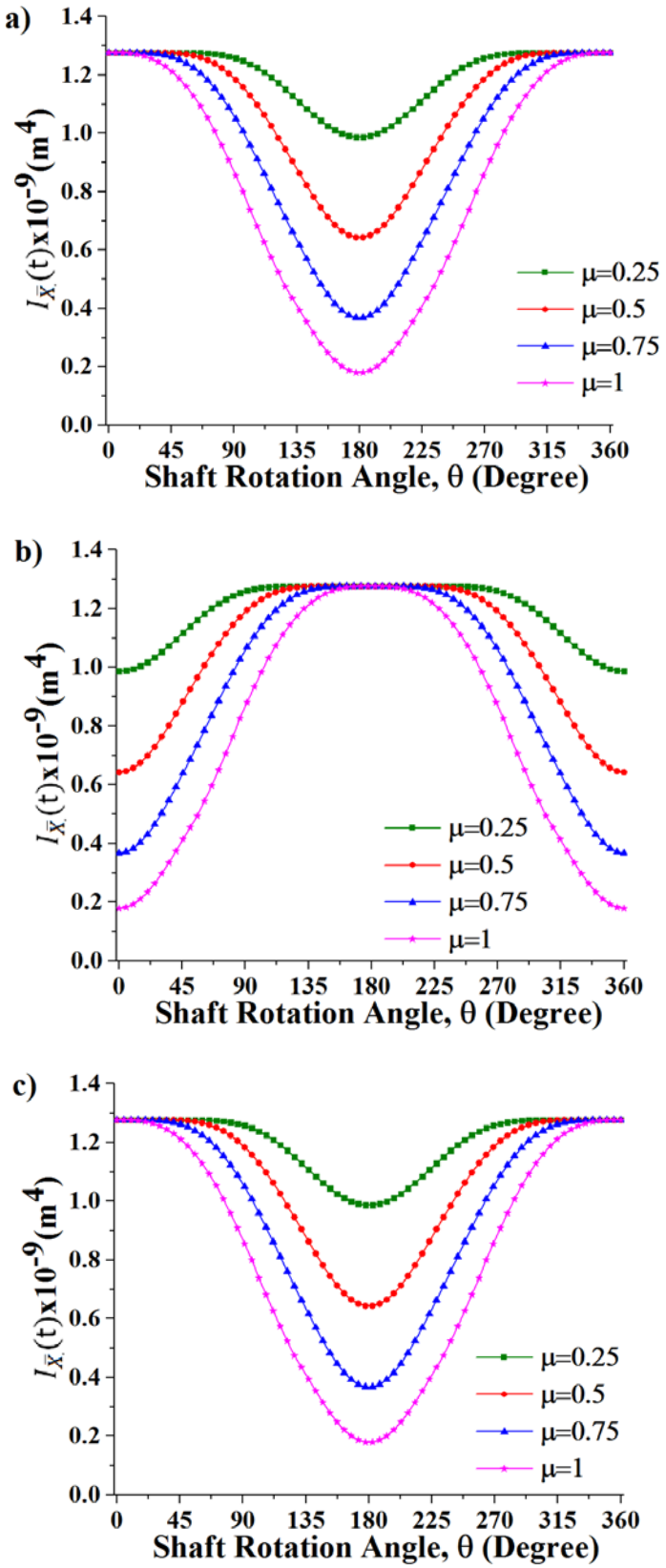

Figure 5-24: Area moment of inertia of $\boldsymbol{I_{\bar{X}}}$ of the balance shaft crack cross-section closed area over a full shaft rotation, θ, different crack depth ratios, μ, at crack locations (a) λ = 0.15, (b) λ = 0.5 and (c) λ = 0.85

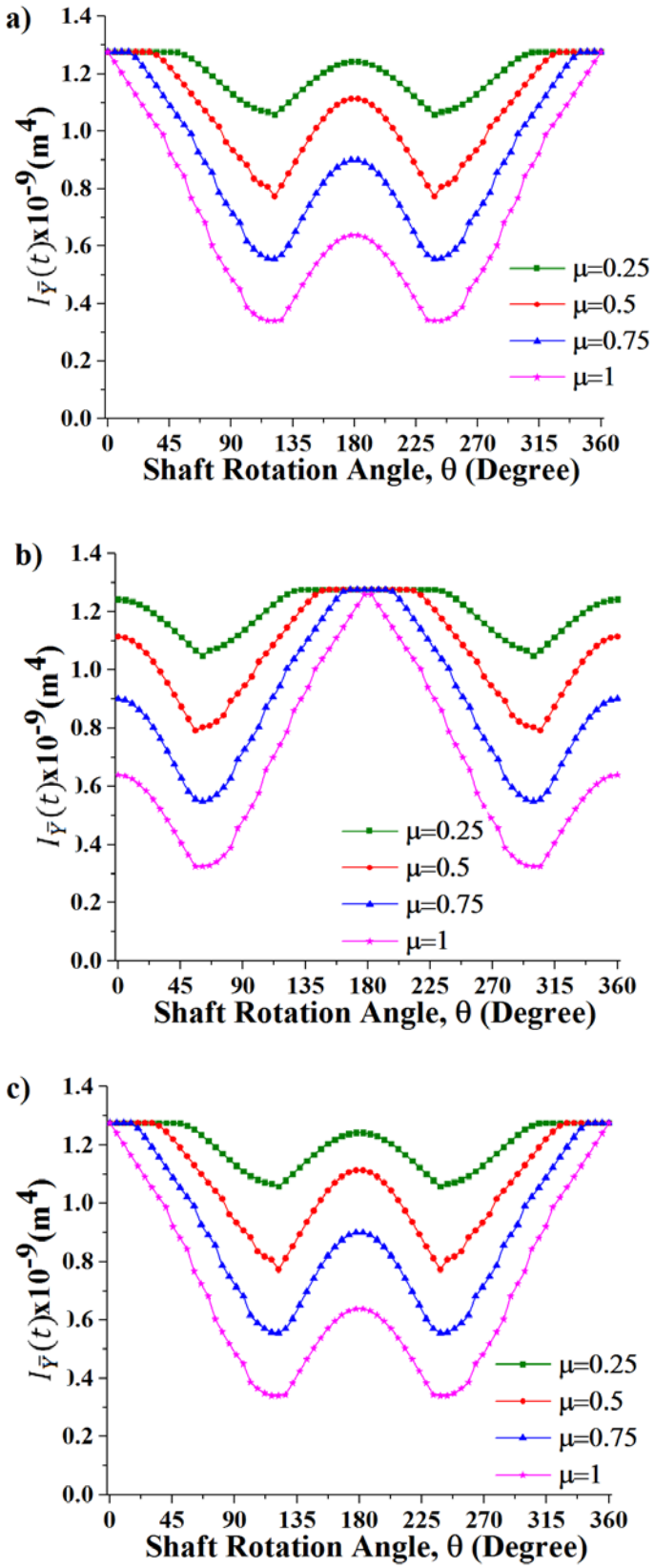

Figure 5-25: Area moment of inertia of $\boldsymbol{I_{\bar{Y}}}$ of the balance shaft crack cross-section closed area , $\boldsymbol{A_{ce}(t)}$, over a full shaft rotation, θ, different crack depth ratios, μ, at crack locations (a) λ = 0.15, (b) λ = 0.5 and (c) λ = 0.85

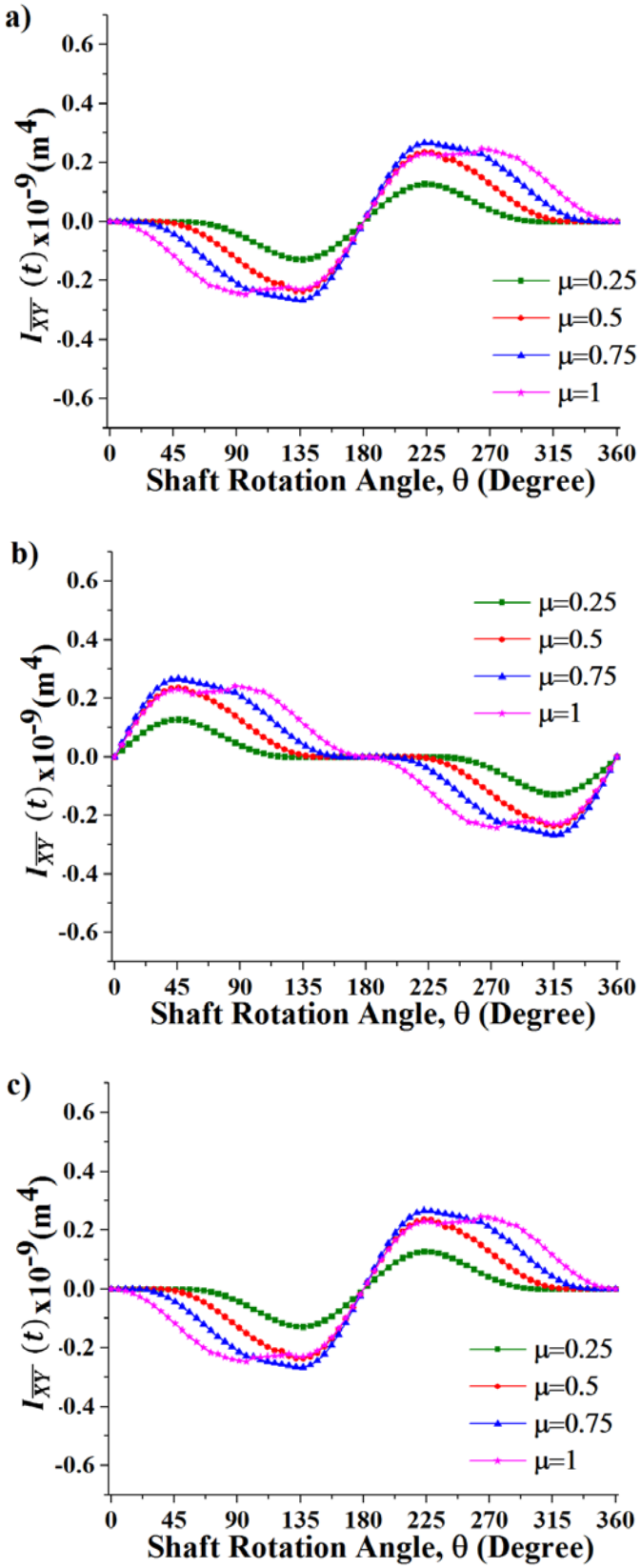

Figure 5-26: Area moment of inertia of $I_{\overline{XY}}$ of the balance shaft crack cross-section closed area , $A_{ce}(t)$, over a full shaft rotation, θ, different crack depth ratios, μ, at crack locations (a) λ = 0.15, (b) λ = 0.5 and (c) λ = 0.85

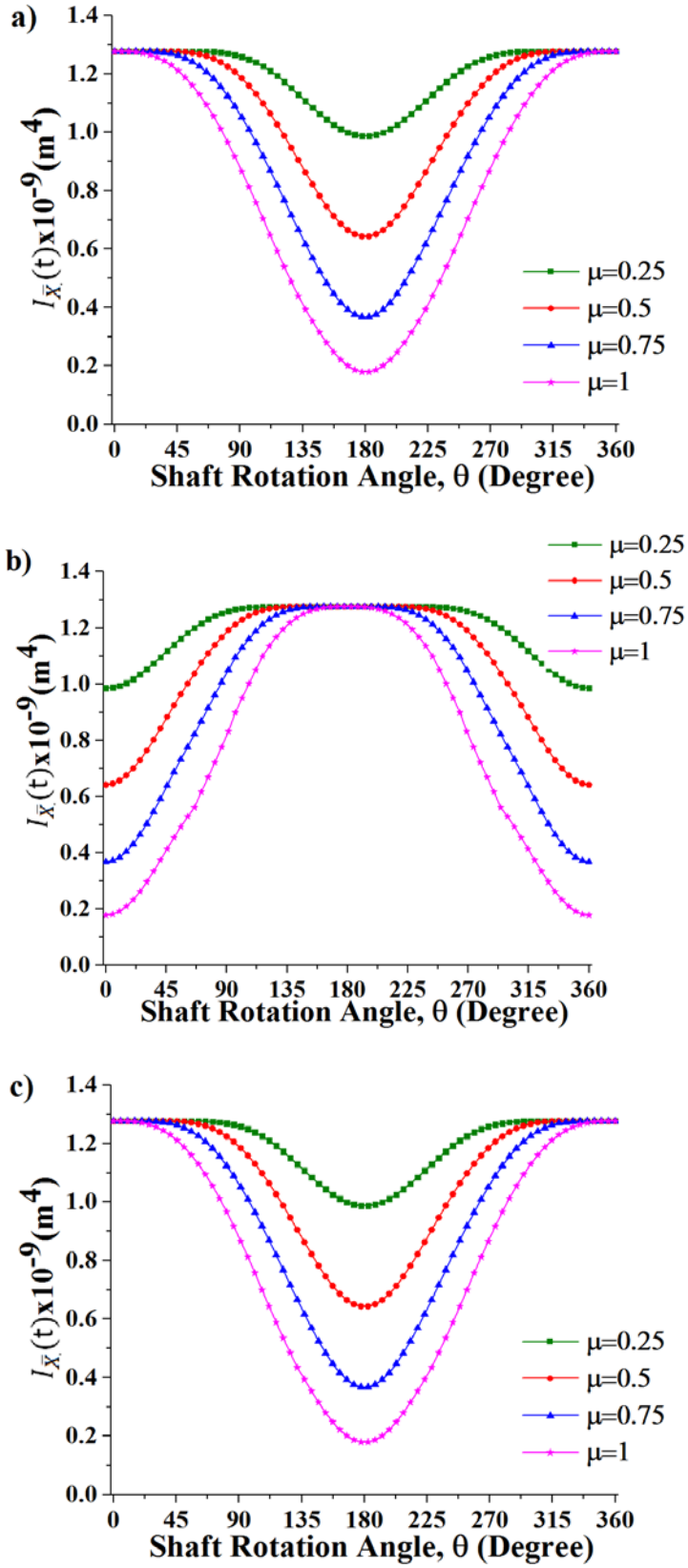

Figure 5-27: Area moment of inertia of $\boldsymbol{I_{\bar{X}}}$ unbalance shaft (η = 5 & β = 0°) crack cross-section closed area, $\boldsymbol{A_{ce}(t)}$, over a full shaft rotation, θ, different crack depth ratios, μ, at crack locations (a) λ = 0.15, (b) λ = 0.5 and (c) λ = 0.85

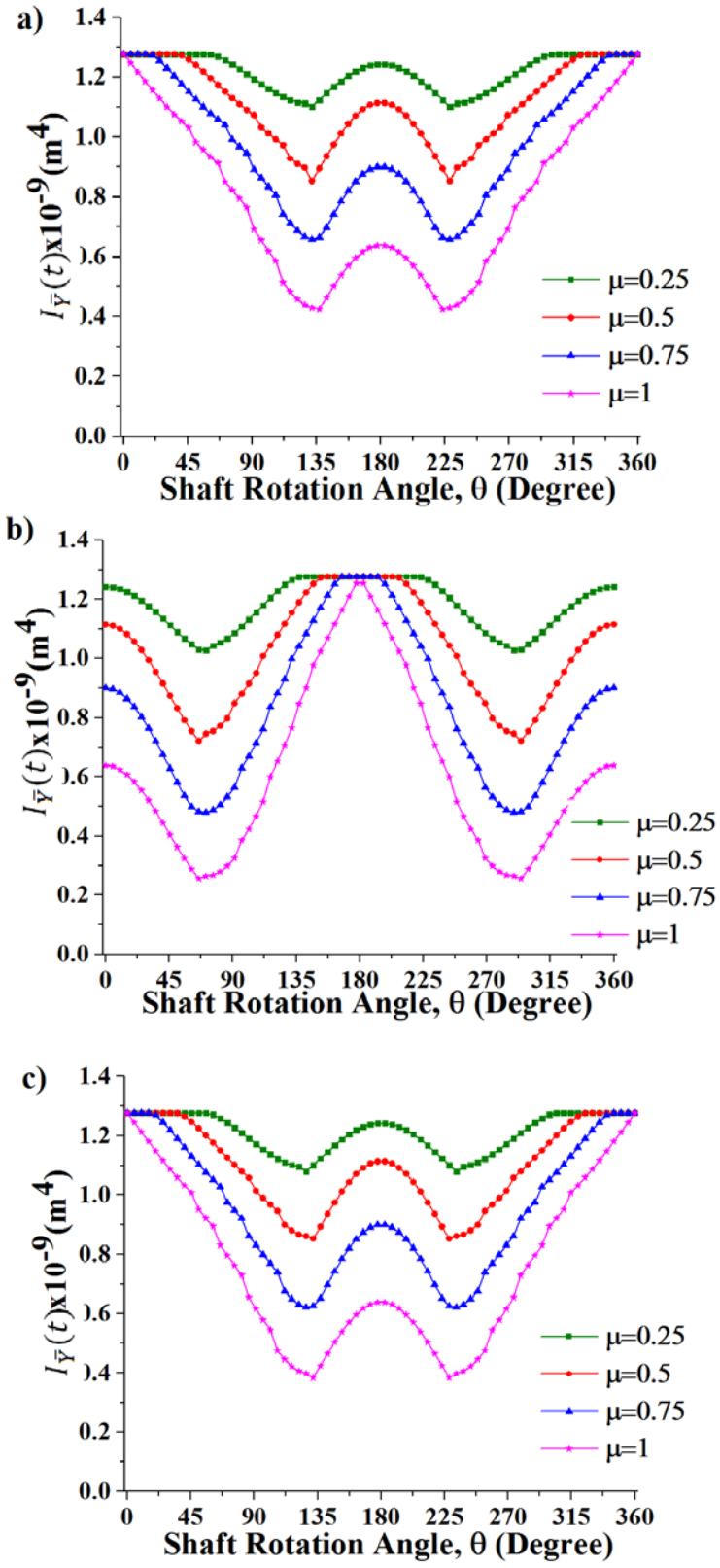

Figure 5-28: Area moment of inertia of $\boldsymbol{I_{\bar{Y}}}$ of unbalance shaft (η = 5 & β = 0°) crack cross-section closed area , $\boldsymbol{A_{ce}(t)}$, over a full shaft rotation, θ, different crack depth ratios, μ, at crack locations (a) λ = 0.15, (b) λ = 0.5 and (c) λ = 0.85

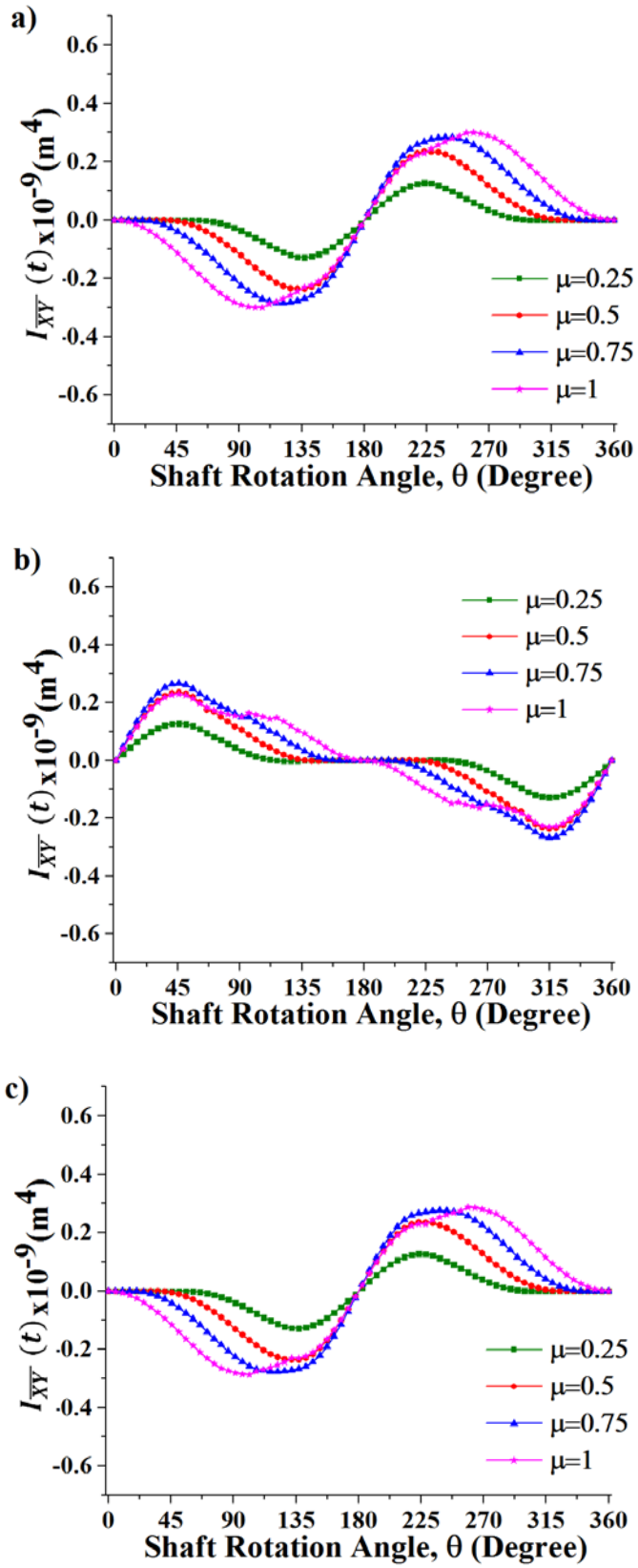

Figure 5-29: Area moment of inertia of $\boldsymbol{I_{\overline{XY}}}$ of unbalance shaft (η = 5 & β = 0°) crack cross-section closed area , $\boldsymbol{A_{ce}(t)}$, over a full shaft rotation, θ, different crack depth ratios, μ, at crack locations (a) λ = 0.15, (b) λ = 0.5 and (c) λ = 0.85

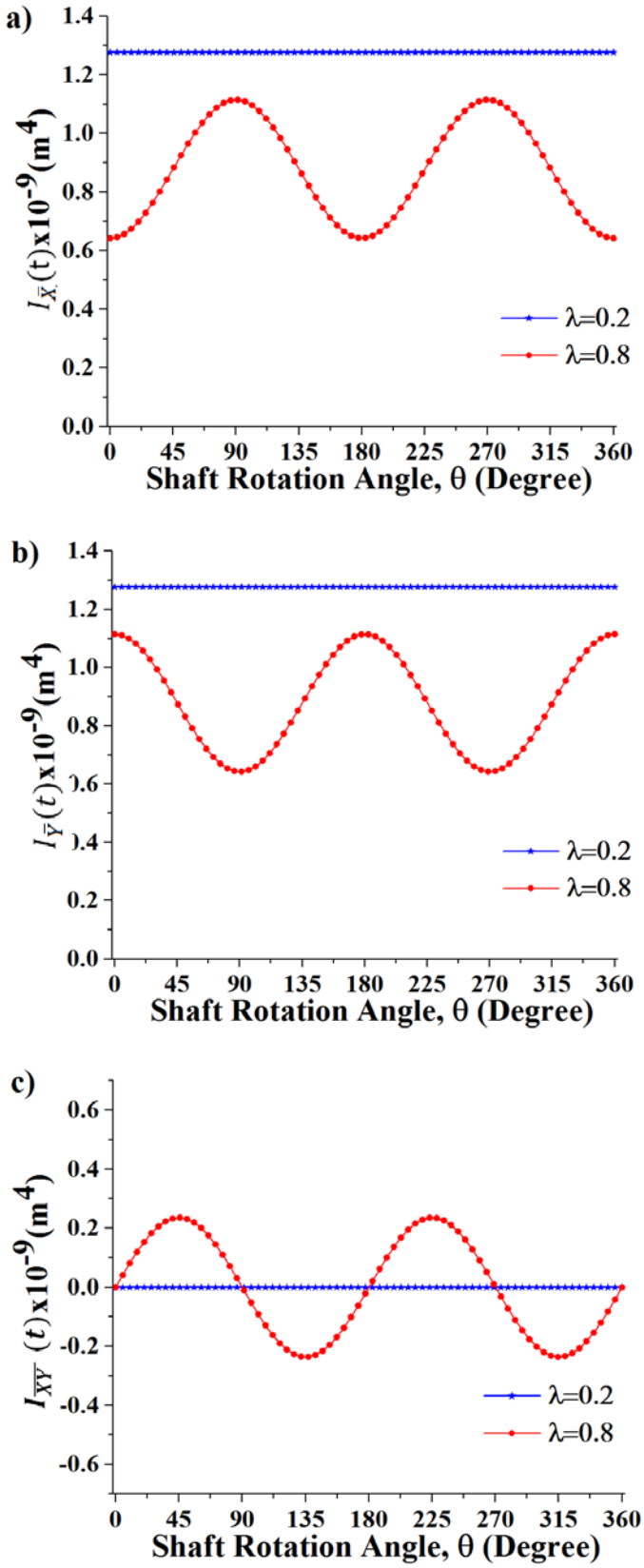

Figure 5-30: Area moment of inertia of the unbalance shaft (η = 5 & β = 0°) crack cross-section closed area , $\boldsymbol{A_{ce}(t)}$, at crack locations 0.2 and 0.8 about (a) $\boldsymbol{I_{\bar{X}}}$, (b) $\boldsymbol{I_{\bar{Y}}}$ and (c) $\boldsymbol{I_{\overline{XY}}}$

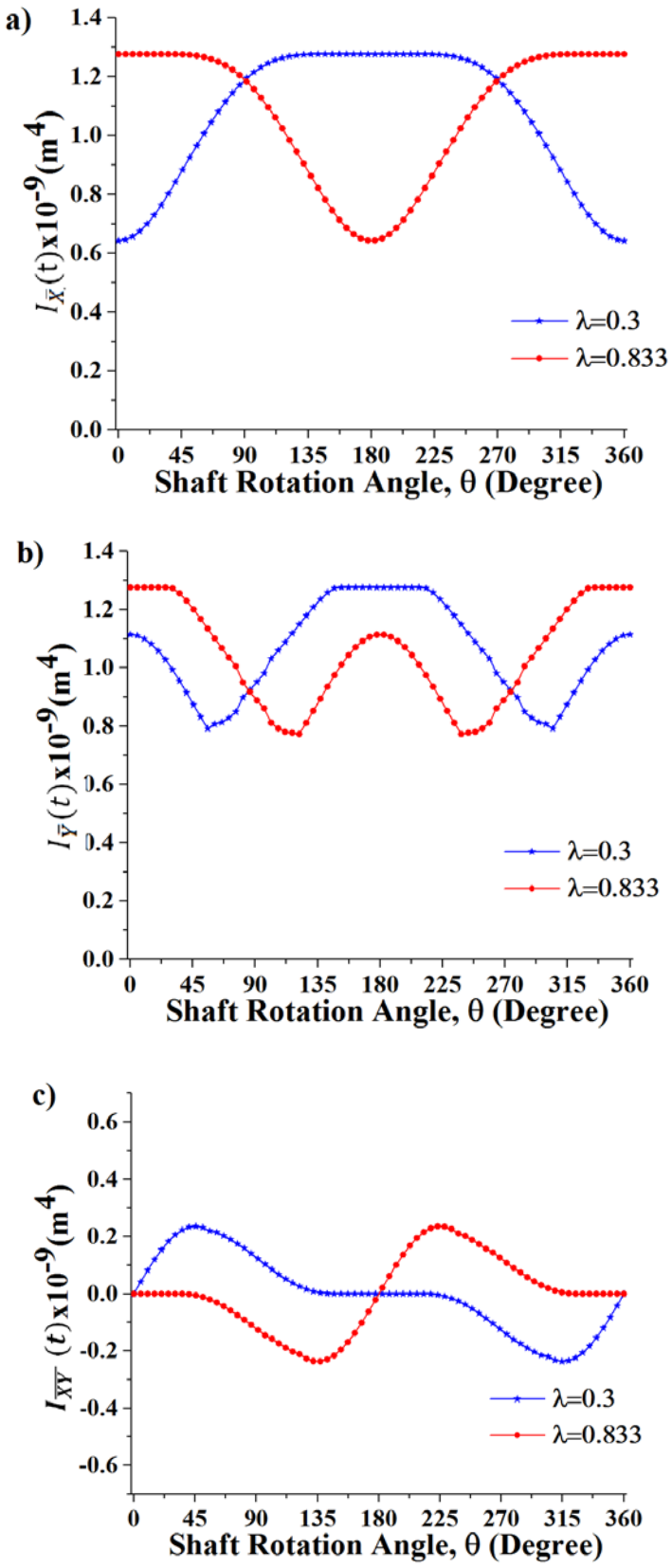

Figure 5-31: Area moment of inertia of the unbalance shaft (η = 5 & β = 0°) crack cross-section closed area, $\boldsymbol{A_{ce}(t)}$, at crack locations 0.3 and 0.833 about (a) $\boldsymbol{I_{\bar{X}}}$, (b) $\boldsymbol{I_{\bar{Y}}}$ and (c) $\boldsymbol{I_{\overline{XY}}}$

5.7 Summary

Cracked rotor dynamics is an active area of research with a considerable amount of studies directed towards solving the problem of detecting fatigue cracks in a rotating machine from its vibration characteristics. Much of this research is currently confined to the challenge of mathematically describing the mechanical behaviour of cracked shafts. In this chapter, one of the most popular methods of mathematical crack modelling was reworked to improve its accuracy.

The mathematics of calculating the mechanical properties of the cross-sections, namely, the second area moment and centroid location, were improved in this chapter by removing the assumption of collinearity between the bending moment and neutral axis at the crack location. An algorithm composed of a nest of iterative calculations was used to evaluate the second area moment as a function of the crack locations and shaft's angle of rotation about centroid axes. It was found highly dependent on crack location, similar to crack breathing behaviours.

Chapter 6 : Breathing of Slant Crack

6.1 Introduction

In this chapter, the breathing mechanism of a transverse slant crack is investigated through the FEM analysis, which has been widely adopted in the published literature. A slant crack is a common shaft crack formed by repeated torsional loads along with instantaneous bending/buckling in a rotating rotor (Bachschmid et al., 2010). First, a two-disc rotor model with a fixed shaft end is simulated to investigate the crack breathing mechanism under the coupling influence of unbalance force and rotor weight. A full 3D rotor model is simulated with slant crack and unbalance mass. Then, the crack breathing behaviours are visualised by analysing the crack status and the variation of the crack closed area and represented quantitatively by the percentage of the closing of the crack. Finally, to examine the effects of the slant crack on the dynamic response of a cracked rotor, the shaft orbits at different crack locations are analysed using Abaqus Steady-State Dynamics, Direct.

6.2 Modelling of Cracked Rotor System

6.2.1 Slant crack modelling

A transverse slant crack with crack depth h and inclined angle α to the cross-section of the shaft is considered in the analysis as shown in Figure 6-1. The crack section is generated by joining two shafts together using the Abaqus 'Tie constraint' function, which constitutes the intact part of the cracked section. Both normal and tangential properties of crack surfaces are defined in the finite element numerical model by contact interaction. The 'hard' contact is selected for the normal property to avoid penetration between the crack surfaces when the crack is closed. The chosen tangential property, 'rough' friction, generates an infinite friction coefficient. Consequently, the relative sliding between two crack surfaces is avoided. The simulation details for the crack cross-section are displayed in Figure 6-2. The upper part is the intact section while the lower area corresponds to the cracked section.

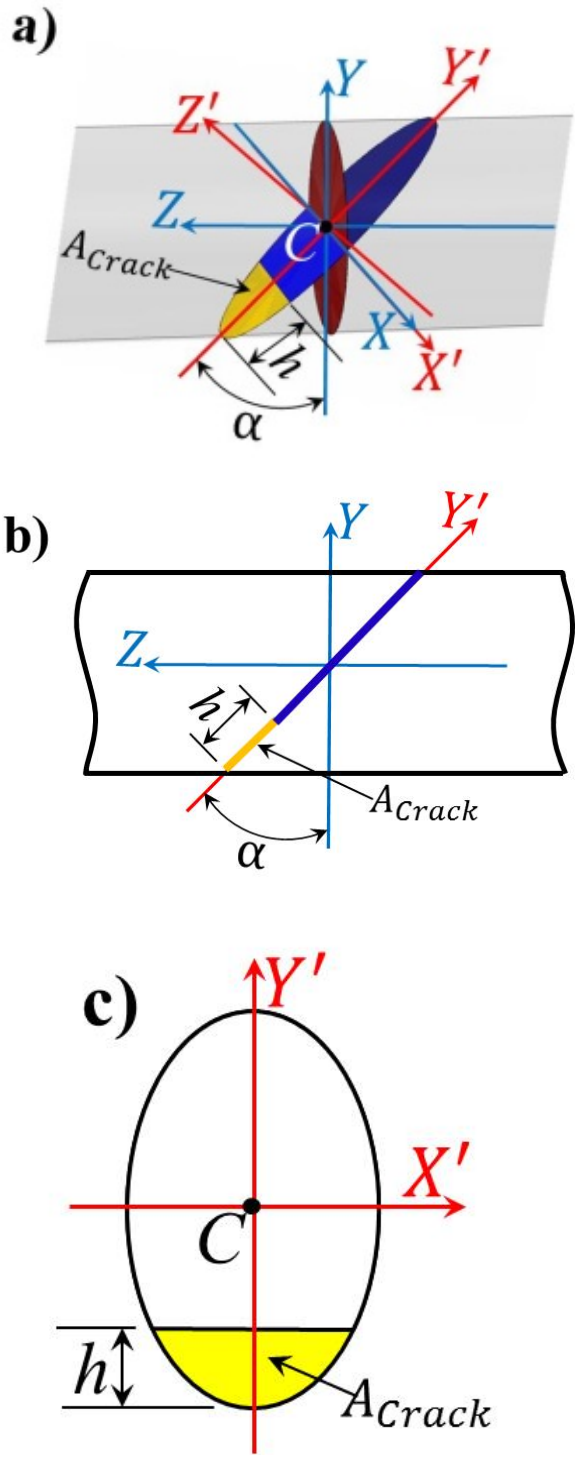

Figure 6-1: Slant crack: (a) orientation (b) front view and (c) crack plane

A slant crack with depth, h = 0.5R, where R is the shaft radius, and inclined angle α = 45° is simulated. The shaft is rotated anticlockwise, and the crack has an original direction along the negative Y'-axis. The following configurations of crack location and angular position are considered:

1. 40 different crack locations along the shaft length varying from 0 to L with an increment of $0.025L$, where L is the total shaft length
2. 24 different angular positions of the crack or shaft rotational angles, θ, varying from 0^o to 360^o with an increment of 15^o.

6.2.2 Mesh sensitivity analyses

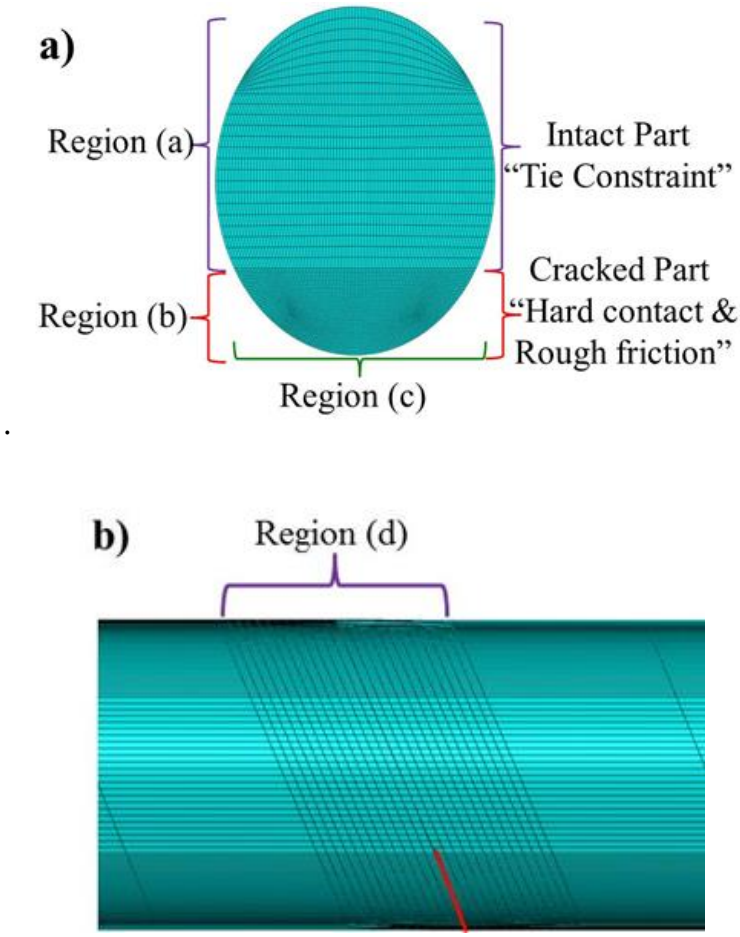

Figure 6-2: Simulation details for the crack cross-section and mesh around the crack in (a) transversal and (b) longitudinal directions

The shaft is meshed by using an element named linear hexahedral element of type C3D8R. As shown in Figure 6-2, the mesh density is much higher around the crack in both directions. The mesh size is obtained after a convergence test of the results through mesh sensitivity analyses. The convergence test results for the balance case at crack location $0.5L$ and $\theta = 90°$ are presented in Table 6-1. It is observed that the closing percentage converges after the numbers of mesh in four regions (a, b, c and d) reach 24, 36, 110 and 24. The percentage of closing is described later in detail.

Table 6-1: Slant crack mesh sensitivity analyses

Test Cases	Number of Elements	Percentage of Closing
1	a:12; b:24; c:50 & d:12	8.96
2	a:14; b:26; c:60 & d:14	15.64
3	a:16; b:28; c:70 & d:16	22.12
4	a:18; b:30; c:80 & d:18	25.45
5	a:20; b:32; c:90 & d:20	28.25
6	a:22; b:34; c:100 & d:22	29.73
7 (Selected)	a:24; b:36; c:110 & d:24	30.33
8	a:26; b:38; c:120 & d:26	30.33

6.2.3 Unbalance force modelling

The unbalance force is considered a rotational force F_{un} owing to additional mass m_u at radial distance d from the centre of the shaft when the shaft rotates at ω rad/sec. The direction of the rotational unbalance force is $(\theta + \beta)$, where θ is the shaft rotation angle, and β is the fixed angular position relative to the crack direction as shown in Figure 6-3; it is considered that the unbalance force is located on the right-side disk (see Figure 6-4). In the simulation, the following unbalance configurations are considered:

1. 5 different ratios of unbalance force to the rotor weight (two disks and shaft), that is, η = 5, 10, 20, 100 and ∞ (balance)
2. 5 different angular positions of unbalance force, β = 0^o, 45^o, 90^o, 135^o and 180^o.

Only half of the angular range of unbalance force (0° to 180°) is considered because of the symmetry.

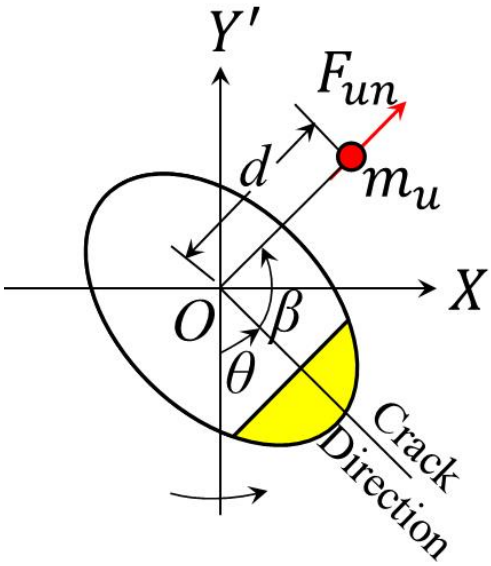

Figure 6-3: Relative orientation between unbalance force and the crack on the shaft cross-section plane

6.2.4 Loading and boundary conditions

A full 3D rotor model is simulated since rotor symmetry no longer exists in the unbalance shaft. The simulation is conducted as a series of static problems with different crack locations along the shaft length and different shaft rotation angles. The parameters of the rotor model are in Table 6-2.

Figure 6-4 shows the loading and boundary conditions of the 3D FE model. The model represents a two-disk rotor with fixed end supports. The shaft self-weight is applied as a gravitational force, and two disk weights are applied as the concentrated forces. Further, unbalance force is applied as a concentrated force in the horizontal [$F_{un}cos(\theta + \beta)$] and vertical [$F_{un}sin(\theta + \beta)$] directions of the shaft cross-section at the right disk.

Table 6-2: Parameters of the transverse slant crack model

Description	Value
Shaft Length, L	724 mm
Shaft Radius, R	6.35 mm
Density, ρ	7800 kg/m^3
Young's Modulus, E	210GPa
Poisson ratio, v	0.3
Disk mass, m_d	0.50 kg
Disk-1 location, l_1	181 mm
Disk-2 location, l_2	543 mm
Crack location, l_0	Variable
Crack depth ratio, μ	0.5
Inclined angle, α	45°

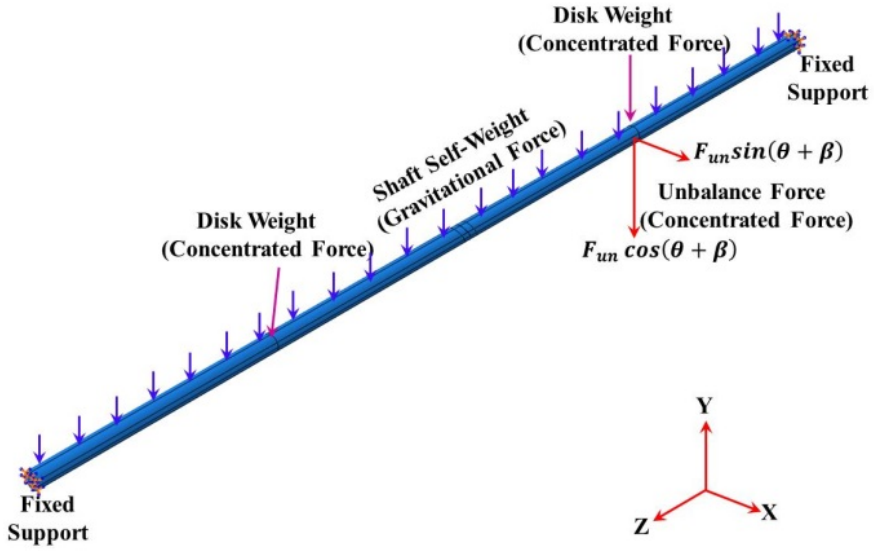

Figure 6-4: Loading and boundary conditions of the transverse slant crack model

6.3 Analysis of Slant Crack Breathing Mechanism

Crack breathing behaviours are visualised in terms of the status of the crack and the percentage of the closing of the crack. The status of the crack (open/closed/partially open/closed) is obtained directly from Abaqus field outputs by selecting Field Output Request/Contact/CSTATUS (Contact status). Crack breathing behaviours are visualised by the variation of the crack closed area and represented quantitatively by the percentage of the closing of the crack as follows:

$$\Lambda\,(\%) = \frac{A_{closed}}{A_{crack}} \times 100 \tag{6-1}$$

where A_{crack} is the fully open crack segment area as shown in Figure 6-1 and A_{closed} is the closed area of the crack during rotation (see Figure 6-5). The area of A_{closed} is obtained directly by selecting History Output Request/Contact/CAREA (Total area in contact) in Abaqus. The maximum and minimum values of Λ correspond to 100% and 0% for a fully closed crack and a completely open crack, respectively.

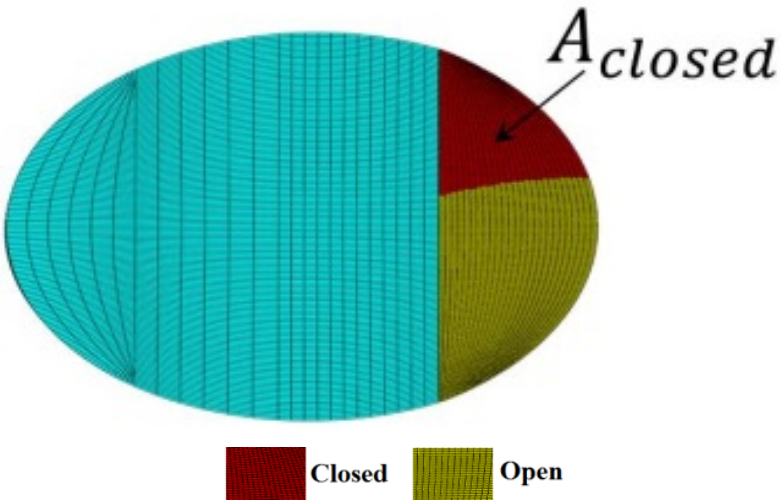

Figure 6-5: Representation of closed portion of crack segment

To verify the 'Tie constraint' crack, the specific fracture tool 'Seam' in Abaqus is also chosen to create a crack. The Seam tool duplicates the nodes at the cracked section to allow a crack to open and close during shaft rotation. The percentages of the closing of the crack using Tie constraint is compared with those obtained using the Seam tool. Figure 6-6 shows an excellent agreement between the two methods

for a crack at the middle span of the balance shaft. In this work, only the Tie constraint crack is chosen in the simulations.

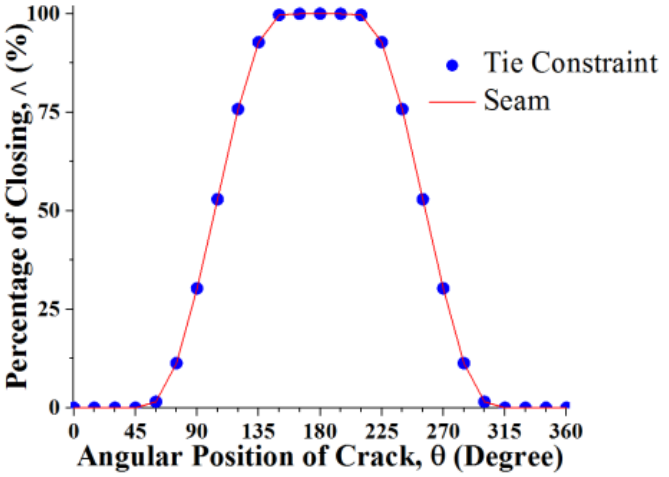

Figure 6-6: Comparison between the 'Tie Constraint' and 'Seam' crack at the middle span of the balance shaft

Figure 6-7 exemplifies the percentage of the closing of the crack as a function of crack location with varying force ratios. For the balance shaft, Λ remains constant but has sharp jumps at crack locations $0.2L$ and $0.8L$. This behaviour can be easily understood from Figure 6-8(a), where the slope of the shaft deflection curve at either $0.2L$ or $0.8L$ is 0 and shaft bending direction changes by 180° across either one of two inflection points.

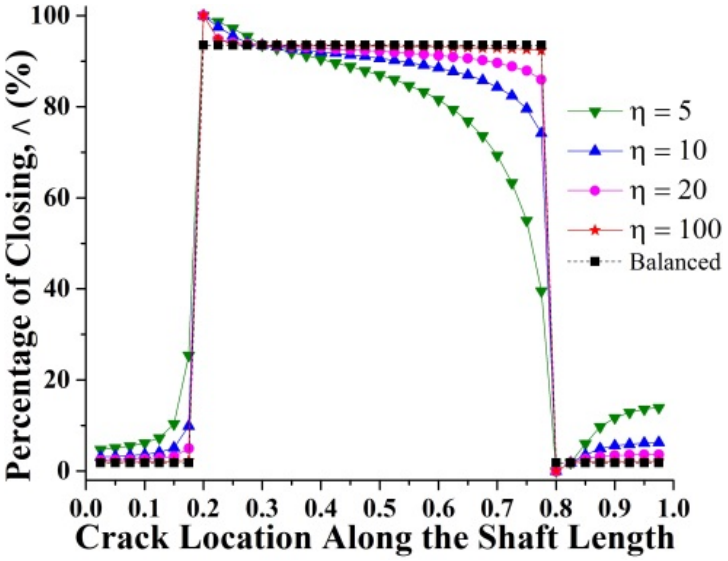

Figure 6-7: Dependence of percentage of the closing of the crack on its location with $\beta = 0°$ and $\theta = 135°$

Figure 6-9 and Figure 6-10 display the crack status and percentage of closing in the balance shaft on the crack cross-section, rotated by shaft rotational angles. It is observed that crack statuses are symmetrical about shaft rotation angle $\theta = 180°$, that is, the closed area of the crack at $\theta = 45°$ is the same as that at $\theta = 315°$. When the crack is located at $0.15L$, it experiences a sequential transition from fully closed to partially open/closed, fully open, partially open/closed and then to a fully closed status. Conversely, when the crack is located at $0.7L$, the crack changes from fully open to partially open/closed, fully closed, partially open/closed and then to fully open. However, in these two cases, the angular range of each crack status remains the same, that is, 90° in fully open status and 60° in fully closed status respectively and 210° in partially open/closed status (see Figure 6-10). Therefore, the crack breathing and stiffness of the balance cracked shaft during a full shaft rotation can be considered independent of crack location.

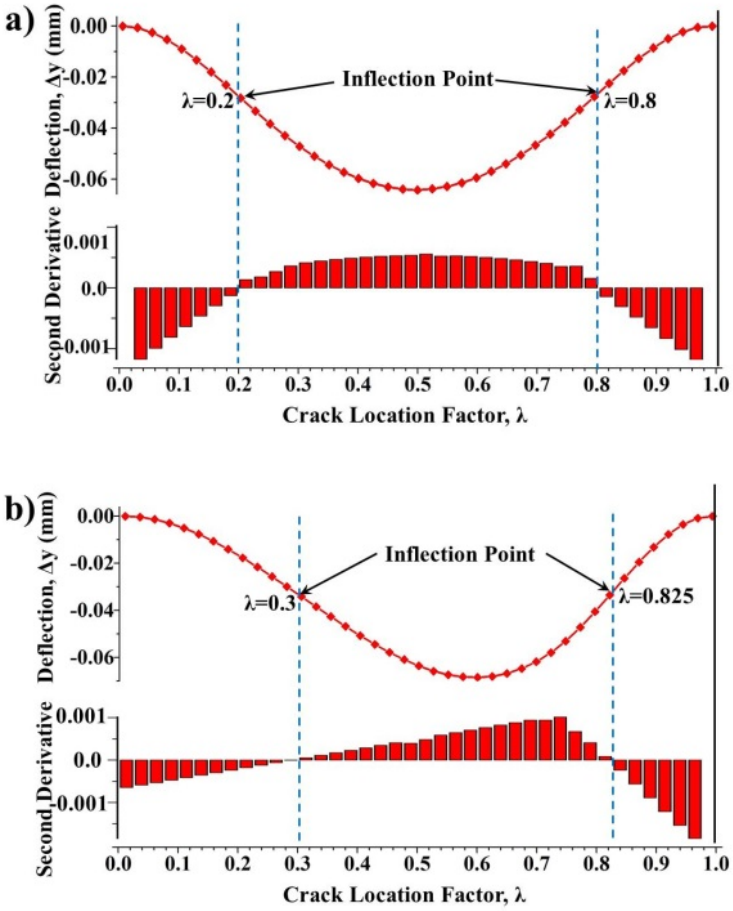

Figure 6-8: Deflection curve and second derivative of deflection curve for (a) balance shaft and (b) owing to unbalance force only ($\beta = 0°$, $\theta = 0°$)

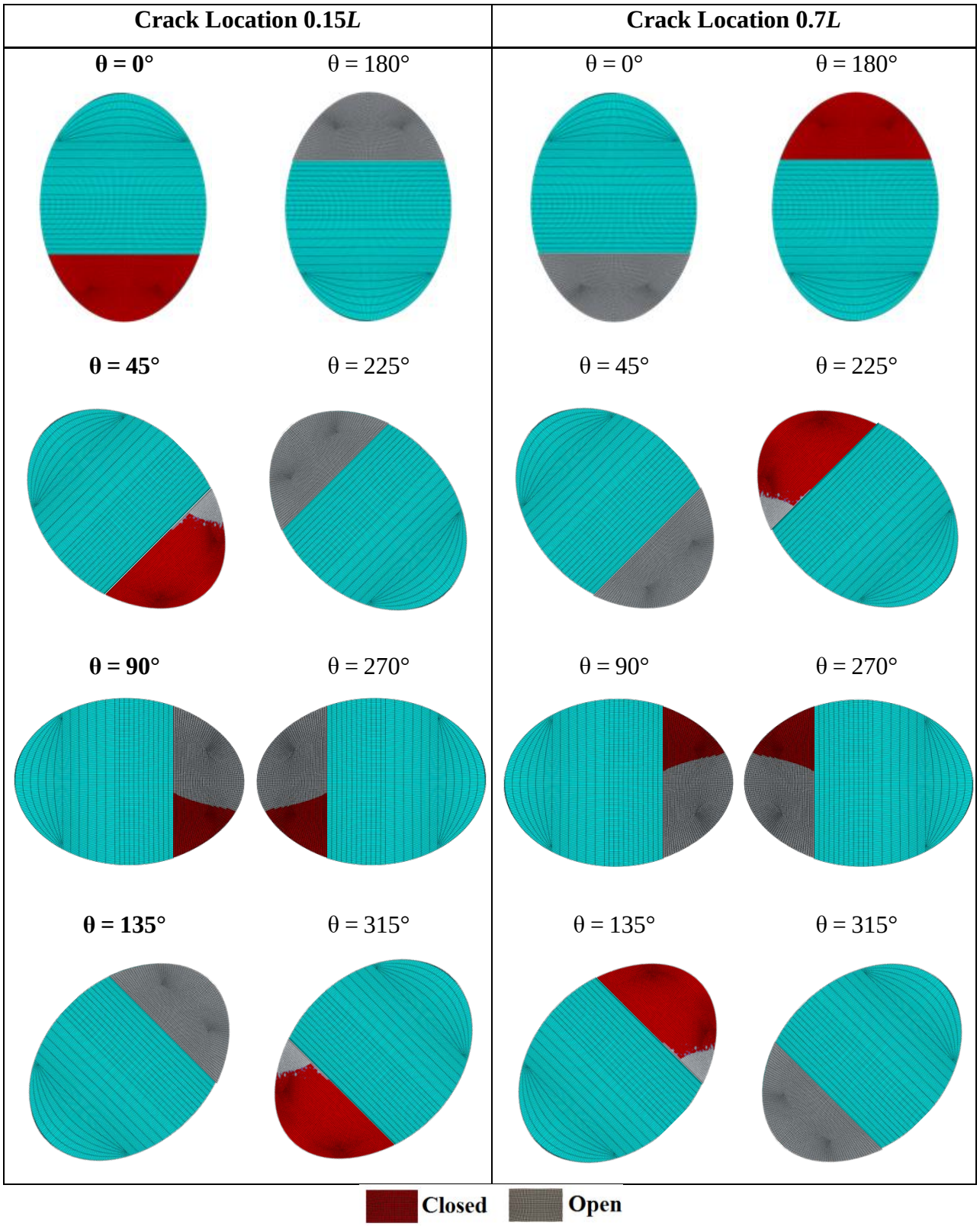

Figure 6-9: Status of the crack in the balance shaft at two selected locations 0.15*L* and 0.7*L*

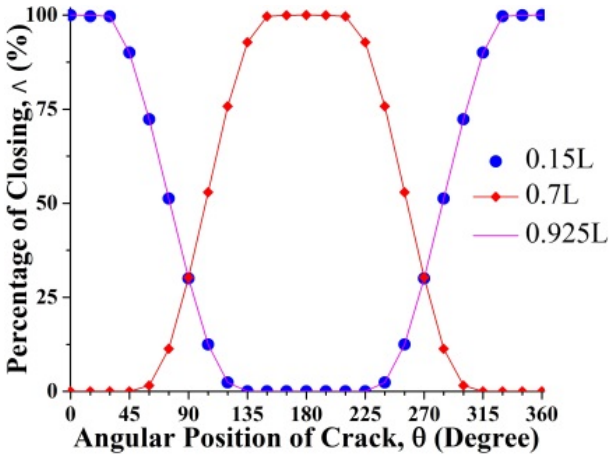

Figure 6-10: Percentage of closing of the crack for the balance shaft at 0.15*L*, 0.7*L* and 0.925*L*

For the unbalance shaft, as observed in Figure 6-7, the percentage of closing depends strongly on the crack location and force ratio. At 0.3*L* and 0.825*L*, the percentages of closing have the same values as those of the balance shaft. Further, Figure 6-11 clearly shows that the unbalance force does not affect the crack breathing and the crack breathes during shaft rotation exactly like in the balance shaft. This can be explained in Figure 6-8(b), where the unbalance force does not contribute to shaft bending at 0.3*L* and 0.825*L* and crack breathing is controlled solely by the rotor weight. Consequently, the crack starts with a fully open status at 0.3*L*, while it begins with a fully closed status at 0.825*L* (see Figure 6-11), which can also be observed in Figure 6-12. As a result, if a crack is located in these two locations, the stiffness of the unbalance shaft would be the same as that of the balance shaft.

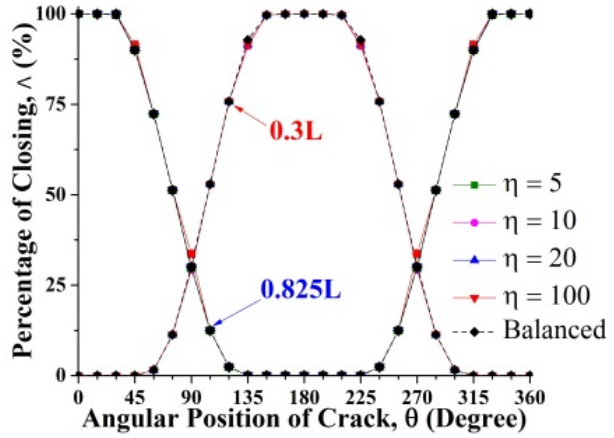

Figure 6-11: Percentage of closing of the crack with different force ratios at crack locations 0.3*L* and 0.825*L* with $\beta = 0°$

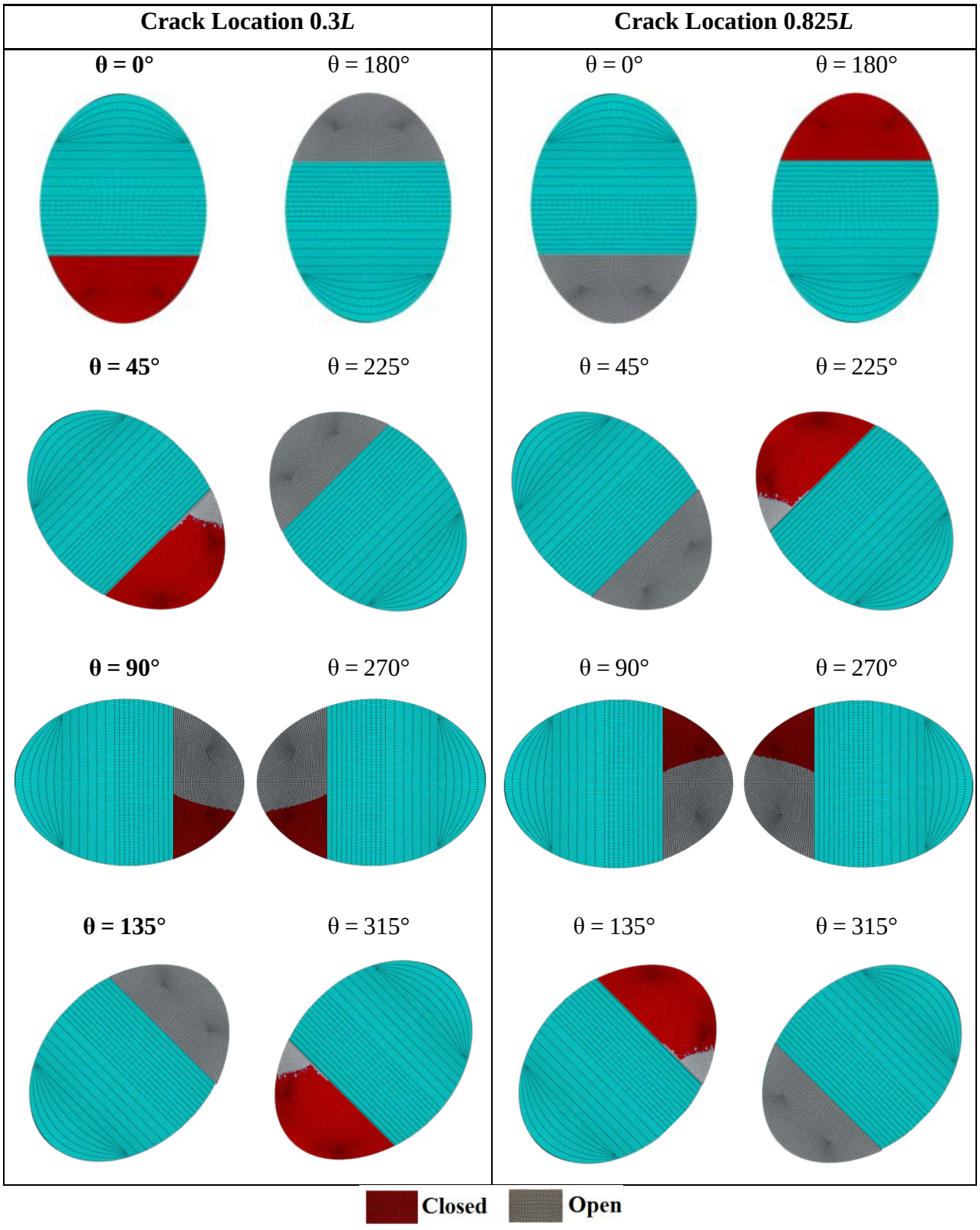

Figure 6-12: Crack status in the unbalance shaft (η = 10 & β = 0°) at crack locations 0.3L and 0.825L

The other two special crack locations in the unbalance shaft are 0.2L and 0.8L, where the percentage of closing remains unchanged during rotation and also independent of the force ratio as observed in Figure 6-13. In Figure 6-14, crack breathing can be further visualised. Therefore, a crack at 0.2L is fully closed and would never open during rotation when $\beta = 0°$. The shaft would be virtually identical to an intact one and would have maximum stiffness. At crack location 0.8L, the crack remains fully open and would never close, resulting in minimum shaft stiffness. As discussed previously (referring to Figure 6-8), this is because the rotor weight does not introduce any shaft bending at these two locations and crack opening and closing are determined by the unbalance force only. At the former location, the shaft bends upwards, keeping the crack closed while at the latter, it bends downwards, keeping the crack open.

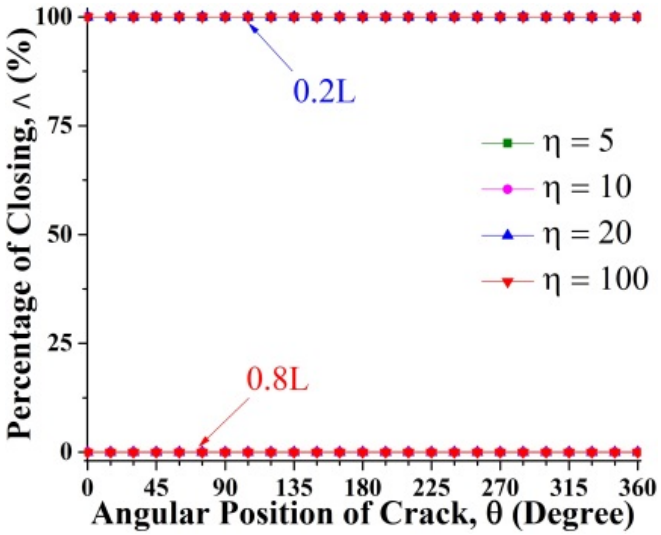

Figure 6-13: Percentage of closing of the crack with different force ratios at crack locations 0.2L and 0.8L with $\beta = 0°$

Figure 6-7 also indicates that the percentage of closing progressively approaches that of the balance shaft as the unbalance force ratio increases (unbalance force decreases), which can also be observed in Figure 6-15 for the full shaft rotation. This result shows that the two models are in excellent agreement at a large force ratio. Figure 6-15 also shows that variations of Λ with force ratio and crack location depend strongly on the shaft rotational angle.

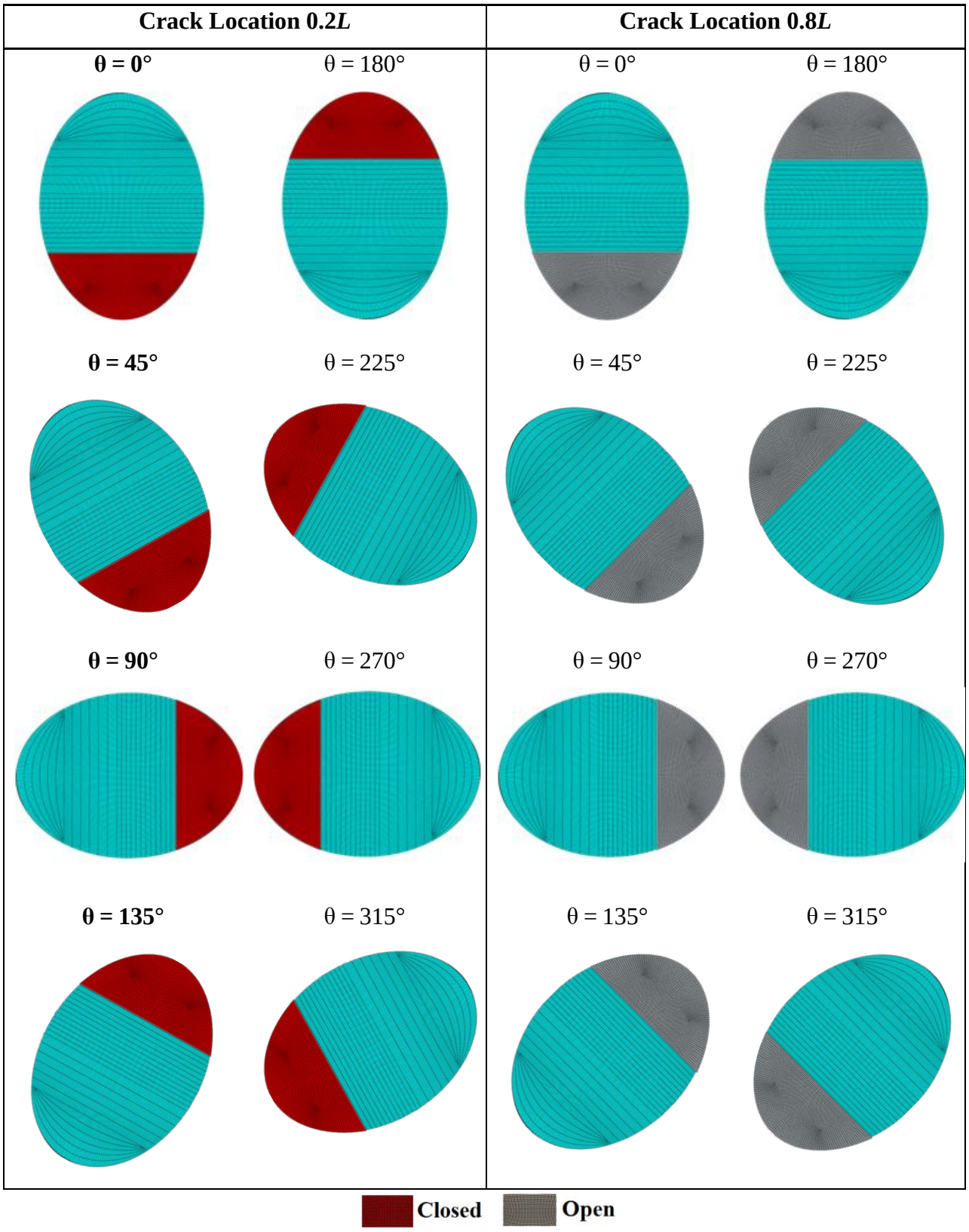

Figure 6-14: Crack status in an unbalance shaft (η = 10 & β = 0°) at crack locations 0.2L and 0.8L, respectively

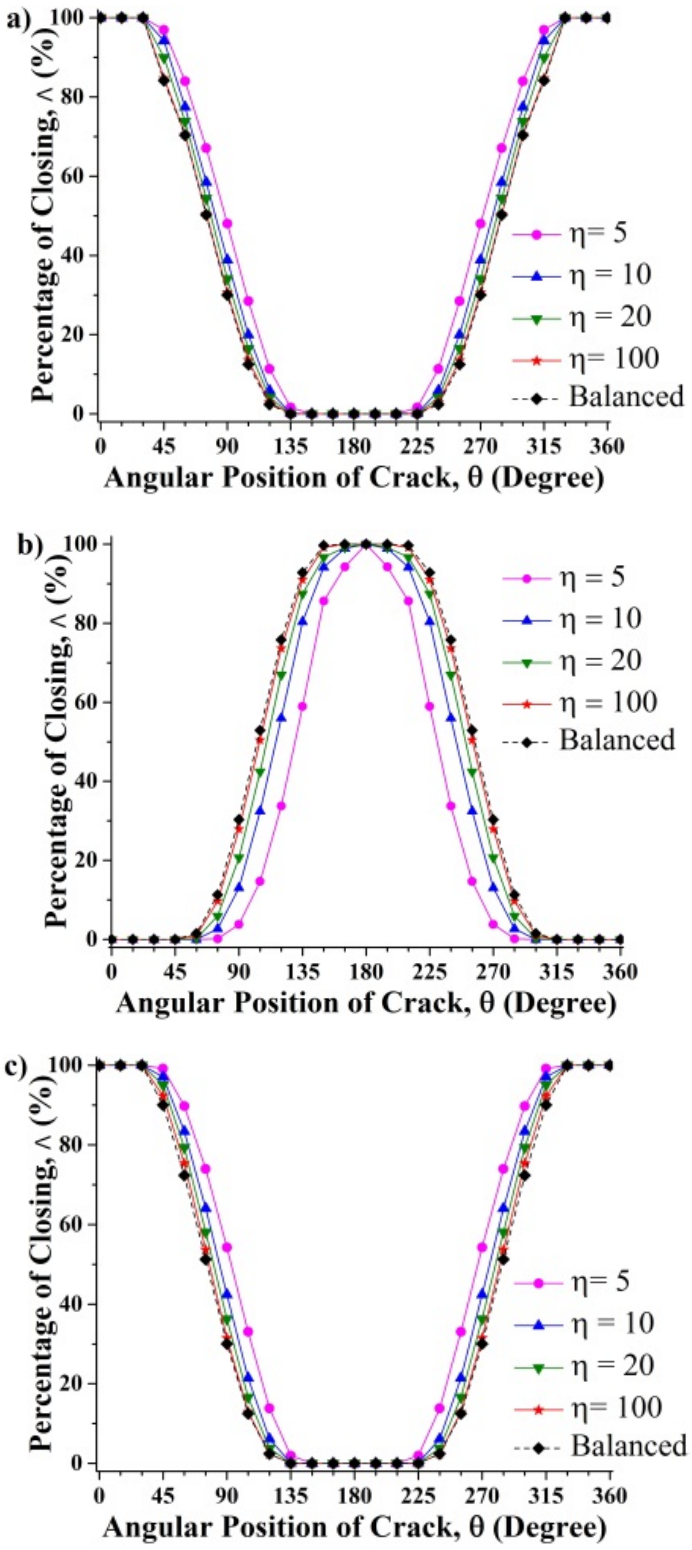

Figure 6-15: Percentage of closing of the crack with different force ratios when $\beta = 0°$, (a) 0.15L, (b) 0.7L and (c) 0.925L

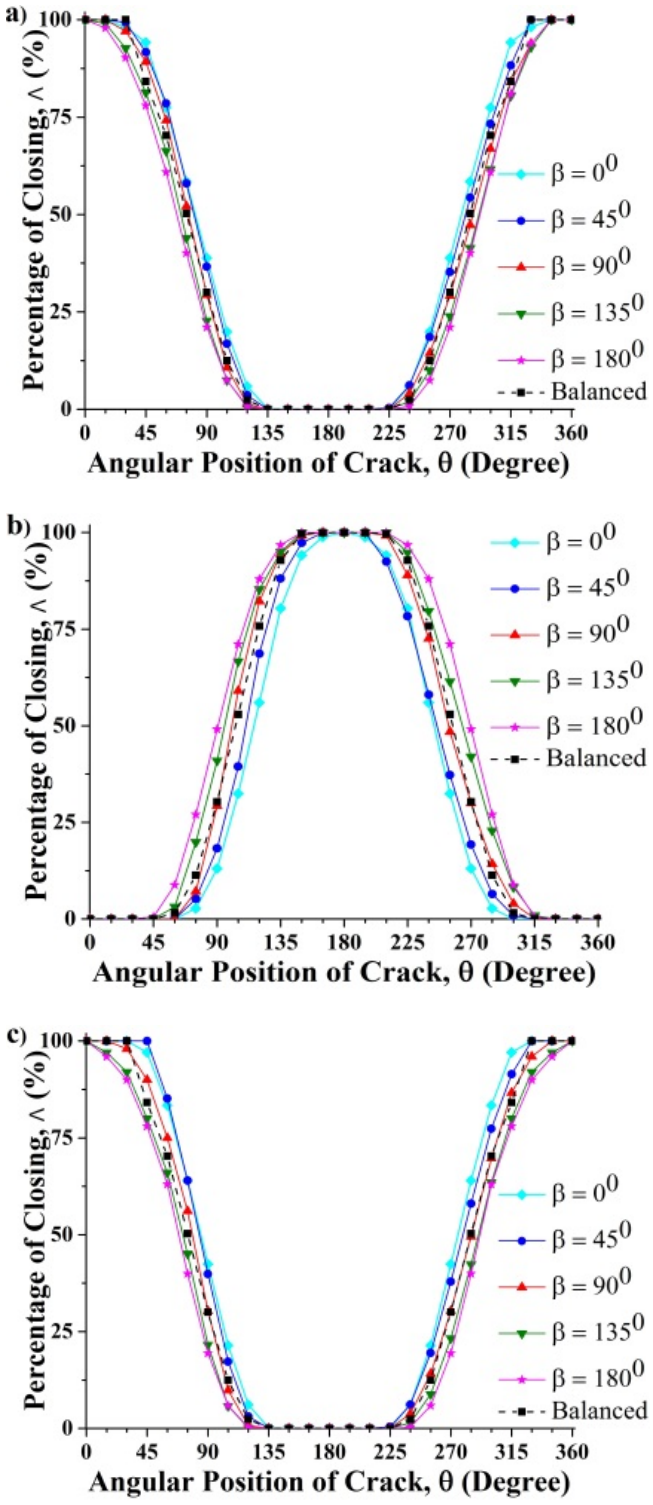

Figure 6-16: Effect of unbalance force orientation on crack breathing behaviour with a force ratio of 10 at (a) 0.15*L* (b) 0.7*L* and (c) 0.925*L*

During full shaft rotation, the shaft will experience two processes, namely, a stiffening process corresponding to the increasing in Λ and a softening process corresponding to the decreasing in Λ. These two processes are symmetrical to the shaft rotational angle of 180°. The flat region on the curve indicates either a fully

closed range ($\Lambda = 100\%$) or a fully open range ($\Lambda = 0\%$). Further, when the crack is located at 0.7*L*, Λ is smaller at each rotational angle than that for the balance one, resulting in a more flexible unbalance shaft as observed in Figure 6-15(b). However, when the crack is situated at 0.15*L* or 0.925*L*, it is larger than that for the balance shaft, showing a stiffer unbalance shaft (see Figure 6-15(a) and Figure 6-15(c)). It is observed that the global shape of curves in Figure 6-15(a) with a crack at 0.15L differs by 180° from that of curves in Figure 6-15(b) with a crack at 0.7L. This is because the bending direction of the shaft at the former crack location differs by 180 degrees from that of the shaft with a crack at the latter location when $\theta = 0°$ or 180°. The deflection curves for $\theta = 0°$ are shown in Figure 6-8.

Figure 6-15 represents only a special case where the angular position of unbalance force $\beta = 0°$. Figure 6-16 presents the percentage of closing of the crack at different angular positions of the unbalance force. It is identified that when the crack is located at 0.7*L* (see Figure 6-16 (b)), the unbalance shaft has smaller flexibility when $\beta = 0°$ and $\beta = 45°$ and the stiffness of the shaft with $\beta = 0°$ is the smallest. However, the unbalance shaft is overall stiffer than the balance counterpart when the angular position of unbalance force is $\beta = 135°$ and $\beta = 180°$. In particular, when $\beta = 180°$ the shaft is the stiffest. Further, when the crack is at 0.15*L* or 0.925*L*, the variation of overall stiffness of the unbalance shaft with unbalance angular force position is just opposite to those when the crack is at the middle span.

In general, three ranges of stiffness variation along shaft length, bordered at 0.3*L* and 0.825*L*, are identified as observed in Figure 6-7. When the angular position of an unbalance force is in the range of $0° \leq \beta < 90°$ or $270° < \beta \leq 360°$ and the crack is between 0.3*L* and 0.825*L*, the unbalance force effect on the crack breathing leads to a more flexible shaft. When a crack is located in two side ranges, the unbalance shaft is stiffer. These trends will be reversed when β is between $90° < \beta < 270°$. Crack status during full rotation are illustrated in Figure 6-17 for $\eta = 10$ and $\beta = 0°$ and in Figure 6-18 for $\eta = 10$ and $\beta = 180°$ at crack locations 0.15*L* and 0.7*L*. Corresponding diagrams for the balance shaft are in Figure 6-9.

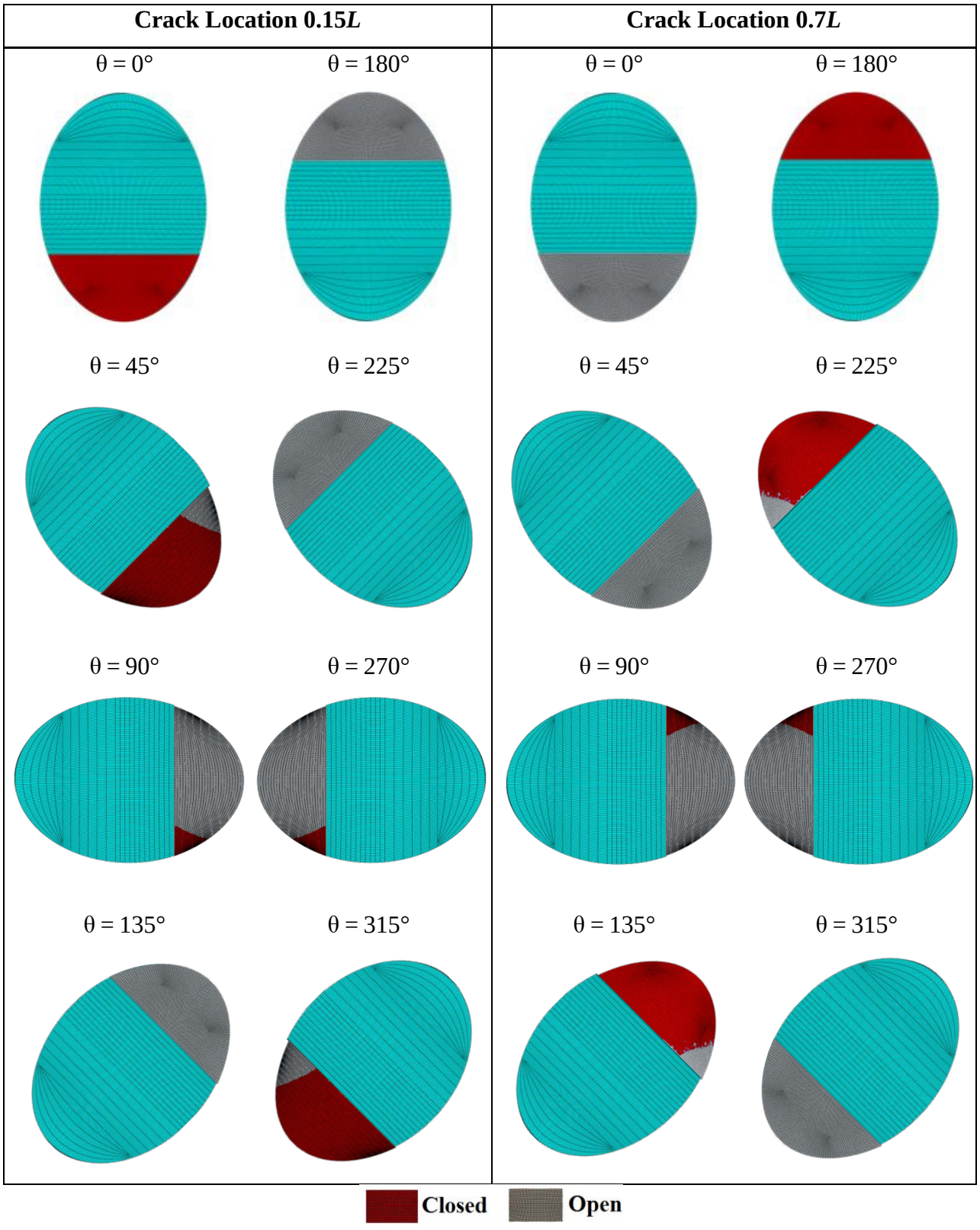

Figure 6-17: Status of the crack of the unbalance shaft ($\eta = 10$ & $\beta = 0°$) at crack locations 0.15*L* and 0.7*L*, respectively

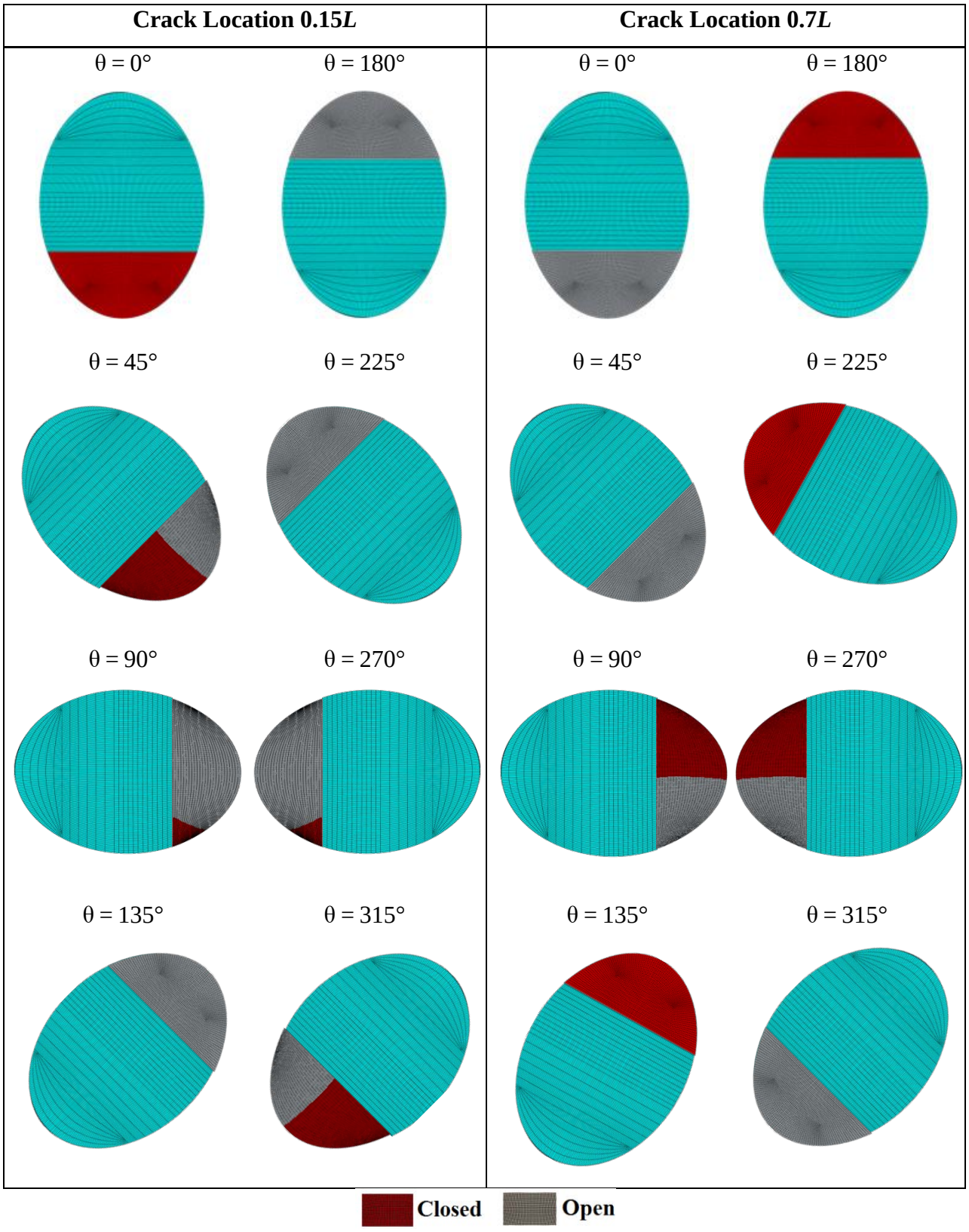

Figure 6-18: Status of the crack for the unbalance shaft (η = 10 & β = 180°) at crack locations 0.15L and 0.7L

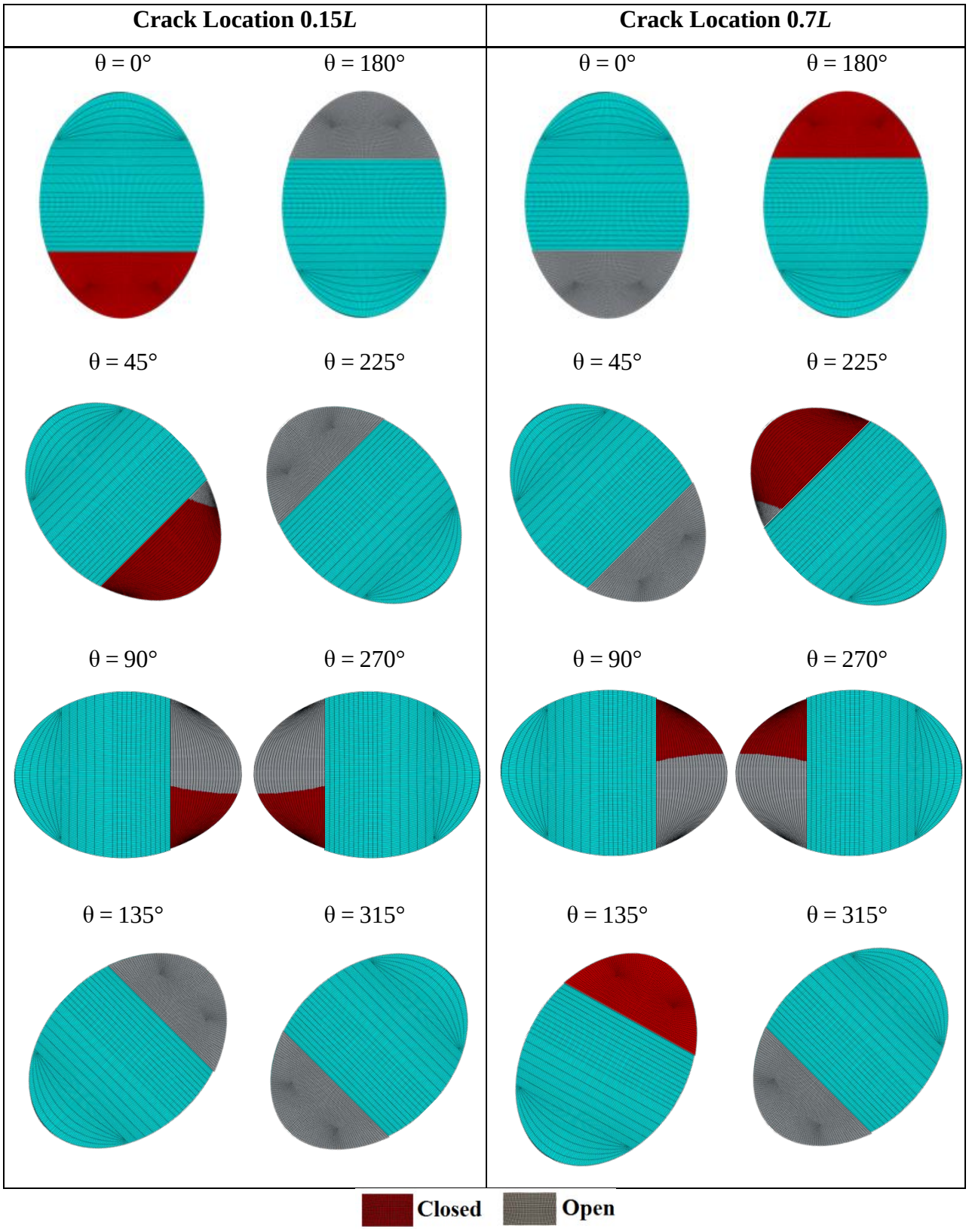

Figure 6-19: Status of the crack of the unbalance shaft (η = 10 & β = 90°) at crack locations 0.15L and 0.7L

Regardless of crack location, the angular position of unbalance force $\beta = 90°$ is identified as a special orientation. At this orientation, the percentage of closing for the unbalance shaft may be larger or smaller than that for the balance counterpart, depending on the shaft rotational angle as shown in Figure 6-16. The results reveal that the unbalance shaft's overall stiffness during a full shaft rotation has little difference from that of the balance one. Crack statuses during a full rotation for $\eta = 10$ and $\beta = 90°$ are displayed in Figure 6-19 at crack locations $0.15L$ and $0.7L$. Figure 6-16 also shows that except for $\beta = 0°$ and $\beta = 180°$, the stiffening and softening processes are no longer symmetrical since the closing percentage has different values at two symmetrical rotational angles, such as 105° and 255°. The relative direction of the unbalance force to the crack can generate significant influence on the vibration behaviours of the cracked rotor. Cheng, Li, Chen, and He (2011) observed that the minimum and maximum vibrations exist when the unbalance force aligns in the crack direction and opposite the crack, respectively.

6.4 Analysis of Centroidal Orbits of a Crack Cross-Section

To examine the effects of crack breathing on the dynamic response of a cracked rotor, the shaft orbits at different shaft locations are simulated using Abaqus Steady-State Dynamics, Direct. The frequency of the steady-state response is 23 cycles/sec. Unbalance force at any rotational angle is applied through its two components in x and y directions, as in the previous static simulations. The crack depth used in dynamics simulations is $0.5R$ as in the static simulations. Orbits are drawn using amplitudes in x and y directions.

Figure 6-20 shows the orbits of the unbalance shaft at different shaft locations. It is observed that the orbits at four shaft locations with a crack at $0.2L$ are almost the same as that of the solid shaft, which supports the previous conclusion that a crack at $0.2L$ remains fully closed during shaft rotation (see Figure 6-13 and Figure 6-14). When the crack is at $0.8L$ with fully open status, the orbits become larger. The results illustrate an example that quantitative damage detection of the shaft cannot be achieved without considering the effect of crack location on the crack breathing mechanism. Further, when a crack is situated at a special location with fully closed crack status, a cracked shaft may have the same vibration behaviour as a cracked one.

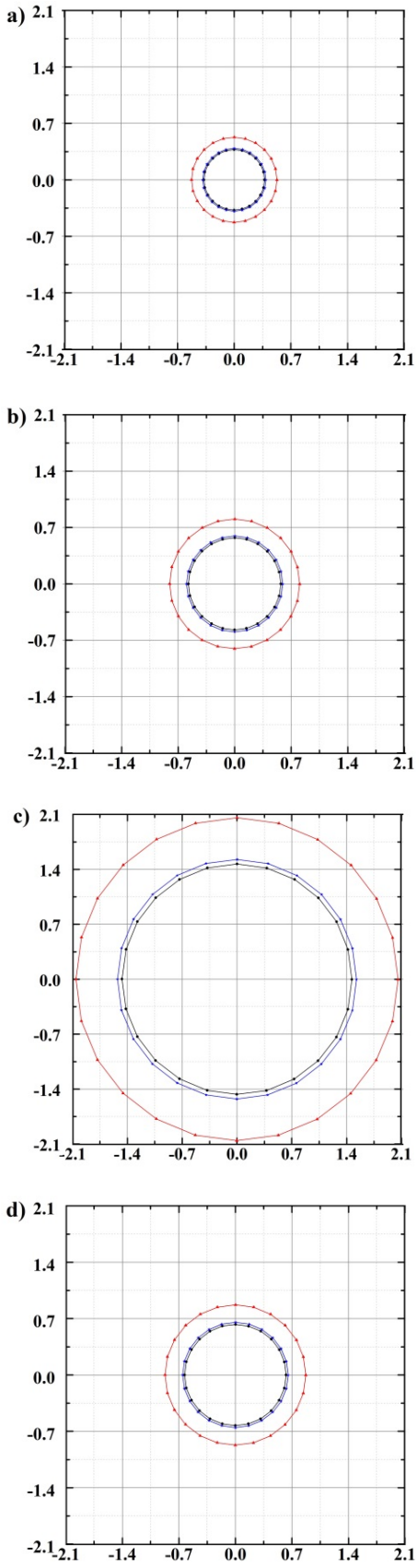

Figure 6-20: Orbits at shaft locations (a) 0.15L, (b) 0.2L, (c) 0.7L and (d) 0.8L, when the crack is at 0.2L and 0.8L, respectively where η = 10 & β = 0°

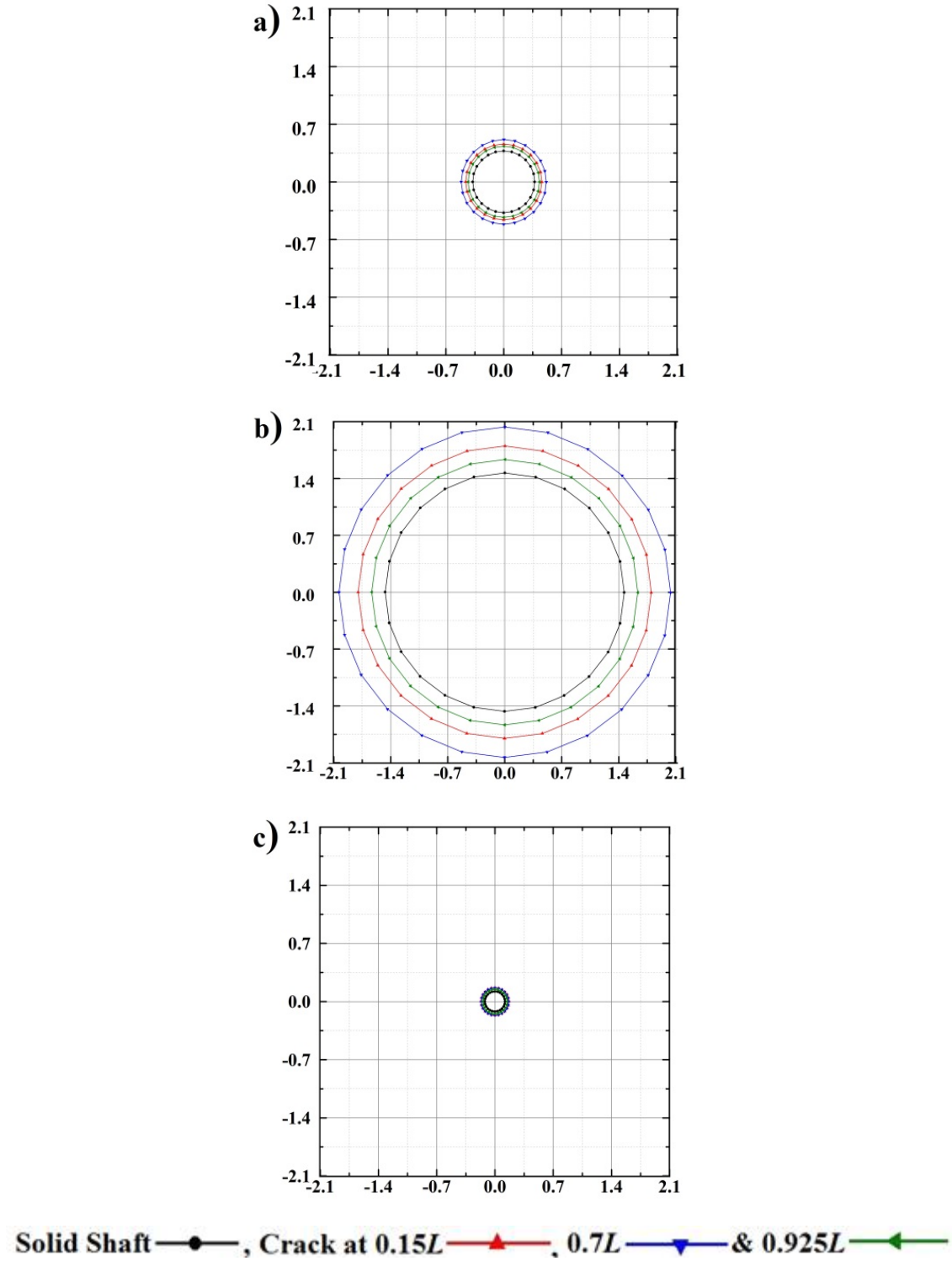

Figure 6-21: Orbits at shaft locations (a) 0.15L, (b) 0.7L and (c) 0.925L when the crack is at 0.15L, 0.7L and 0.925L, respectively with η = 10 & β = 0°

Figure 6-21 shows the shaft orbits of the unbalance shaft at different shaft locations when the crack is located at 0.15L, 0.7L and 0.925L, respectively. As can be observed, when the crack is at 0.7L, the orbit is larger because it is known from the previous result in Figure 6-15 that when the crack is at 0.7L, the unbalance forces

effect on the crack breathing leads to a more flexible shaft. The results demonstrate again that for accurate prediction of damage severity, the effect of crack location on the crack breathing must be considered.

As expected, no lateral vibration is generated without introducing an unbalance force. The breathing model for the balance shaft is just a simplified case, which ignores the unbalance force effect and is usually used in the numerical calculation of vibration response by solving the equation of motions of the rotor system.

6.5 Summary

In this chapter, breathing behaviours of a slant crack in a two-disk-rotor were investigated using 3D FEM. A large number of simulations were performed to examine the influences of crack location, crack angular position, unbalance force ratio and its angular position on the crack opening and closing. The results are also compared with those of the balance shaft. Steady-state vibrations for the unbalance shaft under some configurations are also simulated.

The present study reveals that crack breathing—unlike weight-dominated crack breathing—is largely influenced by the unbalance force and individual rotor physical parameters, generating a dependence of crack breathing on its location at the shaft. This study provides important insights into the modelling of local stiffness matrix through crack breathing. This matrix is usually used to calculate the dynamic response of cracked rotors. Based on the steady-state vibration simulations, it is demonstrated that for more accurate predictions for the dynamic response and damage severity of cracked rotors, it is necessary to consider the effects of unbalance force and individual rotor physical properties on crack breathing. The method and some important results in this work can be applied to the general rotating shafts, such as industrial turbine generators, to develop more accurate online crack detection techniques.

Chapter 7 : Breathing of Elliptical Crack

7.1 Introduction

In this chapter, the breathing mechanism of another more realistic transverse crack—elliptical crack—is investigated. The breathing mechanism of a transverse elliptical crack is investigated numerically in a two-disc rotor under the coupling influence of unbalance force and rotor weight with a fixed shaft end.

First, a full 3D rotor model is simulated with elliptical crack and unbalance mass using Abaqus/standard. Then, the crack breathing behaviours are visualised by analysing the crack status and the variation of the crack closed area and are represented quantitatively by the percentage of the closing of the crack. The results are also compared with those of the existing balance model, where only rotor weight is considered.

7.2 Modelling of Cracked Rotor System

7.2.1 Elliptical crack modelling

A crack with the elliptical shape a/b (a and b being the axis of the elliptical shape; see Figure 7-1(a)), to the cross-section of the shaft is considered for analysis. The 'Tie constraint' is used in the crack section to create the intact part. Surface-to-surface contact interaction is used in crack faces to avoid interpenetration between them during the closing. Details of the contact interaction at the crack cross-section are shown in Figure 7-1(b). The upper portion corresponds to the intact section and the lower to the crack section. In the lower portion, the normal property, 'hard' contact, is used to avoid penetration and the tangential property, 'rough' friction, is used to avoid all relative sliding motions between the two contacting surfaces.

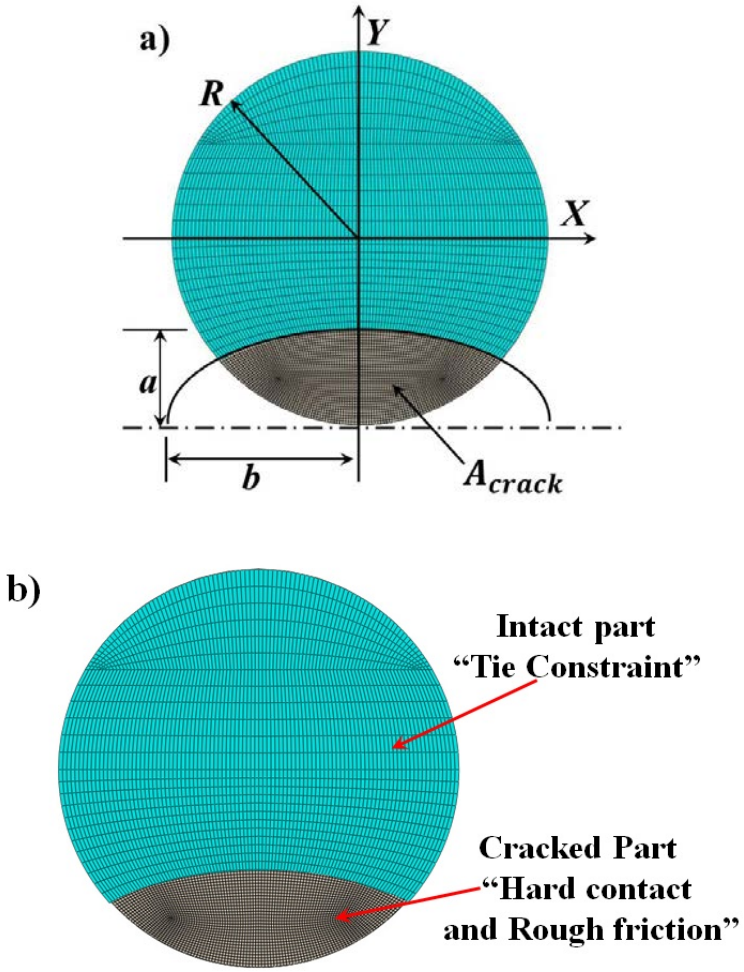

Figure 7-1: Schematic diagram of the elliptical crack; (a) the crack cross-section and (b) surface-to-surface contact interaction in crack cross-section

The analysis is performed as a succession of static problems considering different crack locations. Although the real problem is dynamic, here, the static one is considered at each angular position of the crack to determine the effect of the angular position of the crack. An elliptical crack with shape $a = 0.5R$ and $b = R$ where R is the shaft radius is simulated considering:

1. 40 different crack locations along the shaft length varying from 0 to *1* with increments of 0.025
2. 24 different angular positions of the crack, θ, varying from 0^o to 360^o with increments of 15^o w.r.t. the fixed reference axis.

7.2.2 Mesh sensitivity analyses

A full 3D rotor model is simulated since rotor symmetry no longer exists in the unbalance shaft. The shaft is meshed by using an element named linear hexahedral element of type C3D8R. As shown in Figure 7-2, the mesh density is much higher around the crack in both directions. The mesh size is obtained after a convergence test of the results through mesh sensitivity analyses. The results of the convergence test for the balance case at crack locations $0.5L$ and $\theta = 90°$ are presented in Figure 7-3 and in Table 7-1. It is observed that the closing percentage converges after the numbers of mesh in four regions (a, b, c and d) reach 12, 12, 80 and 24. The percentage of closing is described later in detail.

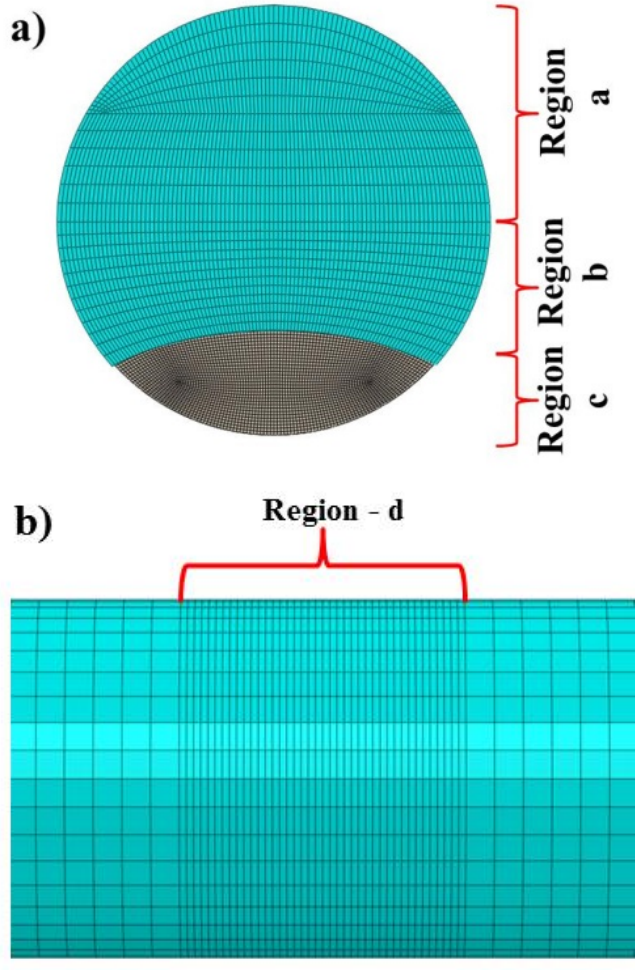

Figure 7-2: Mesh around the elliptical crack section in the longitudinal and transversal directions

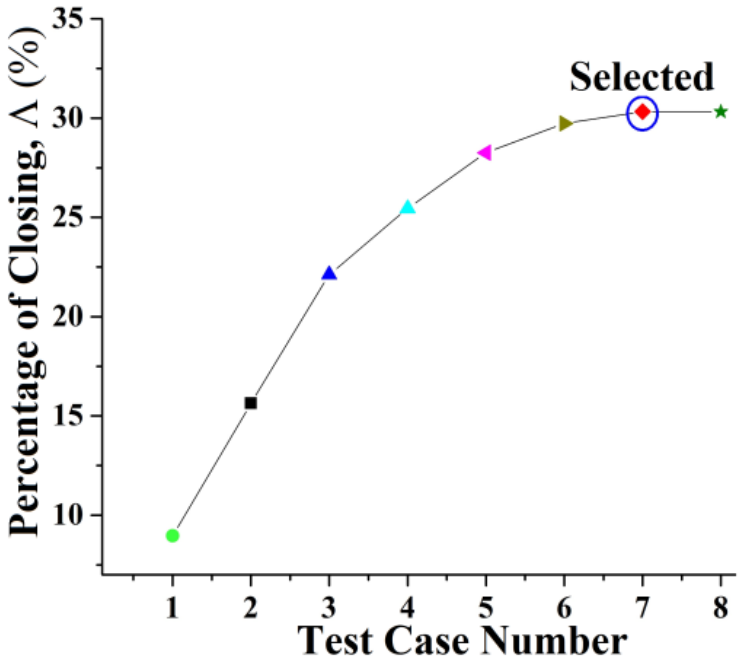

Figure 7-3: Mesh sensitivity analyses of the elliptical crack model

Table 7-1: Mesh sensitivity analyses of the elliptical crack model

Test Cases	Number of Elements	Percentage of Closing
1	a:10; b:10; c:50; d:18	16.64%
2	a:10; b:10; c:60; d:18	20.64%
3	a:12; b:12; c:60; d:18	26.64%
4	a:12; b:12; c:70; d:18	30.25%
5	a:12; b:12; c:70; d:20	32.73%
6	a:12; b:12; c:80; d:20	33.21%
7 (Selected)	a:12; b:12; c:80; d:24	33.74%
8	a:14; b:14; c:90; d:24	33.74%

7.2.3 Unbalance force modelling

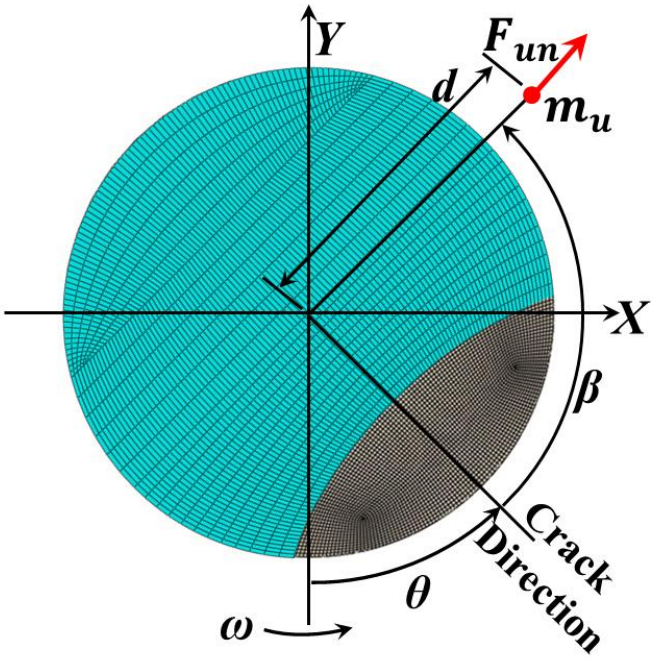

Figure 7-4: Relative positions of the unbalance force with respect to elliptical crack direction

The unbalance force is taken as a rotational force ($F_{un} = m_u\,\omega^2 d$) owing to unbalance mass, $m_{u,}$ at a radial distance d from the centre of the shaft when the shaft rotating speed is ω rad/sec. During the rotation of shaft, the angular position of the unbalance (F_{un}) is $(\theta + \beta)$ where θ is the angular position of the crack or shaft rotation angle w.r.t. the fixed reference axis and β is a fixed angular position of unbalance force relative to the crack direction as shown in Figure 7-4.

Note that unbalance force is not located at the crack plane and it is only a projection of unbalance force on the crack plane. Different unbalance force ratios and different angular positions of unbalance force relative to the crack direction are considered to distinguish the influence of the angular position of the crack and the unbalance force together. To evaluate the slant crack breathing behaviour, a simulation is performed considering:

1. 5 different unbalance force ratios, including balance shaft, η = 1, 2, 10, 100 and ∞ (balance), ratio of the gravitational force and unbalance force

2. 5 different angular positions of unbalance force, β = 0^o, 45^o, 90^o, 150^o and 180^o. These positions of unbalance force within half of the angular positions of unbalance force (0° to 180°) are considered since the effect of angular position of unbalance force on crack breathing behaviour is symmetrical (the first half is the same as the second half of angular positions of unbalance force, 180° to 360°).

7.2.4 Loading and boundary conditions

A full 3D rotor model is simulated since the rotor symmetry no longer exists in the unbalance shaft. The simulation is conducted as a series of static problems with different crack locations along the shaft length and different shaft rotation angles. The parameters of the rotor model are in Table 7-2. Figure 7-5 shows the loading and boundary conditions of the 3D FE model. The model represents a two-disk rotor with fixed end supports. The shaft self-weight is applied as a gravitational force, and two disk weights are applied as the concentrated forces. Unbalance force is also applied as a concentrated force in the horizontal [$F_{un}cos(\theta + \beta)$] and vertical [$F_{un}sin(\theta + \beta)$] directions of the shaft cross-section at the right disk.

Table 7-2: Parameters of the elliptical crack rotor model

Description	Value
Shaft Length, L	724 mm
Shaft Radius, R	6.35 mm
Density, ρ	7800 kg/m^3
Young's Modulus, E	210GPa
Poisson Ratio, v	0.3
Disk mass, m_d	0.50 kg
Disk-1 location, l_1	181 mm
Disk-2 location, l_2	543 mm
Crack location, l_0	Variable
Axis of Elliptical Shape	a = 0.5R
	$b = R$

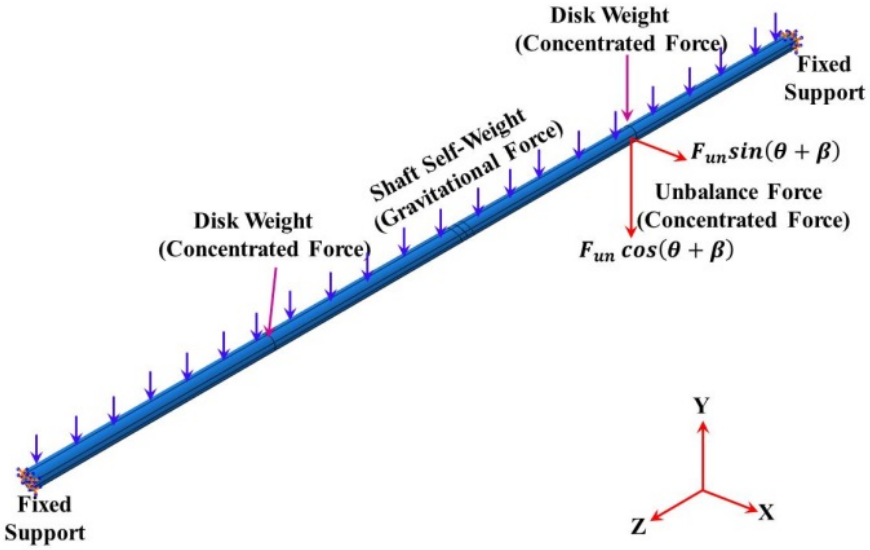

Figure 7-5: Details of loading and boundary conditions of the elliptical crack rotor model

7.3 Analysis of Elliptical Crack Breathing Mechanism

The status of the crack and percentage of the closing of the crack are analysed for a different combination of crack location along the shaft length, angular position of crack, unbalance force ratio and angular position of unbalance force to distinguish the breathing behaviour of cracks. The breathing behaviour of cracks can link to the stiffness changes in the cracked shaft and ultimately facilitate calculation of vibration response. When a crack status is fully closed or percentage of the closing of the crack is 100%, the shaft is as stiff as a solid shaft. The crack will never propagate, and the SIF would be always zero. Similarly, when a crack status is fully opened or percentage of the closing of the crack is 0%, the shaft has minimum stiffness. It will probably propagate, and the SIF would take positive values and could overcome the critical value called fracture toughness. In addition, when a crack status is partially open/closed or percentage of the closing of the crack is between 0% and 100%, the shaft has minimum to maximum stiffness. The specific modules in fracture mechanics analysis of Abaqus are used to determine the status of the crack (open, partially open/closed and closed as shown in Figure 7-6) and crack closed area to calculate the percentage of the closing of the crack.

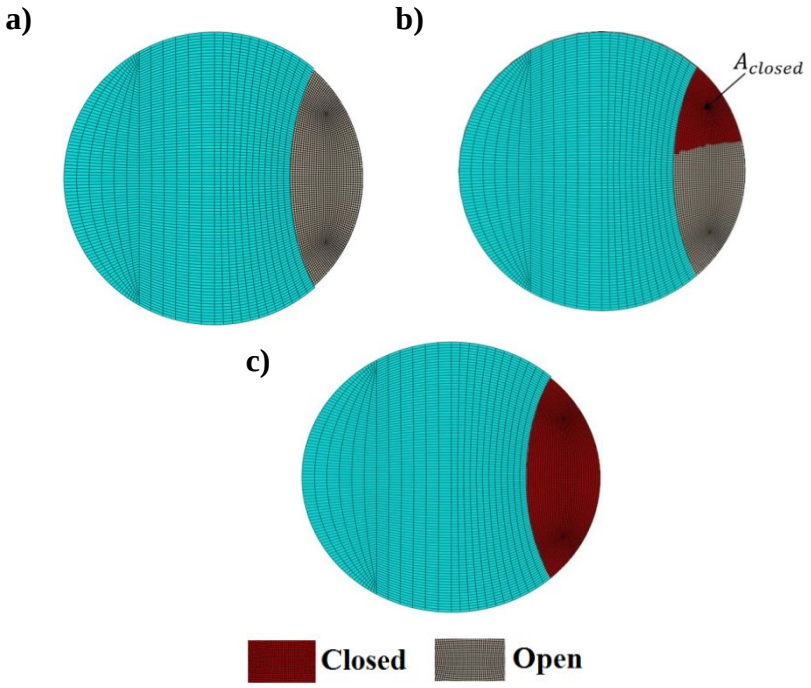

Figure 7-6: Status of the crack (a) fully open (b) partially open/closed and (c) fully closed

The percentage of closing of the crack, Λ, is calculated using Equation (7-1) where A_{crack} is the area of the crack segment at time zero (see Figure 7-1(a)) and A_{closed} is the closed portion of the crack segment during rotation as shown in Figure 7-6 (b). The area of A_{crack} and A_{closed} are found as Abaqus history output. A_{crack} can be calculated by Equation (7-2) where a is the crack depth, b is the major axis, Ω is the central angle, and R is the shaft radius as shown in Figure 7-1(a). Equation (7-2) was derived by Wei et al. (2014), the evaluated forms of the definite integrals are omitted in the interest of space. Here, A_{crack} is also calculated by Equation (7-2) to calculate the difference between two methods. The percentage of difference between Equation (7-2) and Abaqus history output for A_{crack} is found 0.056%.

$$\Lambda\,(\%) = \frac{\boldsymbol{A_{closed}}}{\boldsymbol{A_{crack}}} \times \mathbf{100} \tag{7-1}$$

$$\boldsymbol{A_{crack}} = \mathbf{2}\int_{\boldsymbol{R-a}}^{\boldsymbol{R\cos\Omega}} \frac{\boldsymbol{b}}{\boldsymbol{a}}\sqrt{\boldsymbol{a^2-(y-R)^2}}\,\boldsymbol{dy} + \mathbf{2}\int_{\boldsymbol{R\cos\Omega}}^{\boldsymbol{R}} \sqrt{\boldsymbol{R^2-y^2}}\,\boldsymbol{dy} \tag{7-2}$$

The minimum and maximum values of A_{closed} are zero for a fully open crack and the same as A_{crack} for a fully closed crack respectively. For a fully open crack and

fully closed crack, the percentage of closing of a crack, Λ, is equal to 0 and 100, respectively.

The percentages of the closing of a crack along the shaft length for different force ratios are exemplified in Figure 7-7. It is constant but changes at around crack locations 0.2L and 0.8L for the balance shaft. Hence, two different types of crack breathing behaviours of the balance shaft can be divided at these crack locations along the shaft length. One type is when a crack is located between 0.2L and 0.8L, for example, at crack location 0.5L, and another type is when a crack is located outside this crack region, for example, at crack location 0.125L (see Figure 7-7and Figure 7-8).

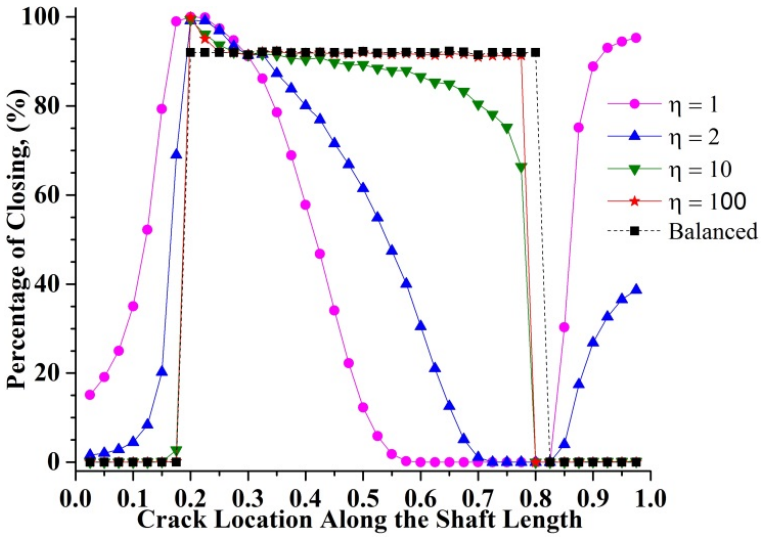

Figure 7-7: Percentage of the closing of a crack along the shaft length for different force ratios where β = 0° and θ = 135°

However, crack statuses for both crack location regions are symmetrical about the first half and second half of the shaft rotation but different sequentially. More specifically, when the crack is located at crack location 0.125L, it follows a sequential change from fully closed to partially open/closed, fully open, partially open/closed and then to fully closed. Conversely, when the crack is located at crack location 0.5L, it follows a sequential change from fully open to partially open/closed, fully closed, partially open/closed and then to fully open (see Figure 7-8 and Figure 7-9). Notably, for both cases the duration of each crack status remains unchanged (see Figure 7-9). Therefore, although the status of the cracks and percentage of the

closing of the crack for a balance shaft depend on the crack location, the stiffness of the balance cracked shaft is independent of crack location along the shaft length.

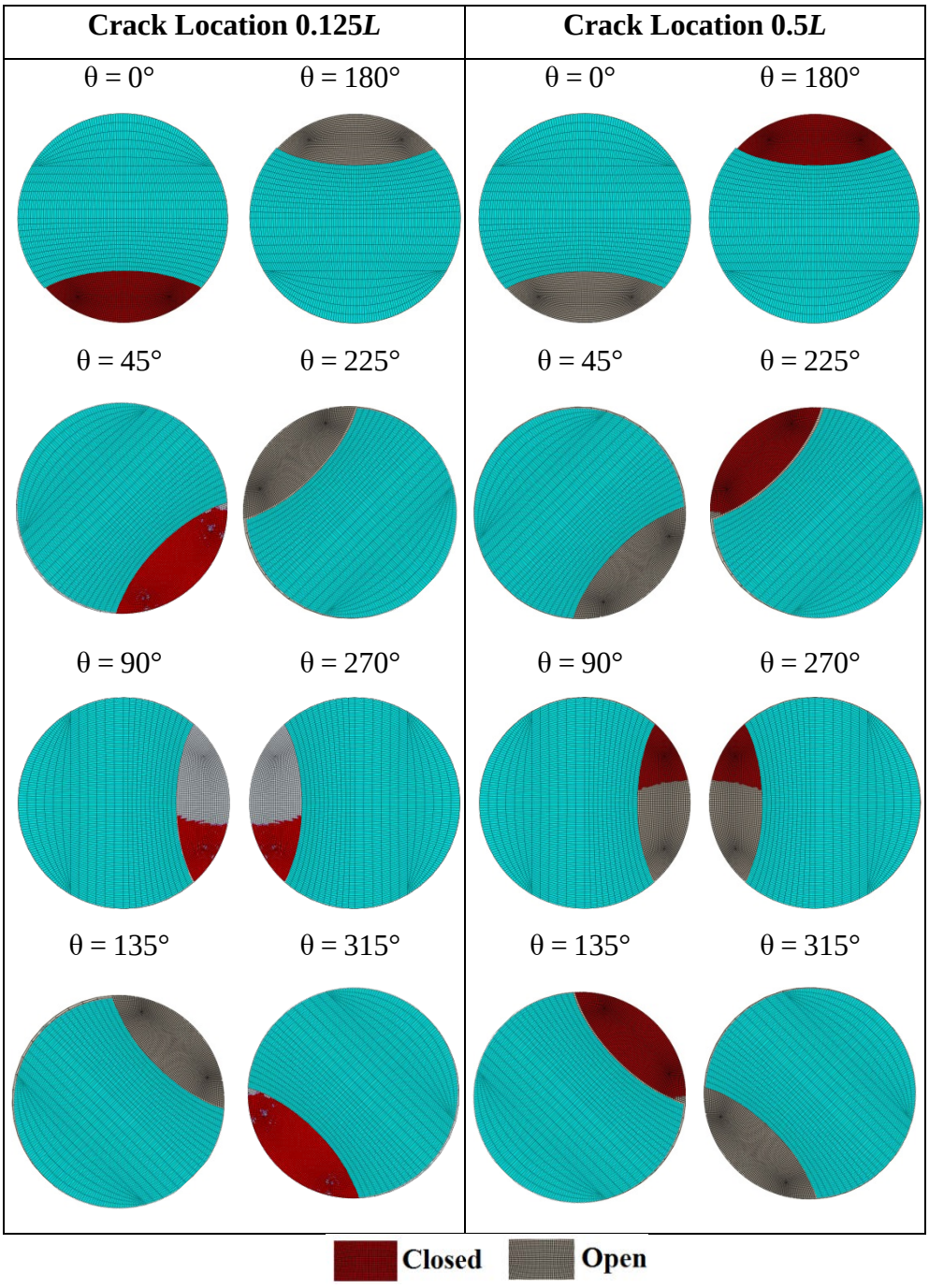

Figure 7-8: Status of crack of a balance shaft at crack locations 0.125*L* and 0.5*L*

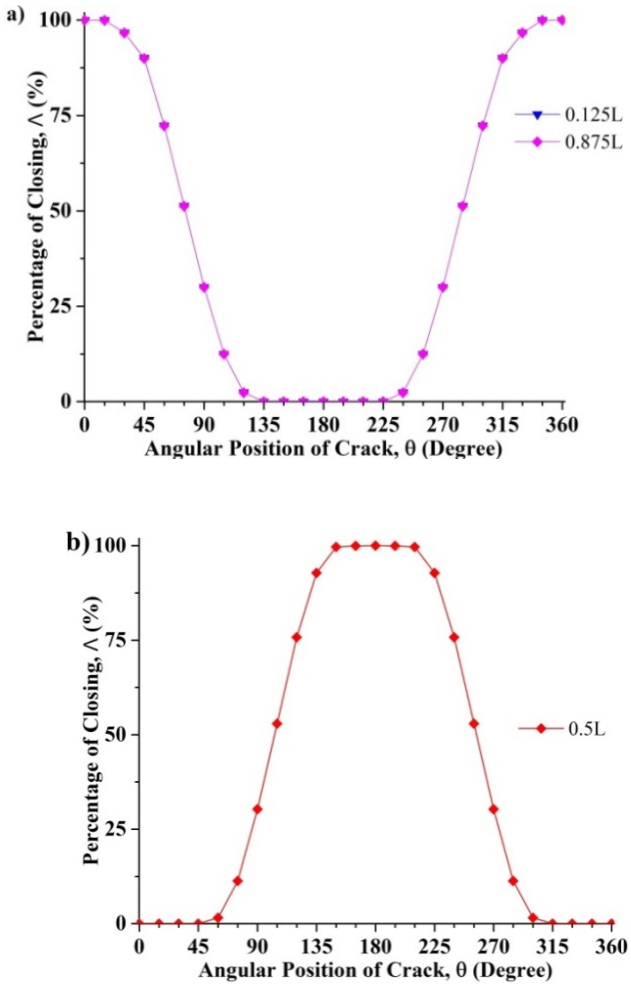

Figure 7-9: Percentage of closing of the crack of balance shaft at crack locations (a) 0.125*L* & 0.875*L* and (b) 0.5*L*

For the unbalance shaft, the percentage of closing of a crack along the shaft length is remarkably different from that of the balance one. However, at crack locations 0.3*L* and 0.825*L*, it is the same as that of the balance shaft; see Figure 7-7 and Figure 7-10 for the full duration of shaft rotation. Hence, these two crack locations are independent of unbalance force. However, at these two crack locations, the crack status is different sequentially since the two crack locations are located in different balance shaft crack regions. At crack location 0.3*L*, first, the crack status is fully open at θ = 0° and it then changes to partially open/closed, fully closed, partially open/closed and then again to fully open. Conversely, at crack location 0.825*L*, first, the crack status is fully closed at θ = 0° and it then changes to partially open/closed, fully open, partially open/closed and then again to fully closed (see Figure 7-10). As a result, if a crack is located around these crack locations, the unbalance shaft crack

will breathe completely like the one in the balance shaft and the shaft stiffness would be the same as that of the balance shaft.

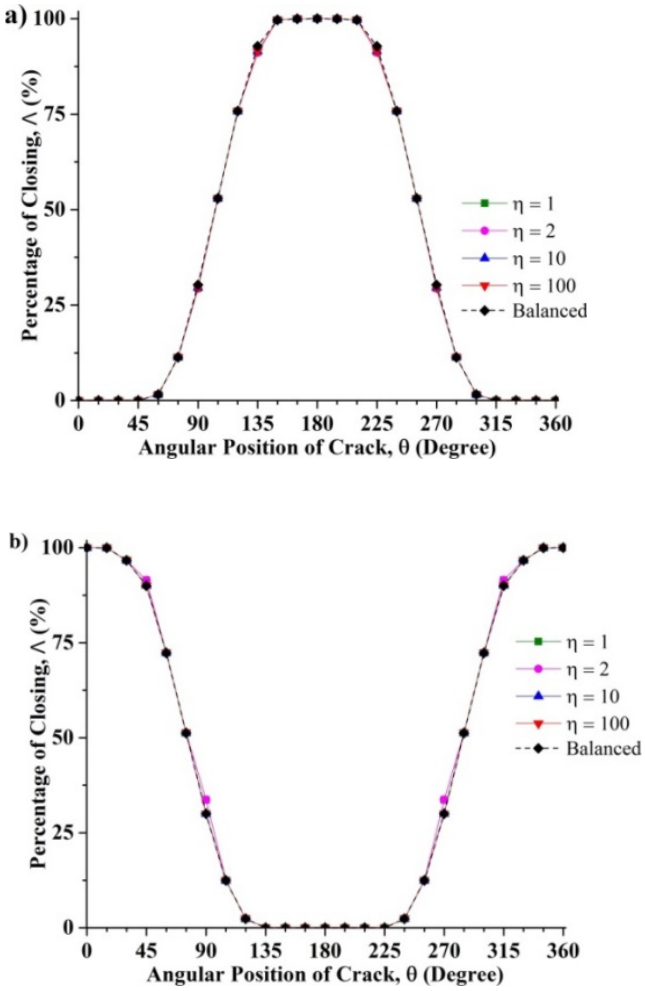

Figure 7-10: Percentage of closing of the crack of different force ratios at crack locations (a) 0.3*L* and (b) 0.825*L*

For the unbalance shaft, two other special crack locations are 0.2*L* and 0.8*L*; the percentage of closing of a crack is identical for different unbalance force ratios (see Figure 7-7 and Figure 7-11 for the full duration of shaft rotation). As a result, if a crack is located around these crack locations, the unbalance shaft crack will breathe independently of the unbalance force ratios. Figure 7-12 shows the status of the crack of an unbalance shaft ($\eta = 1$ & $\beta = 0°$) for a full duration of shaft rotation. At crack location 0.2*L*, a crack in an unbalance shaft has the fully-closed-never-opened status during rotation, similar to an uncracked shaft. The shaft will have maximum stiffness and it becomes virtually identical to an intact shaft. At crack location 0.8*L*, it has the

fully-open-never-closed status, just like a notch. The shaft will have a minimum stiffness.

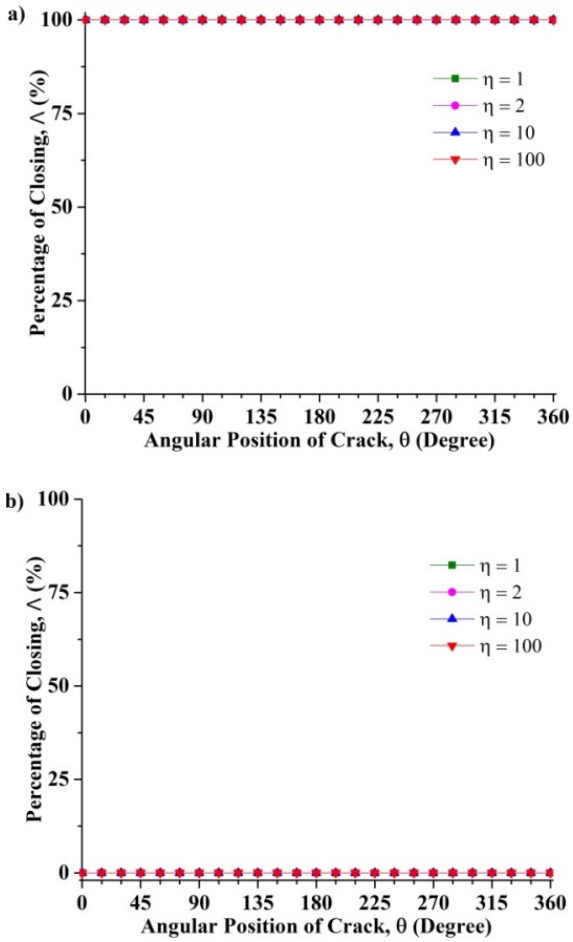

Figure 7-11: Percentage of closing of the crack of different force ratios at crack locations (a) 0.2*L* and (b) 0.8*L*

Moreover, the unbalance shaft percentage of the closing of a crack progressively approaches that of the balance shaft as the unbalance force ratio increases (unbalance force decreases); see Figure 7-7 and Figure 7-13 for the full duration of shaft rotation. This finding indicates that the unbalance model would be finally in agreement with the balance model when unbalance force ratio is sufficiently large.

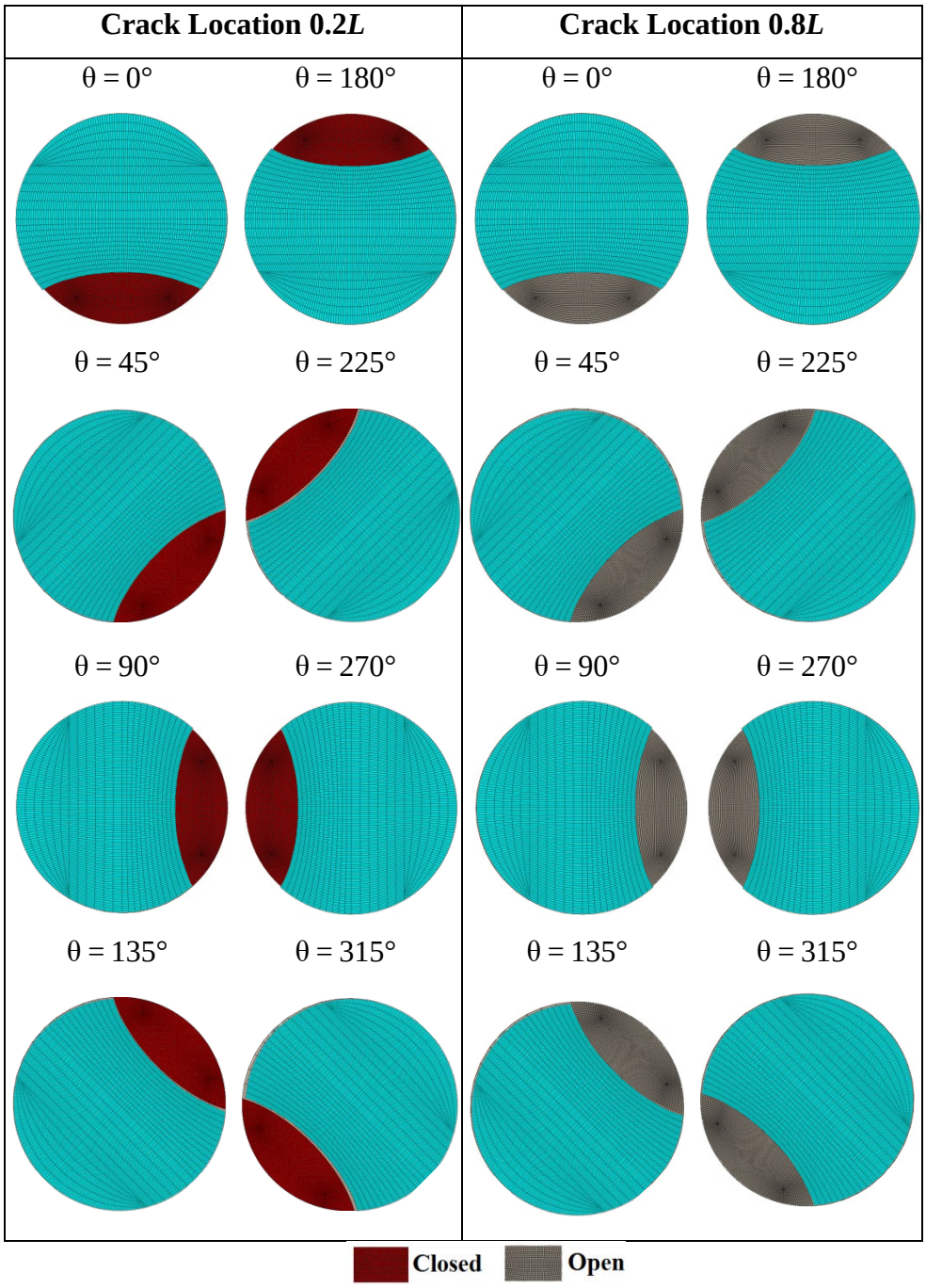

Figure 7-12: Status of crack of an unbalance shaft (η = 1 & β = 0°) at crack locations 0.2L and 0.8L

It is clear that variations of Λ with the crack location also depend strongly on the shaft rotational angles. During full shaft rotation, the shaft will generally experience two processes, that is, a stiffening process corresponding to the increasing in Λ and a softening process corresponding to the decreasing in Λ. These two processes are observed to be symmetrical about θ = 180°. The flat part of the curve corresponds to either a fully open range (Λ = 0%) or a fully closed range (Λ = 100%).

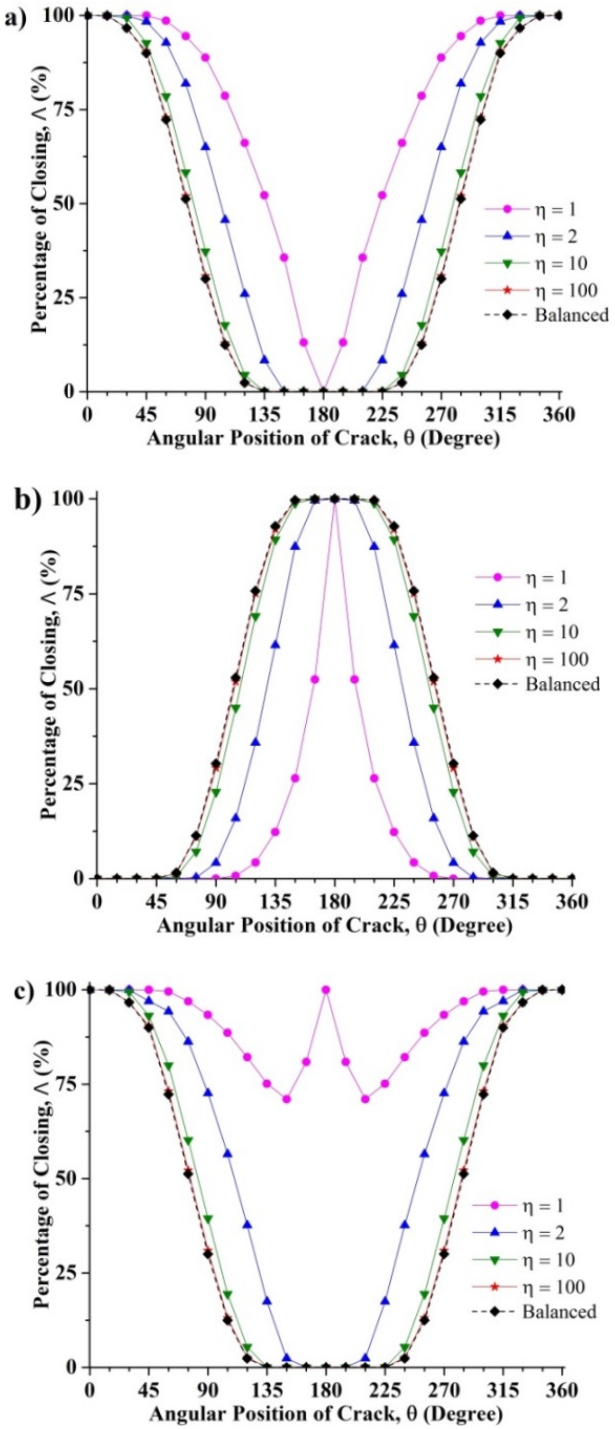

Figure 7-13: Percentage of closing of the crack of different force ratios for crack locations (a) 0.125*L* (b) 0.5*L* and (c) 0.875*L*

In detail, when the crack is located at 0.5*L*, the percentage of closing of the crack for the unbalance shaft is lower than that for the balance counterpart, which indicates that the unbalance shaft is more flexible than the balance shaft (see Figure 7-13b). However, when the crack is located at 0.125*L* and 0.875*L*, the corresponding percentage is higher than that for the balance shaft, and the unbalance shaft becomes

stiffer than the balance shaft (see Figure 7-13a and Figure 7-13c). Small differences in Λ are observed between the balance shaft and unbalance shaft when the shaft is at the early stage of rotation or near the completion of rotation (see Figure 7-13).

Figure 7-13 represents only a special case where the angular position of unbalance force $\beta = 0°$. Figure 7-14 exemplifies the percentage of closing of the crack of the different angular positions of unbalance force. It is identified that when a crack is located at $0.5L$, the unbalance shaft is overall more flexible than the balance counterpart when the angular positions of unbalance force are $\beta = 0°$ and $\beta = 45°$; with $\beta = 0°$, the shaft has the least stiffness (see Figure 7-14b). In addition, the unbalance shaft is overall stiffer than the balance counterpart when a crack is located at $0.125L$ and $0.875L$ for these two angular positions of unbalance force; when $\beta = 0°$, the shaft is stiffest (see Figure 7-14a and Figure 7-14c). Conversely, the unbalance shaft is overall stiffer than the balance one for crack location $0.5L$ when the angular positions of unbalance force are $\beta = 135°$ and $\beta = 180°$ because the percentage of closing of the unbalance shaft is higher than that of the balance shaft. In particular, when $\beta = 180°$, the shaft is the stiffest (see Figure 7-14b). For crack locations $0.125L$ and $0.875L$, for these two angular positions of unbalance force, the unbalance shaft is more flexible than the balance one because the percentage of closing of the unbalance shaft is lower than that of the balance shaft. In particular, when $\beta = 180°$, the former is more flexible than the latter (see Figure 7-14a and Figure 7-14c). However, regardless of crack location, the angular position of unbalance forces $\beta = 90°$ is identified as a special orientation (see Figure 7-14). At this orientation, the percentage of closing of the crack for the unbalance shaft is sometimes larger than that of the balance shaft, and sometimes is smaller during a full shaft rotation. The result demonstrates that the overall stiffness of the unbalance shaft is more or less the same as that of the balance shaft. It is also observed that the symmetry between the stiffening process and softening process during shaft rotation disappears except for $\beta = 0°$ and $\beta = 180°$.

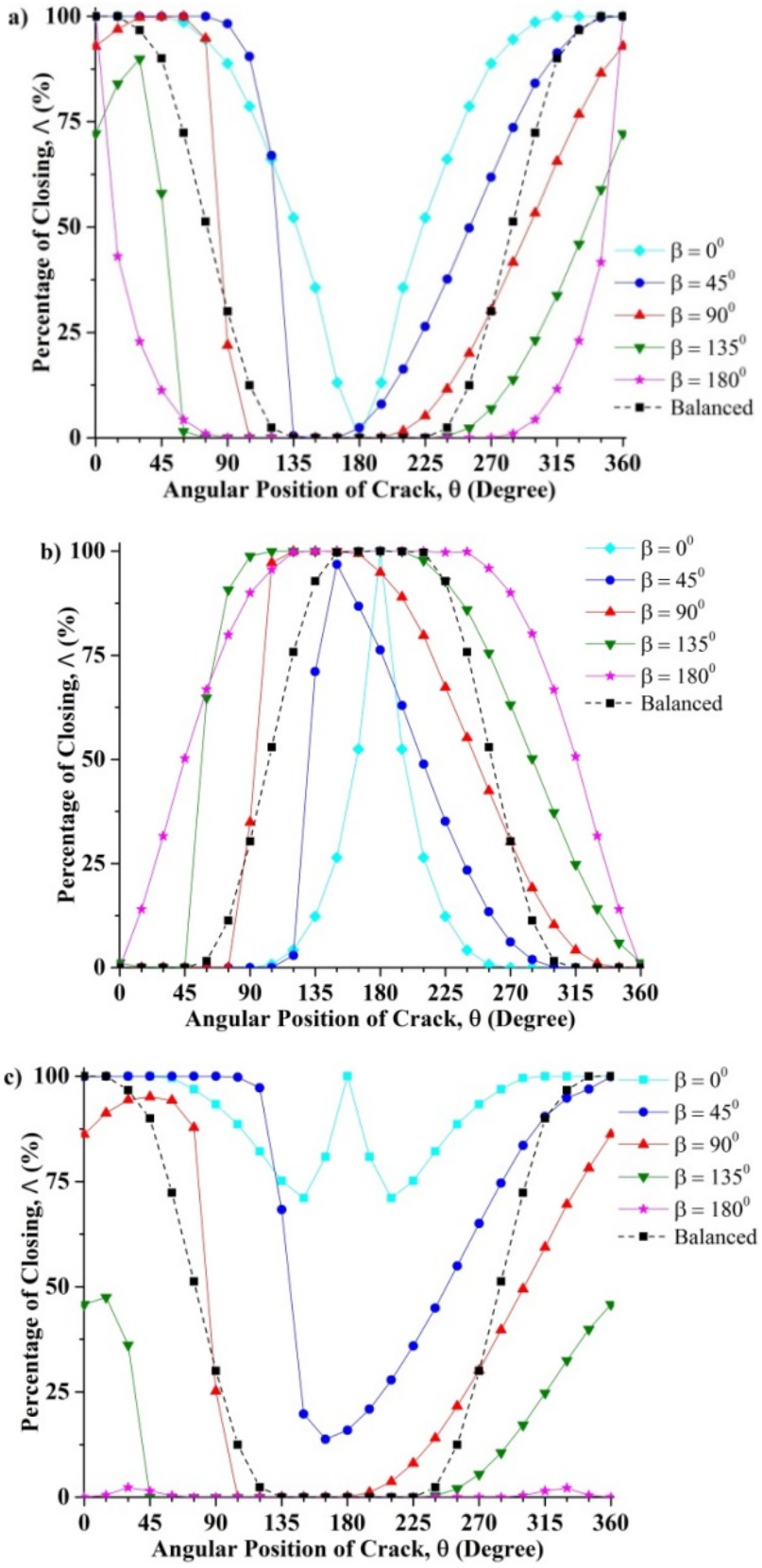

Figure 7-14: Effect of unbalance force orientation on crack breathing behaviour at (a) 0.125*L* (b) 0.5*L* and (c) 0.875*L*

The original direction of the unbalance force will generate a significant effect on the vibration of the cracked shaft as observed previously. Cheng et al., (2011) found that the unbalance orientation played an important role in the peak amplitude of the vibration, where the minimum and maximum vibration amplitude corresponded to the eccentric mass being located at and opposite the crack, respectively.

7.4 Summary

In this chapter, a series of analyses were performed using 3D FEM. Throughout the chapter, the focus was on the effects of different combinations of the crack location along the shaft length, different crack angular positions, different unbalance force ratios and different angular positions of unbalance force on the elliptical crack breathing behaviour. Compared with the symmetrical three-status breathing behaviour for the balance shaft, notably different crack breathing behaviours were identified for the unbalance shaft. The crack in an unbalance shaft shows more breathing patterns, including single status, dual statuses and unsymmetrical behaviour.

The present model can be further extended to obtain the local stiffness matrix of the cracked shaft element with an elliptical crack and then to study the nonlinear dynamic phenomena near the shaft critical speeds or the vibration response with a large unbalance force.

Chapter 8 : Conclusions and Recommendations

8.1 Conclusions

The breathing phenomenon is one of the crucial characteristics of the cracked shaft. It attracts many researchers to focus on it for studying cracked shaft diagnostics. Unfortunately, most researchers relied on simplifying the crack breathing mechanism to obtain the local stiffness matrix of a cracked shaft element and then to calculate the vibration response by solving the equations of motion of the system.

In Chapter 3, a new unbalance model is developed to describe the nonlinear relationship between shaft bending direction and the crack direction. This new model is developed considering the effects of unbalance force, rotor weight, rotor physical and dimensional properties and a more realistic fixed-end boundary condition. It is developed to analyse crack breathing behaviour and to calculate the area moment of inertia of a cracked shaft. The developed model can be further used by other researchers and engineers to obtain local stiffness matrix of a cracked shaft element to predict the vibration response of a cracked rotor and to develop the online crack detection technique, in particular, near the shaft critical speeds or where the rotor-weight-dominant assumption on the crack breathing no longer holds.

The new proposed unbalance model is used to study the actual breathing mechanisms of the transverse fatigue crack in a cracked rotor system. The results are also compared with those of the existing balance model, where only rotor weight is considered. It is identified that a crack in the unbalance model breathes differently from one in the balance model. A crack's breathing mechanism in the unbalance model depends strongly on its location along shaft length. An unbalance shaft is just like an uncracked shaft when the crack is at $\lambda = 0.1946$ and a crack at $\lambda = 0.8053$ is just like a notch and will never close, which will never occur in a balance model. It also behaves completely like one in the balance shaft when the crack is at $\lambda = 0.3$ and $\lambda = 0.8335$. Depending on the crack location, unbalance force magnitude and orientation, the unbalance shaft may be stiffer or more flexible than the balance counterpart. It is also demonstrated that the unbalance model will progressively approach the balance one as unbalance force decreases. Further, different crack breathing mechanisms between two models lead to a large difference along shaft

length in the second area moment of inertia, which forms the elements of local stiffness matrix at the crack location. It is expected that more accurate prediction of the vibration response of a cracked rotor can be achieved when the effect of unbalance force and rotor properties on the crack breathing have been taken into account.

The research presented in Chapter 4 is related to Section 3.4 of Chapter 3, in that a more accurate approach is developed to study the crack breathing mechanism under different weight–unbalance force ratios at different crack locations. This is performed by applying first principals to calculate the second area moment of the irregular cross-section of a breathing crack. Two assumptions used previously are discarded in the process. These are collinearity of the neutral axis and applied bending moment at the crack. Finite element simulations of a cracked shaft subjected to identical loading conditions are used to validate the analytical results. The proposed method results are also compared with the results in Section 3.4 of Chapter 3. Excellent agreement is found between the proposed method and FEM analysis method. It has improved accuracy compared with the results in Section 3.4 of Chapter 3.

The analysis presented in Section 3.5 of Chapter 3 is improved in Chapter 5. To calculate the area moment of inertia at the cracked cross-section of the unbalance shaft, a more accurate approach is developed. Once the crack transitions into a partially closed state, the cross-section geometry is more complex. The orientation of the neutral axis and the coordinates of the centroid of bending are determined using an iterative process. A series of double integrals together with the parallel axis theorem are utilised to precisely calculate the second area moment and the product of area as a function of angular displacement for a continuously rotating shaft. The orientation of the neutral axis is also tracked in the finite element simulations. Both metrics indicate a significant improvement in accuracy when using the proposed method of calculating the second area moment.

In Chapter 6, breathing behaviours of a slant crack in a two-disk-rotor are investigated using the 3D FEM. A large number of simulations are performed to examine the effects of crack location, crack angular position, unbalance force ratio and its angular position on the crack opening and closing. The results are also

compared with those of the balance shaft. Steady-state centroidal orbits of a crack cross-section for unbalance shaft under some configurations are also simulated. The breathing of a crack in the balance shaft is basically independent of crack location with its initial status being opposite at different shaft ranges, showing that the overall stiffness of the balance cracked shaft remains unchanged throughout the shaft length. In the unbalance shaft, crack breathing during shaft rotation is strongly influenced by the unbalance force, and thus, it behaves differently on varying its location. A crack would remain fully closed at $\lambda = 0.2$ and fully open at $\lambda = 0.8$, which will never occur in the balance shaft. A crack at $\lambda = 0.3$ and $\lambda = 0.825$ would exhibit the same breathing behaviour as in the balance shaft.

There exist three regions along the shaft length. In the middle region between $\lambda = 0.3$ and $\lambda = 0.825$, the overall stiffness of the unbalance cracked shaft is higher than that of a balance one when the unbalance force angle β relative to the crack is between 90° and 270°, where an unbalance force tends to close a crack. Further, the unbalance shaft has a lower stiffness than the balance counterpart when the unbalance force angle is in the range of 0° to 90° or 270° to 360°, where an unbalance force tends to open a crack. All these trends reverse if a crack is situated between $\lambda = 0$ and $\lambda = 0.3$, or between $\lambda = 0.825$ and $\lambda = 1$. Further, when the unbalance force angle is $\beta = 90°$ or $\beta = 270°$, the overall stiffness between the unbalance and balance shafts shows little difference. Finally, the proposed unbalance shaft model agrees excellently with the existing balance model when the unbalance force has a small value.

In Chapter 7, an unbalance shaft with an elliptical crack is simulated using Abaqus/standard for analysis of the crack breathing mechanism. Cracks at different locations along the shaft length and at different angular positions with a fixed reference are considered to analyse the effect of crack locations. The influence of unbalance force and angular position of unbalance force relative to the crack direction are investigated. It is found that a crack in the unbalance shaft has more breathing patterns than a crack in the balance shaft, including single status, dual statuses and unsymmetrical behaviour. A few specific crack locations along the shaft length are identified, where the crack may remain fully closed or open during shaft rotation under some loading conditions. The breathing behaviours for the elliptical

crack at special locations are the same as those for a straight crack, as shown in Chapter 3, and a slant crack, as shown in Chapter 6, with an identical rotor.

However, the shaft stiffness based on variations of the crack breathing behaviour along the shaft length depends on a combination of crack location, angular position of crack, unbalance force ratio and angular position of unbalance force found in three regions that differs from the combination for the balance shaft. When the crack is located in the middle region ($\lambda = 0.3$ to $\lambda = 0.825$) and the angular position of an unbalance force is between 90° to 270°, the unbalance shaft is stiffer, and it is flexible when the crack located in two side regions. Conversely, when the crack is in the middle region and the angular position of an unbalance force is between 0° to 90° or 270° to 360°, the unbalance shaft is flexible, and it is stiffer when the crack is located in two side regions.

The presented research in this thesis reveals that crack breathing—unlike weight-dominated crack breathing—is largely influenced by the unbalance force and the individual rotor physical parameters, generating a dependence of crack breathing on its location at the shaft. This research provides important insights into the modelling of local stiffness matrix through crack breathing. This matrix is usually used to calculate the dynamic response of cracked rotors. Based on the steady-state dynamic analysis, it is demonstrated that for more accurate prediction of the dynamic response and damage severity of cracked rotors, researchers must consider the effects of unbalance force and individual rotor physical properties on the crack breathing.

8.2 Recommendations for Future Research

The research presented in this thesis is a quasistatic analysis of crack breathing functions under the effect of unbalance force and extends our understanding of the field. However, crack breathing is very complicated and can be affected by many other factors, and in particular, by vibration-induced effects such as shaft whirling, excited by unbalance force and gyroscopic moment. Under some vibration conditions, these effects on the shaft bending angle may no longer be ignored. As such, vibration-induced crack breathing should be an interesting area for further research.

The area moment of inertia constitutes the elements of the local stiffness matrix of a cracked shaft. The cracked shaft vibration response can be calculated numerically by solving the equations of system motion. The presented method and results in this research can be further extended to obtain the local stiffness matrix of the cracked shaft element and then to study the nonlinear dynamic phenomena near shaft critical speeds, or to predict the vibration response with large unbalance force or to develop the online crack detection techniques. For example, the presented method and results in this research can be applied to general rotating shafts, such as industrial turbine generators, to develop more accurate online crack detection techniques.

The intended application of the breathing function equations presented in Chapters 3, 4 and 5 is for modelling dynamic cracked rotor systems. Consider a shaft composed of N beam finite elements with a crack located at the centre of element C.

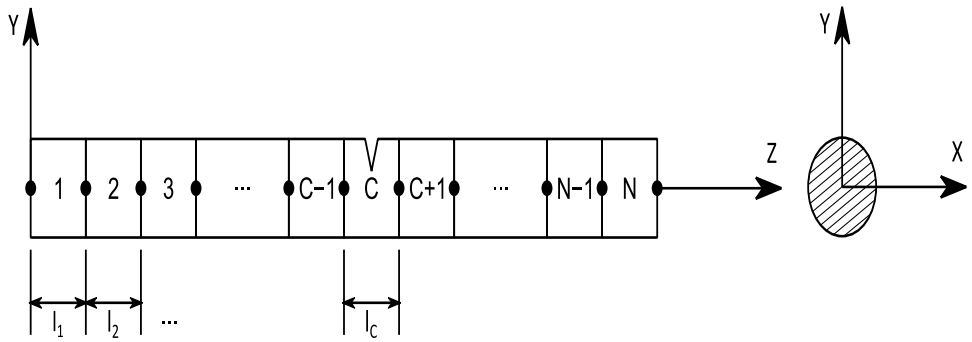

Figure 8-1: Finite element model of a cracked shaft using beam elements

The equation of motion for the shaft shown in Figure 8-1 is:

$$\boldsymbol{M}\ddot{\boldsymbol{q}}(t) + \boldsymbol{C}\dot{\boldsymbol{q}}(t) + \boldsymbol{K}\boldsymbol{q}(t) = \boldsymbol{F} \qquad (8\text{-}1)$$

where $\boldsymbol{M}$, $\boldsymbol{C}$ and $\boldsymbol{K}$ are the mass matrix, gyroscopic and damping matrix and stiffness matrix respectively. $\boldsymbol{F}$ is the nodal load vector, which in a balance rotor contains only the nodal gravitational force elements. In an unbalance rotor, $\boldsymbol{F}$ becomes a time-varying vector owing to the rotation of the eccentric mass. Lastly, $\boldsymbol{q}$ is the nodal displacement vector of the model.

In this type of analysis, the influence of the crack is accounted for by reduction in the stiffness of element C, the crack element shown in Figure 8-1. Equation (8-1) is typically solved numerically using the Runge–Kutta method or a similar method. The stiffness matrix of the cracked element should be revaluated at each time step based on the crack state resulting from the previous time step. The local stiffness matrix of the uncracked elements of the shaft is given by Equation (8-2).

$$\boldsymbol{K}_i = \frac{E}{{l_i}^3}\begin{bmatrix} 12I & 0 & 0 & 6l_iI & -12l_iI & 0 & 0 & 6l_iI \\ 0 & 12I & 6l_iI & 0 & 0 & -12I & -6l_iI & 0 \\ 0 & -6l_iI & 4{l_i}^2I & 0 & 0 & 6l_iI & 2{l_i}^2I & 0 \\ 6l_iI & 0 & 0 & 4{l_i}^2I & -6l_iI & 0 & 0 & 2{l_i}^2I \\ -12l_iI & 0 & 0 & 6l_iI & 12I & 0 & 0 & -6l_iI \\ 0 & -12I & 6l_iI & 0 & 0 & 12I & 6l_iI & 0 \\ 0 & -6l_iI & 2{l_i}^2I & 0 & 0 & 6l_iI & 4{l_i}^2I & 0 \\ 6l_iI & 0 & 0 & 2{l_i}^2I & -6l_iI & 0 & 0 & 4{l_i}^2I \end{bmatrix} \qquad (8\text{-}2)$$

The equation for $\boldsymbol{K}_i$ is a simplification of the more general beam element stiffness matrix found in texts on finite element analysis (Cook, 2007). The general stiffness matrix presented by Cook (2007) and others is for beams with their sectional principal axes aligned with the coordinate axes of the model. This general stiffness matrix can be applied to the cracked element if the principal area moment of inertia are known.

$$\boldsymbol{K}_P = \frac{E}{{l_i}^3}\begin{bmatrix} 12I_{\bar{U}} & 0 & 0 & 6l_cI_{\bar{U}} & -12l_cI_{\bar{U}} & 0 & 0 & 6l_cI_{\bar{U}} \\ 0 & 12I_{\bar{V}} & 6l_cI_{\bar{V}} & 0 & 0 & -12I_{\bar{V}} & -6l_cI_{\bar{V}} & 0 \\ 0 & -6l_cI_{\bar{V}} & 4{l_c}^2I_{\bar{V}} & 0 & 0 & 6l_cI_{\bar{V}} & 2{l_c}^2I_{\bar{V}} & 0 \\ 6l_cI_{\bar{U}} & 0 & 0 & 4{l_c}^2I_{\bar{U}} & -6l_cI_{\bar{U}} & 0 & 0 & 2{l_c}^2I_{\bar{U}} \\ -12l_cI_{\bar{U}} & 0 & 0 & 6l_cI_{\bar{U}} & 12I_{\bar{U}} & 0 & 0 & -6l_cI_{\bar{U}} \\ 0 & -12I_{\bar{V}} & 6l_cI_{\bar{V}} & 0 & 0 & 12I_{\bar{V}} & 6l_cI_{\bar{V}} & 0 \\ 0 & -6l_cI_{\bar{V}} & 2{l_c}^2I_{\bar{V}} & 0 & 0 & 6l_cI_{\bar{V}} & 4{l_c}^2I_{\bar{V}} & 0 \\ 6l_cI_{\bar{U}} & 0 & 0 & 2{l_c}^2I_{\bar{U}} & -6l_cI_{\bar{U}} & 0 & 0 & 4{l_c}^2I_{\bar{U}} \end{bmatrix} \quad (8\text{-}3)$$

The angular offset, ψ, between the principal axes and the coordinate axes of the model is required to perform a coordinate rotation on $\boldsymbol{K}_P$. The transformation matrix $\boldsymbol{T}$ is given by Equation (8-4):

$$\boldsymbol{T} = \begin{bmatrix} \cos\alpha & \sin\alpha & 0 & 0 & 0 & 0 & 0 & 0 \\ -\sin\alpha & \cos\alpha & 0 & 0 & 0 & 0 & 0 & 0 \\ 0 & 0 & \cos\alpha & \sin\alpha & 0 & 0 & 0 & 0 \\ 0 & 0 & -\sin\alpha & \cos\alpha & 0 & 0 & 0 & 0 \\ 0 & 0 & 0 & 0 & \cos\alpha & \sin\alpha & 0 & 0 \\ 0 & 0 & 0 & 0 & -\sin\alpha & \cos\alpha & 0 & 0 \\ 0 & 0 & 0 & 0 & 0 & 0 & \cos\alpha & \sin\alpha \\ 0 & 0 & 0 & 0 & 0 & 0 & -\sin\alpha & \cos\alpha \end{bmatrix} \quad (8\text{-}4)$$

The coordinate transformation is performed using Equation (8-5).

$$\boldsymbol{K}_C = \boldsymbol{T} \times \boldsymbol{K}_P \times \boldsymbol{T}^T \quad (8\text{-}5)$$

The stiffness matrix $\boldsymbol{K}_C$ pertains to the cracked element and is about the fixed global coordinate axes; hence, it can be used in assembling the global stiffness matrix. Alternatively, if the area moment of inertia and the product of area for the crack section are known, $\boldsymbol{K}_c$ can be evaluated directly using Equation (8-6) (Al-Shudeifat, 2013).

$$\boldsymbol{K}_c = \frac{E}{{l_c}^3}\begin{bmatrix} 12I_{\bar{X}} & -12I_{\overline{XY}} & 6l_cI_{\overline{XY}} & 6l_cI_{\bar{X}} & -12l_cI_{\bar{X}} & 12I_{\overline{XY}} & 6l_cI_{\overline{XY}} & 6l_cI_{\bar{X}} \\ -12I_{\overline{XY}} & 12I_{\bar{Y}} & 6l_cI_{\bar{Y}} & -6l_cI_{\overline{XY}} & 12I_{\overline{XY}} & -12I_{\bar{Y}} & -6l_cI_{\bar{Y}} & -6l_cI_{\overline{XY}} \\ 6l_cI_{\overline{XY}} & -6l_cI_{\bar{Y}} & 4{l_c}^2I_{\bar{Y}} & 4{l_c}^2I_{\overline{XY}} & -6l_cI_{\overline{XY}} & 6l_cI_{\bar{Y}} & 2{l_c}^2I_{\bar{Y}} & 2{l_c}^2I_{\overline{XY}} \\ 6l_cI_{\bar{X}} & -6l_cI_{\overline{XY}} & 4{l_c}^2I_{\overline{XY}} & 4{l_c}^2I_{\bar{X}} & -6l_cI_{\bar{X}} & 6l_cI_{\overline{XY}} & 2{l_c}^2I_{\overline{XY}} & 2{l_c}^2I_{\bar{X}} \\ -12l_cI_{\bar{X}} & 12I_{\overline{XY}} & -6l_cI_{\overline{XY}} & 6l_cI_{\bar{X}} & 12I_{\bar{X}} & -12I_{\overline{XY}} & -6l_cI_{\overline{XY}} & -6l_cI_{\bar{X}} \\ 12I_{\overline{XY}} & -12I_{\bar{Y}} & 6l_cI_{\bar{Y}} & 6l_cI_{\overline{XY}} & -12I_{\overline{XY}} & 12I_{\bar{Y}} & 6l_cI_{\bar{Y}} & 6l_cI_{\overline{XY}} \\ 6l_cI_{\overline{XY}} & -6l_cI_{\bar{Y}} & 2{l_c}^2I_{\bar{Y}} & 2l^2I_{\overline{XY}} & -6l_cI_{\overline{XY}} & 6l_cI_{\bar{Y}} & 4{l_c}^2I_{\bar{Y}} & 4{l_c}^2I_{\overline{XY}} \\ 6l_cI_{\bar{X}} & -6l_cI_{\overline{XY}} & 2{l_c}^2I_{\overline{XY}} & 2l^2I_{\bar{X}} & -6l_cI_{\bar{X}} & 6l_cI_{\overline{XY}} & 4{l_c}^2I_{\overline{XY}} & 4{l_c}^2I_{\bar{X}} \end{bmatrix} \quad (8\text{-}6)$$

The equations presented in Chapter 5 can be used to obtain the principal area moment of inertia, the area moment of inertia and product of area for use with Equations (8-4) or (8-5) respectively. Then the vibration response of the cracked rotor can be calculated numerically using Equation (8-1).

Furthermore, the equations presented in Chapter 5 to calculate the accurate values of area moment of inertia can be used to obtain a set of approximations equations base on low order Fourier series. Evaluating the low order Fourier series will, much less computationally expensive than calculating the exact values with only a slight loss in accuracy, make it better suited to dynamic studies that require time-based numerical integration of nodal displacements. The area moments of inertia about the non-rotating centroid axes as showed in Chapter 5 relatively complex shapes. Approximating these functions using Fourier series would be difficult. However, the area moments of inertia and the product of inertia can be fully described by the principle area moments of inertia if both principle area moments, and the orientation of the principle axes are known. Equations for calculating both are given in Chapter 5. The shapes of the principle area moment of inertia curves will be relatively straight forward which will advantageous for deriving the Fourier series. The coefficients of the Fourier series will be functions of two critical shaft rotation angles. The first being the angle at which the crack transitions from a fully open state to a partially closed one. The second is when the crack has fully closed. Equations for calculating the two critical shaft rotation angles are given in Chapter 4.

The presented work in this thesis is based on the analytical study of crack breathing behaviours under different mechanical conditions. However, as mentioned above the crack breathing is very complicated and can be affected by many other factors, and in particular, by vibration-induced effects such as shaft whirling, excited by unbalance force and gyroscopic moment. Under some vibration conditions, these effects on the crack breathing behaviours may no longer be ignored. So, to provide further verification of new findings in this work, the experimental study should be an interesting area for further research.

After vibration responses of the cracked rotor are obtained, further work can be done to develop the crack detection technique to identify crack location and depth by comparing vibration characteristics of the cracked rotor with varying crack location

and depth. With the accurate crack breathing mechanism under a general unbalance force being established in this thesis, it is expected that more accurate crack detection is possible, in particular, at the early stage of the fatigue crack growth.

References

A.D.Dimarogonas. (1996). Vibration of cracked structures: a state of the art review. *Engineering Fracture Mechanics, 55*, 831–857.

Adams, M. (2010). Rotating Machinery Vibration: From Analysis To Troubleshooting, Second Edition. *CRC Press*.

Al-Shudeifat, M. A. (2013). On the finite element modeling of the asymmetric cracked rotor. *Journal of Sound and Vibration, 332*(11), 2795-2807. doi:http://dx.doi.org/10.1016/j.jsv.2012.12.026

Al-Shudeifat, M. A., & Butcher, E. A. (2011). New breathing functions for the transverse breathing crack of the cracked rotor system: Approach for critical and subcritical harmonic analysis. *Journal of Sound and Vibration, 330*(3), 526-544. doi:http://dx.doi.org/10.1016/j.jsv.2010.08.022

Al-Shudeifat, M. A., Butcher, E. A., & Stern, C. R. (2010). General harmonic balance solution of a cracked rotor-bearing-disk system for harmonic and sub-harmonic analysis: Analytical and experimental approach. *International Journal of Engineering Science, 48*(10), 921-935.

Andreaus, U., Baragatti, P., Casini, P., & Iacoviello, D. (2017). Experimental damage evaluation of open and fatigue cracks of multi-cracked beams by using wavelet transform of static response via image analysis. *Structural Control and Health Monitoring, 24*(4), 1-16.

Anvari, M., Scheider, I., & Thaulow, C. (2006). Simulation of dynamic ductile crack growth using strain-rate and triaxiality-dependent cohesive elements. *Engineering Fracture Mechanics, 73*, 2210–2228.

Arem, S. E., & Maitournam, H. (2008). A cracked beamfinite element for rotating shaft dynamics and stability analysis. *Journal of Mechanics of Materials and Structures, 3*, 893-910.

Bachschmid, N., P.Pennacchi, & E.Tanzi. (2010). On the evolution of vibrations in cracked rotors. *Proceedings of the Eighth IFToMM International Conference on Rotor Dynamics, Seoul, Korea*, 304-310.

Bachschmid, N., & Pennacchi, P. (2008). Crack effects in rotordynamics. *Mechanical Systems and Signal Processing, 22*(4), 761-762. doi:http://dx.doi.org/10.1016/j.ymssp.2007.11.003

Bachschmid, N., Pennacchi, P., & Tanzi, E. (2010). *Cracked rotors: a survey on static and dynamic behaviour including modelling and diagnosis*: Springer Science & Business Media.

Bachschmid, N., Pennacchi, P., & Tanzi, E. (2010). A sensitivity analysis of vibrations in cracked turbogenerator units versus crack position and depth. *Mechanical Systems and Signal Processing, 24*(3), 844-859. doi:http://dx.doi.org/10.1016/j.ymssp.2009.10.001

Bachschmid, N., Pennacchi, P., Tanzi, E., & Vania, A. (2000). Identification of transverse crack position and depth in rotor systems. *Meccanica, 35*(6), 563-582. doi:10.1023/a:1010562205385

Bachschmid, N., Pennacchi, P., & Vania, A. (2002). IDENTIFICATION OF MULTIPLE FAULTS IN ROTOR SYSTEMS. *Journal of Sound and Vibration, 254*(2), 327-366. doi:http://dx.doi.org/10.1006/jsvi.2001.4116

Bachschmid, N., & Tanzi, E. (2004). Deflections and strains in cracked shafts due to rotating loads: a numerical and experimental analysis. *International Journal of Rotating Machinery, 10*(4), 283-291.

Barenblatt, G. I. (1962). The Mathematical Theory of Equilibrium Cracks in Brittle Fracture. In T. v. K. G. K. F. H. v. d. D. H.L. Dryden & L. Howarth (Eds.), *Advances in Applied Mechanics* (Vol. Volume 7, pp. 55-129): Elsevier.

Batra, U. (2010). Failure analysis of steam turbine rotor disk. *Journal of Failure Analysis and Prevention, 10*(3), 178-182. doi:10.1007/s11668-010-9344-9

Bouboulas, A. S., & Anifantis, N. K. (2011). Finite element modeling of a vibrating beam with a breathing crack: observations on crack detection. *Structural HealthMonitoring, 10*, 131–145.

Bovsunovsky, A., & Surace, C. (2015). Non-linearities in the vibrations of elastic structures with a closing crack: A state of the art review. *Mechanical Systems and Signal Processing, 62–63*, 129-148. doi:http://dx.doi.org/10.1016/j.ymssp.2015.01.021

C.A.Papadopoulos. (2008). The strain energy release approach for modelling cracks in rotors: a state of the art review. *Mechanical Systems and Signal Processing, 22*, 763-789.

Chan, R., & Lai, T. (1995). Digital simulation of a rotating shaft with a transverse crack. *Applied Mathematical Modelling, 19*(7), 411-420.

Cheng, L., Li, N., Chen, X.-F., & He, Z.-J. (2011). The influence of crack breathing and imbalance orientation angle on the characteristics of the critical speed of a cracked rotor. *Journal of Sound and Vibration, 330*(9), 2031-2048. doi:http://dx.doi.org/10.1016/j.jsv.2010.11.012

Cheng, L., Qian, Z., Zhao, B., & Zhang, H. (2010). Influence of nonlinear breathing behavior on the stability of a jeffcott rotor with transverse crack. *Yingyong Lixue Xuebao/Chinese Journal of Applied Mechanics, 27*(2), 219-225.

Cook, R. D. (2007). *Concepts and applications of finite element analysis*: John Wiley & Sons.

Darpe, A. K. (2007). A novel way to detect transverse surface crack in a rotating shaft. *Journal of Sound and Vibration, 305*(1–2), 151-171. doi:http://dx.doi.org/10.1016/j.jsv.2007.03.070

Darpe, A. K., Gupta, K., & Chawla, A. (2004). Transient response and breathing behaviour of a cracked Jeffcott rotor. *Journal of Sound and Vibration, 272*(1–2), 207-243. doi:http://dx.doi.org/10.1016/S0022-460X(03)00327-4

Darpe, A. K., Gupta, K., & Chawla, A. (2006). Dynamics of a bowed rotor with a transverse surface crack. *Journal of Sound and Vibration, 296*(4–5), 888-907. doi:http://dx.doi.org/10.1016/j.jsv.2006.03.013

Darpe, A. K., K.Gupta, & A.Chawla. (2004). Coupled bending, longitudinal and torsional vibrations of a cracked rotor. *Journal of Sound and Vibration, 269*, 33-60.

Dimarogonas, A., & Papadopoulos, C. (1983). Vibration of cracked shafts in bending. *Journal of Sound and Vibration, 91*(4), 583-593.

Dimarogonas, A. D., & Paipetis, S. A. (1983). Analytical Methods in RotorDynamics. *Applied Science Publishers, London, UK*.

Dong, G. M., Chen, J., & Zou, J. (2004). Parameter identification of a rotor with an open crack. *European Journal of Mechanics - A/Solids, 23*(2), 325-333. doi:http://dx.doi.org/10.1016/j.euromechsol.2003.11.003

Fayed, A. (2017). Numerical analysis of mixed mode I/II stress intensity factors of edge slant cracked plates. *Engineering Solid Mechanics, 5*(1), 61-70.

Gasch, R. (1993). A Survey Of The Dynamic Behaviour Of A Simple Rotating Shaft With A Transverse Crack. *Journal of Sound and Vibration, 160*(2), 313-332. doi:http://dx.doi.org/10.1006/jsvi.1993.1026

Gasch, R. (2008). Dynamic behaviour of the Laval rotor with a transverse crack. *Mechanical Systems and Signal Processing, 22*(4), 790-804. doi:http://dx.doi.org/10.1016/j.ymssp.2007.11.023

Giannopoulos, G. I., Georgantzinos, S. K., & Anifantis, N. K. (2015). Coupled vibration response of a shaft with a breathing crack. *Journal of Sound and Vibration, 336*, 191-206. doi:http://dx.doi.org/10.1016/j.jsv.2014.09.037

Gómez-Mancilla, J., Sinou, J.-J., Nosov, V. R., Thouverez, F., & Zambrano, A. (2004). The influence of crack-imbalance orientation and orbital evolution for an extended cracked Jeffcott rotor. *Comptes Rendus Mécanique, 332*(12), 955-962. doi:http://dx.doi.org/10.1016/j.crme.2004.09.007

Grabowski, B. (1984). The vibrational behaviour of a rotating shaft containing a transverse crack. *Dynamics of rotors—-stability and system identification*, 423-465.

Gradshteyn, I. S., & Ryzhik, I. M. (2014). *Table of integrals, series, and products*: Academic press.

Green, I., & Casey, C. (2005). Crack detection in a rotor dynamic system by vibration monitoring - Part I: Analysis. *Journal of Engineering for Gas Turbines and Power, 127*(2), 425-436. doi:10.1115/1.1789514

Guo, C., Al-Shudeifat, M. A., Yan, J., Bergman, L. A., McFarland, D. M., & Butcher, E. A. (2013). Stability analysis for transverse breathing cracks in rotor systems. *European Journal of Mechanics - A/Solids, 42*(0), 27-34. doi:http://dx.doi.org/10.1016/j.euromechsol.2013.04.001

Guo, D., & Peng, Z. K. (2007). Vibration analysis of a cracked rotor using Hilbert–Huang transform. *Mechanical Systems and Signal Processing, 21*(8), 3030-3041. doi:http://dx.doi.org/10.1016/j.ymssp.2007.05.004

Guo, J., Huang, X., & Cui, Y. (2009). Design and analysis of robust fault detection filter using LMI tools. *Computers & Mathematics with Applications, 57*(11), 1743-1747.

Han, Q., & Chu, F. (2012). Parametric instability of a rotor-bearing system with two breathing transverse cracks. *European Journal of Mechanics - A/Solids, 36*(0), 180-190. doi:http://dx.doi.org/10.1016/j.euromechsol.2012.03.003

Han, Q., Zhao, J., Lu, W., Peng, Z., & Chu, F. (2014). Steady-state response of a geared rotor system with slant cracked shaft and time-varying mesh stiffness. *Communications in Nonlinear Science and Numerical Simulation, 19*(4), 1156-1174. doi:http://dx.doi.org/10.1016/j.cnsns.2013.08.018

Hou, L., Chen, Y., Cao, Q., & Lu, Z. (2016). Nonlinear vibration analysis of a cracked rotor-ball bearing system during flight maneuvers. *Mechanism and Machine Theory, 105*, 515-528. doi:http://dx.doi.org/10.1016/j.mechmachtheory.2016.07.024

Ishida, Y. (2008). Cracked rotors: Industrial machine case histories and nonlinear effects shown by simple Jeffcott rotor. *Mechanical Systems and Signal Processing, 22*(4), 805-817. doi:http://dx.doi.org/10.1016/j.ymssp.2007.11.005

Ishida, Y., & Yamamoto, T. (2013). Linear and Nonlinear Rotordynamics : A Modern Treatment with Applications. *Wiley, Hoboken.*

Ishida, Y., & Yamamoto, T. (2013). Linear and Nonlinear Rotordynamics: A Modern Treatment with Applications, Second Edition. *Wiley-VCH Verlag GmbH & Co. KGaA.*

J.J.Sinou, & A.W.Lees. (2007). A nonlinear study of a cracked rotor. *European Journal of Mechanics A: Solids, 26*, 152-170.

J.S.Rao. (2011). History of Rotating Machinery Dynamics. *Springer-Verlag, Berlin.*

J.T.Sawicki, M.I.Friswell, Z.Kulesza, A.Wroblewski, & J.D.Lekki. (2011). Detecting cracked rotors using auxiliary harmonic excitation. *Journal of Sound and Vibration, 330*, 1365–1381.

Jain, A. K., Rastogi, V., & Agrawal, A. K. (2016). Experimental Investigation of Vibration Analysis of Multi-Crack Rotor Shaft. *Procedia Engineering, 144*, 1451-1458. doi:http://dx.doi.org/10.1016/j.proeng.2016.05.177

Jain, J. R., & Kundra, T. K. (2004). Model based online diagnosis of unbalance and transverse fatigue crack in rotor systems. *Mechanics Research Communications, 31*(5), 557-568. doi:http://dx.doi.org/10.1016/j.mechrescom.2003.11.002

Jun, O. S., & Gadala, M. S. (2008). Dynamic behavior analysis of cracked rotor. *Journal of Sound and Vibration, 309*(1–2), 210-245. doi:http://dx.doi.org/10.1016/j.jsv.2007.06.065

Kulesza, Z., Sawicki, J., & Gyekenyesi, A. L. (2012). Robust fault detection filter using linear matrix inequalities' approach for shaft crack diagnosis. *Journal of Vibration and Control*, 1077546312447838.

Kulesza, Z., & Sawicki, J. T. (2012). Rigid finite element model of a cracked rotor. *Journal of Sound and Vibration, 331*, 4145–4169.

Kumar, C., & Rastogi, V. (2009). A brief review on dynamics of a cracked rotor. *International Journal of Rotating Machinery*, 6.

Lee, J., Wu, F., Zhao, W., Ghaffari, M., Liao, L., & Siegel, D. (2014). Prognostics and health management design for rotary machinery systems—Reviews, methodology and applications. *Mechanical Systems and Signal Processing, 42*(1–2), 314-334. doi:http://dx.doi.org/10.1016/j.ymssp.2013.06.004

Lees, A., & Friswell, M. (1997). The evaluation of rotor imbalance in flexibly mounted machines. *Journal of Sound and Vibration, 208*(5), 671-683.

Lin, Y., & Chu, F. (2010). The dynamic behavior of a rotor system with a slant crack on the shaft. *Mechanical Systems and Signal Processing, 24*(2), 522-545. doi:http://dx.doi.org/10.1016/j.ymssp.2009.05.021

Liong, R. T., & CarstenProppe. (2013). Application of the cohesive zone model for the evaluation of stiffness losses in a rotor with a transverse breathing crack *Journal of Sound and Vibration, 332*, 2098–2110.

Liong, R. T., & Proppe, C. (2011). Cohesive zone model for a transverse breathing crack in a rotor. *Proc. Appl. Math. Mech., 11*, 163 – 164. doi:DOI 10.1002/pamm.201110073

Liong, R. T., & Proppe, C. (2013). Finite Element Multi body Simulation of a Breathing Crack in a Rotor with a Cohesive Zone Model. *ISRN Mechanical Engineering, Article ID 249035*. doi:http://dx.doi.org/10.1155/2013/249035

Mayes, I., & Davies, W. (1984). Analysis of the response of a multi-rotor bearing system containing a transverse crack in a rotor. *Journal of Vibration, Acoustics, Stress and Reliabilityin Design, 106*, 139–145.

Mobley, R. K. (2002). Plant Engineering : An Introduction to Predictive Maintenance. *Butterworth-Heinemann, Burlington, MA, USA., 2nd Edition*.

Nandi, A. (2004). Reduction of finite element equations for a rotor model on non-isotropic spring support in a rotating frame. *Finite Elements in Analysis and Design, 40*(9–10), 935-952. doi:http://dx.doi.org/10.1016/S0168-874X(03)00121-5

Nayfeh, A. H., & Mook, D. T. (2008). *Nonlinear oscillations*: John Wiley & Sons.

Papadopoulos, C. A. (2004). Some comments on the calculation of the local flexibility of cracked shafts. *Journal of Sound and Vibration, 278*(4–5), 1205-1211. doi:http://dx.doi.org/10.1016/j.jsv.2003.12.023

Papadopoulos, C. A. (2008). The strain energy release approach for modeling cracks in rotors: A state of the art review. *Mechanical Systems and Signal Processing, 22*(4), 763-789. doi:http://dx.doi.org/10.1016/j.ymssp.2007.11.009

Papadopoulos, C. A., & Dimarogonas, A. D. (1987a). Coupled longitudinal and bending vibrations of a rotating shaft with an open crack. *Journal of Sound and Vibration, 117*(1), 81-93. doi:http://dx.doi.org/10.1016/0022-460X(87)90437-8

Papadopoulos, C. A., & Dimarogonas, A. D. (1987b). *STABILITY OF CRACKED ROTORS IN THE COUPLED VIBRATION MODE.* Paper presented at the American Society of Mechanical Engineers, Design Engineering Division (Publication) DE.

Patel, T. H., & Darpe, A. K. (2008). Vibration response of a cracked rotor in presence of rotor–stator rub. *Journal of Sound and Vibration, 317*(3–5), 841-865. doi:http://dx.doi.org/10.1016/j.jsv.2008.03.032

Pennacchi, P., Bachschmid, N., & Vania, A. (2006). A model-based identification method of transverse cracks in rotating shafts suitable for industrial machines. *Mechanical Systems and Signal Processing, 20*(8), 2112-2147.

Penny, J., & Friswell, M. I. (2003). *Simplified modelling of rotor cracks.* Paper presented at the Key Engineering Materials.

Pilkey, W. D. (2002). *Analysis and design of elastic beams: Computational methods*: John Wiley & Sons.

Prabhakar, S., Sekhar, A. S., & Mohanty, A. R. (2002). Transient lateral analysis of a slant-cracked rotor passing through its flexural critical speed. *Mechanism and Machine Theory, 37*(9), 1007-1020. doi:http://dx.doi.org/10.1016/S0094-114X(02)00020-4

Ramesh Babu, T., Srikanth, S., & Sekhar, A. S. (2008). Hilbert–Huang transform for detection and monitoring of crack in a transient rotor. *Mechanical Systems and*

Signal Processing, 22(4), 905-914. doi:http://dx.doi.org/10.1016/j.ymssp.2007.10.010

Ren, Z., Zhou, S., E, C., Gong, M., Li, B., & Wen, B. (2015). Crack fault diagnosis of rotor systems using wavelet transforms. *Computers & Electrical Engineering, 45*, 33-41. doi:http://dx.doi.org/10.1016/j.compeleceng.2015.04.010

Ricci, R., & Pennacchi, P. (2012). Discussion of the dynamic stability of a multi-degree-of-freedom rotor system affected by a transverse crack. *Mechanism and Machine Theory, 58*(0), 82-100. doi:http://dx.doi.org/10.1016/j.mechmachtheory.2012.08.002

Rubio, L., & Fernández-Sáez, J. (2012). A new efficient procedure to solve the nonlinear dynamics of a cracked rotor. *Nonlinear Dynamics, 70*(3), 1731-1745.

Rubio, L., Muñoz-Abella, B., & Loaiza, G. (2011). Static behaviour of a shaft with an elliptical crack. *Mechanical Systems and Signal Processing, 25*(5), 1674-1686. doi:http://dx.doi.org/10.1016/j.ymssp.2010.12.013

Rubio, L., Muñoz-Abella, B., Rubio, P., & Montero, L. (2014). Quasi-static numerical study of the breathing mechanism of an elliptical crack in an unbalance rotating shaft. *Latin American Journal of Solids and Structures, 11*, 2333-2350.

Rubio, P., Rubio, L., Muñoz-Abella, B., & Montero, L. (2015). Determination of the Stress Intensity Factor of an elliptical breathing crack in a rotating shaft. *International Journal of Fatigue, 77*, 216-231. doi:http://dx.doi.org/10.1016/j.ijfatigue.2015.01.018

S.K.Georgantzinos, & N.K.Anifantis. (2008). An insight into the breathing mechanism of a crack in a rotating shaft. *Journal of Sound and Vibration, 318*, 279–295.

Saavedra, P., & Cuitino, L. (2002). Vibration analysis of rotor for crack identification. *Journal of Vibration and Control, 8*(1), 51-67.

Sabnavis, G., Kirk, R. G., Kasarda, M., & Quinn, D. (2004). Cracked shaft detection and diagnostics: a literature review. *Shock and Vibration Digest, 36*, 287–296, .

Sawicki, J. T., Wu, X., Baaklini, G. Y., & Gyekenyesi, A. L. (2003). *Vibration-based crack diagnosis in rotating shafts during acceleration through resonance.* Paper presented at the Proceedings of SPIE - The International Society for Optical Engineering.

Sekhar, A. S. (2004). Crack identification in a rotor system: a model-based approach. *Journal of Sound and Vibration, 270*(4–5), 887-902. doi:http://dx.doi.org/10.1016/S0022-460X(03)00637-0

Sekhar, A. S., Mohanty, A. R., & Prabhakar, S. (2005). Vibrations of cracked rotor system: transverse crack versus slant crack. *Journal of Sound and Vibration, 279*(3–5), 1203-1217. doi:http://dx.doi.org/10.1016/j.jsv.2004.01.011

Sekhar, A. S., & Prabhu, B. S. (1994a). Transient Analysis of a Cracked Rotor Passing Through Critical Speed. *Journal of Sound and Vibration, 173*(3), 415-421. doi:http://dx.doi.org/10.1006/jsvi.1994.1238

Sekhar, A. S., & Prabhu, B. S. (1994b). Vibration and Stress Fluctuation in Cracked Shafts. *Journal of Sound and Vibration, 169*(5), 655-667. doi:http://dx.doi.org/10.1006/jsvi.1994.1039

Siegmund, T., & Brocks, W. (2000). A numerical study on the correlation between the work of separation and the dissipation rate in ductile fracture. *Engineering Fracture Mechanics, 67*, 139-154.

Silani, M., Ziaei-Rad, S., & Talebi, H. (2013). Vibration analysis of rotating systems with open and breathing cracks. *Applied Mathematical Modelling, 37*(24), 9907-9921. doi:http://dx.doi.org/10.1016/j.apm.2013.05.040

Sinha, J. K., Lees, A. W., & Friswell, M. I. (2004). Estimating unbalance and misalignment of a flexible rotating machine from a single run-down. *Journal of Sound and Vibration, 272*(3–5), 967-989. doi:http://dx.doi.org/10.1016/j.jsv.2003.03.006

Sinou, J.-J. (2007). Effects of a crack on the stability of a non-linear rotor system. *International Journal of Non-Linear Mechanics, 42*(7), 959-972. doi:http://dx.doi.org/10.1016/j.ijnonlinmec.2007.04.002

Sinou, J.-J. (2008). Detection of cracks in rotor based on the 2× and 3× super-harmonic frequency components and the crack–unbalance interactions. *Communications in*

Nonlinear Science and Numerical Simulation, 13(9), 2024-2040. doi:http://dx.doi.org/10.1016/j.cnsns.2007.04.008

Sinou, J. J., & Lees, A. W. (2005). The influence of cracks in rotating shafts. *Journal of Sound and Vibration, 285*(4–5), 1015-1037. doi:http://dx.doi.org/10.1016/j.jsv.2004.09.008

Staff, W. W. P. A. (1996). *Western Woods Use Book* (4th edition ed.): Western Wood Products Association.

Stoisser, C. M., & Audebert, S. (2008). A comprehensive theoretical, numerical and experimental approach for crack detection in power plant rotating machinery. *Mechanical Systems and Signal Processing, 22*(4), 818-844. doi:http://dx.doi.org/10.1016/j.ymssp.2007.11.013

Sudhakar, G. N. D. S., & Sekhar, A. S. (2011). Identification of unbalance in a rotor bearing system. *Journal of Sound and Vibration, 330*(10), 2299-2313. doi:http://dx.doi.org/10.1016/j.jsv.2010.11.028

Tian, Z., Jin, T., Wu, B., & Ding, F. (2011). Condition based maintenance optimization for wind power generation systems under continuous monitoring. *Renewable Energy, 36*(5), 1502-1509. doi:http://dx.doi.org/10.1016/j.renene.2010.10.028

Tiwari, R., & Chougale, A. (2014). Identification of bearing dynamic parameters and unbalance states in a flexible rotor system fully levitated on active magnetic bearings. *Mechatronics, 24*(3), 274-286. doi:http://dx.doi.org/10.1016/j.mechatronics.2014.02.010

V.Kumar, & C.Rastogi. (2009). A brief review on dynamics of a cracked rotor. *International Journal of Rotating Machinery*, 1-6.

Walker, R. B., Vayanat, R., Perinpanayagam, S., & Jennions, I. K. (2014). Unbalance localization through machine nonlinearities using an artificial neural network approach. *Mechanism and Machine Theory, 75*, 54-66. doi:http://dx.doi.org/10.1016/j.mechmachtheory.2014.01.006

Wang, K. S., Guo, D., & Heyns, P. S. (2012). The application of order tracking for vibration analysis of a varying speed rotor with a propagating transverse crack. *Engineering Failure Analysis, 21*(0), 91-101. doi:http://dx.doi.org/10.1016/j.engfailanal.2011.11.020

Wang, K. S., & Heyns, P. S. (2011). Application of computed order tracking, Vold–Kalman filtering and EMD in rotating machine vibration. *Mechanical Systems and Signal Processing, 25*(1), 416-430. doi:http://dx.doi.org/10.1016/j.ymssp.2010.09.003

Wauer, J. (1990). Modelling and formulation of equations of motion for cracked rotating shafts. *International Journal of Solids and Structures, 26*(8), 901-914. doi:http://dx.doi.org/10.1016/0020-7683(90)90076-8

Wei, X., Liu, D., Zhao, L. & Zhang, Q. (2014). Time-varying stiffness analysis on rotating shaft with elliptical-front crack. *International Journal of Industrial and Systems Engineering, 17*, 302-314.

Williams, M. (1961). The bending stress distribution at the base of a stationary crack. *Journal of applied mechanics, 28*(1), 78-82.

Wu, X., Sawicki, J. T., Friswell, M. I., & Baaklini, G. Y. (2005). *Finite element analysis of coupled lateral and torsional vibrations of a rotor with multiple cracks.* Paper presented at the ASME Turbo Expo 2005: Power for Land, Sea, and Air.

Xiang, J., Zhong, Y., Chen, X., & He, Z. (2008). Crack detection in a shaft by combination of wavelet-based elements and genetic algorithm. *International Journal of Solids and Structures, 45*(17), 4782-4795.

Xu, M., & Marangoni, R. D. (1994). Vibration Analysis Of A Motor-Flexible Coupling-Rotor System Subject To Misalignment And Unbalance, Part I: Theoretical Model And Analysis. *Journal of Sound and Vibration, 176*(5), 663-679. doi:http://dx.doi.org/10.1006/jsvi.1994.1405

Yan, G., De Stefano, A., Matta, E., & Feng, R. (2013). A novel approach to detecting breathing-fatigue cracks based on dynamic characteristics. *Journal of Sound and Vibration, 332*(2), 407-422.

Yang, B., & Suh, C. S. (2006). On fault induced nonlinear rotary response and instability. *International Journal of Mechanical Sciences, 48*(10), 1103-1125. doi:http://dx.doi.org/10.1016/j.ijmecsci.2006.04.002

Zhou, T., Sun, Z., Xu, J., & Han, W. (2005). Experimental analysis of cracked rotor. *Journal of Dynamic Systems, Measurement and Control, Transactions of the ASME, 127*(3), 313-320. doi:10.1115/1.1978908

Glossary

φ	effectual bending angle; bending direction of the shaft relative to the crack direction
δ	bending direction of the shaft relative to the negative Y-axis
β	the angular position of unbalance force relative to the crack direction
θ	shaft rotation angle
μ	the ratio of crack depth
η	the ratio of the total weight force and the unbalance force
λ	the ratio of the crack position and the shaft length
Λ	percentage of opening of the crack
A_1	area of the uncracked cross-section at $t = 0$
$A_2(t)$	area of the closed portion of the crack segment at time t
A_c	area of the crack segment
F_{un}	rotational unbalance force
L	total shaft length
l_0	location of the crack
l_1	location of the left disk
l_2	location of the unbalance force disk
$M_{m_d g}$	gravitational moment owing to two disks
$M_{m_S g}$	gravitational moment owing to shaft self-weight
M_{un}	dynamic moment owing to the rotational unbalance force
M_X	summation of the moment in X-axis
M_Y	summation of the moment in Y-axis
M_R	resultant moment
m_d	the mass of a disk
$m_d g$	gravitational force of a disk
m_s	mass of the shaft
$m_s g$	the gravitational force of the shaft
X, Y	fixed coordinate system
$\bar{X}, \bar{Y}$	centroid coordinate system
X', Y'	rotational coordinate system

Appendices

Appendix A: MATLAB Script for Balance Model (Increments: Crack Location)

```
% ========================================================
%                 Balance Model (Increments: Crack Location)
%========================================================
% The following is achieved in this script:
% 1. calculation of the effectual loading angle based on design parameters
% 2. determination of percentage of opening of crack of chosen configuration
% 3. determination of area moment of inertia of chosen configuration.
% ========================================================
clc;clear all
% ------------------------------------------------------------------------------------------------------
% Set the Rotor Model Parameters:
% ------------------------------------------------------------------------------------------------------
% Increments: crack location
        Lemda = 0:0.01:1;
% Rotational angle of shaft (0° to 360°)
        om_t = 0*pi/180;
% Crack depth ratio (0 to 1)
        mu = 0.5;
% ------------------------------------------------------------------------------------------------------
% Design Parameters in SI Units:
% ------------------------------------------------------------------------------------------------------
% Length of shaft
        L = 0.724;
% Radius of shaft
        R = 0.00635;
% Density of shaft
        rho_S = 7800;
% Mass of shaft
        m_S = pi*R^2*L*rho_S;
% Force due to the Shaft Self-weight
        Fs= m_S*9.81;
% Thickness of disk
        t_d = 25*10^-3;
% Disk inner radius
        R_i = 13*10^-3;
% Disk outer radius
        R_o = 130*10^-3;
% Density of disk
        rho_d = 7800;
% Mass of disk
        m_d = pi*(R_i-R_o)^2*t_d*rho_d;
% Gravity force due to disk weight
```

```
        Fmg = m_d*9.81;
% Crack location
        L0 = L*Lemda;
% Balance disk distance from Support 1
        L1= L/4;
% Unbalance disk distance from Support 1
        L2= L-L1;
% ------------------------------------------------------------------------------------------
% Crack Initial Geometric Parameters
% ------------------------------------------------------------------------------------------
% Gamma, ratio between half-length of crack front to shaft radius
        ga = sqrt(mu*(2-mu));
% b, distance from origin to crack segment
        b = R*(1-mu);
% Crack half angle
        hAL = acos(1-mu);
% Ac, area of cracked segment when angular displacement is zero
        Ac = R^2*(acos(1-mu)-(1-mu)*ga);
% A1, area of uncracked segment when angular displacement is zero
        A1 = R^2*(pi-acos(1-mu)+(1-mu)*ga);
% e, centroid location of area A1 about Y-axis
        e = (2*R^3/(3*A1))*(ga)^3;
% ------------------------------------------------------------------------------------------
% Moment Calculation of the Balance Cracked Shaft
% ------------------------------------------------------------------------------------------
% Pre-allocate matrices
            Mz = zeros(1,numel(Lemda));
        for  kp = 1:numel(Lemda)
% Moment due to shaft self-weight at any point
            Mz1(kp) = Fs*(6*L*L0(kp)-L^2-6*L0(kp)^2)/(12*L);
% Moment due to two balance disks
        if L0(kp) >= 0 && L0(kp) < L1
% Between Support 1 and Disk 1
            Mz2(kp)= Fmg*L0(kp) - Fmg*L1*(L-L1)/L;
% Between Disk 1 and Disk 2
        elseif L0(kp) >= L1 && L0(kp) <= L2
            Mz2(kp)= Fmg*L1 - Fmg*L1*(L-L1)/L;
% Between Disk 2 and Support 2
        elseif L0(kp) > L2 && L0(kp) <= L
            Mz2(kp)= Fmg*(L-L0(kp)) - Fmg*L1*(L-L1)/L;
end
% Resultant moment in Z direction
            Mz(kp) =  Mz1(kp)+Mz2(kp);
% Direction of the bending direction with respect to (-) Y-axis
         if Mz (kp) >= 0
       % if Mz is positive
            Delta (kp) = 0;
      % if Mz is negative
        elseif Mz (kp)< 0
            Delta (kp) = pi;
```

```
        end
    end
% ------------------------------------------------------------------------------------------------

% ------------------------------------------------------------------------------------------------
% Effectual Bending Angle Calculation
% ------------------------------------------------------------------------------------------------
% Angle bending direction to crack direction (anticlockwise):
 % Pre-allocate matrices
              Phi = zeros(1,numel(Delta));
 for  ui = 1:numel(Delta)
 % if Phi = om_t-Delta is positive
          if  om_t-Delta(ui) > 0
              Phi(ui) = om_t-Delta(ui);
 % if Phi = om_t-Delta is negative
          elseif om_t-Delta(ui) < 0
             Phi(ui) = om_t-Delta(ui)+ 2*pi;
          end
 end
% ------------------------------------------------------------------------------------------------
% Breathing Mechanism
% ------------------------------------------------------------------------------------------------
% Phi1, angle of rotation threshold: partially open/closed crack
          Phi1 = atan((e+b)/(R*ga));
% Phi2, angle of rotation threshold: fully closed crack
          Phi2 = (pi/2)+acos(1-mu);
% 2pi-Phi2, angle of rotation threshold: partially open/closed crack
          Phi2_2pi = 2*pi-Phi2;
% 2pi-Phi1, angle of rotation threshold: fully open crack
          Phi1_2pi = 2*pi-Phi1;

% ------------------------------------------------------------------------------------------------
% Balance shaft data (for crack in a single location)
% Data calculated based on Appendix H MATLAB Script [17]
% Reading values from Excel file containing area values
% ------------------------------------------------------------------------------------------------
if mu == 0.25
% Crack cross-section closed area
          Ace = xlsread ('Ref_Data.xlsx','Mu=0.25','F6:F2006');
% X Moment of inertia of Ace about the centroid axis
          IXXAce = xlsread ('Ref_Data.xlsx','Mu=0.25','B6:B2006');
% Y Moment of inertia of Ace about the centroid axis
          IYYAce = xlsread ('Ref_Data.xlsx','Mu=0.25','C6:C2006');
% Coordinate of the centroid axis
          Xce = xlsread('Ref_Data.xlsx','Mu=0.25','D6:D2006');
          Yce = xlsread('Ref_Data.xlsx','Mu=0.25','E6:E2006');
end

if mu == 0.5
% Crack cross-section closed area
```

```
        Ace = xlsread ('Ref_Data.xlsx','Mu=0.5', 'F6:F2006');
% X Moment of inertia of Ace about the centroid axis
        IXXAce = xlsread ('Ref_Data.xlsx','Mu=0.5', 'B6:B2006');
% Y Moment of inertia of Ace about the centroid axis
        IYYAce = xlsread ('Ref_Data.xlsx','Mu=0.5', 'C6:C2006');
% Coordinate of the centroid axis
        Xce = xlsread ('Ref_Data.xlsx','Mu=0.5', 'D6:D2006');
        Yce = xlsread ('Ref_Data.xlsx','Mu=0.5', 'E6:E2006');
End

if mu == 0.75
% Crack cross-section closed area
        Ace = xlsread ('Ref_Data.xlsx','Mu=0.75', 'F6:F2006');
% X Moment of inertia of Ace about the centroid axis
        IXXAce = xlsread ('Ref_Data.xlsx','Mu=0.75', 'B6:B2006');
% Y Moment of inertia of Ace about the centroid axis
        IYYAce = xlsread ('Ref_Data.xlsx','Mu=0.75', 'C6:C2006');
% Coordinate of the centroid axis
        Xce = xlsread ('Ref_Data.xlsx','Mu=0.75', 'D6:D2006');
   Yce = xlsread ('Ref_Data.xlsx','Mu=0.75', 'E6:E2006');
end

if mu == 1
% Crack cross-section closed area
        Ace = xlsread ('Ref_Data.xlsx','Mu=1.0', 'F6:F2006');
% X Moment of inertia of Ace about the centroid axis
        IXXAce = xlsread ('Ref_Data.xlsx','Mu=1.0', 'B6:B2006');
% Y Moment of inertia of Ace about the centroid axis
        IYYAce = xlsread ('Ref_Data.xlsx','Mu=1.0', 'C6:C2006');
% Coordinate of the centroid axis
        Xce = xlsread ('Ref_Data.xlsx','Mu=1.0', 'D6:D2006');
        Yce = xlsread ('Ref_Data.xlsx','Mu=1.0', ‘E6:E2006’);
end

% No crack
if mu == 0
% Crack cross-section closed area
        Ace = xlsread ('Ref_Data.xlsx','Mu=0', 'F6:F2006');
% X Moment of inertia of Ace about the centroid axis
        IXXAce = xlsread ('Ref_Data.xlsx','Mu=0', 'B6:B2006');
% Y Moment of inertia of Ace about the centroid axis
        IYYAce = xlsread ('Ref_Data.xlsx','Mu=0', 'C6:C2006');
% Coordinate of the centroid axis
        Xce = xlsread ('Ref_Data.xlsx','Mu=0', 'D6:D2006');
   Yce = xlsread ('Ref_Data.xlsx','Mu=0', 'E6:E2006');
end
% ------------------------------------------------------------------------------------------
```

```
% ------------------------------------------------------------------------------------------
% Determination of Data for Different Crack Locations based on Effectual Bending
Angle
% ------------------------------------------------------------------------------------------
        increment = pi/1000;
        tolerance = increment/2;
        om_t = 0:increment:2*pi;

        for z = 1:numel(Phi);
           for q = 1:numel(om_t);
              if abs(Phi(z)-om_t(q)) <= tolerance
                 Phi_omt(z) = q;
              end
           end

% The values for IYYAce, IXXAce, Ace, Xce and Yce are rearranged based on
unbalance condition relative to the balance case
        Phi_IYYAce(z) = IYYAce(Phi_omt(z));
        Phi_IXXAce(z) = IXXAce(Phi_omt(z));
        Phi_Ace(z) = Ace(Phi_omt(z));
        Phi_Xce(z) = Xce(Phi_omt(z));
        Phi_Yce(z) = Yce(Phi_omt(z));
% Unbalance case percentage of opening area
        Phi_A2(z) = Phi_Ace(z)-A1;
        PctOpen(z) = (Ac-Phi_A2(z))/Ac*100;
end
% ==========================================================
```

Appendix B: MATLAB Script for Balance Model (Increments: Shaft Rotation Angle)

```
% ============================================================
%                  Balance Model (Increments: Shaft Rotation Angle)
%============================================================
% The following is achieved in this script:
% 1. calculation of the effectual loading angle based on design parameters
% 2. determination of percentage of opening of crack of chosen configuration
% 3. determination of area moment of inertia of chosen configuration.
% ============================================================
clc;clear all

% ------------------------------------------------------------------------------------------------------
% Set the Rotor Model Parameters:
% ------------------------------------------------------------------------------------------------------
% 1001 increments of shaft rotation between 0 and 2 pi
        increment = pi/1000;
% Rotational angle of shaft
        om_t = 0:increment:2*pi;
% Crack depth ratio (0 to 1)
        mu = 0.5;
% Crack location ratio (0 to 1)
        Lemda = 0.5;
% ------------------------------------------------------------------------------------------------------
% Design Parameters in SI Units
% ------------------------------------------------------------------------------------------------------
% Length of shaft
        L = 0.724;
% Radius of shaft
        R = 6.35*10^-3;
% Density of shaft
        rho_S = 7800;
% Mass of shaft
        m_S = pi*R^2*L*rho_S;
% Force due to the shaft self-weight
        Fs= m_S*9.81;
% Thickness of disk
        t_d = 25*10^-3;
% Disk inner radius
        R_i = 13*10^-3;
% Disk outer radius
        R_o = 130*10^-3;
% Density of disk
        rho_d = 7800;
% Mass of disk
        m_d = pi*(R_i-R_o)^2*t_d*rho_d;
% Gravity force due to disk weight
        Fmg = m_d*9.81;
```

```
% Crack location
        L0 = L*Lemda;
% Balance disk distance from Support 1
        L1= L/4;
% Unbalance disk distance from Support 1
        L2= L-L1;
% ------------------------------------------------------------------------------------------------
% Crack Initial Geometric Parameters
% ------------------------------------------------------------------------------------------------
% Gamma, ratio between half-length of crack front to shaft radius
        ga = sqrt(mu*(2-mu));
% b, distance from origin to crack segment
        b = R*(1-mu);
% Crack half angle
        hAL = acos(1-mu);
% Ac, area of cracked segment when angular displacement is zero
        Ac = R^2*(acos(1-mu)-(1-mu)*ga);
% A1, area of uncracked segment when angular displacement is zero
        A1 = R^2*(pi-acos(1-mu)+(1-mu)*ga);
% e, centroid location of area A1 about Y-axis
        e = (2*R^3/(3*A1))*(ga)^3;
% ------------------------------------------------------------------------------------------------
% Moment Calculation
% ------------------------------------------------------------------------------------------------
% Moment due to shaft self-weight at any point
        Mz1 =  Fs*(6*L*L0-L^2-6*L0^2)/(12*L);
% Moment due to two balance disks
if L0 >= 0 && L0 < L1
% Between Support 1 and Disk 1
                Mz2= Fmg*L0 - Fmg*L1*(L-L1)/L;
% Between Disk 1 and Disk 2
        elseif L0 >= L1 && L0 <= L2
                Mz2= Fmg*L1 - Fmg*L1*(L-L1)/L;
% Between Disk 2 and Support 2
        elseif L0 > L2 && L0 <= L
                Mz2= Fmg*(L-L0) - Fmg*L1*(L-L1)/L;
end
% Total moment calculations
        Mz = Mz1+Mz2;
% Direction of the bending direction with respect to (-) Y-axis
if Mz >= 0
    % if Mz is positive
        Delta = 0;
   % if Mz is negative
        elseif Mz < 0
                Delta =  pi;
 end
% ------------------------------------------------------------------------------------------------
```

```
% ------------------------------------------------------------------------------------------------
% Effectual Bending Angle Calculation
% ------------------------------------------------------------------------------------------------
% Angle between the bending direction and crack direction (anticlockwise):
            for ui = 1:numel(om_t)
                        Phi(ui) = om_t(ui)-Delta;
                if Phi(ui) <0
                        Phi(ui) = 2*pi +Phi(ui);
                end
          end
% ------------------------------------------------------------------------------------------------
% Breathing Mechanism
% ------------------------------------------------------------------------------------------------
% Phi1, angle of rotation threshold: partially open/closed crack
        Phi1 = atan((e+b)/(R*ga));
% Phi2, angle of rotation threshold: fully closed crack
        Phi2 = ((pi/2)+acos(1-mu));
% 2pi-Phi2, angle of rotation threshold: partially open/closed crack
        Phi2_2pi = (2*pi-Phi2);
% 2pi-Phi1, angle of rotation threshold: fully open crack
        Phi1_2pi = (2*pi-Phi1);
% ------------------------------------------------------------------------------------------------
% Balance shaft data (for crack in a single location)
% Data calculated based on Appendix H MATLAB Script [17]
% Reading values from Excel file containing area values
% ------------------------------------------------------------------------------------------------
if mu == 0.25
% Crack cross-section closed area
        Ace = xlsread ('Ref_Data.xlsx','Mu=0.25','F6:F2006');
% X Moment of Inertia of Ace about the centroid axis
        IXXAce = xlsread ('Ref_Data.xlsx','Mu=0.25','B6:B2006');
% Y Moment of Inertia of Ace about the centroid axis
        IYYAce = xlsread ('Ref_Data.xlsx','Mu=0.25','C6:C2006');
% Coordinate of the centroid axis
        Xce = xlsread('Ref_Data.xlsx','Mu=0.25','D6:D2006');
        Yce = xlsread('Ref_Data.xlsx','Mu=0.25','E6:E2006');
end

if mu == 0.5
% Crack cross-section closed area
        Ace = xlsread ('Ref_Data.xlsx','Mu=0.5', 'F6:F2006');
% X Moment of inertia of Ace about the centroid axis
        IXXAce = xlsread ('Ref_Data.xlsx','Mu=0.5', 'B6:B2006');
% Y Moment of inertia of Ace about the centroid axis
        IYYAce = xlsread ('Ref_Data.xlsx','Mu=0.5', 'C6:C2006');
% Coordinate of the centroid axis
        Xce = xlsread ('Ref_Data.xlsx','Mu=0.5', 'D6:D2006');
        Yce = xlsread ('Ref_Data.xlsx','Mu=0.5', 'E6:E2006');
End
```

```
if mu == 0.75
% Crack cross-section closed area
        Ace = xlsread ('Ref_Data.xlsx','Mu=0.75', 'F6:F2006');
% X moment of inertia of Ace about the centroid axis
        IXXAce = xlsread ('Ref_Data.xlsx','Mu=0.75', 'B6:B2006');
% Y Moment of inertia of Ace about the centroid axis
        IYYAce = xlsread ('Ref_Data.xlsx','Mu=0.75', 'C6:C2006');
% Coordinate of the centroid axis
        Xce = xlsread ('Ref_Data.xlsx','Mu=0.75', 'D6:D2006');
   Yce = xlsread ('Ref_Data.xlsx','Mu=0.75', 'E6:E2006');
end

if mu == 1
% Crack cross-section closed area
        Ace = xlsread ('Ref_Data.xlsx','Mu=1.0', 'F6:F2006');
% X Moment of inertia of Ace about the centroid axis
        IXXAce = xlsread ('Ref_Data.xlsx','Mu=1.0', 'B6:B2006');
% Y Moment of inertia of Ace about the centroid axis
        IYYAce = xlsread ('Ref_Data.xlsx','Mu=1.0', 'C6:C2006');
% Coordinate of the centroid axis
        Xce = xlsread ('Ref_Data.xlsx','Mu=1.0', 'D6:D2006');
        Yce = xlsread ('Ref_Data.xlsx','Mu=1.0', ‘E6:E2006’);
end

% No crack
if mu == 0
% Crack cross-section closed area
        Ace = xlsread ('Ref_Data.xlsx','Mu=0', 'F6:F2006');
% X moment of inertia of Ace about the centroid axis
        IXXAce = xlsread ('Ref_Data.xlsx','Mu=0', 'B6:B2006');
% Y moment of inertia of Ace about the centroid axis
        IYYAce = xlsread ('Ref_Data.xlsx','Mu=0', 'C6:C2006');
% Coordinate of the centroid axis
        Xce = xlsread ('Ref_Data.xlsx','Mu=0', 'D6:D2006');
   Yce = xlsread ('Ref_Data.xlsx','Mu=0', 'E6:E2006');
end
% ------------------------------------------------------------------------------------------
% Determination of Data for Different Crack Locations based on Effectual Bending
Angle
% ------------------------------------------------------------------------------------------
        tolerance = increment/2;

        for z = 1:numel(Phi);
           for q = 1:numel(om_t);
              if abs(Phi(z)-om_t(q)) <= tolerance
                 Phi_omt(z) = q;
              end
           end
```

```
   % The values for IYYAce, IXXAce, Ace, Xce and Yce are rearranged based on
unbalance condition relative to the balance case
            Phi_IYYAce(z) = IYYAce(Phi_omt(z));
            Phi_IXXAce(z) = IXXAce(Phi_omt(z));
            Phi_Ace(z) = Ace(Phi_omt(z));
            Phi_Xce(z) = Xce(Phi_omt(z));
            Phi_Yce(z) = Yce(Phi_omt(z));
% Percentage of opening area
            Phi_A2(z) = Phi_Ace(z)-A1;
            PctOpen(z) = (Ac-Phi_A2(z))/Ac*100;

end
% ============================================================
```

Appendix C: MATLAB Script for Unbalance Model (Increments: Crack Location)

```
% ============================================================
%                  Unbalance Model (Increments: Crack Location)
%============================================================
% The following is achieved in this script:
% 1. calculation of the effectual loading angle based on design parameters
% 2. determination of percentage of opening of crack of chosen configuration
% 3. determination of area moment of inertia of chosen configuration.
% ============================================================
clc;clear all

% ------------------------------------------------------------------------------------------------------
% Set the Rotor Model Parameters:
% ------------------------------------------------------------------------------------------------------
% Increments: crack location
        Lemda = 0:0.01:1;
% Rotational angle of shaft (0° to 360°)
        om_t =0*pi/180;
% Angle between rotating unbalance mass and crack direction (0° to 360°)
        beta = 0*pi/180;
% Force ratio is ratio of the gravity force to unbalance force (0 to ∞)
        FR = 5 ;
% Crack depth ratio (0 to 1)
        mu = 0.5;
% ------------------------------------------------------------------------------------------------------
% Design Parameters in SI Units
% ------------------------------------------------------------------------------------------------------
% Length of shaft
        L = 0.724;
% Radius of shaft
        R = 6.35*10^-3;
% Density of shaft
        rho_S = 7800;
% Mass of shaft
        m_S = pi*R^2*L*rho_S;
% Force due to the shaft self-weight
        Fs= m_S*9.81;
% Thickness of disk
        t_d = 25*10^-3;
% Disk inner radius
        R_i = 13*10^-3;
% Disk outer radius
        R_o = 130*10^-3;
% Density of disk
        rho_d = 7800;
% Mass of disk
        m_d = pi*(R_i-R_o)^2*t_d*rho_d;
```

```
% Gravity force due to disk weight
        Fmg = m_d*9.81;
% Crack location
        L0 = L*Lemda;
% Balance disk distance from Support 1
        L1= L/4;
% Unbalance disk distance from Support 1
        L2= L-L1;
% ------------------------------------------------------------------------------------------
% Crack Initial Geometric Parameters
% ------------------------------------------------------------------------------------------
% Gamma, ratio between half-length of crack front to shaft radius
        ga = sqrt(mu*(2-mu));
% b, distance from origin to crack segment
        b = R*(1-mu);
% Crack half angle
        hAL = acos(1-mu);
% Ac, area of cracked segment when angular displacement is zero
        Ac = R^2*(acos(1-mu)-(1-mu)*ga);
% A1, area of uncracked segment when angular displacement is zero
        A1 = R^2*(pi-acos(1-mu)+(1-mu)*ga);
% e, centroid location of area A1 about Y-axis
        e = (2*R^3/(3*A1))*(ga)^3;
% ------------------------------------------------------------------------------------------
% Unbalance force
        Fum = (Fs + 2*Fmg)/FR;
% ------------------------------------------------------------------------------------------
% Moment Calculation
% ------------------------------------------------------------------------------------------
% Moment of the unbalance cracked shaft
% Pre-allocate matrices
        Mz = zeros(1,numel(Lemda));
        My = zeros(1,numel(Lemda));
        DeltaPrim = zeros(1,numel(Lemda));
        Delta = zeros(1,numel(Lemda));
for kp = 1:numel(Lemda)
% Moment due to shaft self-weight at any point
        Mz1(kp) = Fs*(6*L*L0(kp)-L^2-6*L0(kp)^2)/(12*L);
%  Moment due to two balance disks
        if L0(kp) >= 0 && L0(kp) < L1
% Between Support 1 and Disk 1
        Mz2(kp)= Fmg*L0(kp) - Fmg*L1*(L-L1)/L;
% Between Disk 1 and Disk 2
        elseif L0(kp) >= L1 && L0(kp) <= L2
        Mz2(kp)= Fmg*L1 - Fmg*L1*(L-L1)/L;
% Between Disk 2 and Support 2
        elseif L0(kp) > L2 && L0(kp) <= L
        Mz2(kp)= Fmg*(L-L0(kp)) - Fmg*L1*(L-L1)/L;
end
% Moment due to unbalance mass
```

```
        if L0(kp) >= 0 && L0(kp) <= L2
% Between Support 1 and unbalance disk in Z direction
        Mun(kp) = (Fum*L1^2*L0(kp)*(L1+3*L2)/L^3-Fum*L1^2*L2/L^2);
        Mz3z(kp) = Mun(kp)*cos(om_t+beta);
% Between Support 1 and unbalance disk in Y direction
        My3y(kp) = Mun(kp)*sin(om_t+beta);
        elseif L0(kp) > L2 && L0(kp) <= L
% Between unbalance disk and Support 2 in Z direction
        Mun(kp) =(Fum*L2^2*(L-L0(kp))*(3*L1+L2)/L^3-Fum*L1*L2^2/L^2);
        Mz3z(kp) = Mun(kp)*cos(om_t+beta);
% Between unbalance disk and Support 2in Y direction
        My3y(kp) =Mun(kp)*sin(om_t+beta);
 end
% Resultant moment in Z direction
        Mz12 (kp) = Mz1(kp)+Mz2(kp);
        Mz(kp) = Mz1(kp)+Mz2(kp)+Mz3z(kp);
% Resultant moment in Y direction
        My(kp) = My3y(kp);
% Total resultant moment
        M(kp) = sqrt(Mz(kp)^2+My(kp)^2);
% Direction of resultant moment with respect to Z axis
        DeltaPrim(kp) = atan(My(kp)/Mz(kp));
% Direction of the bending direction with respect to (-) Y-axis (anticlockwise)
        if Mz(kp) > 0 && My(kp) > 0
% if Mz is positive and My is positive
        Delta(kp) = DeltaPrim(kp);
% if Mz is positive and My is negative
        elseif Mz(kp) > 0 && My(kp) < 0
        Delta(kp) = 2*pi + DeltaPrim(kp) ;
% if Mz is negative and My is positive
        elseif Mz(kp) < 0 && My(kp) > 0
        Delta(kp) = pi+DeltaPrim(kp);
% if Mz is negative and My is negative
        elseif Mz(kp) < 0 && My(kp) < 0
        Delta(kp) = pi + DeltaPrim(kp);
        elseif Mz(kp) < 0 && My(kp) == 0
        Delta(kp) = pi ;
        elseif Mz(kp) > 0 && My(kp) == 0
        Delta(kp) = 0 ;
        elseif Mz(kp) == 0 && My(kp) > 0
        Delta(kp) = pi/2;
        elseif Mz(kp) == 0 && My(kp) < 0
        Delta(kp) = 3*pi/2;
        end
end
% ------------------------------------------------------------------------------------------
```

```
% ---------------------------------------------------------------------------------------------
% Effectual Bending Angle Calculation
% ---------------------------------------------------------------------------------------------
% Angle bending direction to crack direction (anticlockwise):
% Pre-allocate matrices
        Phi = zeros(1,numel(Delta));
 for ui = 1:numel(Delta)
% if Phi = om_t-Delta is positive
         if om_t-Delta(ui) > 0
        Phi(ui) = om_t-Delta(ui);
% if Phi = om_t-Delta is negative
        elseif om_t-Delta(ui) < 0
        Phi(ui) = om_t-Delta(ui)+ 2*pi;
        end
 end
% ---------------------------------------------------------------------------------------------
% Balance shaft data (for crack in a single location)
% Data calculated based on Appendix H MATLAB Script [17]
% Reading values from Excel file containing area values
% ---------------------------------------------------------------------------------------------
if mu == 0.25
% Crack cross-section closed area
        Ace = xlsread ('Ref_Data.xlsx','Mu=0.25','F6:F2006');
% X Moment of inertia of Ace about the centroid axis
        IXXAce = xlsread ('Ref_Data.xlsx','Mu=0.25','B6:B2006');
% Y Moment of inertia of Ace about the centroid axis
        IYYAce = xlsread ('Ref_Data.xlsx','Mu=0.25','C6:C2006');
% Coordinate of the centroid axis
        Xce = xlsread('Ref_Data.xlsx','Mu=0.25','D6:D2006');
        Yce = xlsread('Ref_Data.xlsx','Mu=0.25','E6:E2006');
end

if mu == 0.5
% Crack cross-section closed area
        Ace = xlsread ('Ref_Data.xlsx','Mu=0.5', 'F6:F2006');
% X Moment of inertia of Ace about the centroid axis
        IXXAce = xlsread ('Ref_Data.xlsx','Mu=0.5', 'B6:B2006');
% Y Moment of inertia of Ace about the centroid axis
        IYYAce = xlsread ('Ref_Data.xlsx','Mu=0.5', 'C6:C2006');
% Coordinate of the centroid axis
        Xce = xlsread ('Ref_Data.xlsx','Mu=0.5', 'D6:D2006');
        Yce = xlsread ('Ref_Data.xlsx','Mu=0.5', 'E6:E2006');
End

if mu == 0.75
% Crack cross-section closed area
        Ace = xlsread ('Ref_Data.xlsx','Mu=0.75', 'F6:F2006');
% X Moment of inertia of Ace about the centroid axis
        IXXAce = xlsread ('Ref_Data.xlsx','Mu=0.75', 'B6:B2006');
% Y Moment of inertia of Ace about the centroid axis
```

```
        IYYAce = xlsread ('Ref_Data.xlsx','Mu=0.75', 'C6:C2006');
% Coordinate of the centroid axis
        Xce = xlsread ('Ref_Data.xlsx','Mu=0.75', 'D6:D2006');
   Yce = xlsread ('Ref_Data.xlsx','Mu=0.75', 'E6:E2006');
end

if mu == 1
% Crack cross-section closed area
        Ace = xlsread ('Ref_Data.xlsx','Mu=1.0', 'F6:F2006');
% X Moment of inertia of Ace about the centroid axis
        IXXAce = xlsread ('Ref_Data.xlsx','Mu=1.0', 'B6:B2006');
% Y Moment of inertia of Ace about the centroid axis
        IYYAce = xlsread ('Ref_Data.xlsx','Mu=1.0', 'C6:C2006');
% Coordinate of the centroid axis
        Xce = xlsread ('Ref_Data.xlsx','Mu=1.0', 'D6:D2006');
        Yce = xlsread ('Ref_Data.xlsx','Mu=1.0', 'E6:E2006');
end

% No Crack
if mu == 0
% Crack cross-section closed area
        Ace = xlsread ('Ref_Data.xlsx','Mu=0', 'F6:F2006');
% X Moment of inertia of Ace about the centroid axis
        IXXAce = xlsread ('Ref_Data.xlsx','Mu=0', 'B6:B2006');
% Y Moment of inertia of Ace about the centroid axis
        IYYAce = xlsread ('Ref_Data.xlsx','Mu=0', 'C6:C2006');
% Coordinate of the centroid axis
        Xce = xlsread ('Ref_Data.xlsx','Mu=0', 'D6:D2006');
   Yce = xlsread ('Ref_Data.xlsx','Mu=0', 'E6:E2006');
end
% ------------------------------------------------------------------------------------------
% Determination of Data for Different Crack Locations based on Effectual Bending
Angle
% ------------------------------------------------------------------------------------------
        increment = pi/1000;
        tolerance = increment/2;
        Phi_Ace = zeros(1,numel(om_t));
        OrbLength = sqrt(Yce.^2+Xce.^2);
        OrbAngle = atan(Yce./Xce);
        om_t = 0:increment:2*pi;

        for gh = 1:numel(om_t)
           if Xce(gh) > 0 && Yce(gh) > 0;
              OrbAngle(gh) = OrbAngle(gh);
           elseif Xce(gh) < 0 && Yce(gh) > 0;
              OrbAngle(gh) = pi+OrbAngle(gh);
           elseif Xce(gh) == 0 && Yce(gh) == 0;
              OrbAngle(gh) = 0;
           elseif Xce(gh) == 0 && Yce(gh) > 0;
              OrbAngle(gh) = pi/2;
```

```
        end
    end

    for z = 1:numel(Phi);
        for q = 1:numel(om_t);
            if abs(Phi(z)-om_t(q)) <= tolerance
                Phi_omt(z) = q;
            end
        end
% The values for IYYAce, IXXAce, Ace, Xce and Yce are rearranged based on unbalance condition relative to the balance case
        Phi_IYYAce(z) = IYYAce(Phi_omt(z));
        Phi_IXXAce(z) = IXXAce(Phi_omt(z));
        Phi_Ace(z) = Ace(Phi_omt(z));
        Phi_Xce(z) = Xce(Phi_omt(z));
        Phi_Yce(z) = Yce(Phi_omt(z));
% Calculates angle sum of delta and 'alpha'
    Delta_Phi(z) = OrbAngle(Phi_omt(z))+Delta(z);
% Calculates the radial distance of the centroid ('e')
    OrbLength_Phi(z) = OrbLength(Phi_omt(z));
% Calculates the new position of X-centroid value about original axes
    dp_Xce(z) = OrbLength(Phi_omt(z))*cos(Delta_Phi(z));
% Calculates the new position of Y-centroid value about original axes
    dp_Yce(z) = OrbLength(Phi_omt(z))*sin(Delta_Phi(z));
% Unbalance case percentage of opening area
    Phi_A2(z) = Phi_Ace(z)-A1;
    PctOpen(z) = (Ac-Phi_A2(z))/Ac*100;
 end
% ============================================================
```

Appendix D: MATLAB Script for Unbalance Model (Increments: Shaft Rotation Angle)

```
% ========================================================
%                 Unbalance Model (Increments: Shaft Rotation Angle)
%========================================================
% The following is achieved in this script:
% 1. calculation of the effectual loading angle based on design parameters
% 2. determination of percentage of opening of crack of chosen configuration
% 3. determination of area moment of inertia of chosen configuration.
% ========================================================
clc;clear all

% ------------------------------------------------------------------------------------------------------
% Set the Rotor Model Parameters:
% ------------------------------------------------------------------------------------------------------
% 1001 increments of shaft rotation between 0 and 2 pi
        increment = pi/1000;
% Rotational angle of shaft
        om_t = 0: increment: 2*pi;
% Force ratio is ratio of the disk weight forces to the unbalance force (0 to ∞)
        FR = 5;
% Crack depth ratio (0 to 1)
        mu = 0.5;
% Angle between rotating unbalance mass and the crack direction (0° to 360°)
        beta = sym(0*pi/180);
% Crack location ratio (0 to 1)
        Lemda = 0.5  ;
% ------------------------------------------------------------------------------------------------------
% Design parameters in SI units
% ------------------------------------------------------------------------------------------------------
% Length of shaft
        L = 0.724;
% Radius of shaft
        R = 6.35*10^-3;
% Density of shaft
        rho_S = 7800;
% Mass of shaft
        m_S = pi*R^2*L*rho_S;
% Force due to the shaft self-weight
        Fs= m_S*9.81;
% Thickness of disk
        t_d = 25*10^-3;
% Disk inner radius
        R_i = 13*10^-3;
% Disk outer radius
        R_o = 130*10^-3;
% Density of disk
        rho_d = 7800;
```

```
% Mass of disk
        m_d = pi*(R_i-R_o)^2*t_d*rho_d;
% Gravity force due to disk weight
        Fmg = m_d*9.81;
% Crack location
        L0 = L*Lemda;
% Balance disk distance from Support 1
        L1= L/4;
% Unbalance disk distance from Support 1
        L2= L-L1;
% ------------------------------------------------------------------------------------------
% Crack Initial Geometric Parameters
% ------------------------------------------------------------------------------------------
% Gamma, ratio between half-length of crack front to shaft radius
        ga = sqrt(mu*(2-mu));
% b, distance from origin to crack segment
        b = R*(1-mu);
% Crack half angle
        hAL = acos(1-mu);
% Ac, area of cracked segment when angular displacement is zero
        Ac = R^2*(acos(1-mu)-(1-mu)*ga);
% A1, area of uncracked segment when angular displacement is zero
        A1 = R^2*(pi-acos(1-mu)+(1-mu)*ga);
% e, centroid location of area A1 about Y-axis
        e = (2*R^3/(3*A1))*(ga)^3;
% ------------------------------------------------------------------------------------------
% Unbalance force
Fum = (Fs + 2*Fmg)/FR;
% ------------------------------------------------------------------------------------------
% Moment Calculation
% ------------------------------------------------------------------------------------------
% Moment due to shaft self-weight at any point
        Mz1 =  Fs*(6*L*L0-L^2-6*L0^2)/(12*L);
% Moment due to two balance disks
if L0 >= 0 && L0 < L1
% Between Support 1 to Disk 1
        Mz2= Fmg*L0 - Fmg*L1*(L-L1)/L;
% Between Disk 1 to Disk 2
        elseif L0 >= L1 && L0 <= L2
        Mz2= Fmg*L1 - Fmg*L1*(L-L1)/L;
% Between Disk 2 to Support 2
        elseif L0 > L2 && L0 <= L
        Mz2= Fmg*(L-L0) - Fmg*L1*(L-L1)/L;
end
% Moment due to unbalance mass
if L0 >= 0 && L0 <= L2
% Between Support 1 to unbalance disk in Z direction
        Mz3z= double((Fum.*L1^2*L0*(L1+3*L2)/L^3-Fum.*L1^2*L2/L^2).*cos
                (om_t+beta));
% Between Support 1 to unbalance disk in Y direction
```

```
        My3y=double((Fum.*L1^2*L0*(L1+3*L2)/L^3-Fum.*L1^2*L2/L^2).*sin
            (om_t+beta));
        elseif L0 > L2 && L0 <= L
% Between unbalance disk to Support 2 in Z direction
        Mz3z=double((Fum.*L2^2*(L-L0)*(3*L1+L2)/L^3-Fum.*L1*L2^2/L^2).*
            cos(m_t+beta));
% Between unbalance disk to Support 2 in Y direction
        My3y=double((Fum.*L2^2*(L-L0)*(3*L1+L2)/L^3-Fum.*L1*L2^2/L^2).*
            sin(om_t+beta));
end
% Total moment calculations
        Mz = zeros(1,numel(om_t));
        My = zeros(1,numel(om_t));
% Moment in Z direction
        Mz12 = Mz1+Mz2;
        Mz = Mz1+Mz2+Mz3z;
% Moment in Y direction
        My = My3y;
% Resultant moment
        M = sqrt(Mz.^2+My.^2);
% Pre-allocate matrices
        DeltaPrim = zeros(1,numel(om_t));
 for zv = 1:numel(om_t)
% Direction of resultant moment with respect to Z axis
        DeltaPrim(zv) = atan(My(zv)/Mz(zv));
% Direction of the bending direction with respect to (-) Y-axis
        if Mz(zv) > 0 && My(zv) > 0
% if Mz is positive and My is positive h
        Delta(zv) = DeltaPrim(zv);
% if Mz is positive and My is negative
        elseif Mz(zv) > 0 && My(zv) < 0
       Delta(zv) =  2*pi+DeltaPrim(zv);
% if Mz is negative and My is positive
        elseif Mz(zv) < 0 && My(zv) > 0
        Delta(zv) =  pi+DeltaPrim(zv);
% if Mz is negative and My is negative
        elseif Mz(zv) < 0 && My(zv) < 0
        Delta(zv) = pi+  DeltaPrim(zv);
        elseif Mz(zv) < 0 && My(zv) == 0
        Delta(zv) = pi ;
        elseif Mz(zv) > 0 && My(zv) == 0
        Delta(zv) = 0 ;
        elseif Mz(zv) == 0 && My(zv) > 0
        Delta(zv) = 0.5*pi;
        elseif Mz(zv) == 0 && My(zv) < 0
        Delta(zv) = 3*pi/2;
        end
 end
% ------------------------------------------------------------------------------------------
```

```
% ------------------------------------------------------------------------------------------------
% Effectual Bending Angle Calculation
% ------------------------------------------------------------------------------------------------
% Angle between the bending direction and crack direction (anticlockwise):
% Pre-allocate matrices
        Phi = zeros(1,numel(om_t));
for ui = 1:numel(om_t)
        Phi(ui) = om_t(ui)-Delta(ui);
        if Phi(ui) <0
        Phi(ui) = 2*pi +Phi(ui);
        end
 end
% ------------------------------------------------------------------------------------------------
% Balance shaft data (for crack in a single location)
% Data calculated based on Appendix H MATLAB Script [17]
% Reading values from Excel file containing area values
% ------------------------------------------------------------------------------------------------
if mu == 0.25
% Crack cross-section closed area
        Ace = xlsread ('Ref_Data.xlsx','Mu=0.25','F6:F2006');
% X Moment of inertia of Ace about the centroid axis
        IXXAce = xlsread ('Ref_Data.xlsx','Mu=0.25','B6:B2006');
% Y Moment of inertia of Ace about the centroid axis
        IYYAce = xlsread ('Ref_Data.xlsx','Mu=0.25','C6:C2006');
% Coordinate of the centroid axis
        Xce = xlsread('Ref_Data.xlsx','Mu=0.25','D6:D2006');
        Yce = xlsread('Ref_Data.xlsx','Mu=0.25','E6:E2006');
end

if mu == 0.5
% Crack cross-section closed area
        Ace = xlsread ('Ref_Data.xlsx','Mu=0.5', 'F6:F2006');
% X Moment of Inertia of Ace about the centroid axis
        IXXAce = xlsread ('Ref_Data.xlsx','Mu=0.5', 'B6:B2006');
% Y Moment of Inertia of Ace about the centroid axis
        IYYAce = xlsread ('Ref_Data.xlsx','Mu=0.5', 'C6:C2006');
% Coordinate of the centroid axis
        Xce = xlsread ('Ref_Data.xlsx','Mu=0.5', 'D6:D2006');
        Yce = xlsread ('Ref_Data.xlsx','Mu=0.5', 'E6:E2006');
End

if mu == 0.75
% Crack cross-section closed area
        Ace = xlsread ('Ref_Data.xlsx','Mu=0.75', 'F6:F2006');
% X moment of inertia of Ace about the centroid axis
        IXXAce = xlsread ('Ref_Data.xlsx','Mu=0.75', 'B6:B2006');
% Y moment of inertia of Ace about the centroid axis
        IYYAce = xlsread ('Ref_Data.xlsx','Mu=0.75', 'C6:C2006');
% Coordinate of the centroid axis
        Xce = xlsread ('Ref_Data.xlsx','Mu=0.75', 'D6:D2006');
```

```
   Yce = xlsread ('Ref_Data.xlsx','Mu=0.75', 'E6:E2006');
end

if mu == 1
% Crack cross-section closed area
        Ace = xlsread ('Ref_Data.xlsx','Mu=1.0', 'F6:F2006');
% X moment of inertia of Ace about the centroid axis
        IXXAce = xlsread ('Ref_Data.xlsx','Mu=1.0', 'B6:B2006');
% Y moment of inertia of Ace about the centroid axis
        IYYAce = xlsread ('Ref_Data.xlsx','Mu=1.0', 'C6:C2006');
% Coordinate of the centroid axis
        Xce = xlsread ('Ref_Data.xlsx','Mu=1.0', 'D6:D2006');
        Yce = xlsread ('Ref_Data.xlsx','Mu=1.0', ‘E6:E2006’);
end

% No crack
if mu == 0
% Crack cross-section closed area
        Ace = xlsread ('Ref_Data.xlsx','Mu=0', 'F6:F2006');
% X moment of inertia of Ace about the centroid axis
        IXXAce = xlsread ('Ref_Data.xlsx','Mu=0', 'B6:B2006');
% Y moment of inertia of ace about the centroid axis
        IYYAce = xlsread ('Ref_Data.xlsx','Mu=0', 'C6:C2006');
% Coordinate of the centroid axis
        Xce = xlsread ('Ref_Data.xlsx','Mu=0', 'D6:D2006');
   Yce = xlsread ('Ref_Data.xlsx','Mu=0', 'E6:E2006');
end
% ------------------------------------------------------------------------------------------
% Determination of Data for Different Crack Locations based on Effectual Bending
Angle
% ------------------------------------------------------------------------------------------
         tolerance = increment/2;
           Phi_Ace = zeros(1,numel(om_t));
           OrbLength = sqrt(Yce.^2+Xce.^2);
           OrbAngle = atan(Yce./Xce);
         for gh = 1:numel(om_t)
           if Xce(gh) > 0 && Yce(gh) > 0;
              OrbAngle(gh) = OrbAngle(gh);
           elseif Xce(gh) < 0 && Yce(gh) > 0;
              OrbAngle(gh) = pi+OrbAngle(gh);
           elseif Xce(gh) == 0 && Yce(gh) == 0;
              OrbAngle(gh) = 0;
           elseif Xce(gh) == 0 && Yce(gh) > 0;
              OrbAngle(gh) = 0.5*pi;
           end
         end
         for z = 1:numel(Phi);
           for q = 1:numel(om_t);
              if abs(Phi(z)-om_t(q)) <= tolerance
                 Phi_omt(z) = q;
```

```
        end
    end

% The values for IYYAce, IXXAce, Ace, Xce, Yce are rearranged based on unbalance condition relative to the Ref data
        Phi_IYYAce(z) = IYYAce(Phi_omt(z));
        Phi_IXXAce(z) = IXXAce(Phi_omt(z));
        Phi_Ace(z) = Ace(Phi_omt(z));
        Phi_Xce(z) = Xce(Phi_omt(z));
        Phi_Yce(z) = Yce(Phi_omt(z));

% Calculates angle sum of delta and 'alpha'
    Delta_Phi(z) = OrbAngle(Phi_omt(z))+Delta(z);
% Calculates the radial distance of the centroid ('e')
    OrbLength_Phi(z) = OrbLength(Phi_omt(z));
% Calculates the new position of X-centroid value about original axes
    dp_Xce(z) = OrbLength(Phi_omt(z))*cos(Delta_Phi(z));
% Calculates the new position of Y-centroid value about original axes
    dp_Yce(z) = OrbLength(Phi_omt(z))*sin(Delta_Phi(z));
% Percentage of opening area
    Phi_A2(z) = Phi_Ace(z)-A1;
    PctOpen(z) = (Ac-Phi_A2(z))/Ac*100;
end
%=========================================================
```

Appendix E: MATLAB Script for Unbalance Model (Increments: Angular Position of Unbalance Force)

```
% ========================================================
%                Unbalance Model (Increments: Angular Position of Unbalance Force)
%========================================================
% The following is achieved in this script:
% 1. calculation of the effectual loading angle based on design parameters
% 2. determination of percentage of opening of crack of chosen configuration
% 3. determination of area moment of inertia of chosen configuration
% ========================================================

clc;clear all
% ------------------------------------------------------------------------------------------------------
% Set the Rotor Model Parameters:
% ------------------------------------------------------------------------------------------------------
% 1001 increments of shaft rotation between 0 and 2 pi
        increment = pi/1000;
% Rotational angle of shaft (0° to 360°)
        om_t = 0*pi/180;
% Force ratio is ratio of the disk weight forces to the unbalance force (0 to ∞)
        FR = 1 ;
% Crack depth ratio (0 to 1)
        mu = 0.5;
% Angle between rotating unbalance mass and crack direction (0° to 360°)
        beta = 0:increment:360*pi/180;
% Crack location ratio (0 to 1)
        Lemda = 0.5;
% ------------------------------------------------------------------------------------------------------
% Design Parameters in SI Units
% ------------------------------------------------------------------------------------------------------
% Length of shaft
        L = 0.724;
% Radius of shaft
        R = 6.35*10^-3;
% Density of shaft
        rho_S = 7800;
% Mass of shaft
        m_S = pi*R^2*L*rho_S;
% Force due to the shaft self-weight
        Fs= m_S*9.81;
% Thickness of disk
         t_d = 25*10^-3;
% Disk inner radius
        R_i = 13*10^-3;
% Disk outer radius
        R_o = 130*10^-3;
% Density of disk
        rho_d = 7800;
```

```
% Mass of the disk
        m_d = pi*(R_i-R_o)^2*t_d*rho_d;
% Gravity force due to disk weight
         Fmg = m_d*9.81;
% Crack Location
        L0 = L*Lemda;
% Balance disk distance from Support 1
        L1= L/4;
% Unbalance disk distance from Support 1
        L2= L-L1;
% ------------------------------------------------------------------------------------------------
% Crack Initial Geometric Parameters
% ------------------------------------------------------------------------------------------------
% Gamma, ratio between half-length of crack front to shaft radius
        ga = sqrt(mu*(2-mu));
% b, distance from origin to crack segment
        b = R*(1-mu);
% Crack half angle
        hAL = acos(1-mu);
% Ac, area of cracked segment when angular displacement is zero
        Ac = R^2*(acos(1-mu)-(1-mu)*ga);
% A1, area of uncracked segment when angular displacement is zero
        A1 = R^2*(pi-acos(1-mu)+(1-mu)*ga);
% e, centroid location of area A1 about Y-axis
        e = (2*R^3/(3*A1))*(ga)^3;
% ------------------------------------------------------------------------------------------------
% Unbalance force
        Fum = (Fs + 2*Fmg)/FR;
% ------------------------------------------------------------------------------------------------
% Moment Calculation
% ------------------------------------------------------------------------------------------------
% Moment due to shaft self-weight at any point
        Mz1 =  Fs*(6*L*L0-L^2-6*L0^2)/(12*L);
% Moment due to two balance disks
if L0 >= 0 && L0 < L1
% Between Support 1 to Disk 1
        Mz2= Fmg*L0 - Fmg*L1*(L-L1)/L;
% Between Disk 1 to Disk 2
elseif L0 >= L1 && L0 <= L2
        Mz2= Fmg*L1 - Fmg*L1*(L-L1)/L;
% Between Disk 2 to Support 2
elseif L0 > L2 && L0 <= L
        Mz2= Fmg*(L-L0) - Fmg*L1*(L-L1)/L;
end
% Moment due to unbalance mass
if L0 >= 0 && L0 <= L2
% Between Support 1 to unbalance disk in Z direction
        Mz3z= (Fum.*L1^2*L0*(L1+3*L2)/L^3-Fum.*L1^2*L2/L^2).*
                cos(om_t+beta);
% Between Support 1 to unbalance disk in Y direction
```

```
        My3y= (Fum.*L1^2*L0*(L1+3*L2)/L^3-Fum.*L1^2*L2/L^2).*
                sin(om_t+beta);
elseif L0 > L2 && L0 <= L
% Between unbalance disk to Support 2 in Z direction
        Mz3z= (Fum.*L2^2*(L-L0)*(3*L1+L2)/L^3-Fum.*L1*L2^2/L^2).*
                cos(om_t+beta);
% Between unbalance disk to Support 2 in Y direction
        My3y= (Fum.*L2^2*(L-L0)*(3*L1+L2)/L^3-Fum.*L1*L2^2/L^2).*
                sin(om_t+beta);
end
% Total moment calculations
        Mz = zeros(1,numel(om_t));
        My = zeros(1,numel(om_t));
% Moment in Z direction
        Mz = Mz1+Mz2+Mz3z;
% Moment in Y direction
        My = My3y;
% Resultant moment
        M = sqrt(Mz.^2+My.^2);
% Pre-allocate matrices
        DeltaPrim = zeros(1,numel(beta));
 for zv = 1:numel(beta)
% Direction of resultant moment with respect to Z axis
        DeltaPrim(zv) = atan(My(zv)/Mz(zv));
% Direction of the bending direction with respect to (-) Y-axis
    if Mz(zv) > 0 && My(zv) > 0
% if Mz is positive and My is positive h
        Delta(zv) = DeltaPrim(zv);
% if Mz is positive and My is negative
    elseif Mz(zv) > 0 && My(zv) < 0
        Delta(zv) =  2*pi+DeltaPrim(zv);
% if Mz is negative and My is positive
    elseif Mz(zv) < 0 && My(zv) > 0
        Delta(zv) =  pi+DeltaPrim(zv);
% if Mz is negative and My is negative
    elseif Mz(zv) < 0 && My(zv) < 0
        Delta(zv) = pi+  DeltaPrim(zv);
    elseif Mz(zv) < 0 && My(zv) == 0
        Delta(zv) = pi ;
    elseif Mz(zv) > 0 && My(zv) == 0
        Delta(zv) = 0 ;
    elseif Mz(zv) == 0 && My(zv) > 0
        Delta(zv) = 0.5*pi;
  elseif Mz(zv) == 0 && My(zv) < 0
        Delta(zv) = 3*pi/2;
 end
 end
% ------------------------------------------------------------------------------------------
```

```
% ------------------------------------------------------------------------------------------------
% Effectual Bending Angle Calculation
% ------------------------------------------------------------------------------------------------
% Angle between the bending direction and crack direction (anticlockwise):
   % Pre-allocate matrices
        Phi = zeros(1,numel(beta));
 for ui = 1:numel(beta)
        Phi(ui) = om_t-Delta(ui);
    if Phi(ui) <0
        Phi(ui) = 2*pi +Phi(ui);
    end
 end
% ------------------------------------------------------------------------------------------------
% Breathing Mechanism
% ------------------------------------------------------------------------------------------------
% Phi1, angle of rotation threshold: partially open/closed crack
        Phi1 = atan((e+b)/(R*ga));
% Phi2, angle of rotation threshold: fully closed crack
        Phi2 = ((pi/2)+acos(1-mu));
% 2pi-Phi2, angle of rotation threshold: partially open/closed crack
        Phi2_2pi = (2*pi-Phi2);
% 2pi-Phi1, angle of rotation threshold: fully open crack
        Phi1_2pi = (2*pi-Phi1);
% ------------------------------------------------------------------------------------------------
% Balance shaft data (for crack in a single location)
% Data calculated based on Appendix H MATLAB Script [17]
% Reading values from Excel file containing area values
% ------------------------------------------------------------------------------------------------
if mu == 0.25
% Crack cross-section closed area
        Ace = xlsread ('Ref_Data.xlsx','Mu=0.25','F6:F2006');
% X Moment of inertia of Ace about the centroid axis
        IXXAce = xlsread ('Ref_Data.xlsx','Mu=0.25','B6:B2006');
% Y Moment of inertia of Ace about the centroid axis
        IYYAce = xlsread ('Ref_Data.xlsx','Mu=0.25','C6:C2006');
% Coordinate of the centroid axis
        Xce = xlsread('Ref_Data.xlsx','Mu=0.25','D6:D2006');
        Yce = xlsread('Ref_Data.xlsx','Mu=0.25','E6:E2006');
end
if mu == 0.5
% Crack cross-section closed area
        Ace = xlsread ('Ref_Data.xlsx','Mu=0.5', 'F6:F2006');
% X moment of inertia of Ace about the centroid axis
        IXXAce = xlsread ('Ref_Data.xlsx','Mu=0.5', 'B6:B2006');
% Y moment of inertia of Ace about the centroid axis
        IYYAce = xlsread ('Ref_Data.xlsx','Mu=0.5', 'C6:C2006');
% Coordinate of the centroid axis
        Xce = xlsread ('Ref_Data.xlsx','Mu=0.5', 'D6:D2006');
        Yce = xlsread ('Ref_Data.xlsx','Mu=0.5', 'E6:E2006');
end
```

```
if mu == 0.75
% Crack cross-section closed area
        Ace = xlsread ('Ref_Data.xlsx','Mu=0.75', 'F6:F2006');
% X moment of inertia of Ace about the centroid axis
        IXXAce = xlsread ('Ref_Data.xlsx','Mu=0.75', 'B6:B2006');
% Y moment of inertia of Ace about the centroid axis
        IYYAce = xlsread ('Ref_Data.xlsx','Mu=0.75', 'C6:C2006');
% Coordinate of the centroid axis
        Xce = xlsread ('Ref_Data.xlsx','Mu=0.75', 'D6:D2006');
        Yce = xlsread ('Ref_Data.xlsx','Mu=0.75', 'E6:E2006');
end

if mu == 1
% Crack cross-section closed area
        Ace = xlsread ('Ref_Data.xlsx','Mu=1.0', 'F6:F2006');
% X moment of inertia of Ace about the centroid axis
        IXXAce = xlsread ('Ref_Data.xlsx','Mu=1.0', 'B6:B2006');
% Y moment of inertia of Ace about the centroid axis
        IYYAce = xlsread ('Ref_Data.xlsx','Mu=1.0', 'C6:C2006');
% Coordinate of the centroid axis
        Xce = xlsread ('Ref_Data.xlsx','Mu=1.0', 'D6:D2006');
        Yce = xlsread ('Ref_Data.xlsx','Mu=1.0', ‘E6:E2006’);
end

% No crack
if mu == 0
% Crack cross-section closed area
        Ace = xlsread ('Ref_Data.xlsx','Mu=0', 'F6:F2006');
% X moment of inertia of Ace about the centroid axis
        IXXAce = xlsread ('Ref_Data.xlsx','Mu=0', 'B6:B2006');
% Y moment of inertia of Ace about the centroid axis
        IYYAce = xlsread ('Ref_Data.xlsx','Mu=0', 'C6:C2006');
% Coordinate of the centroid axis
        Xce = xlsread ('Ref_Data.xlsx','Mu=0', 'D6:D2006');
        Yce = xlsread ('Ref_Data.xlsx','Mu=0', 'E6:E2006');
end
% ------------------------------------------------------------------------------------------
% Determination of Data for Different Crack Locations based on Effectual Bending
Angle
% ------------------------------------------------------------------------------------------
        tolerance = increment/2;
        Phi_Ace = zeros(1,numel(beta));
        OrbLength = sqrt(Yce.^2+Xce.^2);
        OrbAngle = atan(Yce./Xce);

for gh = 1:numel(beta)
   if Xce(gh) > 0 && Yce(gh) > 0;
        OrbAngle(gh) = OrbAngle(gh);
   elseif Xce(gh) < 0 && Yce(gh) > 0;
        OrbAngle(gh) = pi+OrbAngle(gh);
```

```
   elseif Xce(gh) == 0 && Yce(gh) == 0;
          OrbAngle(gh) = 0;
   elseif Xce(gh) == 0 && Yce(gh) > 0;
          OrbAngle(gh) = 0.5*pi;
   end
end
% ------------------------------------------------------------------------------------------
          om_t2 = 0: increment:2*pi;
          for z = 1:numel(beta);
             for q = 1:numel(om_t2);
                if abs(Phi(z)-om_t2(q)) <= tolerance
                   Phi_omt(z) = q;
                end
             end

% The values for IYYAce, IXXAce, Ace, Xce and Yce are rearranged based on
unbalance condition relative to the Ref data
             Phi_IYYAce(z) = IYYAce(Phi_omt(z));
             Phi_IXXAce(z) = IXXAce(Phi_omt(z));
             Phi_Ace(z) = Ace(Phi_omt(z));
             Phi_Xce(z) = Xce(Phi_omt(z));
             Phi_Yce(z) = Yce(Phi_omt(z));

% Calculates angle sum of delta and 'alpha'
          Delta_Phi(z) = OrbAngle(Phi_omt(z))+Delta(z);
% Calculates the radial distance of the centroid ('e')
          OrbLength_Phi(z) = OrbLength(Phi_omt(z));
% Calculates the new position of X-centroid value about original axes
          dp_Xce(z) = OrbLength(Phi_omt(z)).*cos(Delta_Phi(z));
% Calculates the new position of Y-centroid value about original axes
          dp_Yce(z) = OrbLength(Phi_omt(z)).*sin(Delta_Phi(z));
% Percentage of opening area
          Phi_A2(z) = Phi_Ace(z)-A1;
          PctOpen(z) = (Ac-Phi_A2(z))/Ac*100;
end
% ========================================================
```

Appendix F: MATLAB Script for Exact Breathing Crack Model

```
% ========================================================
%                Exact Breathing Crack Mode
%========================================================
% The script uses a series of iterative processes that approach the exact value of the desired following outputs:
% 1. determination of percentage of opening of crack of chosen configuration
% 2. determination of area moment of inertia of chosen configuration.
% ========================================================
The function takes the shaft rotation angle, radius and crack depth of a balance rotor and evaluates the area moment of inertia about the centroid X- and Y-axes of the crack section.
function [Ix Iy Ixy] = newBreathingFunctionXi( theta,R,mu )
% ------------------------------------------------------------------------------------------------
% To simplify the process, the shaft rotation angle is truncated to the range of 0 < theta < 2*pi
        while theta > 2*pi
           theta = theta - 2*pi;
        end

        while theta < 0
           theta = theta + 2*pi;
        end
% Large theta flag used to change the sign of Ixy and xi
        flip = 0;
 % If theta > pi, it is easier to perform the calculations for 2×pi-theta and then compensate for it by changing the sign of the product of area at the end of the script
        if theta > pi
           theta = 2*pi - theta;
           flip = 1;
        end
% ------------------------------------------------------------------------------------------------
% Relative width of the crack front
        gamma = sqrt(mu*(2-mu));
% area of uncracked region
        A1 = R^2*(pi - acos(1-mu)+(1-mu)*gamma);
% distance between shaft axis and centroid of section
        e = 2*R^3*gamma^3/3/A1 ;
% this is the angular width of the crack front and is not to be confused with alpha, used to describe the principal axes for which this variable name is used later
        alpha = 2*acos(1-mu);
% X coordinate of the centroid for the uncracked region
        X1 = -e*sin(theta);
% Y coordinate of the centroid for the uncracked region
        Y1 = e*cos(theta);

diff = 1;
% is equivalent to A1*e^2
                A1ee = 4/9/(pi-acos(1-mu)+(1-mu)*gamma)*gamma^6;
```

```
First principal area moment of inertia for the uncracked region
        Iu = pi/4 - 1/12*((1-mu)*(2*mu^2-4*mu-3)*gamma + 3*asin (gamma));
% Second principal area moment of inertia for the uncracked region
        Iv = pi/8 + 1/4*((1-mu)*(2*mu^2-4*mu+1)*gamma + asin(1-mu)) - A1ee;
        RI = Iu/Iv;

% theta1 is the angle at which the crack starts to close. There is no closed-form
expression for theta1. Instead, an iterative process is used that will converge on
theta1. An initial estimate value for theta1 is used to start the process

 % initial estimate for theta1
        theta1 = pi/4;
        while diff > 0.0001
           x1 = -e*sin(theta1);
           y1 = e*cos(theta1);
           x2 = sin(theta1 + alpha/2);
           y2 = -cos(theta1 + alpha/2);
           theta11 = atan((y2-y1)/(x2-x1))+ pi/2 - atan(RI*tan(pi/2-theta1));
           diff = abs(theta11-theta1);
           theta1 = theta11;
        end

% theta1 is incremented by 0.01 degree to prevent program errors in the area
calculations when theta is close to theta1
        theta1 = theta1 + 0.01*pi/180;
% angle at which the crack is fully closed
        theta2 = pi/2+acos(1-mu);
% area moment for uncracked shaft
        I = pi*R^4/4;
% area moment for crack region about X-axis
        Ixc = pi*R^4/8-R^4/4*((1-mu)*(2*mu^2-4*mu+1)*gamma+asin(1-mu));
% area moment for crack region about Y-axis
        Iyc = R^4/12*((1-mu)*(2*mu^2-4*mu-3)*gamma+3*asin(gamma));
% area moment for crack cross-section closed area  about x-axis
        I1 = I - Ixc;
% area moment for crack cross-section closed area  about y-axis
        I2 = I - Iyc;
% area moment for A1 about centroid X-axis
        I1c = I1 - A1*e^2;
% area moment for A1 about centroid y-axis
        I2c = I2;
% is the crack fully open?
        if (theta <= theta1)
 % the centroid area moment of inertia are found by performing coordinate rotations
on the principal area moment of inertia for the uncracked region
        Ix = (I2c + I1c)/2 - (I2c - I1c)/2*cos(2*theta);
        Iy = (I2c + I1c)/2 + (I2c - I1c)/2*cos(2*theta);
        Ixy = (I2c - I1c)/2*sin(2*theta);
```

```
% is the crack fully closed?
        elseif (theta >= theta2)
        Ix = pi*R^4/4;
        Iy = pi*R^4/4;
        Ixy = 0;
 else
% if the crack is neither fully open nor fully closed, it must be in a partially open state. Evaluating Ix, Iy and Ixy in this state requires that the centroid coordinates and the neutral axis. inclination be found. These can only be found using initial estimatees for both parameters and iteratively revaluating them.
% initial estimate value for neutral axis inclination
        xi = 0*pi/180;
% once this term approaches zero, xi will have converged
        deltaxi = 1;
while deltaxi > 0.0001
% initial estimate for the vertical centroid coordinate
        Yce = Y1;
% initial estimate for the horizontal centroid coordinate
        Xce = X1;
        deltaX = 1;
        deltaY = 1;

      while deltaX > 0.0001 || deltaY > 0.0001
        a1 = R*sin(theta + alpha/2);
        b1 = -R*cos(theta + alpha/2);
        m1 = tan(xi);
        v1 = Yce - m1*Xce;

        a = 1 + m1^2;
        d = 2*m1*v1;
        c = v1^2 - R^2;
        a2 = (-d + sqrt(d^2 - 4*a*c))/2/a;
        b2 = sqrt(R^2 - a2^2);

        if theta ~= pi/2
          m2 = tan(theta);
          v2 = b1 - m2*a1;
          a3 = (v2-v1)/(m1-m2);
          b3 = m1*a3 + v1;
          a4 = (b2-b3)/m2 + a3;
        else
          a3 = R*(1-mu);
          b3 = m1*a3 + v1;
          a4 = a3;
        end

        b4 = b2;
        b5 = b2;
```

```
        A3      =       0.5*(a2*sqrt(R^2-a2^2)-a1*sqrt(R^2-a1^2)+R^2*(asin(a2/R)-
asin(a1/R)))+b2*(a1-a2);
        Y3 = 1/6/A3*(a1^3-a2^2+3*(a2-a1)*(R^2-b2^2));
        X3 = 1/3/A3*((sqrt(R^2-a1^2))^3-(sqrt(R^2-a2^2))^3-3*b2*(a2-a1));

        A4 = 0.5*(b1-b2)*(a1-a4);
        X4 = a4 + 2*(a1-a4)/3;
        Y4 = b2 + (b1-b2)/3;

        A5 = (b2 - b3)*(a2/2 - a4/2);
        Y5 = (2*b2)/3 - (2*b3)/3 + b3;
        X5 = a2/3 - (2*a3)/3 + a4/3 + a3;

% new estimated value for Xce and Yce
        XceN = (A1*X1 + A3*X3 + A4*X4 + A5*X5)/(A1 + A3 + A4 + A5);
        YceN = (A1*Y1 + A3*Y3 + A4*Y4 + A5*Y5)/(A1 + A3 + A4 + A5);
% calculate the proportional change in Xce
        deltaX = abs(1-XceN/Xce);
        deltaY = abs(1-YceN/Yce);
        Xce = (0.5*(XceN+Xce));
        Yce = (0.5*(YceN+Yce));
end

% total area of the crack region
        A2o = pi*R^2 - A1;
% open area of the crack region
        A2t = A2o - A3 - A4 - A5;
% open proportion of crack
        AcoP = A2t/A2o;

% rotating the area moment of inertia of the uncracked region
        Ix1 = (I2c + I1c)/2 - (I2c - I1c)/2*cos(2*theta);
        Iy1 = (I2c + I1c)/2 + (I2c - I1c)/2*cos(2*theta);
        Ixy1 = (I2c - I1c)/2*sin(2*theta);

% area moment and product of inertia for A3
        Ix3=1/24*(2*(a2*(sqrt(R^2-a2^2))^3-a1*(sqrt(R^2-a1^2))^3) +3*R^2*
                (a2*sqrt(R^2-a2^2)+R^2*asin(a2/R)-a1*sqrt(R^2-a1^2)-
                R^2*asin(a1/R)) -b2^2*(a2-a1)) - A3*Y3^2;
        Iy3=1/24*(6*a1*(sqrt(R^2-a1^2))^3-6*a2*(sqrt(R^2-a2^2))^3+
                3*R^2*(a2*sqrt(R^2-a2^2)-a1*sqrt(R^2-a1^2) + R^2*(asin(a2/R)
                -asin(a1/R)))+ 8*b2*(a2^3-a1^3)) - A3*X3^2;
        Ixy3 = 1/4*(a2^2 - a1^2)*(R^2 - b2^2) - 1/8*(a2^4 - a1^4) - A3*X3*Y3;

% area moment and product of inertia for A4
      Ix4 = 1/36*(b1-b2)^3*(a1-a4);
      Iy4 = 1/36*(b1-b2)*(a1-a4)^3;
      Ixy4 = 1/72*(b1-b2)^2*(a1-a4)*(a1-a4);
```

```
% area moment and product of inertia for A5
        Ix5 = ((a2 - a4)*(b2 - b3)^3)/36;
        Iy5 = -((a2 - a4)*(b2 - b3)*(- a2^2 + a2*a3 + a2*a4 - a3^2 + a3*a4 -
        a4^2))/36;
        Ixy5 = ((a2 - a4)*(b2 - b3)^2*(a2 - 2*a3 + a4))/72;

% summing the area moment and products of inertia for all areas
% about the centroid of the effective section
        Ix = Ix1 + Ix3 + Ix4 + Ix5 + A1*(Yce - Y1)^2+ A3*(Yce - Y3)^2 +
             A4*(Yce - Y4)^2 + A5*(Yce - Y5)^2;
        Iy = Iy1 + Iy3 + Iy4 + Iy5 + A1*(Xce - X1)^2+ A3*(Xce - X3)^2 +
             A4*(Xce - X4)^2 + A5*(Xce - X5)^2;
        Ixy = Ixy1 + Ixy3 + Ixy4 + Ixy5 + A1*(X1 - Xce)*(Y1 - Yce) +
              A3*(X3 - Xce)*(Y3 - Yce) + A4*(X4 - Xce)*(Y4 - Yce) +
              A5*(X5 - Xce)*(Y5 - Yce);

% evaluating the principal area moment of inertia and the
% inclination of the principal axes
        [ Iu Iv alphaP ] = PMA( Ix, Iy, Ixy, 0, 0 );

% revaluating the inclination of the neutral axis and comparing it with the previous
value
        xiN = atan(Iu/Iv*tan(abs(alphaP))) - abs(alphaP);
        deltaxi = abs(xi-xiN);
        damp = 2;
        xi = (1/damp)*xiN + (1-1/damp)*xi;
end
end
        if flip == 1
           Ixy = -Ixy;
        end
end

function [ Iu Iv alpha ] = PMA( IXX, IYY, IXY, phi, theta )

% This function calculates the principal area moment of inertia from the centroid
area moment and product of inertia
        Iu = (IXX + IYY)/2 + sqrt((IXX - IYY)^2/4 + IXY^2);
        Iv = (IXX + IYY)/2 - sqrt((IXX - IYY)^2/4 + IXY^2);

         if IXX == IYY
           if IXY < 0
              alpha = pi/4;
           elseif IXY == 0
              alpha = 0;
           else
              alpha = 3*pi/4;
           end
        elseif IXX > IYY
```

```
beta = abs(atan(2*IXY/(IXX-IYY)));
   if IXY < 0
      alpha = 0.5*beta;
   elseif IXY == 0
      alpha = 0;
   else
      alpha = pi - 0.5*beta;
   end
else

 beta = abs(atan(2*IXY/(IXX-IYY)));
   if IXY < 0
      alpha = pi/2 - 0.5*beta;
   elseif IXY == 0
      alpha = pi/2;
   else
      alpha = pi/2 + 0.5*beta;
   end
end

alpha = alpha + ( theta - phi);

while alpha < -pi/2
   alpha = alpha + pi;
end

while alpha > pi/2
   alpha = alpha - pi;
end

end
```

Appendix G: MATLAB Script for Adopted Balance Model

```
%=============================================================
%                  Adopted Balance Model (Crack at a Fixed Point)
%=============================================================
% The following is achieved in this script:
% 1. determination of percentage of opening of crack
% 2. determination of area moment of inertia
% ============================================================
clc;clear all
% ------------------------------------------------------------------------------------------------
% Set the Rotor Model Parameters:
% ------------------------------------------------------------------------------------------------
% Radius
        R = 6.35*10^-3;
% HH is the nondimensional crack depth
        HH=.5;
% ------------------------------------------------------------------------------------------------
% Alpha is 2x 'alpha/2'
        Alpha=2*acos(1-HH);
% bb is 'b', the radius of the inner circle
        bb=R*cos(Alpha/2);
% 'Ac' here is equivalent to A1
        Ac=R^2*(pi-Alpha/2)+bb*(R^2-bb^2)^.5;
% Yc is the Y value of e
        Yc=(2/(3*Ac))*(R^2-bb^2)^(3/2);
        e=Yc;
        BBB=asin(e/R);
% th1 is correct
        TH1= atan((Yc+R-R*HH)/(R*(HH*(2-HH))^.5));
% th2 is correct
        TH2=(pi/2+acos(1-HH));
% corresponds to the value's' - half crack front length
        ss=R*sin(Alpha/2);
% IA3a is Icx
        IA3a=(1/4)*pi*R^4-((pi*R^4/8)+(1/4)*(((R^2-bb^2)^.5)*(bb*R^2-2*bb^3)-
                (R^4)*asin(bb/R)));
% IA3b is Icy
        IA3b=(1/4)*pi*R^4-(-(1/12)*(-3*(R^4)*asin(ss/R)+((R^2-
                 ss^2)^.5)*(3*ss*(R^2)-6*ss^3)+8*bb*ss^3));
% IA3xx and IA3yy are the exact area moment of inertia
        IA3xx=IA3a-Ac*Yc^2;
        IA3yy=IA3b;
 % 'Gama' is delta
        Gama=asin(Yc/R);
% 'Gama1' is maybe convenience parameter
        Gama1=TH1+Alpha/2-pi/2;
% Initial Ac value
        Ac(1)=Ac;
% Initial Yce value
```

```
        Yc(1)=Yc;
% Appears to be some kind of check - the expression results in the value for th1
        pi/2-(Alpha/2-Gamal)

 for jj=1:2001
% Populating 'Ac' with all initial values of Ac
        Ac(jj)=Ac(1);
% Shaft rotation vector (0, pi/100, 2pi/100, ... etc.)
        Theta(jj)=pi*(jj-1)/1000;

% if condition: less than 180 and greater than th2 – therefore, refers to closed region
if ((Theta(jj) <= pi) && (Theta(jj)>(pi/2+Alpha/2)))
% IX and IY for full circle
        IX(jj)=pi*R^4/4;
        IY(jj)=pi*R^4/4;
        XX(jj)=0;
        YY(jj)=0;
        IAlx(jj)=0;
        IAly(jj)=0;
% Area of full circle
        AA(jj)=pi*R^2;
        trackAA(jj)=AA(jj);
% between zero and theta 1
elseif Theta(jj) < TH1
% setting 'Ac' array to 'initial' value of A1
        Ac(jj)=Ac(1);
% Yce is equal to e [will vary based on angle when used in equations]
        Yc(jj)=Yc(1);
        IX(jj)=(1/2)*((IA3a+IA3b)+(IA3a-IA3b)*cos(2*Theta(jj)))-
        Ac(jj)*(Yc(jj)*cos(Theta(jj)))^2;
        IY(jj)=(1/2)*((IA3a+IA3b)-(IA3a-IA3b)*cos(2*Theta(jj)))-
        Ac(jj)*(Yc(jj)*sin(Theta(jj)))^2;
% Orbits are as expected for X and Y (pre-th1)
        XX(jj)=-e*sin(Theta(jj));
        YY(jj)=e*cos(Theta(jj));
% Values of Yce for pre-th1
        Gama=asin(YY(jj)/R);
        trackGama(jj)=Gama;
% To print values of theta
        Theta(jj);
% Parameter 'AA' values are copied from 'Ac'. Therefore, AA is A1
        AA(jj)=Ac(jj);
        trackAA(jj)=AA(jj);
% FFF carries values of delta
        FFF=Gama;
% Range between th1 and 90 degrees
elseif ((Theta(jj) >= TH1) && (Theta(jj)<pi/2))
        trackTheta(jj) = Theta(jj);
        GGG=Gama;
        trackGGG(jj)=GGG;
```

```
% beta is the same as in the paper except for 'Gama' question
        Beta(jj)=Theta(jj)-pi/2+(Alpha/2-Gama);
% b1 should be equivalent to Yce
        b1(jj)=R*sin(Gama);
% b2 is the same as in the paper
        b2(jj)=R*sin(Gama+Beta(jj));
% a1 is the same as in the paper
        a1(jj)=R*cos(Gama+Beta(jj));
        tracka1(jj)=a1(jj);
% a2 is the same as in the paper
        a2(jj)=R*cos(Gama);
% a0 is the same as in the paper (tan portion is equation to tan(rho))
        ao(jj)=a1(jj)-(b2(jj)-b1(jj))*tan(Alpha/2-Gama-Beta(jj));
        trackao(jj)=ao(jj);
        rho(jj) = Alpha/2-Gama-Beta(jj);
%Moment of inertia of Al
        ss(jj)=a1(jj);
        Ia1(jj)=-(1/24)*(-3*(R^4)*asin(ss(jj)/R)+((R^2-...
        ss(jj)^2)^.5)*(3*ss(jj)*(R^2)-6*ss(jj)^3)+8*b1(jj)*ss(jj)^3);
        ss(jj)=a2(jj);
        Ia2(jj)=-(1/24)*(-3*(R^4)*asin(ss(jj)/R)+((R^2-...
        ss(jj)^2)^.5)*(3*ss(jj)*(R^2)-6*ss(jj)^3)+8*b1(jj)*ss(jj)^3);
        IAly(jj)=Ia2(jj)-Ia1(jj);
        ss(jj)=b1(jj);
        Ib1(jj)=-(1/24)*(-3*(R^4)*asin(ss(jj)/R)+((R^2-...
        ss(jj)^2)^.5)*(3*ss(jj)*(R^2)-6*ss(jj)^3)+8*a1(jj)*ss(jj)^3);
        ss(jj)=b2(jj) ;
        Ib2(jj)=-(1/24)*(-3*(R^4)*asin(ss(jj)/R)+((R^2-...
        ss(jj)^2)^.5)*(3*ss(jj)*(R^2)-6*ss(jj)^3)+8*a1(jj)*ss(jj)^3);
        IAlx(jj)=Ib2(jj)-Ib1(jj) ;
% Centroids of Al, XA1 and XA2
% This is the evaluation for A3
        Aa1(jj) = ((R^2)*asin(a1(jj)/R)+a1(jj)*((R^2-a1(jj)^2)^.5)-2*b1(jj)*a1(jj))/2;
        Aa2(jj)=((R^2)*asin(a2(jj)/R)+a2(jj)*((R^2-a2(jj)^2)^.5)-2*b1(jj)*a2(jj))/2;
        A1(jj)=Aa2(jj)-Aa1(jj);
% To check
Ab1(jj)=((R^2)*asin(b1(jj)/R)+b1(jj)*((R^2-b1(jj)^2)^.5)-2*a1(jj)*b1(jj))/2;
Ab2(jj)=((R^2)*asin(b2(jj)/R)+b2(jj)*((R^2-b2(jj)^2)^.5)-2*a1(jj)*b2(jj))/2;
A1check(jj)=Ab2(jj)-Ab1(jj);
xa1(jj)=-(1/A1(jj))*(1/6)*(2*(R^2-a1(jj)^2)^.5*(R^2- a1(jj)^2)+3*b1(jj)*a1(jj)^2) ;
xa2(jj)=-(1/A1(jj))*(1/6)*(2*(R^2-a2(jj)^2)^.5*(R^2-a2(jj)^2)+3*b1(jj)*a2(jj)^2);
XA1(jj)=xa2(jj)-xa1(jj);
xb1(jj)=-(1/A1(jj))*(1/6)*(2*(R^2-b1(jj)^2)^.5*(R^2-b1(jj)^2)+3*a1(jj)*b1(jj)^2);
xb2(jj)=-(1/A1(jj))*(1/6)*(2*(R^2-b2(jj)^2)^.5*(R^2-b2(jj)^2)+3*a1(jj)*b2(jj)^2);
YA1(jj)=xb2(jj)-xb1(jj);
```

```
% Triangular cross-section
% 'XA2' is X4
        XA2(jj)=ao(jj)+(2/3)*(a1(jj)-ao(jj));
        XA2track(jj) = XA2(jj);
% 'YA2' is Y4, same as in the paper
        YA2(jj)=b1(jj)+(1/3)*(b2(jj)-b1(jj));
% A2 is A4
        A2(jj)=(1/2)*(b2(jj)-b1(jj))*(a1(jj)-ao(jj));
        IA2x(jj)=(1/36)*(b2(jj)-b1(jj))^3*(a1(jj)-ao(jj))+A2(jj)*YA2(jj)^2;
        IA2y(jj)=(1/36)*(b2(jj)-b1(jj))*(a1(jj)-ao(jj))^3+A2(jj)*XA2(jj)^2;
        IA3x(jj)=(1/2)*((IA3a+IA3b)+(IA3a-IA3b)*cos(2*Theta(jj)));
        IA3y(jj)=(1/2)*((IA3a+IA3b)-(IA3a-IA3b)*cos(2*Theta(jj)));
        XA3(jj)=-e*sin(Theta(jj));
        YA3(jj)=e*cos(Theta(jj));
        AA(jj)=Ac(jj)+A1(jj)+A2(jj) ;
        trackAA(jj)=AA(jj);
        XX(jj)=(XA1(jj)*A1(jj)+XA2(jj)*A2(jj)+XA3(jj)*Ac(jj))/AA(jj) ;
        YY(jj) = (YA1(jj)*A1(jj)+YA2(jj)*A2(jj)+YA3(jj)*Ac(jj))/AA(jj) ;
        Gama=asin(YY(jj)/R);
        IXX(jj)=IA3x(jj)+IA2x(jj)+IAlx(jj);
        IYY(jj)=IA3y(jj)+IA2y(jj)+IAly(jj);
        IX(jj)=IXX(jj)-AA(jj)*YY(jj)^2;
        IY(jj)=IYY(jj)-AA(jj)*XX(jj)^2;
        elseif ((Theta(jj) >= (pi/2)) && (Theta(jj)<(pi-Alpha/2)))
        trackTheta2(jj) = Theta(jj);
        Beta(jj)=Theta(jj)+Alpha/2-Gama-pi/2;
        GGG=Gama;
        b1(jj)=R*sin(Gama);
        b2(jj)=R*sin(Gama+Beta(jj));
        a1(jj)=R*cos(Gama+Beta(jj));
        tracka1(jj)=a1(jj);
        a2(jj)=R*cos(Gama);
        ao(jj)=a1(jj)+(b2(jj)-b1(jj))*tan(-Alpha/2+Gama+Beta(jj));
        trackao(jj)=ao(jj);
        rho(jj)=-Alpha/2+Gama+Beta(jj);
%Moment of inertia of Al
        ss(jj)=a1(jj);
        Ia1(jj)=-(1/24)*(-3*(R^4)*asin(ss(jj)/R)+((R^2-...
        ss(jj)^2)^.5)*(3*ss(jj)*(R^2)-6*ss(jj)^3)+8*b1(jj)*ss(jj)^3);
        ss(jj)=a2(jj);
        Ia2(jj)=-(1/24)*(-3*(R^4)*asin(ss(jj)/R)+((R^2-...
        ss(jj)^2)^.5)*(3*ss(jj)*(R^2)-6*ss(jj)^3)+8*b1(jj)*ss(jj)^3);
        IAly(jj)=Ia2(jj)-Ia1(jj);
        ss(jj)=b1(jj);
        Ib1(jj)=-(1/24)*(-3*(R^4)*asin(ss(jj)/R)+((R^2-...
        ss(jj)^2)^.5)*(3*ss(jj)*(R^2)-6*ss(jj)^3)+8*a1(jj)*ss(jj)^3);
        ss(jj)=b2(jj);
        Ib2(jj)=-(1/24)*(-3*(R^4)*asin(ss(jj)/R)+((R^2-...
        ss(jj)^2)^.5)*(3*ss(jj)*(R^2)-6*ss(jj)^3)+8*a1(jj)*ss(jj)^3);
```

```
        IAlx(jj)=Ib2(jj)-Ib1(jj) ;
% Centroids of Al, XA1 and XA2
        Aa1(jj)=((R^2)*asin(a1(jj)/R)+a1(jj)*((R^2-a1(jj)^2)^.5)-2*b1(jj)*a1(jj))/2;
        Aa2(jj)=((R^2)*asin(a2(jj)/R)+a2(jj)*((R^2-a2(jj)^2)^.5)-2*b1(jj)*a2(jj))/2;
        A1(jj)=Aa2(jj)-Aa1(jj);
% Check
Ab1(jj)=((R^2)*asin(b1(jj)/R)+b1(jj)*((R^2-b1(jj)^2)^.5)-2*a1(jj)*b1(jj))/2;
Ab2(jj)=((R^2)*asin(b2(jj)/R)+b2(jj)*((R^2-b2(jj)^2)^.5)-2*a1(jj)*b2(jj))/2;
A1check(jj)=Ab2(jj)-Ab1(jj);
xa1(jj)=-(1/A1(jj))*(1/6)*(2*(R^2-a1(jj)^2)^.5*(R^2-a1(jj)^2)+3*b1(jj)*a1(jj)^2);
xa2(jj)=-(1/A1(jj))*(1/6)*(2*(R^2-a2(jj)^2)^.5*(R^2-a2(jj)^2)+3*b1(jj)*a2(jj)^2);
XA1(jj)=xa2(jj)-xa1(jj);
xb1(jj)=-(1/A1(jj))*(1/6)*(2*(R^2-b1(jj)^2)^.5*(R^2-b1(jj)^2)+3*a1(jj)*b1(jj)^2);
xb2(jj)=-(1/A1(jj))*(1/6)*(2*(R^2-b2(jj)^2)^.5*(R^2-b2(jj)^2)+3*a1(jj)*b2(jj)^2);
YA1(jj)=xb2(jj)-xb1(jj);

% Triangular cross-section
        XA2(jj)=a1(jj)+(1/3)*(ao(jj)-a1(jj));
        XA2track(jj) = XA2(jj);
        YA2(jj)=b1(jj)+(1/3)*(b2(jj)-b1(jj));
        A2(jj)=(1/2)*(b2(jj)-b1(jj))*(ao(jj)-a1(jj));
        IA2x(jj)=(1/36)*(b2(jj)-b1(jj))^3*(ao(jj)-a1(jj))+A2(jj)*YA2(jj)^2;
        IA2y(jj)=(1/36)*(b2(jj)-b1(jj))*(ao(jj)-a1(jj))^3+A2(jj)*XA2(jj)^2;
        IA12x(jj)=IAlx(jj)-IA2x(jj);
        IA12y(jj)=IAly(jj)-IA2y(jj) ;
        A12(jj)=A1(jj)-A2(jj);
        XA12(jj)=(A1(jj)*XA1(jj)-A2(jj)*XA2(jj))/A12(jj);
        YA12(jj)=(A1(jj)*YA1(jj)-A2(jj)*YA2(jj))/A12(jj);
        IA3x(jj)=(1/2)*((IA3a+IA3b)+(IA3a-IA3b)*cos(2*Theta(jj)));
        IA3y(jj)=(1/2)*((IA3a+IA3b)-(IA3a-IA3b)*cos(2*Theta(jj)));
        XA3(jj)=-e*sin(Theta(jj));
        YA3(jj)=e*cos(Theta(jj));
        AA(jj)=Ac(jj)+A12(jj) ;
        trackAA(jj)=AA(jj);
        XX(jj)=(XA12(jj)*A12(jj)+XA3(jj)*Ac(jj))/AA(jj);
        trackXX(jj) = XX(jj);
        YY(jj)=(YA12(jj)*A12(jj)+YA3(jj)*Ac(jj))/AA(jj);
        trackYY(jj) = YY(jj);
        Gama=asin(YY(jj)/R);
        IXX(jj)=IA3x(jj)+IA12x(jj);
        IYY(jj)=IA3y(jj)+IA12y(jj);
        IX(jj)=IXX(jj)-AA(jj)*YY(jj)^2;
        IY(jj)=IYY(jj)-AA(jj)*XX(jj)^2;
        elseif ((Theta(jj)>=pi-Alpha/2) && (Theta(jj)<(pi/2+Alpha/2)))
        trackTheta3(jj) = Theta(jj);
        Beta(jj)=Theta(jj)+Alpha/2-Gama-pi/2;
        fff=Gama;
        trackGama2(jj) = Gama;
        b1(jj)=R*sin(Gama);
        b2(jj)=R*sin(Gama+Beta(jj));
```

```
        a1(jj)=R*cos(Gama+Beta(jj));
        tracka1(jj)=a1(jj);
        a2(jj)=R*cos(Gama);
        ao(jj)=a1(jj)+(b2(jj)-b1(jj))*tan(-Alpha/2+Gama+Beta(jj));
        trackao(jj)=ao(jj);
        rho(jj) = -Alpha/2+Gama+Beta(jj);

% Moment of inertia and centroid of Al
IAly(jj)=-(1/12)*(-3*(R^4)*asin(a2(jj)/R)+((R^2-a2(jj)^2)^.5)*(3*a2(jj)*(R^2)-
6*a2(jj)^3)+8*b1(jj)*a2(jj)^3);
IAlx(jj)=(pi*R^4/8)+(1/4)*(((R^2-b1(jj)^2)^.5)*(b1(jj)*R^2-2*b1(jj)^3)-
R^4*asin(b1(jj)/R));
A1(jj)=pi*(R^2)/2-((R^2)*asin(b1(jj)/R)+b1(jj)*((R^2-b1(jj)^2)^.5));
XA1(jj)=0;
YA1(jj)=(1/A1(jj))*(2*(R^2-b1(jj)^2)^.5*(R^2-b1(jj)^2))/3;

% Triangular cross-section A2
        XA2(jj)=a1(jj)+(1/3)*(ao(jj)-a1(jj));
        XA2track(jj) = XA2(jj);
        YA2(jj)=b1(jj)+(1/3)*(b2(jj)-b1(jj));
        A2(jj)=(1/2)*(b2(jj)-b1(jj))*(ao(jj)-a1(jj));
        IA2x(jj)=(1/36)*(b2(jj)-b1(jj))^3*(ao(jj)-a1(jj))+A2(jj)*YA2(jj)^2;
        IA2y(jj)=(1/36)*(b2(jj)-b1(jj))*(ao(jj)-a1(jj))^3+A2(jj)*XA2(jj)^2;
% Moment of inertia of Segment AA3
        ss(jj)=abs(a1(jj));
        Ia1(jj)=-(1/24)*(-3*(R^4)*asin(ss(jj)/R)+((R^2-ss(jj)^2)^.5)*(3*ss(jj)*(R^2)-
        6*ss(jj)^3)+8*b1(jj)*ss(jj)^3);
        ss(jj)=a2(jj);
        Ia2(jj)=-(1/24)*(-3*(R^4)*asin(ss(jj)/R)+((R^2-ss(jj)^2)^.5)*(3*ss(jj)*(R^2)-
        6*ss(jj)^3)+8*b1(jj)*ss(jj)^3);
        IAA3y(jj)=Ia2(jj)-Ia1(jj);
        ss(jj)=b1(jj);
        Ib1(jj)=-(1/24)*(-3*(R^4)*asin(ss(jj)/R)+((R^2-ss(jj)^2)^.5)*(3*ss(jj)*(R^2)-
        6*ss(jj)^3)-8*a1(jj)*ss(jj)^3);
        ss(jj)=b2(jj);
        Ib2(jj)=-(1/24)*(-3*(R^4)*asin(ss(jj)/R)+((R^2-ss(jj)^2)^.5)*(3*ss(jj)*(R^2)-
        6*ss(jj)^3)-8*a1(jj)*ss(jj)^3);
        IAA3x(jj)=Ib2(jj)-Ib1(jj);
% Centroids of Al, XA1 and XA2
        Aa1(jj)=((R^2)*asin(-a1(jj)/R)-a1(jj)*((R^2-a1(jj)^2)^.5)+2*b1(jj)*a1(jj))/2;
        Aa2(jj)=((R^2)*asin(a2(jj)/R)+a2(jj)*((R^2-a2(jj)^2)^.5)-2*b1(jj)*a2(jj))/2;
        AA3(jj)=Aa2(jj)-Aa1(jj);
% Check
Ab1(jj)=((R^2)*asin(b1(jj)/R)+b1(jj)*((R^2-b1(jj)^2)^.5)+2*a1(jj)*b1(jj))/2;
Ab2(jj)=((R^2)*asin(b2(jj)/R)+b2(jj)*((R^2-b2(jj)^2)^.5)+2*a1(jj)*b2(jj))/2;
AA3check(jj)=Ab2(jj)-Ab1(jj);
xa1(jj)=-(1/AA3(jj))*(1/6)*(2*(R^2-a1(jj)^2)^.5*(R^2-a1(jj)^2)+3*b1(jj)*a1(jj)^2);
xa2(jj)=-(1/AA3(jj))*(1/6)*(2*(R^2-a2(jj)^2)^.5*(R^2-a2(jj)^2)+3*b1(jj)*a2(jj)^2);
XAA3(jj)=-(xa2(jj)-xa1(jj));
xb1(jj)=-(1/AA3(jj))*(1/6)*(2*(R^2-b1(jj)^2)^.5*(R^2-b1(jj)^2)-3*a1(jj)*b1(jj)^2);
```

```
xb2(jj)=-(1/AA3(jj))*(1/6)*(2*(R^2-b2(jj)^2)^.5*(R^2-b2(jj)^2)-3*a1(jj)*b2(jj)^2);
YAA3(jj)=xb2(jj)-xb1(jj);
% Moment AND Centroids AA=A1-A2-AA3
        IAAx(jj)=IAlx(jj)-IA2x(jj)-IAA3x(jj);
        IAAy(jj)=IAly(jj)-IA2y(jj)-IAA3y(jj);
        A123(jj)=A1(jj)-A2(jj)-AA3(jj);
        XA123(jj) = (A1(jj)*XA1(jj)-A2(jj)*XA2(jj)-AA3(jj)*XAA3(jj))/A123(jj) ;
        YA123(jj)=(A1(jj)*YA1(jj)-A2(jj)*YA2(jj)-AA3(jj)*YAA3(jj))/A123(jj);
        IA3x(jj)=(1/2)*((IA3a+IA3b)+(IA3a-IA3b)*cos(2*Theta(jj)));
        IA3y(jj)=(1/2)*((IA3a+IA3b)-(IA3a-IA3b)*cos(2*Theta(jj)));
        XA3(jj)=-e*sin(Theta(jj));
        YA3(jj)=e*cos(Theta(jj));
        AA(jj)=Ac(jj)+A123(jj);
        trackAA(jj)=AA(jj);
        XX(jj)=(XA123(jj)*A123(jj)+XA3(jj)*Ac(jj))/AA(jj);
        trackXX2(jj) = XX(jj);
        YY(jj)=(YA123(jj)*A123(jj)+YA3(jj)*Ac(jj))/AA(jj);
        trackYY2(jj) = YY(jj);
        Gama=asin(YY(jj)/R);
        IXX(jj)=IA3x(jj)+IAAx(jj);
        IYY(jj)=IA3y(jj)+IAAy(jj);
        IX(jj)=IXX(jj)-AA(jj)*YY(jj)^2;
        IY(jj)=IYY(jj)-AA(jj)*XX(jj)^2;
        elseif ((Theta(jj) <= (pi)) && (Theta(jj)>=(pi/2+Alpha/2)))
        IX(jj)=pi*R^4/4;
        IY(jj)=pi*R^4/4;
        IAlx(jj)=0;
        IAly(jj)=0;
        IA2x(jj)=0;
        IA2y(jj)=0;
        AA(jj)=pi*R^2;
        trackAA(jj)=AA(jj);
        else
        kk=2002-jj;
        XX(jj)=-XX(kk);
        YY(jj)=YY(kk);
        IX(jj)=IX(kk);
        IY(jj)=IY(kk);
        AA(jj)=AA(kk);
        trackAA(jj)=AA(jj);
        end
        RXY(jj)=(IX(jj)+IY(jj));
        RX(jj)=IX(jj)/AA(jj);
        RY(jj)=IY(jj)/AA(jj);
        end
        Ace = trackAA;
        A3A4 = Ace - Ac(1);
        A0 = (pi*R^2-Ac(1))-A3A4;
        Apct = (A0./(pi*R^2-Ac(1)))*100;
        I=(1/4)*pi*R^4;
```